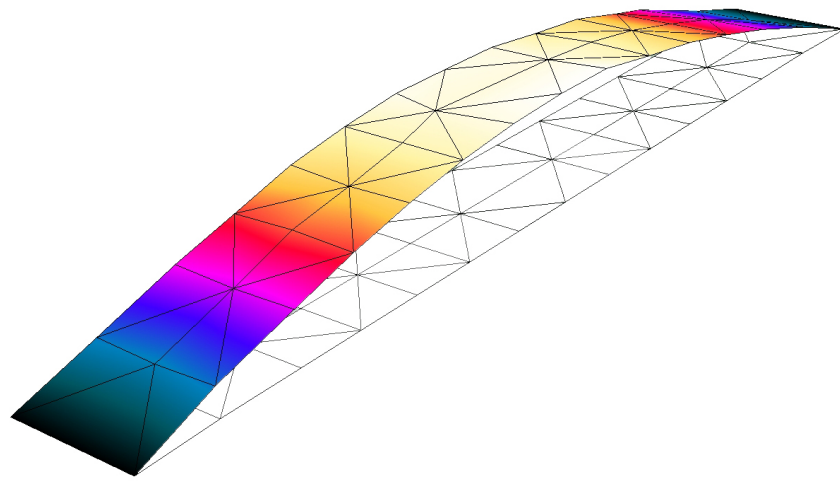




**LUND**  
UNIVERSITY



# **MODAL TESTING AND STRUCTURAL IDENTIFICATION**

TOBIAS KRISTENSSON

Structural  
Mechanics

*Master's Dissertation*



DEPARTMENT OF CONSTRUCTION SCIENCES  
DIVISION OF STRUCTURAL MECHANICS

ISRN LUTVDG/TVSM--14/5202--SE (1-168) | ISSN 0281-6679

MASTER'S DISSERTATION

# MODAL TESTING AND STRUCTURAL IDENTIFICATION

TOBIAS KRISTENSSON

Supervisors: **PER-ERIK AUSTRELL**, Assoc. Prof., Div. of Structural Mechanics, LTH, Lund  
and **BJÖRN THUNELL**, Scanscot Technology AB.

Examiner: **KENT PERSSON**, PhD, Div. of Structural Mechanics, LTH, Lund.

Copyright © 2014 Division of Structural Mechanics  
Faculty of Engineering (LTH), Lund University, Sweden.

Printed by Media-Tryck LU, Lund, Sweden, October 2014 (*PI*).

**For information, address:**

Div. of Structural Mechanics, LTH, Lund University, Box 118, SE-221 00 Lund, Sweden.

Homepage: <http://www.byggmek.lth.se>



# Acknowledgement

This master thesis was carried out at The Division of Structural Mechanics at Lund University Faculty of Engineering (LTH) and this work marks the end of my Master's degree in Structural and Civil engineering.

First I would like to express my gratitude to my supervisor Per-Erik Austrell that gave me inspiration to start this project and also for support and guidance during the process. I would also like to thank Björn Thunell at Scanscot Technology for providing me with both literature and information about modal testing and signal processing. Many thanks to Anders Sjöström for giving me access to the lab and letting me borrow the equipment. Also thanks for taking time to supervise some of the measurements even though you have a tight time schedule.

All equipment and analysis software used in this thesis were manufactured and produced by Brüel & Kjær.

At last I would also like to thank my family and my girlfriend Caroline for supporting me all the way through my education.

Lund, 2014

Tobias Kristensson

A handwritten signature in black ink, reading "Tobias Kristensson". The signature is written in a cursive style with a long, sweeping underline.



# Abstract

Bridges have been built around the world for at least 3000 years and have made it possible for man to travel over obstacles like valleys and rivers, which has contributed to the rapidly growing infrastructure we have today. Efforts made to save materials and reduce production costs have led to lighter and slender structures, which in turn can cause dynamic problems where the bridge is sensitive to vibrations. Vibrations from traffic, wind, wave and seismic loads may cause major problems for a lightweight design as the risk of fatigue of structural elements is very large. Therefore, it is important to always study the dynamic parameters: natural frequencies, mode shapes and damping ratios using both measurement techniques and computer models.

The classical measuring method is called Experimental Modal Analysis (EMA), where both the applied force on the structure and the structure's response are measured. The force can be generated by either an impact hammer or a shaker and recorded using an attached force sensor. The structure's response is then measured with accelerometers. Since EMA is difficult to perform on larger structures and is sensitive to disturbing vibrations, it has become more common to use so called Operational Modal Analysis (OMA). The OMA technique is based on measuring only the structure's response from random unknown vibrations. This is very advantageous when performing measurements on for example a bridge, because it can be fully operational during the measurements without disturbing the traffic.

The aim of this thesis is to study and compare different types of measurement methods used to identify structures' dynamic parameters and to compare them with numerical calculations. To facilitate the comparisons between the methods and to avoid environmental interference, measurements were carried out in a lab on a well-defined steel structure. A computer model of the structure was made by using the finite element software ABAQUS, where both the natural frequencies and the mode shapes were predicted. Measurements were performed by using equipment and software from Brüel & Kjær.

Measured and calculated natural frequencies and mode shapes of the steel structure have good compliance for all of the different measurement methods. The modal damping was difficult to estimate since it varied a lot between measurements. The measurement with the impact hammer was quick and flexible to perform since the procedure does not require much equipment. The shaker measurement required more equipment but gave much more accurate and clearer results than the measurement with the impact hammer. The results obtained by the OMA were very similar to the results from the EMA with the shaker. The OMA technique has proven to work well even with poor time signals that are far from ideal white noise. The major drawback with the OMA technique is that the measurements require

long time signals, but with today's low storage costs and powerful CPUs that process large amounts of data, this is no longer an issue. The conclusion is that the OMA technique seems to be the most appropriate method to use for measurements on large structures such as towers and bridges that are difficult to excite artificially. The EMA technique could possibly be used for lighter and smaller structures such as footbridges made of wood or steel.

**Key words:** modal testing, modal analysis, structural identification, vibration, signal, EMA, OMA

# Sammanfattning

Broar har byggts runt om i världen i omkring 3000 år och har gjort det möjligt för människan att färdas över hinder som dalar och floder, vilket har bidragit till den snabbt växande infrastrukturen vi har idag. Strävan efter att spara material och sänka produktionskostnader medför att konstruktionerna blir allt lättare och slankare, vilket i sin tur kan orsaka dynamiska problem där bron blir känslig för vibrationer. Vibrationer från trafik-, vind-, våg- och seismiska laster kan utgöra stora problem för en lätt konstruktion då risken för utmattning av bärande element är mycket stor. Det är därför viktigt att alltid studera en konstruktions dynamiska egenskaper såsom: egenfrekvenser, modformer och dämpningsparametrar med hjälp av både mätmetoder och datamodeller.

Den klassiska mätmetoden kallas Experimental Modal Analysis (EMA) och bygger på att både lasten som appliceras på strukturen och strukturens respons mäts. Lasten kan genereras av antingen en impulshammare eller en shaker och registreras med hjälp av en ditmonterad kraftsensor. Strukturens respons mäts sedan med hjälp av accelerometrar. Då EMA-metoden är svår att utföra på större strukturer och är känslig för omgivande vibrationer har det blivit allt vanligare att använda sig av en metod kallad Operational Modal Analysis (OMA). OMA-tekniken bygger på att mäta endast strukturens respons från slumpmässiga och okända vibrationer. Detta är mycket fördelaktigt då mätningar utförs på exempelvis en bro, eftersom bron då kan vara i bruk under mätningarna och därmed hindras inte trafiken.

Målet med detta examensarbete är att studera och jämföra olika typer av mätmetoder som används för att identifiera en strukturs dynamiska parametrar och jämföra dessa med numeriska beräkningar. För att underlätta jämförelserna mellan metoderna och undvika störningar från omgivningen utfördes mätningarna i ett labb på en väldefinierad stålstruktur. En datormodell av strukturen gjordes med hjälp av finita element-programmet ABAQUS, där både egenfrekvenser och modformer beräknades. Mätningarna utfördes med hjälp av utrustning och mjukvara från Brüel & Kjær.

Uppmätta och beräknade egenfrekvenser och modformer på stålstrukturen har bra överensstämmelse för alla olika mätmetoder. Den modala dämpningen var svår att uppskatta då den varierade mycket mellan mätningarna. Mätningen med impulshammare var snabb och flexibel att utföra då metoden inte kräver så mycket utrustning. Shakermätningen krävde mer utrustning, men gav betydligt noggrannare och tydligare resultat än mätningen med impulshammare. Resultaten från OMA-mätningen var mycket lika resultaten från EMA-mätningen med shaker. OMA-tekniken visade sig fungera bra även vid dåliga tidssignaler, långt från idealt vitt brus. Den stora nackdelen med OMA-tekniken är att mätningarna

kräver långa tidssignaler, men med dagens låga lagringspriser och kraftfulla CPU:er som bearbetar stora mängder data är detta inte längre ett problem.

Slutsatsen är att OMA-tekniken verkar vara den bäst lämpade metoden att använda vid mätningar på stora strukturer som t.ex. höghus och broar, som är svåra att excitera artificiellt. EMA-tekniken kan eventuellt användas på lättare och mindre strukturer som t.ex. gångbroar gjorda av trä eller stål.

**Nyckelord:** modala mätningar, modal analys, strukturidentifiering, vibration, signal, EMA, OMA

# Table of Contents

Acknowledgement.....	I
Abstract.....	III
Sammanfattning .....	V
Nomenclature.....	XI
Abbreviations.....	XI
Notation.....	XI
<b>1 Introduction .....</b>	<b>1</b>
1.1 Modal Analysis .....	2
1.2 Aim and Method.....	3
<b>2 Structural Dynamics.....</b>	<b>5</b>
2.1 Eigenfrequencies and Eigenmodes .....	5
2.2 The Laplace Transform .....	7
2.3 Frequency Response Function .....	10
<b>3 Signals and Equipment.....</b>	<b>17</b>
3.1 Periodic Signals .....	17
3.2 Transient Signals .....	19
3.3 Random Signals.....	20
3.4 Measuring Equipment.....	21
3.4.1 Measurement Front-ends.....	21
3.4.2 Piezoelectric Accelerometers.....	22
3.4.3 Piezoelectric Force Transducers .....	24
3.4.4 Impact Hammers.....	25
3.4.5 Shakers .....	27
<b>4 Experimental Modal Analysis.....</b>	<b>31</b>
4.1 Measurement and Signal Processing .....	33
4.2 Identification Methods .....	37
<b>5 Operational Modal Analysis.....</b>	<b>39</b>
5.1 Structural Health Monitoring.....	40
5.2 Extraction Methods.....	42
5.2.1 Frequency Domain Decomposition .....	42

5.2.2	Enhanced Frequency Domain Decomposition.....	43
5.2.3	Stochastic Subspace Identification .....	44
5.3	Modal Assurance Criterion .....	45
<b>6</b>	<b>Finite Element Model</b> .....	<b>47</b>
6.1	Structure.....	48
6.2	FE-Model in ABAQUS .....	49
6.3	Structure with Added Mass.....	55
<b>7</b>	<b>Measurements</b> .....	<b>57</b>
7.1	EMA Impact Hammer .....	57
7.2	EMA Shaker.....	63
7.3	OMA.....	69
7.4	OMA with Finer Grid.....	74
<b>8</b>	<b>Discussion</b> .....	<b>75</b>
8.1	Overview .....	75
8.2	EMA Impact Hammer .....	78
8.3	EMA Shaker.....	80
8.4	OMA.....	81
8.5	OMA with Finer Grid.....	83
8.6	Structure with Added Mass.....	85
<b>9</b>	<b>Final Remarks</b> .....	<b>89</b>
9.1	Conclusions.....	89
9.2	Further Studies .....	91
<b>10</b>	<b>Bibliography</b> .....	<b>93</b>
<b>Appendix A</b> .....		<b>97</b>
<b>Appendix B</b> .....		<b>101</b>
B.1	EMA Impact Hammer .....	101
B.2	EMA Shaker.....	106
B.3	OMA .....	116
<b>Appendix C</b> .....		<b>131</b>
<b>Appendix D</b> .....		<b>143</b>
D.1	ABAQUS Results.....	144
D.2	EMA Impact Hammer.....	146
D.3	OMA.....	150

Appendix E .....	157
E.1 SDOF Example.....	157
E.2 MDOF Example .....	163



# Nomenclature

## Abbreviations

ADC	Analog-to-Digital-Converter
B&K	Brüel & Kjær
CPU	Central Processing Unit
DC	Direct Current
EFDD	Enhanced Frequency Domain Decomposition
EMA	Experimental Modal Analysis
FDD	Frequency Domain Decomposition
FE(M)	Finite Element (Method)
FFT	Fast Fourier Transform
FRF	Frequency Response Function
GRFP	Global Rational Fraction Polynomial
IDFT	Inverse Discrete Fourier Transform
LAN	Local Area Network
MAC	Modal Assurance Criterion
MDOF	Multi-Degree-Of-Freedom
MIMO	Multiple-Input-Multiple-Output
OMA	Operational Modal Analysis
RFP	Rational Fraction Polynomial
SDOF	Single-Degree-Of-Freedom
SHM	Structural Health Monitoring
SIMO	Single-Input-Multiple-Output
SISO	Single-Input-Single-Output
SNR	Signal-to-Noise-Ratio
SSI	Stochastic Subspace Identification
SVD	Singular Value Decomposition

## Notation

$\mathcal{L}[\ ]$	Laplace transform of [ ]	
$A, \mathbf{A}$	Residue, residue matrix	
$c, \mathbf{C}$	Damping, damping matrix	Ns/m
$f$	Frequency	Hz
$f(t), \mathbf{F}(t), \mathbf{F}$	Force, force vector, input force	N
$\varphi, \Phi$	Mode shape, Mode shape matrix	
$\gamma_{yx}^2(f)$	Coherence function	

$H(\omega), \mathbf{H}(\omega)$	Frequency response function	$m/N, m/Ns, m/Ns^2$
$H(s)$	Transfer function	
$h(t), \mathbf{h}(t)$	Impulse response function	$m/Ns$
$k, \mathbf{K}$	Stiffness, stiffness matrix	$N/m$
$\xi$	Relative damping	
$m, \mathbf{M}$	Mass, mass matrix	$kg$
$\mu$	Sensitivity factor	$pC/ms^{-2}$
$\omega$	Angular frequency	$rad/s$
$\omega_d$	Damped natural frequency	$rad/s$
$q$	Electrical charge	$V$
$R_d$	Deformation response factor	
$s$	Laplace operator	
$S$	Singular values	
$\mathbf{S}^{-1}$	Inverse pole matrix	
$\sigma$	Damping rate	
$t, \tau$	Time	$s$
$T$	Period time	$s$
$u, \dot{u}, \ddot{u}, \mathbf{u}, \dot{\mathbf{u}}, \ddot{\mathbf{u}}$	Displacement, velocity, acceleration	$m, m/s, m/s^2$
$U$	Output signal	
$\mathbf{V}_1, \mathbf{V}_2$	Left- and right singular vectors	
$w_e(t)$	Exponential window	

# 1

## Introduction

Bridges have been built around the world for at least 3000 years. They have been very useful for connecting countries and allowing transport over obstacles like valleys and rivers. Today bridges play a significant role in our society (the largest bridge in Sweden is shown in Figure 1.1) [1].



Figure 1.1: The Öresund Bridge connects Sweden and Denmark, 7.85 km long [2].

In Sweden there are bridges worth at least 70 billion SEK and many of them need to be repaired or reinforced to manage today's increasing traffic. Trucks and other transportation vehicles have grown larger and heavier to carry more goods per distance. This will reduce the number of transports and also the emissions of greenhouse gases, but it will generate

larger loads on roads and bridges. Many bridges aren't designed to carry these heavy loads and therefore they need to be reinforced or torn apart [3].

In some cases it's more economical to reinforce the old bridges instead of building new. The rapid development of measuring techniques and devices could make this decision much easier. Finite element software can be used to create computer models and simulate the dynamic behavior of the structure. The accuracy of the calculated results can then be verified by comparing them to results obtained from measurements. This will provide a lot of information about how the structure will react on different loads and where the critical sections is located on the bridge [3].

Today it's possible to build strong and lightweight structures by optimizing the amount of constructive material. The span length of bridges has increased exponentially over the years and at the same time the bridges have become more and more slender. This will reduce the self-weight of the bridge but it will also make it more sensitive to dynamic loads. Large vibrations can make the bridge uncomfortable to cross over and also impose structural effects like fatigue or flutter. Therefore it's very important to predict the dynamic properties of bridges, so they can be designed to reduce these vibrations [4].

## 1.1 Modal Analysis

Modal analysis is an engineering tool to evaluate the structure's response due to vibration. It's very important to consider the consequence of vibrations when designing the structure to ensure that effects like noise, discomfort and fatigue is reduced as much as possible. The most common and disturbing source are the vibrations from vehicles and machines. Vibrations generated by the environment (earthquakes, hurricanes, tornados etc.) are the most severe and could cause permanent damage to the structure or in a worst case scenario destruction [5]. Tacoma Narrows Bridge (see Figure 1.2) is a perfect example where the wind destroyed the bridge by hitting the eigenfrequency of the structure causing large amplitudes that finally led to a collapse of the bridge.



Figure 1.2: Tacoma Narrows bridge collapse 7 November 1940 [6].

## 1.2 Aim and Method

The aim of this master thesis is to verify some of the most common measurement and structural identification methods. The thesis will provide an overview of different methods and the theory behind structural identification. To verify the accuracy of the identification methods, a laboratory experiment will be conducted where the modal testing is performed on a simplified, bridge shaped steel structure. A finite element model of the structure will be used to verify the accuracy of the different measurement and identification procedures.



# 2

## Structural Dynamics

This chapter provides basic knowledge about structural dynamics and vibrations. Some of the figures are generated by MATLAB and the code is attached in Appendix E.

### 2.1 Eigenfrequencies and Eigenmodes

The simplest dynamic system is the SDOF-system (single-degree-of-freedom) and it's illustrated in Figure 2.1 with the three fundamental properties: mass ( $m$ ), stiffness ( $k$ ) and damping ( $c$ ) [7].

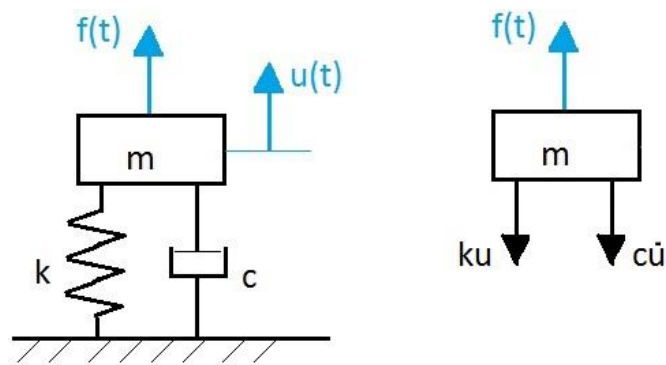


Figure 2.1: SDOF-system.

Spring and damper forces together with Newton's second law give the equation of motion:

$$m\ddot{u} + c\dot{u} + ku = f(t) \quad (2.1)$$

where  $u(t)$  and  $f(t)$  are the time dependent displacement and excitation force respectively.

If there is no damping in the SDOF system and no external load Eq.(2.1) is reduced to:

$$m\ddot{u} + ku = 0 \quad (2.2)$$

In order to solve Eq.(2.2) trial solutions are introduced:

$$u = A \sin \omega t \quad \ddot{u} = -A\omega^2 \sin \omega t \quad (2.3)$$

Applying these solutions into Eq.(2.2) gives:

$$(-\omega^2 m + k)A \sin \omega t = 0 \quad \rightarrow \quad \omega_n^2 = \frac{k}{m} \quad (2.4)$$

The natural circular frequency for the SDOF-system is  $\omega_n = \sqrt{\frac{k}{m}}$  where:  $f_n = \frac{\omega_n}{2\pi}$  and  $T_n = \frac{1}{f_n}$ .

Larger and more complex structures require more degrees-of-freedom, these systems are called MDOF (multi-degree-of-freedom) systems. The equation of motion for MDOF systems are given in matrix form as:

$$\mathbf{M}\ddot{\mathbf{u}} + \mathbf{C}\dot{\mathbf{u}} + \mathbf{K}\mathbf{u} = \mathbf{F}(t) \quad (2.5)$$

where  $\mathbf{M}$ ,  $\mathbf{C}$  and  $\mathbf{K}$  are the mass-, damping- and stiffness matrix and  $\ddot{\mathbf{u}}$ ,  $\dot{\mathbf{u}}$  and  $\mathbf{u}$  are the time-varying acceleration-, velocity- and displacement vector.  $\mathbf{F}$  is a vector and it contains the time-varying external excitation forces. If there is  $n$  degrees-of-freedom in the system the matrixes and vectors have dimensions  $nxn$  and  $nx1$  [5].

The free vibration form of Eq.(2.5) is given by:

$$\mathbf{M}\ddot{\mathbf{u}} + \mathbf{K}\mathbf{u} = 0 \quad (2.6)$$

The trial solutions to Eq. (2.6) are:

$$\mathbf{u} = A \sin \omega t \mathbf{\Phi} \quad \ddot{\mathbf{u}} = -A\omega^2 \sin \omega t \mathbf{\Phi} \quad (2.7)$$

Inserting Eq.(2.7) in Eq.(2.6) gives:

$$[\mathbf{K} - \omega^2 \mathbf{M}] \mathbf{\Phi} A \sin \omega t = 0 \quad (2.8)$$

$A \sin \omega t \neq 0$  gives:

$$[\mathbf{K} - \omega^2 \mathbf{M}] \mathbf{\Phi} = 0 \quad (2.9)$$

Solving the eigenvalue problem:

$$\det[\mathbf{K} - \omega^2 \mathbf{M}] = 0 \quad (2.10)$$

By inserting each frequency in Eq.(2.9) the eigenvectors can be solved ( $\mathbf{\Phi}$  is called the mode shape matrix):

$$\mathbf{\Phi} = [\varphi_1, \varphi_2, \varphi_3 \dots \varphi_n]$$

Eq.(2.6) is derived into an eigenvalue problem where the eigenvalues are the undamped natural frequencies of the system,  $\omega_1, \omega_2, \omega_3 \dots \omega_n$ . The solution also contains  $n$  eigen vectors and these are the system's mode shapes,  $\Phi = [\varphi_1, \varphi_2, \varphi_3 \dots \varphi_n]$ . Each frequency has a corresponding mode shape that visualizes the structure's movement when it's excited by different frequencies [5].

## 2.2 The Laplace Transform

Now let's go back to the SDOF-system mentioned in section 2.1 and introduce the Laplace transform. The Laplace transform is a method for deriving the dynamic response of a system. A signal  $x(t)$  is transformed by the Laplace method and takes the following form:

$$X(s) = \mathcal{L}\{x(t)\} = \int_{0^-}^{\infty} x(t)e^{-st} dt \quad (2.11)$$

where  $s$  is known as the Laplace operator and is a complex function. The real and imaginary parts of the Laplace operator are given by Eq.(2.12):

$$s_{1,2} = \sigma \pm i\omega_d \quad (2.12)$$

where

$$\omega_d = \omega_n \sqrt{1 - \xi^2} \quad (2.13)$$

and

$$\sigma = -\xi\omega_n \quad (2.14)$$

where  $\omega_d$  is the damped natural frequency and  $\xi$  is the relative damping

$$\xi = \frac{c}{2\sqrt{mk}} \quad (2.15)$$

$s_1$  and  $s_2$  are roots (poles) to the transfer function (Eq.(2.17)). The real part controls the damping in the system ( $\sigma$  is the damping rate) and the imaginary part describes the damped natural frequency,  $\omega_d$  [8].

If the Laplace transform is applied on Eq.(2.1) on both sides it takes the following form

$$\mathcal{L}\{m\ddot{u} + c\dot{u} + ku\} =$$

$$m[s^2U(s) - su(0) - \dot{u}(0)] + c[sU(s) - u(0)] + kU(s) =$$

$$(ms^2 + cs + k)U(s) - msu(0) - m\dot{u}(0) - cu(0)$$

and

$$\mathcal{L}\{f(t)\} = F(s)$$

where  $u(0)$  and  $\dot{u}(0)$  are the initial conditions for the system. If both the initial displacement and velocity are zero the equation takes the form

$$(ms^2 + cs + k)U(s) = F(s) \quad (2.16)$$

where  $F(s)$  and  $U(s)$  are the transformed input- and output signals [8].

Eq.(2.16) is then expressed by this relationship:

$$H(s) = \frac{U(s)}{F(s)} = \frac{1}{ms^2 + cs + k} \quad (2.17)$$

where  $H(s)$  is the transfer function of the system. The transfer function can be rewritten by inserting Eq.(2.15) and the natural frequency  $\omega_n$ :

$$H(s) = \frac{1/m}{s^2 + 2\xi\omega_n s + \omega_n^2} \quad (2.18)$$

By applying the Laplace operator (Eq.(2.12)) into Eq.(2.18) the transfer function is given by

$$H(s) = \frac{1/m}{(s - s_1)(s - s_2)} \quad (2.19)$$

According to [5] Eq.(2.19) can be rewritten in the following form by performing partial fraction expansion:

$$H(s) = \sum_{r=1}^{N_q} \frac{A_r}{(s - s_r)} = \frac{A_1}{(s - s_1)} + \frac{A_2}{(s - s_2)} \quad (2.20)$$

where  $A_1$  and  $A_2$  are complex conjugates and are referred to the residues  $\left(A = \frac{1}{i2m\omega_d}\right)$  of the transfer function:

$$A_r = (s - s_r) \frac{U(s)}{F(s)} \Big|_{s=s_r} \quad (2.21)$$

The transfer function for a SDOF-system is illustrated in Figure 2.2 (and in Figure A - 1 in Appendix A) as a surface in the Laplace domain [5].

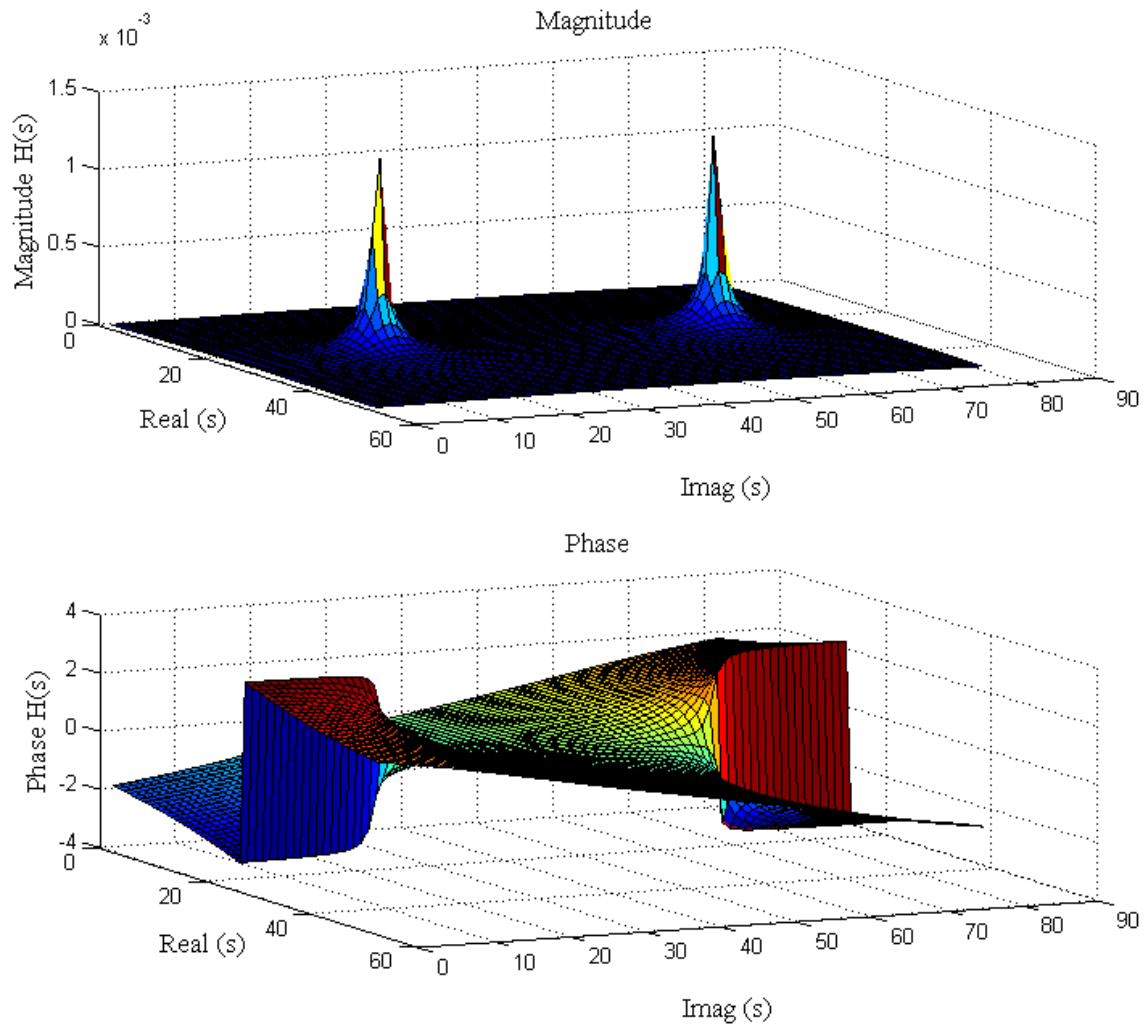


Figure 2.2: Magnitude and phase of the transfer function  $H(s)$ , SDOF example (see Appendix E).

If the initial conditions are zero and  $F(s) = 1$  for a system, then the impulse response function  $h(t)$  could be calculated with [8]:

$$h(t) = \mathcal{L}^{-1}\{H(s)\} = A_1 e^{s_1^* t} + A_2 e^{s_2^* t} \quad (2.22)$$

An impulse response function for a SDOF-system can be viewed in Figure 2.3.

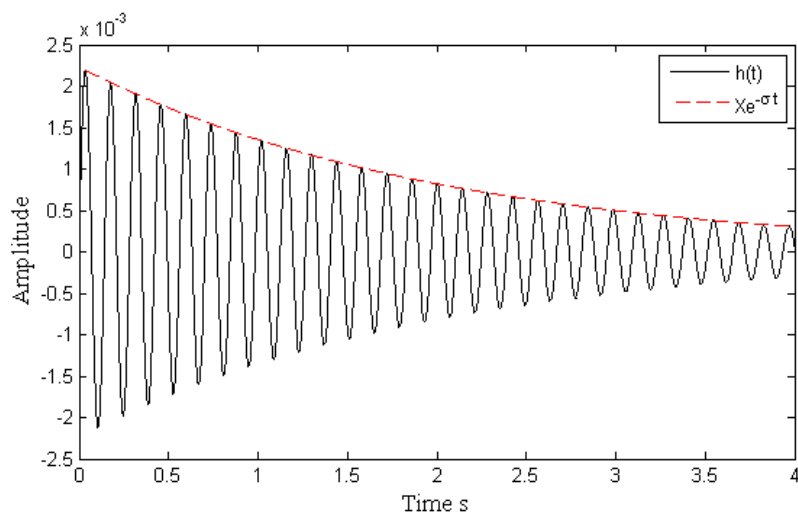


Figure 2.3: Impulse response plot, SDOF example (see Appendix E).

## 2.3 Frequency Response Function

The Frequency Response Function (FRF) is obtained by rewriting Eq.(2.17) into frequency domain by letting  $s = i\omega$ :

$$H_u(i\omega) = \frac{U(i\omega)}{F(i\omega)} = \frac{1}{m(i\omega)^2 + ci\omega + k} = \frac{1}{(k - \omega^2 m) + i\omega c} \quad (2.23)$$

The derived FRF is just one of the potential forms of an FRF and it's referred to as receptance ( $H_u$ ). This equation describes the relationship between the excitation force and the displacement response and it is illustrated in Figure 2.4.

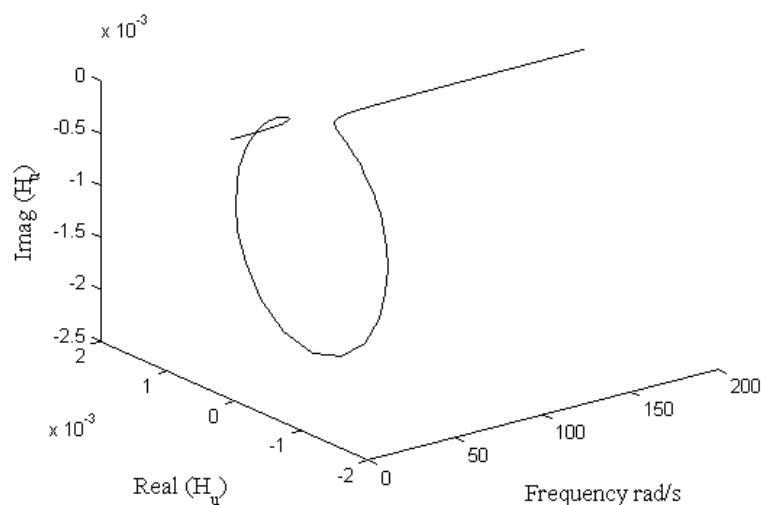


Figure 2.4: FRF (3D representation), SDOF example (see Appendix E).

Figure 2.4 can be divided into two plots, one imaginary/frequency and one real/frequency plot (see Figure 2.5):

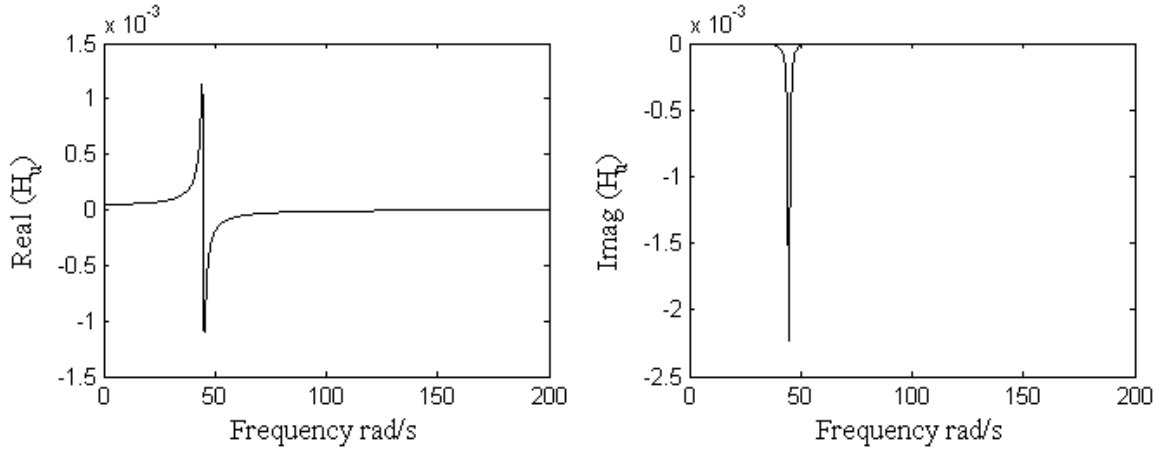


Figure 2.5: Real- and imaginary plots of receptance, SDOF example (see Appendix E).

At resonance the real part crosses the frequency axis while the imaginary part reaches its maximum. It's also common to present the FRF as magnitude and in a so called Nyquist diagram, this can be viewed in Figure A - 3 in Appendix A. The FRF could be presented in terms of velocity and acceleration as well. The three possible ways of presenting the FRF are given in Table 2.1 and in Figure A - 2 and in Figure A - 4 in Appendix A [5].

Table 2.1: FRF representations.

Different forms of the FRF	
Receptance	$H_u(i\omega) = \frac{\text{displacement response}}{\text{force excitation}} = \frac{1}{(k - \omega^2 m) + i\omega c}$
Mobility	$H_v(i\omega) = \frac{\text{velocity response}}{\text{force excitation}} = \frac{i\omega}{(k - \omega^2 m) + i\omega c}$
Accelerance	$H_a(i\omega) = \frac{\text{acceleration response}}{\text{force excitation}} = \frac{-\omega^2}{(k - \omega^2 m) + i\omega c}$

Eq.(2.23) can be manipulated so the FRF is expressed by its natural frequency

$$\omega_n = \sqrt{\frac{k}{m}}$$

$$H(i\omega) = \frac{1}{k} \frac{1}{\left(1 - \frac{\omega^2 m}{k}\right) + \frac{i\omega c}{k}} = \frac{1}{k} \frac{1}{\left(1 - \frac{\omega^2}{\omega_n^2}\right) + \frac{i\omega c}{\omega_n^2 m}} \quad (2.24)$$

Inserting the equation for the relative damping  $\xi = \frac{c}{2m\omega_n}$  into Eq.(2.24) gives:

$$H(i\omega) = \frac{1}{k} \frac{1}{\left(1 - \frac{\omega^2}{\omega_n^2}\right) + i2\xi \frac{\omega}{\omega_n}} \quad (2.25)$$

According to [7] the deformation response factor  $R_d$  is given by the following expression:

$$R_d = \frac{|H(i\omega)|}{u_{st}} = \frac{1}{\sqrt{\left(1 - \frac{\omega^2}{\omega_n^2}\right)^2 + \left(i2\xi \frac{\omega}{\omega_n}\right)^2}} \quad (2.26)$$

where  $u_{st} = 1/k$ . The deformation response factor and the phase angle for different damping ratios  $\xi$  are illustrated in Figure 2.6. While increasing the damping ratio the deformation response factor is decreasing.

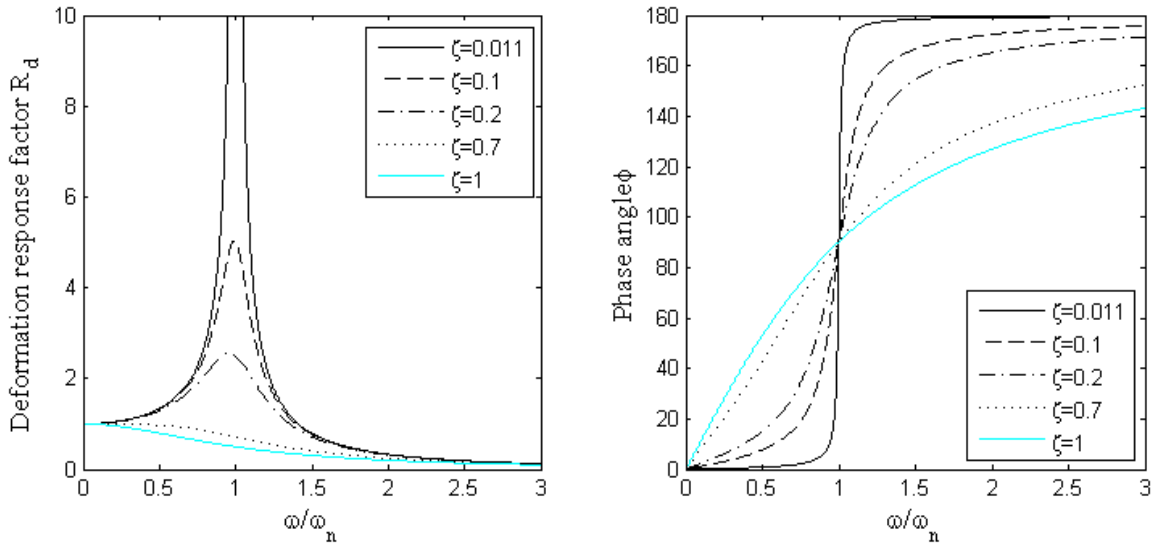


Figure 2.6: Deformation response factor  $R_d$  and phase angle  $\phi$ , the black solid line represents the SDOF example (see Appendix E).

The derivation of the FRF for MDOF systems is very similar to the previous SDOF example. By applying the Laplace transform on Eq.(2.5) gives:

$$[s^2\mathbf{M} + s\mathbf{C} + \mathbf{K}]U(s) = F(s) \quad (2.27)$$

where  $s$  is the Laplace operator and  $U$  and  $F$  are displacement and force vectors. The FRF matrix  $\mathbf{H}$  is given by:

$$\mathbf{H}(s)F(s) = U(s) \quad (2.28)$$

or

$$\mathbf{H}^{-1} = [s^2\mathbf{M} + s\mathbf{C} + \mathbf{K}] \quad (2.29)$$

Multiplying both sides with mode shape matrix gives the following expression:

$$\Phi^T \mathbf{H}^{-1} \Phi = \Phi^T [s^2\mathbf{M} + s\mathbf{C} + \mathbf{K}] \Phi \quad (2.30)$$

The FRF matrix is then given by

$$\mathbf{H} = \Phi [s^2\mathbf{M} + s\mathbf{C} + \mathbf{K}]^{-1} \Phi^T \quad (2.31)$$

Now it's time to define a new diagonal matrix called the inverse pole matrix,  $\mathbf{S}^{-1}$ . The elements  $(s_{rr})$  in the diagonal of  $\mathbf{S}^{-1}$  for mode  $r$  are given by Eq.(2.32).

$$s_{rr} = \frac{1}{s^2 m_r + s c_r + k_r} = \frac{1/m_r}{(s - s_r)(s - s_r^*)} \quad (2.32)$$

The FRF matrix can now be expressed:

$$\mathbf{H} = \Phi \mathbf{S}^{-1} \Phi^T \quad (2.33)$$

or with notations

$$H_{pq}(s) = \sum_{r=1}^N \frac{\varphi_{pr} \varphi_{qr}}{m_r (s - s_r)(s - s_r^*)} \quad (2.34)$$

where  $\varphi_{pr}$  is the mode shape coefficient for mode  $r$  in point  $p$ . By performing partial fraction expansion Eq.(2.34) can be written by a sum of residues ( $A_{pqr}$ ) divided by  $(s - s_r)$ .

$$H_{pq}(s) = \sum_{r=1}^N \frac{A_{pqr}}{s - s_r} + \frac{A_{pqr}^*}{s - s_r^*} \quad (2.35)$$

where  $A_{pqr}$  is given by:

$$A_{pqr} = \frac{1}{i2\omega_{dr} m_r} \varphi_{pr} \varphi_{qr} \quad (2.36)$$

The general expression for MDOF frequency response functions is then derived by letting  $s = i\omega$ .

$$H_{pq}(i\omega) = \sum_{r=1}^N \frac{A_{pqr}}{i\omega - s_r} + \frac{A_{pqr}^*}{i\omega - s_r^*} \quad (2.37)$$

Eq.(2.37) is called the modal superposition equation and is a very important equation in experimental modal analysis (see Chapter 4) as it relates to experimentally estimated FRFs. This equation plays a significant role in the estimation of modal parameters from measurements. The same equation in matrix form is given in Eq.(2.38).

$$\mathbf{H}(i\omega) = \sum_{r=1}^N \frac{\mathbf{A}_r}{i\omega - s_r} + \frac{\mathbf{A}_r^*}{i\omega - s_r^*} \quad (2.38)$$

According to [8] Eq.(2.38) can be inverse transformed into an impulse response function (Eq. (2.39)).

$$\mathbf{h}(t) = \sum_{r=1}^N \mathbf{A}_r e^{s_r t} + \mathbf{A}_r^* e^{s_r^* t} \quad (2.39)$$

Figure 2.7 illustrates a simple MDOF system. The assembled mass-, stiffness- and damping matrices are given below.

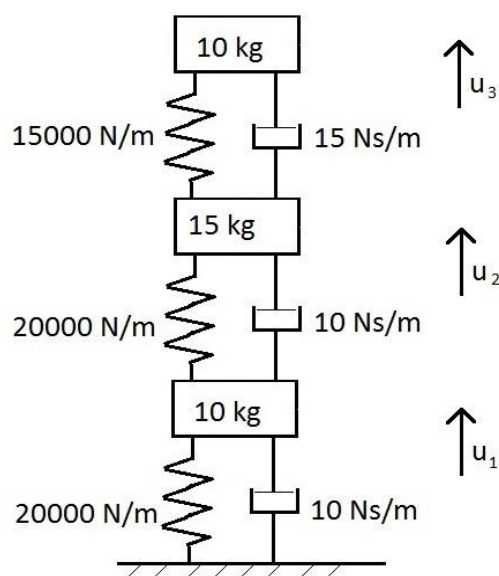


Figure 2.7: MDOF (3DOF) system.

$$\mathbf{M} = \begin{bmatrix} 10 & 0 & 0 \\ 0 & 15 & 0 \\ 0 & 0 & 10 \end{bmatrix} \text{kg} \quad \mathbf{K} = \begin{bmatrix} 40 & -20 & 0 \\ -20 & 35 & -15 \\ 0 & -15 & 15 \end{bmatrix} \text{kN/m} \quad \mathbf{C} = \begin{bmatrix} 20 & -10 & 0 \\ -10 & 25 & -15 \\ 0 & -15 & 15 \end{bmatrix} \text{Ns/m}$$

The eigenvalues and eigenvectors are obtained by:

$$\det[\mathbf{K} - \omega^2 \mathbf{M}] = 0 \rightarrow \det \left[ \begin{bmatrix} 40000 & -20000 & 0 \\ -20000 & 35000 & -15000 \\ 0 & -15000 & 15000 \end{bmatrix} - \omega^2 \begin{bmatrix} 10 & 0 & 0 \\ 0 & 15 & 0 \\ 0 & 0 & 10 \end{bmatrix} \right] = 0$$

$$\begin{aligned} \omega_1^2 &= 327,7 & f_1 &= 2,8 \text{ Hz} \\ \omega_2^2 &= 2383,0 & \rightarrow & f_2 = 7,8 \text{ Hz} \\ \omega_3^2 &= 5122,7 & f_3 &= 11,4 \text{ Hz} \end{aligned}$$

The obtained mode shapes are:

$$[\mathbf{K} - \omega^2 \mathbf{M}] \Phi = 0$$

$$\Phi = [\varphi_1, \varphi_2, \varphi_3] = \begin{bmatrix} -0,09 & 0,16 & -0,26 \\ -0,17 & 0,13 & 0,14 \\ -0,22 & -0,22 & -0,06 \end{bmatrix}$$

The three possible FRF and phase plots for the 3DOF system are illustrated in Figure 2.8 (generated by Abravibe toolbox [9]). In the FRF  $H_1$  the force and displacement are in the same point and at approximately 4 Hz it occurs a phenomenon called antiresonance. The antiresonance lifts the phase by  $+180^\circ$  so that the phase relationship for the first eigenfrequency is the same for the second eigenfrequency. In  $H_3$  there is no antiresonance at 4 Hz and therefore there is a sign change from  $-180^\circ$  to  $+180^\circ$  in the phase curve.

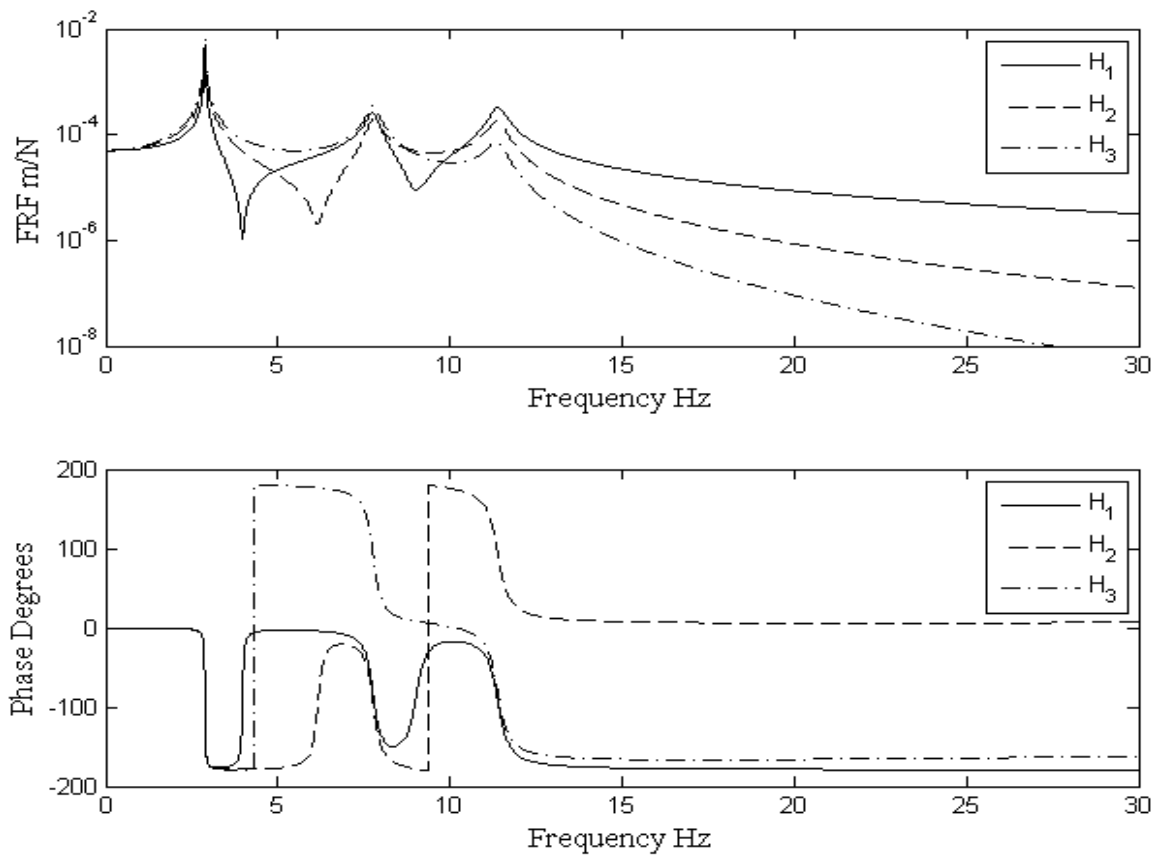


Figure 2.8: FRFs (above) and phase angle plots (below) for 3DOF system, made by Abravibe toolbox (see Appendix E). A 3D representation of  $H_1$  is given in Figure A - 6 in Appendix A.

An impulse response function for the 3DOF example is given in Figure A - 5 in Appendix A.

# 3

## Signals and Equipment

This chapter explains different types of signals and some of the equipment that is required to measure vibrations.

### 3.1 Periodic Signals

The characteristic of all types of signals is that they are a function of time ( $f(t)$ ). It could be acceleration, velocity or displacement that changes over time. The periodic signals repeat themselves with a period ( $T = \frac{1}{f}$ ) and are therefore classified as deterministic signals. A deterministic signal can be expressed mathematically and by only taking a small part of the signal the entire signal can be predicted, past or present. The simplest periodic signal is the sine wave that is defined by three parameters: amplitude ( $A$ ), angular frequency ( $\omega$ ) and phase angle ( $\emptyset$ ) (see Eq.(3.1)).

$$u(t) = A \sin(\omega t + \emptyset) \quad (3.1)$$

An example of a typical sine function can be observed in Figure 3.1 (left). The sine signal can be transformed into frequency domain by performing a Fast Fourier Transform (FFT), this will reveal both amplitude and frequency of the signal [8].

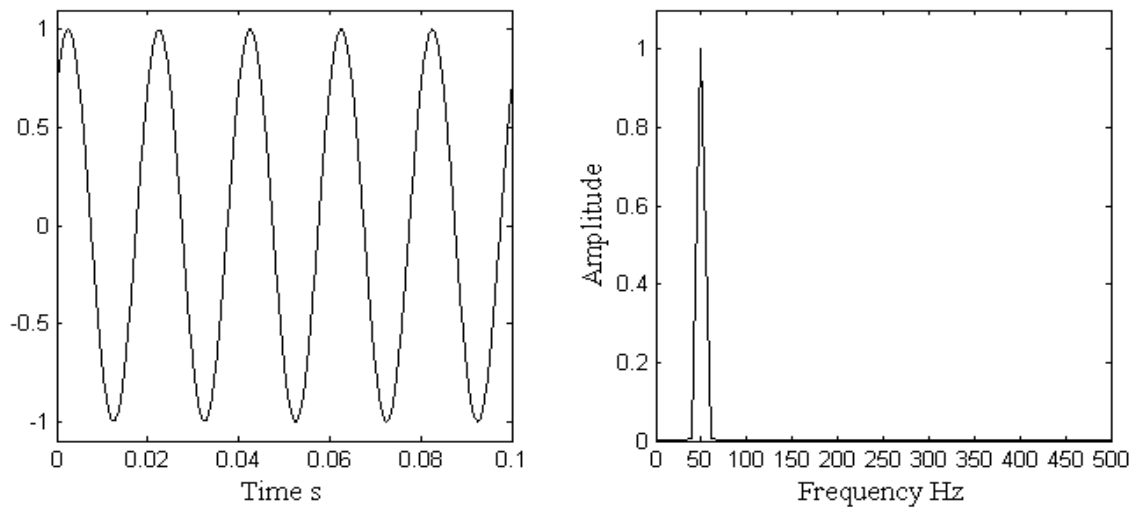


Figure 3.1: Sine wave with  $A = 1$ ,  $\omega = 100\pi$  ( $f = 50$  Hz) and  $\phi = \pi/4$ .

A more complex periodic signal is plotted in Figure 3.2 (left) and the equation is given in Eq.(3.2).

$$u(t) = A_1 \cdot \sin(2\pi \cdot f_1 \cdot t) + A_2 \cdot \sin(2\pi \cdot f_2 \cdot t) + A_3 \cdot \sin(2\pi \cdot f_3 \cdot t) \quad (3.2)$$

The frequency domain plot (right part in Figure 3.2) of this signal shows that it contains three frequencies:  $f_1 = 50$  Hz,  $f_2 = 100$  Hz and  $f_3 = 250$  Hz. It also reveals the amplitude for each frequency ( $A_1 = 1$ ,  $A_2 = 0,8$  and  $A_3 = 0,3$ ).

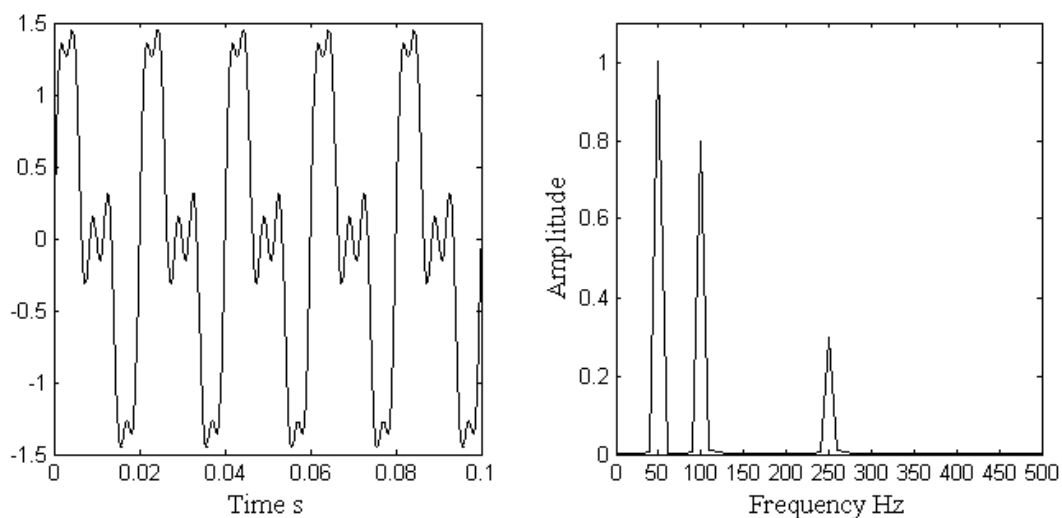


Figure 3.2: Complex sine signal.

### 3.2 Transient Signals

A transient signal decays over time until it finally dies out. These types of signals are usually deterministic and can occur when striking a hammer on a steel plate. The steel plate will vibrate a lot at first, but eventually the vibrations will decrease and fade away. A simple example of a transient signal with exponential decay is illustrated in Figure 3.3 (left) and the equation is given in Eq.(3.3) ( $d = 3$  and  $f = 5 \text{ Hz}$ ) [8].

$$a(t) = e^{-dt}\sin(2\pi ft) \quad (3.3)$$

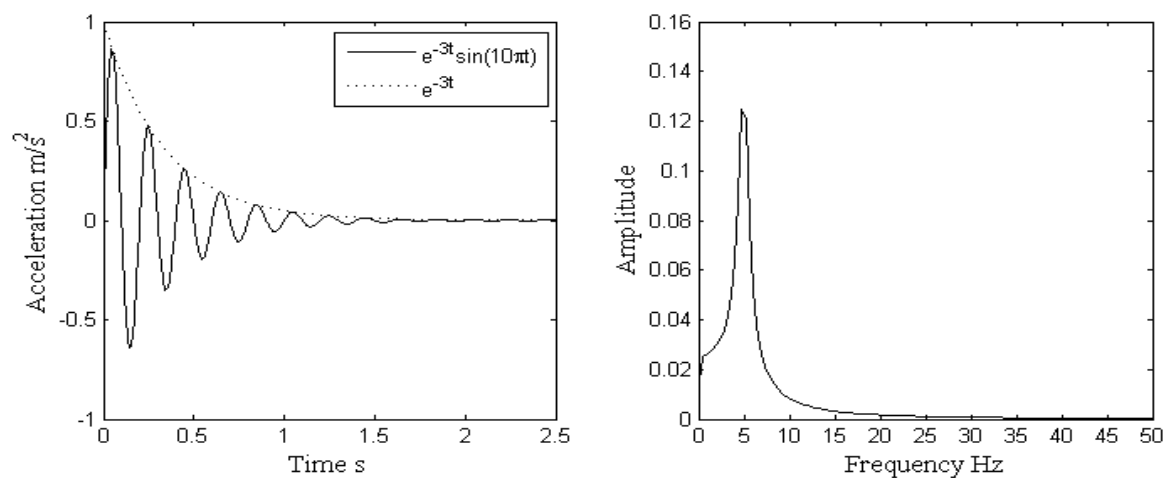


Figure 3.3: Exponentially decaying sine (left), frequency domain (right).

If the strike with the hammer is recorded, it will generate a plot where the applied force is a function of time. The left plot in Figure 3.4 shows two impacts, the solid line has a longer impact time than the dashed line. When performing a FFT on the two impact functions reveals that a shorter impulse gives a longer frequency range (right plot in Figure 3.4) [8].

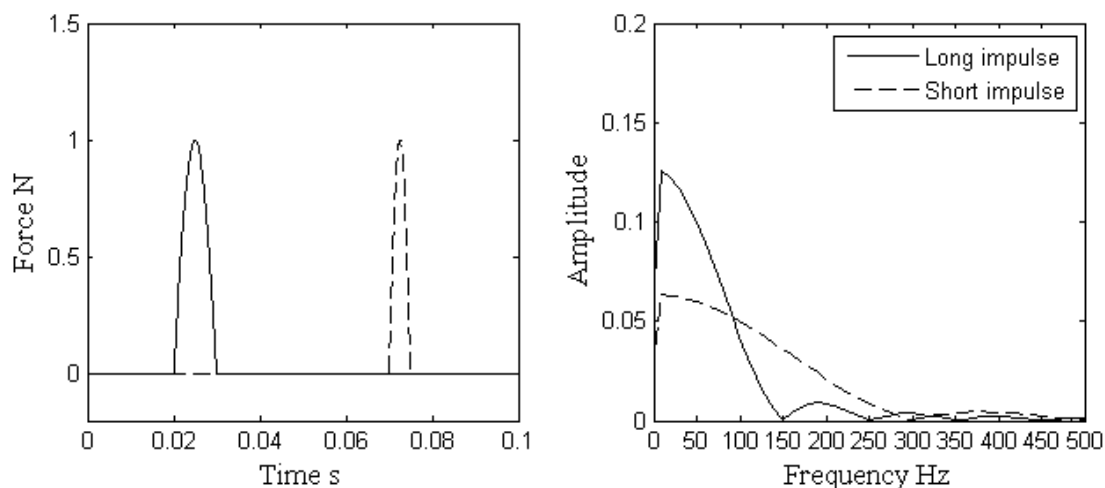


Figure 3.4: Impulse plot (left), frequency domain (right).

### 3.3 Random Signals

These types of signals are nondeterministic and are mathematically described by stochastic processes. There is no way to predict past or present values of a random signal, because every time increment  $\Delta t$  is independent. Random signals can occur when vibrations are generated by car tires that run over rough asphalt or wind turbulence around a wind-turbine blade. An example of a random signal is shown in Figure 3.5 [8].

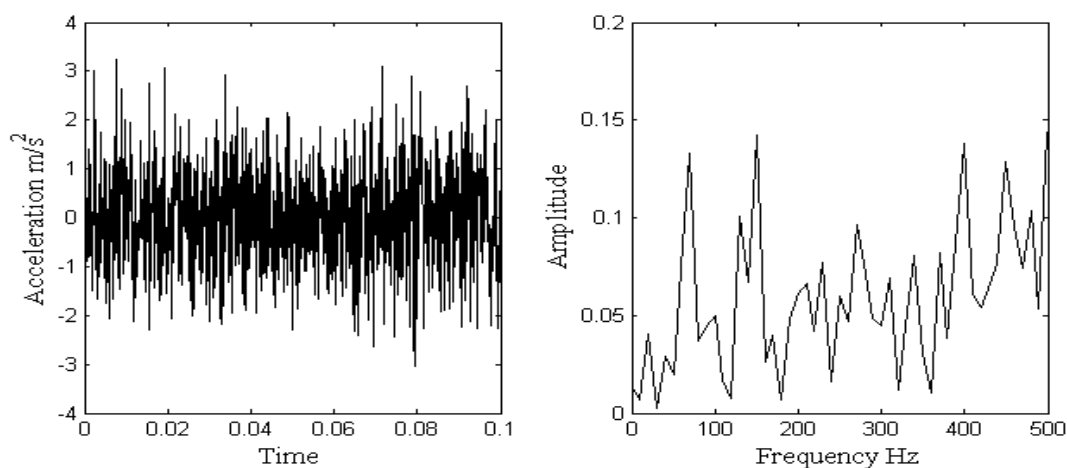


Figure 3.5: Random signal (left), frequency domain (right).

There are a few statistical analysis methods to check the quality of a recorded random signal. The most common method is to check the probability distribution of the recorded samples.

The probability density shown in Figure 3.6 of this random signal was created by using the Abravibe toolbox [9]. The bars in the histogram follow the ideal probability distribution (overlaid green dashed line) in the left figure and in the right figure the line that represents the signal (blue) follows the ideal shape of the probability line (green).

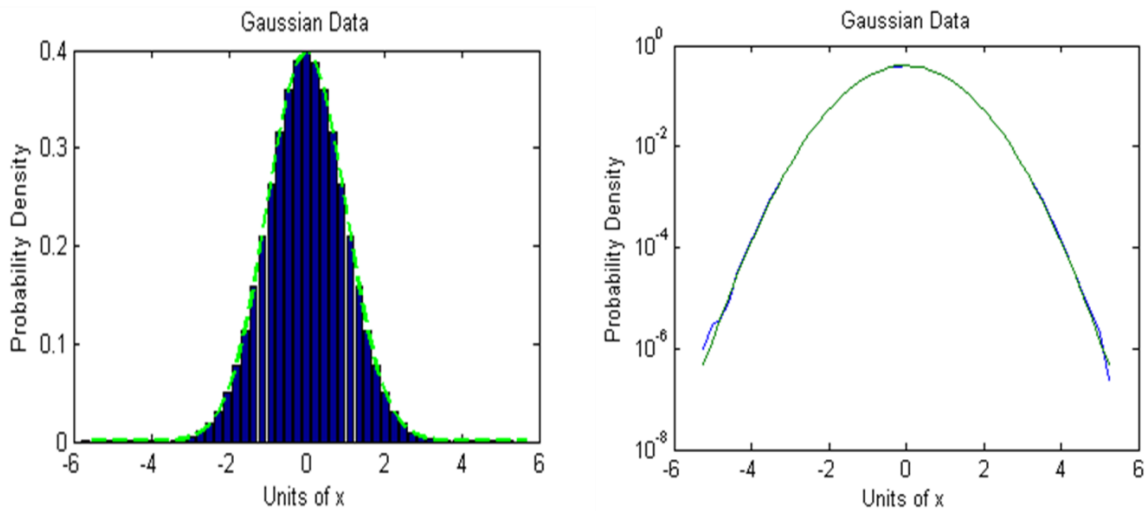


Figure 3.6: Probability density (histogram to the left and logarithmic plot to the right).

### 3.4 Measuring Equipment

This section will provide basic knowledge about equipment required to measure vibrations. A few years back the most common hardware were signal analyzers that were used to capture the signals generated by the piezoelectric transducers (see section 3.4.2 and 3.4.3). To connect a shaker a signal generator is also required to generate the signal to excite the structure [5]. A lot have happened over the years and these devices have been replaced by powerful LAN-XI systems.

#### 3.4.1 Measurement Front-ends

The equipment used in this thesis is the modern LAN-XI Data Acquisition Hardware developed by B&K (see Figure 3.7). This type of system is very flexible and allows large and complex configurations due to the independent front-end modules. The front-end is connected by a standard LAN (Local Area Network) cable which transfers data and powers the device. In order to connect more front-ends a network switch is used and it's connected to a computer with data analyzing software. The front-end can capture and send out signals with the input- and output-channels on the front of the device [10].



Figure 3.7: LAN-XI Data Acquisition Hardware from B&K [10].

### 3.4.2 Piezoelectric Accelerometers

The piezoelectric effect occurs naturally in crystal materials (quartz, salt, sugar etc.) and when a force is applied on the crystal a charge is produced. The generated charge ( $q$ ) is proportional to the force ( $f$ ) according to:

$$q = \mu \cdot f \quad (3.4)$$

where  $\mu$  is the sensitivity factor. Today the most common material used in piezoelectric transducers is quartz. The piezoelectric accelerometer could be manufactured in two different ways, the pressure mode design or the shear mode design (see Figure 3.8). Both designs have a stiff base that is in contact with the structure and will transfer the acceleration to the seismic mass and crystal that are glued together with the stiff base. The pressure mode design generates a pressure force by the seismic mass and this force is registered by the crystal. The reaction force that is acting on the crystal is proportional to the acceleration given by Newton's second law ( $F=m\ddot{u}$ ). The springs in the pressure mode design is preloading the mass and crystal so the reaction force is always positive. The two main disadvantages with the pressure mode design are that it's relatively sensitive to high temperatures and it has a high base strain. To reduce these problems the shear mode design has been developed. This type of sensor works in shear force mode instead of pressure force mode [8].

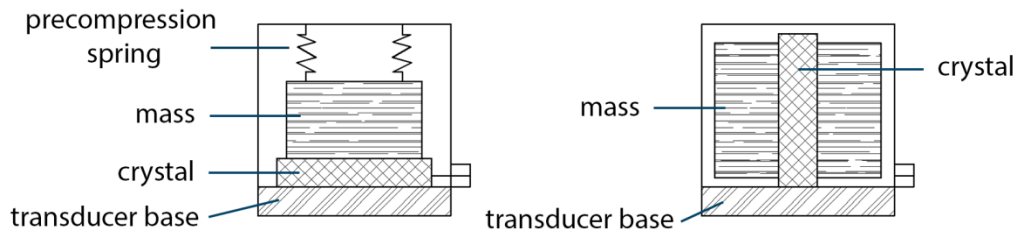


Figure 3.8: Piezoelectric accelerometer, pressure mode to the left and shear mode to the right.

There are several ways to attach the accelerometers on the structure like screws, glue, wax and magnets. It's important to notice that the different ways of mounting accelerometers can have unwanted effects on the measurement depending on the studied frequency range. More information about mounting accelerometers can be found in [8] and [11].

It is important to calibrate the accelerometers before the measurements so they don't contain any potential errors. These errors could come from the manufacturing process, high temperature changes (>250 °C), nuclear radiation, magnetic fields, humidity or hard impacts (if they were accidentally dropped on a hard floor). If the accelerometers are treated carefully and haven't been exposed to high temperatures or excessive shocks, the change in the characteristics over a period of several years is below 2 % [12].

Errors from the mechanical motion of the accelerometer cable can be avoided by taping or gluing the cable on the structure as close to the accelerometer as possible (see Figure 3.9) [12].

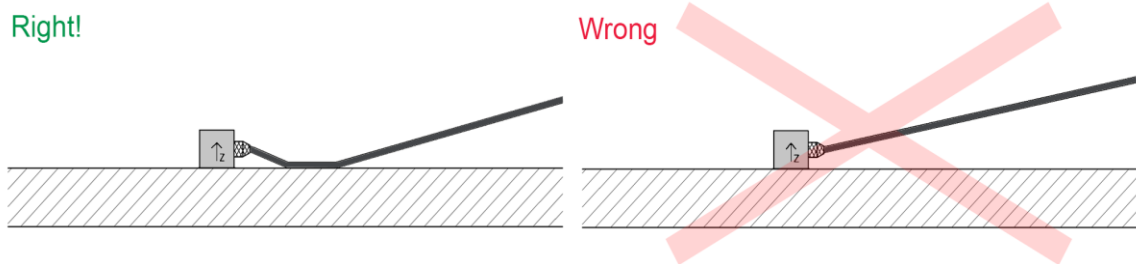


Figure 3.9: Using duct tape or glue to prevent the cable from mechanical motion close to the accelerometer.

### 3.4.3 Piezoelectric Force Transducers

The components of the force transducer are the same as for the accelerometer. It has a stiff base that should be mounted on the structure with a mounting stud. On top of the base the piezoelectric crystal and mass are glued. The mass is preloaded by springs (see Figure 3.10) so that the crystal always is subjected to compressive force, this allows the force transducer to measure tensile forces. The springs have a restricted preloading, which makes the force transducer to allow more compression force than tensile force. One drawback with this design is that the piezoelectric crystal is in direct contact with the base, which makes the transducer very sensitive to transverse forces [8].

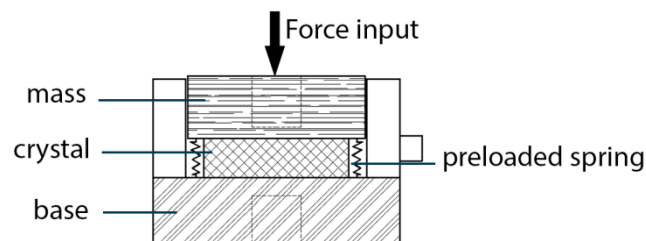


Figure 3.10: Design principle of a force transducer.

A force transducer is used to measure the excitation force, from either an impact hammer (see section 3.4.4) or a shaker (see section 3.4.5). On an impact hammer the force transducer is mounted behind the hammer tip. In a shaker measurement the force transducer is mounted (often screwed) directly on the structure and then to a shaker. To reduce the transverse forces a stinger can be mounted between the force transducer and the shaker [8].

As for the accelerometer it is very important to calibrate the force transducer, to be certain that the true force applied on the structure is measured.

### 3.4.4 Impact Hammers

Impact testing with an impact hammer is a very common excitation method because it's very simple to use. The benefits of this method are the short measurement times and the small set of hardware that is required to perform the test (does not need a signal generator or a power amplifier). The impact hammer can provide a broad range of frequencies and because it's not attached to the structure like shakers, the mass loading effect is avoided. The amplitude of the impact force is controlled by the mass (various hammer sizes in Figure 3.11) of the hammer and the velocity of the impact [5] [13].



Figure 3.11: Impact hammers [14].

To change the frequency content of the impact, the tip of the hammer can be changed into a softer or a harder tip, a softer tip gives a longer pulse than a harder tip and lower frequency content [13]. Figure 3.12 shows two types of hammer tips that were tried during the impact measurement in section 7.1. The grey line represents the softer tip that gives a longer impulse with less frequency content than the harder tip (black line). The harder tip (black line) shows some small “noise” before and after the impact (Figure 3.13), this result is due to the fact that the bandwidth for the pulse is larger than the bandwidth of the data acquisition, this phenomena is very common and has no bad influence on the measurement. To get a clearer and smoother plot of the impulse in the time domain the sampling frequency should be increased, this will also increase the bandwidth of the signal [8].

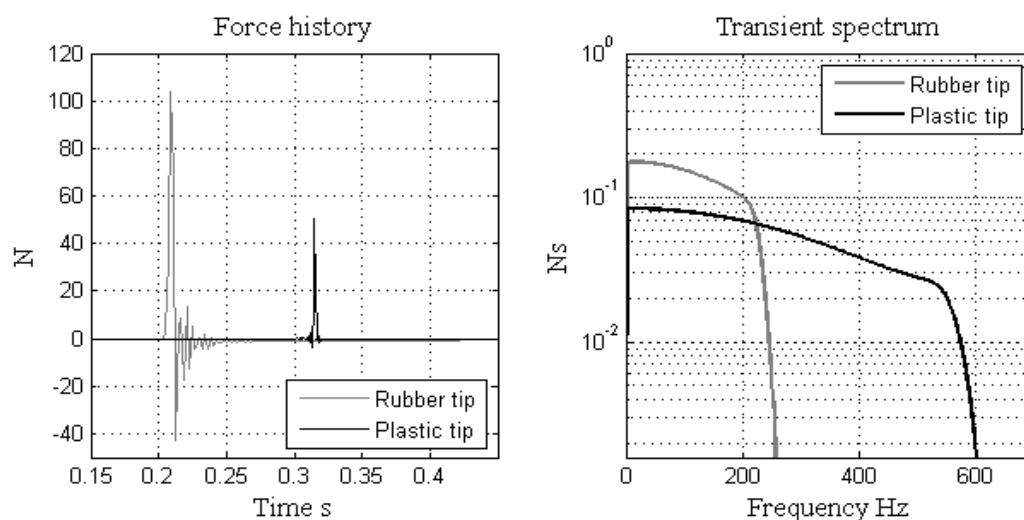


Figure 3.12: Force history and Transient spectrum for different hammer tips.

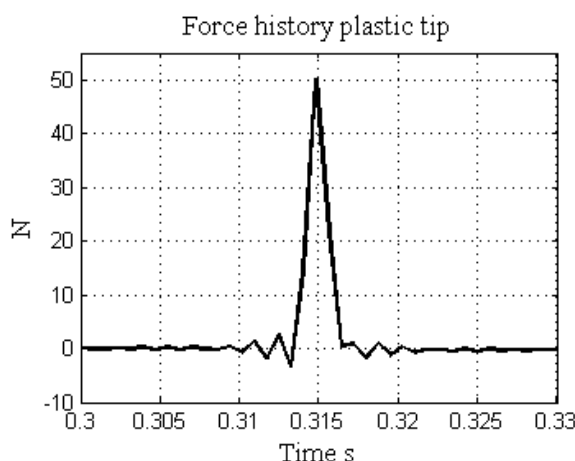


Figure 3.13: Plastic tip (low bandwidth and low sampling frequency causes “ringing” before and after impulse).

When the most suitable tip has been chosen there are some settings that need to be carried out before the impact measurements can be made. In modern measurement software the first step is to adjust the hammer trigger. The pre-trigger is set so the force starts a few hundred samples into the time-frame. By recording some samples before the impact will prevent any truncated signals. After the impact there is some noise in the force spectrum and it's deteriorating the signal. This noise can be reduced by applying a force window (see Figure 3.14). The final step is to apply an exponential window ( $w_e(t) = e^{-at}$ ) to the response signal. This will improve the signal-to-noise ratio (SNR) by adjusting the exponential constant  $a$ , which will suppress the upper part of the signal (see Figure 3.14) [8].

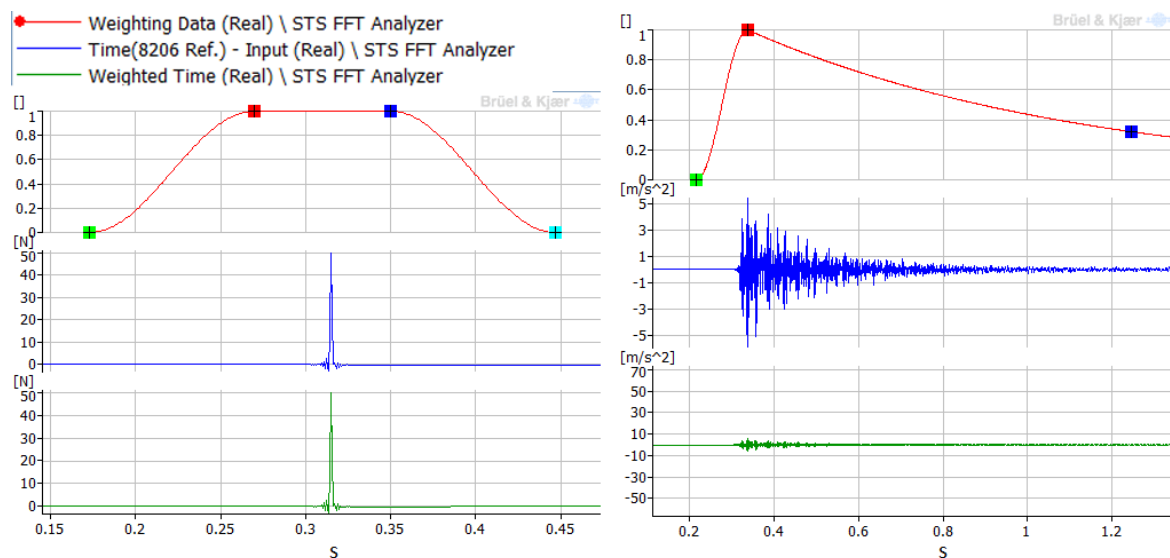


Figure 3.14: Hammer weighting (left) and response weighting (right).

The impact hammer is suitable for structures that are lightly damped and where the modal test doesn't require results with high precision. Impact testing could also be useful for locating potential excitation points for a shaker [8].

There are some drawbacks using impact hammers. Long time records could give rise to noisy force- and response signals. If the time record is too short there will be some leakage in the response signal. Mentioned in [8] the hammer excitation could bring errors that are caused by nonlinearities. To avoid these problems the force from the hammer should be as small as possible, otherwise the force could cause deformations at the excitation point on the structure and ruin the measurement. Errors from nonlinearities could also come from excited modes outside the frequency range, which can occur when a too hard tip is chosen.

### 3.4.5 Shakers

A more precise measurement can be achieved by attaching a shaker at a fix position on the structure. A shaker provides both longer and more controlled excitation (varying in both frequency and amplitude: sine, random etc.) than the impact hammer, which increases the accuracy of the FRF. There are three different types of shakers mentioned in [11]: mechanical-, electromagnetic- and electrohydraulic shakers.

Mechanical shakers can generate a prescribed force with different frequencies by an out-of-balance rotating mass. The drawback with mechanical shakers is that the magnitude of the

force can't be controlled while the measurement is processed. Another disadvantage is that these shakers are ineffective at low frequencies.

The hydraulic shakers have the benefit of creating much higher forces than electromagnetic shakers. These forces are generated by hydraulics and can rise up to several thousand kilograms. The drawback with these shakers is the low frequency range that is about 1 kHz and below. More information regarding mechanical and hydraulic shakers is found in [11].

The electromagnetic shakers are the most suitable in modal testing and they can operate in frequencies from 5 Hz to 20 kHz depending on size. The maximum force is also depending on the size of the shaker and it's generated by a moving electric coil in a magnetic field. The magnetic field that is created in the shaker could come from a permanent magnet or a coil fed by DC current (same principle as an electromagnet). Larger shakers will require a stronger magnetic field and therefore they have an electromagnet powered by DC current instead of a permanent magnet (see Figure 3.15) [8].

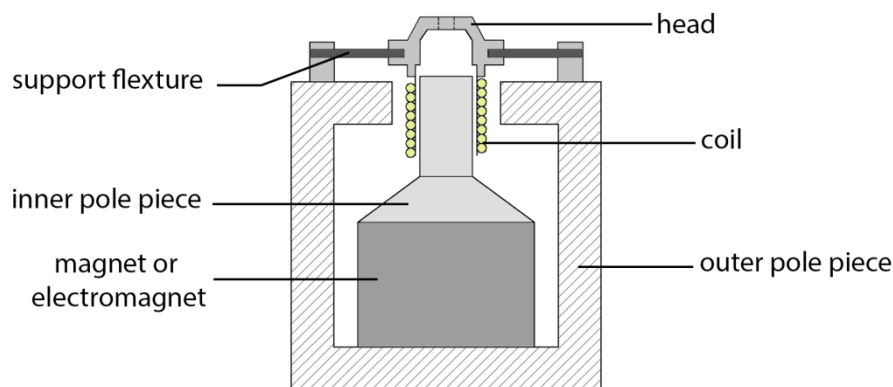


Figure 3.15: Illustration of the basic principle of an electromagnetic shaker.

Two types of input signals were tested in the shaker measurements (with an electromagnetic shaker) in section 7.2, sine sweep- and random signal (see Figure 3.16). The sine sweep signal provides a sinusoidal excitation where the frequency of the sine is increasing to a predefined limit. The sine sweep could also go backwards, decreasing from a selected maximum. This could be useful for comparing the estimated eigenfrequencies in the FRF, which tends to deviate when performing increasing or decreasing sine sweeps. At each step in the sine sweep there will be transient effects, which must have enough time to settle otherwise they will be included in the measurement. If the deviation between the peaks in the FRF is too large then a slower sine sweep with smaller increments (frequency/s) should be used [5]. The main advantage of using sine signals is the large SNR for both force- and response measurements.

This is because the well-defined sine signal is concentrated at only one frequency and the extraneous noise is spread over all frequencies. The sine sweep excitation is a slow method and is often used to study nonlinear or lightly damped structures [8]. Another disadvantage is that while the sine signal is sweeping over a resonance peak it will cause large amplitudes, which could bring errors from nonlinear behavior in the structure [5].

The random signal (explained in section 3.3) contains a wide range of frequencies that are exciting the structure simultaneously. A pure random signal is continuous and has a Gaussian (normal) probability distribution. This means that a random input force will create a random output signal, given that the system is linear. The benefits of using random signals are that there are no large amplitudes in the structure while performing the measurement (compared to a sinusoidal excitation), so errors caused by nonlinearities could be neglected [5]. Other common excitation signals that are not treated in this thesis are: burst random, pseudo-random and periodic chirp and the benefits/drawbacks of using these signals are explained in [8].

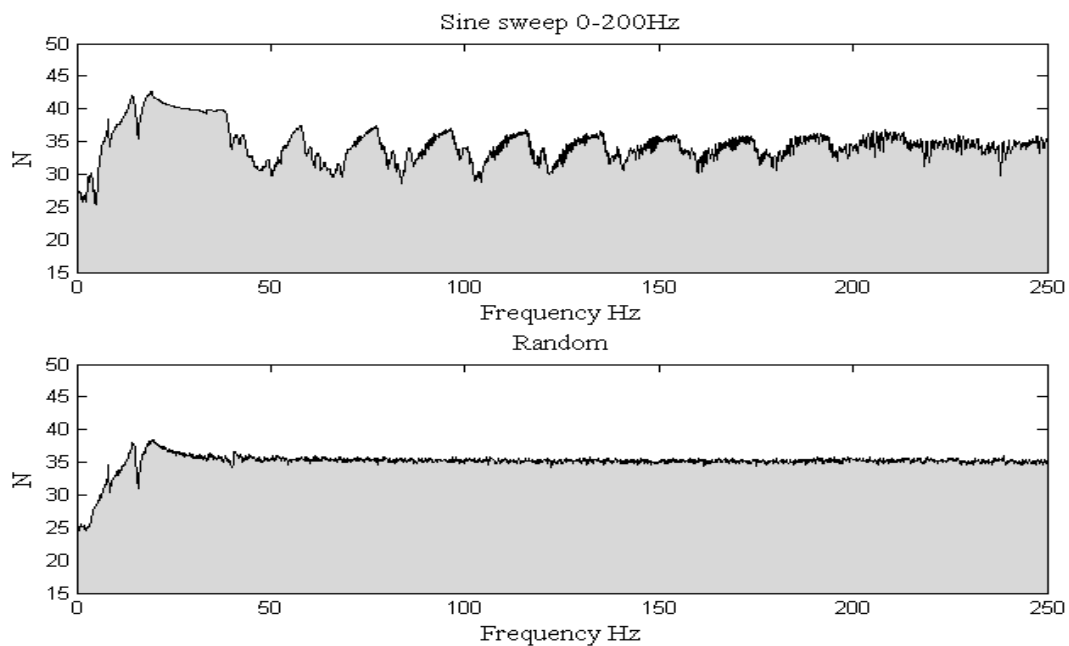


Figure 3.16: Force spectra for sine sweep and random signal (the corresponding force spectras in time domain are given in Figure B - 8 in Appendix B).

The problem with shakers is that they are attached to the structure causing higher mass than what is actually applied to the structure. This problem is noticeable in lightweight structures [13].



# 4

## Experimental Modal Analysis

The FRF explained in section 2.3 is the most fundamental entity in Experimental Modal Analysis (EMA). The FRF  $\mathbf{H}(f)$  is a complex ratio between input force  $\mathbf{F}(f)$  and output response  $\mathbf{U}(f)$  ( $f = \frac{\omega}{2\pi}$ ):

$$\mathbf{U}(f) = \mathbf{H}(f) \cdot \mathbf{F}(f) \rightarrow \mathbf{H}(f) = \frac{\mathbf{U}(f)}{\mathbf{F}(f)} \quad (4.1)$$

Another name for this type of modal analysis is Input-Output Modal Analysis which means that this technique requires measurement data from both the input force and the structure's response. The input- and output signals are measured by force transducers and accelerometers explained in section 3.4.2 and 3.4.3.

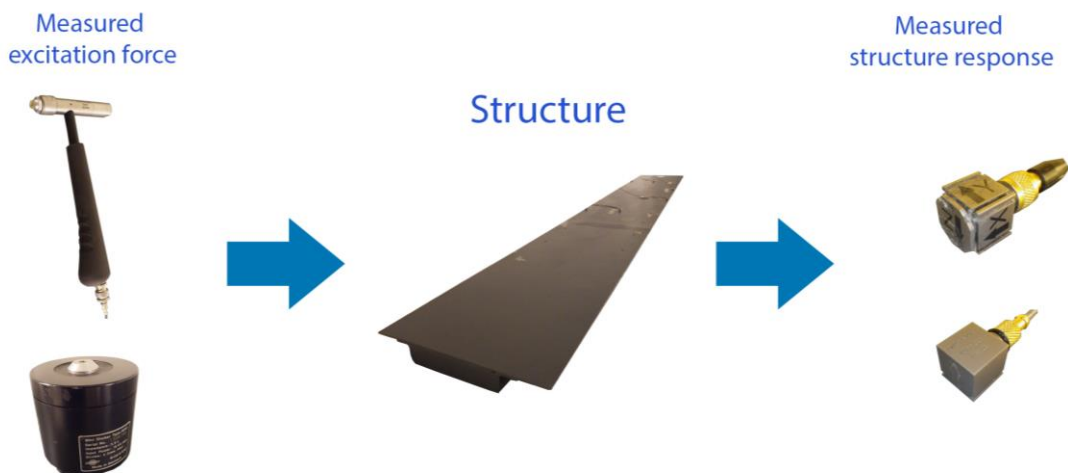


Figure 4.1: EMA principal.

The input force could come from a shaker that creates a load on the structure with different frequencies or an impact hammer that generates an impulse load (Figure 4.1). The impact hammer could be used on small and light structures like footbridges and provide wide-band input data in order to simulate different modes of vibration. Regular impact hammers have some disadvantages like the low frequency resolution and the low energy of the impact could make some modes hard to excite. Laboratories have developed special impulse devices designed to excite bridges see Figure 4.2 [15].



Figure 4.2: Impulse device (left) and electrodynamic shaker and impact hammer (right) [15].

To excite the structure in a lower frequency range and higher frequency resolution a shaker could be used. Large electrodynamic shakers (see Figure 4.2) can provide input signals with great variety (random, sine, etc.). The front-end modules can provide signals varying in both frequency and amplitude [15].

The resonance effect increases when the excitation force triggers the structure's natural frequency. In the FRF curve it's possible to identify the resonance frequencies and by observing the magnitude of the FRF between the point where the forces act on the structure and the measurement point, it's possible to evaluate the damaging effect of the resonance [16].

## 4.1 Measurement and Signal Processing

There are many different ways to perform a vibration test and it's important to understand the benefits of the various options and choose the optimal setup for each test to achieve good measurement results. There are several circumstances that could compromise the vibration test coming from supports, excitation devices or transducers. It is important to notice that there is no "right way" to test structures, every structure has its own difficulties concerning modal testing [5].

The force transducer could either be mounted directly on the structure and then attached to a shaker or it could be mounted behind the tip on an impact hammer. The accelerometers are attached on the structure to measure the vibration response. The analog signals captured from these measuring devices are digitized using an ADC (analog-to-digital converter). Before the digitalization the signals are first filtered by analog filters to reduce errors that could be caused by aliasing [17]. Aliasing occurs if the Nyquist theorem (sampling theorem) is not fulfilled. This theorem states that the sampling frequency should be two times larger than the Nyquist frequency according to Eq.(4.2).

$$f_{Nyquist} = \frac{f_{sampling}}{2} \quad (4.2)$$

This means that if the captured signal has a sampling frequency that is two times larger than the frequency of the signal, then the samples will fully represent the analog signal [8]. For example if the measured signal has a frequency of 200 Hz then the sampling frequency should be at least 400 Hz. Figure 4.3 illustrates what could happen if the sampling frequency is too low. The samples that should represent the signal with 200 Hz represent another signal with a lower frequency.

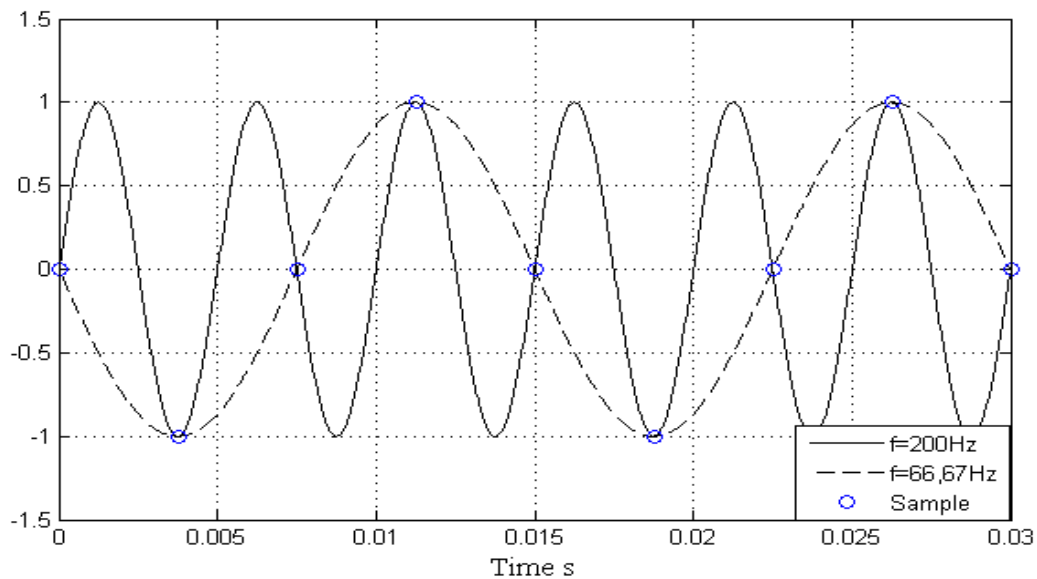


Figure 4.3: Signal with low resolution (low sampling frequency).

It is therefore important to make sure that the signal has enough samples within the frequency range, the more samples the better resolution.

After the digitization of the signals they are transformed from time domain to frequency domain by FFT. This transformation could cause leakage which is a far more devastating processing error than aliasing. Leakage occurs when the frequency content in the signal “leaks” out to frequencies nearby, causing lower amplitudes in the frequency spectra. Errors caused by leakage are reduced by applying windows (weighting functions) to the time signal [8] [18].

The next step in the signal processing is to perform averaging on the linear input-and output spectra to acquire three functions: input power spectrum, output power spectrum and a cross spectrum. These functions are then used to create the two main functions in EMA, the frequency response and the coherence function (Figure 4.4) [17].

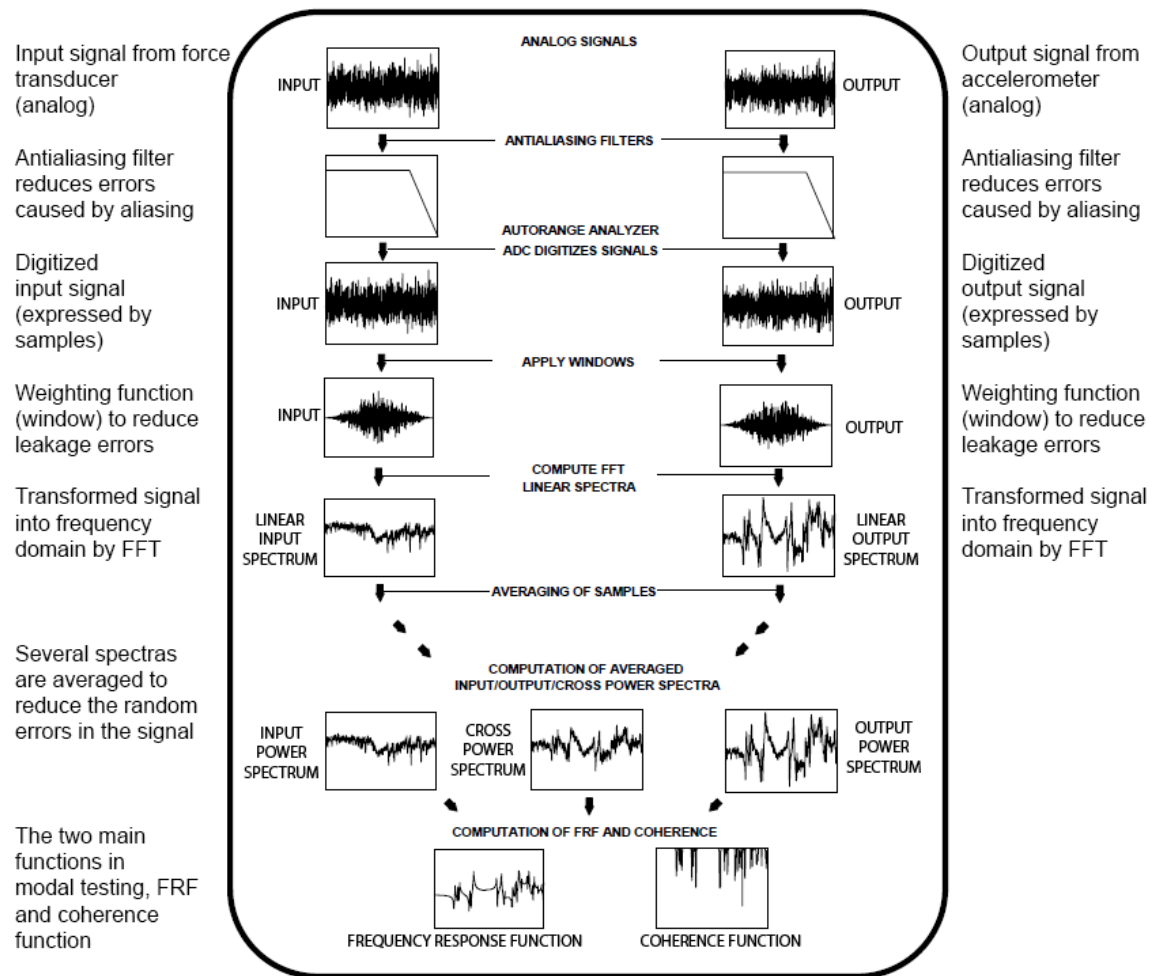
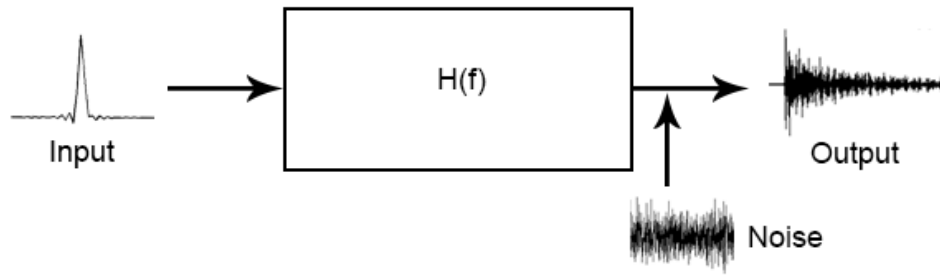
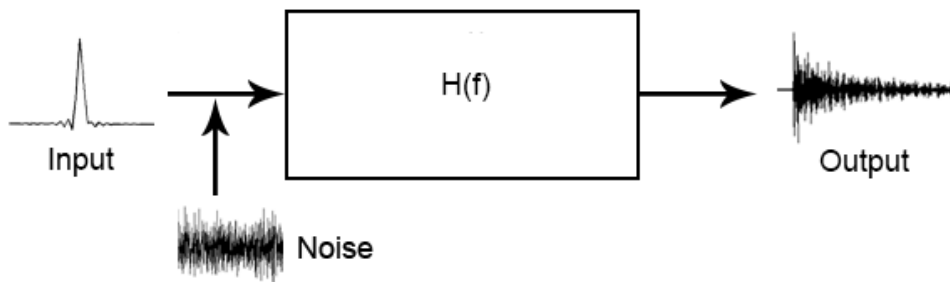


Figure 4.4: Signal processing [17].

The FRF explained in section 2.3 is used to estimate the modal parameters of the structure: eigenfrequencies, mode shapes and damping ratios. The coherence function is used to verify the quality of the FRF. Mentioned in [8] there are two ways to estimate the FRF, the  $H_1$  estimator and the  $H_2$  estimator. The  $H_1$  estimator assumes that the noise in the input signal is negligible and considers only the noise from the output signal (Figure 4.5). The  $H_2$  estimator works the other way around where noise is only present in the input signal (Figure 4.6).

Figure 4.5:  $H_1$  estimator.Figure 4.6:  $H_2$  estimator.

These two estimators are then used to compute the coherence function  $\gamma_{yx}^2(f)$  according to Eq. (4.3):

$$\gamma_{yx}^2(f) = \frac{H_1(f)}{H_2(f)} \quad (4.3)$$

where

$$0 \leq \gamma_{yx}^2(f) \leq 1.$$

If this ratio between the two estimates is  $\gamma_{yx}^2(f) = 1$  then there is no noise contaminating the measurement and the output signal is depending only on the input signal. More information regarding FRFs and coherence functions is found in [8].

### 4.2 Identification Methods

The development of different identification methods has increased rapidly over the last three decades. This was possible through the FFT and the improvement of the instrumental devices. Faster computers and powerful multi-channel analyzers made it possible to go from single input-output to multiple input-output techniques. There are three types of identification methods in EMA: time domain, frequency domain and tuned sinusoidal methods (see Figure 4.7). In the early years of modal testing frequency domain methods were the most common identification methods but the issues with bad frequency resolution, leakage and high modal densities lead to the development of various time domain methods. Time- and frequency domain methods are either indirect or direct. The indirect methods are using the modal model (modal parameters) to identify the FRFs. The identification of the FRFs with the direct methods is based on the spatial model (the general matrix equation of dynamic equilibrium given in Eq.(2.5)).

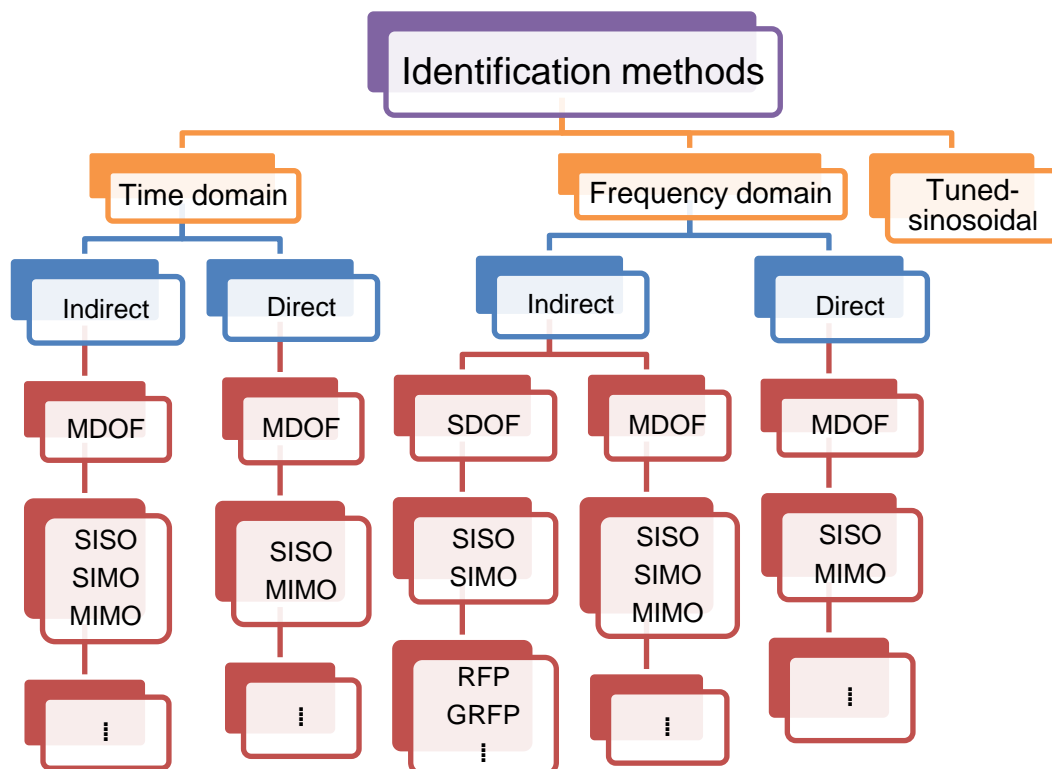


Figure 4.7: EMA identification methods.

In this thesis the Rational Fraction Polynomial (RFP) method has been used to identify the modal parameters in both impact- and shaker measurements. The original script of the RFP

method can only be applied on a single FRF at a time and it's therefore called a SISO method (Single-Input-Single-Output). The RFP method is a frequency domain method and was announced in 1982. The RFP method is widely used and it's included in many commercial modal analysis software. This method has been developed even further and is named the Global Rational Fraction Polynomial (GRFP) method which is a SIMO method (Single-Input-Multiple-Output) and has the ability to analyze several FRFs simultaneously. A more detailed explanation of the RFP and GRFP method is found in [5] and [19].

There is also a third category called MIMO (Multiple-Input-Multiple-Output) methods and these are used if two or more shakers are attached to a structure and generating multiple input forces.

# 5

## Operational Modal Analysis

Operational Modal Analysis (OMA) is also called Output-Only Modal Testing which means that only output responses from the structure are measured from unknown excitation forces (Figure 5.1). This is very advantageous because it's very hard and expensive to artificially excite a large structure. In OMA the natural sources (wind, waves, traffic etc.) could be used to excite the structure and then by measuring the structure's response the modal parameters: eigenfrequencies, mode shapes and damping ratios can be obtained by using certain extraction methods (see section 5.2) [20] [21].

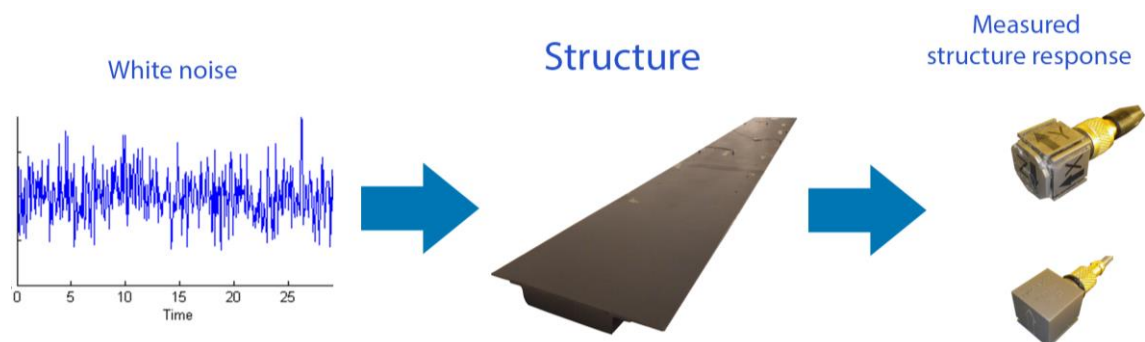


Figure 5.1: OMA principle.

OMA requires “white noise” as input force which is a random signal that contains a broad band of frequencies and has a Gaussian probability distribution (see section 3.3).

## 5.1 Structural Health Monitoring

There are some interesting applications regarding OMA, like Structural Health Monitoring (SHM), damage detection and updating computer models [22].

Bridges and buildings begin to deteriorate when they are built and starting to be used. Bridges should be designed for infrequent high forces such as overweight trucks or high wind speed. In some countries there are extreme forces like earth quakes and tornados. To determine if a bridge is safe to use after having endured such heavy loads is quite difficult. One way to evaluate the structure's current condition is to install accelerometers so it can be monitored. This type of structural observation is called structural health monitoring (SHM) and it will provide modal information while the structure is in use [22].

According to [23] wireless accelerometers are small and compact and because of their low cost it's possible to place a large amount of accelerometers (wireless sensor networks) on a structure to achieve high resolution in the output data. Another benefit of using wireless sensors is that they could be placed on locations that are hard for wires to reach.

Mentioned in [24] the health monitoring procedures do not give accurate information about where the damage is located or how severe the damage is. Methods that only give information if a possible damage has occurred are called global health monitoring methods. These are very useful, because if the data suddenly shows a modal disorder, additional examination could be done to find the location of a possible damage in the structure.

By looking at changes in natural frequencies and structural mode shapes it's possible to determine if there is a possible damage in the structure. But there are some drawbacks with these methods that could give raise to changes in the structures dynamic parameters such as temperature changes, moisture and other factors caused by the environment. So in order to get these methods to work, the signal due to the damage must be significantly higher than the noise from environmental factors [24].

In [22] this health monitoring technology is operational on the new built cable-stayed bridge that crosses the Pitt River in Vancouver (Pitt River Bridge). A 46 channel system is monitoring the dynamics of the bridges every day and the bridge and the sensor locations can be viewed in Figure 5.2.

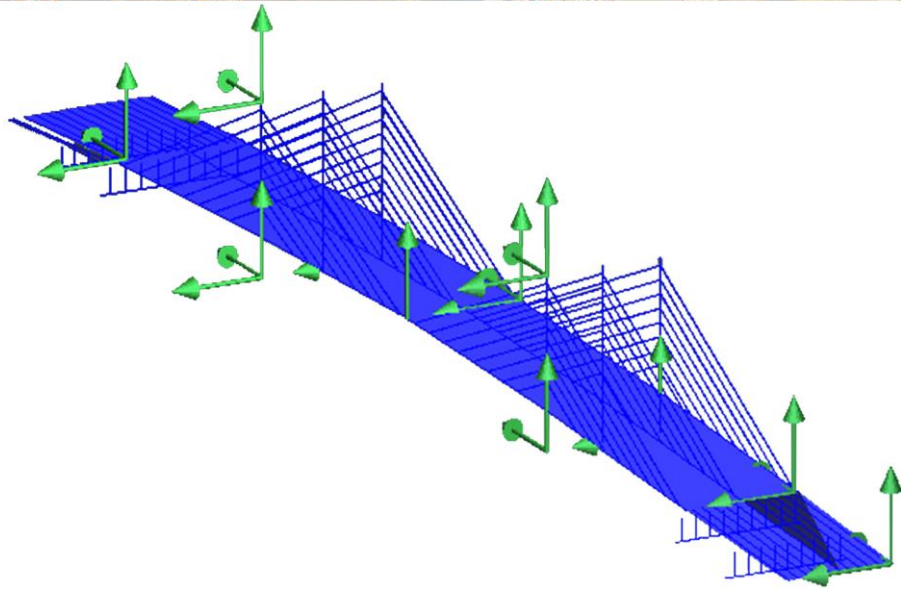


Figure 5.2: Pitt River Bridge (above [25]) and sensor positions (below [26]).

## 5.2 Extraction Methods

Extraction methods are used to collect modal parameters from OMA. Some of these extraction techniques are explained in this section.

### 5.2.1 Frequency Domain Decomposition

Frequency Domain Decomposition (FDD) is often referred to as the Peak-Picking technique and it is used for estimating eigenfrequencies and mode shapes from calculated spectral densities (obtained by performing FFT) using white noise as input force [27]. The estimation of mode shapes is done using Singular Value Decomposition (SVD) and it's one of the most powerful decompositions used in modern engineering. The SVD of a possible matrix  $\mathbf{G}$  is:

$$\mathbf{G} = \mathbf{V}_1 \mathbf{S} \mathbf{V}_2^H \quad (5.1)$$

where the columns in  $\mathbf{V}_1$  and  $\mathbf{V}_2$  are called left- and right singular vectors. The diagonal values in matrix  $\mathbf{S}$  are called singular values. The transpose is an Hermitian transpose where  $\mathbf{V}_2^H = \mathbf{V}_2^{-1}$ . A FDD plot is presented in Figure 5.3 and the peaks in the figure are the singular values in matrix  $\mathbf{S}$ .

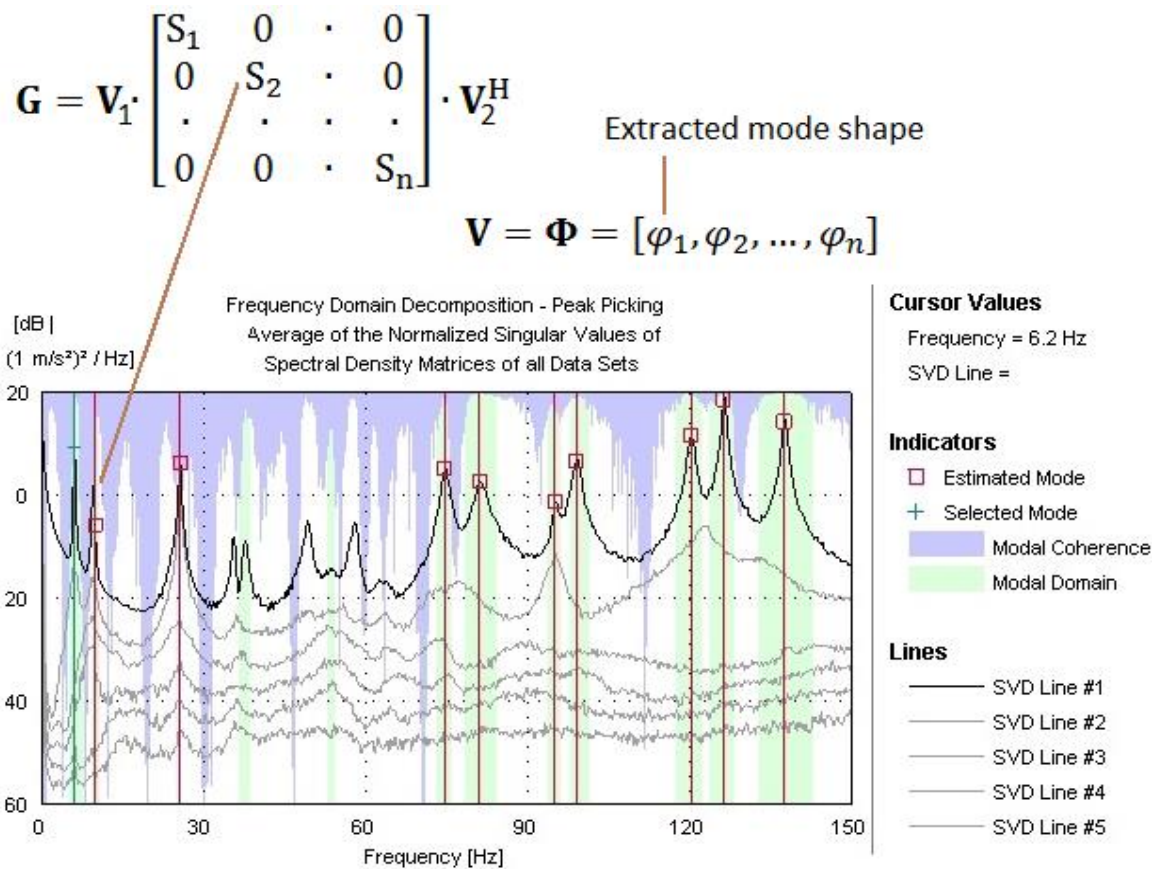


Figure 5.3: FDD plot.

The SVD corresponds to an SDOF identification of the system for each singular value (see Figure 5.4) [8].

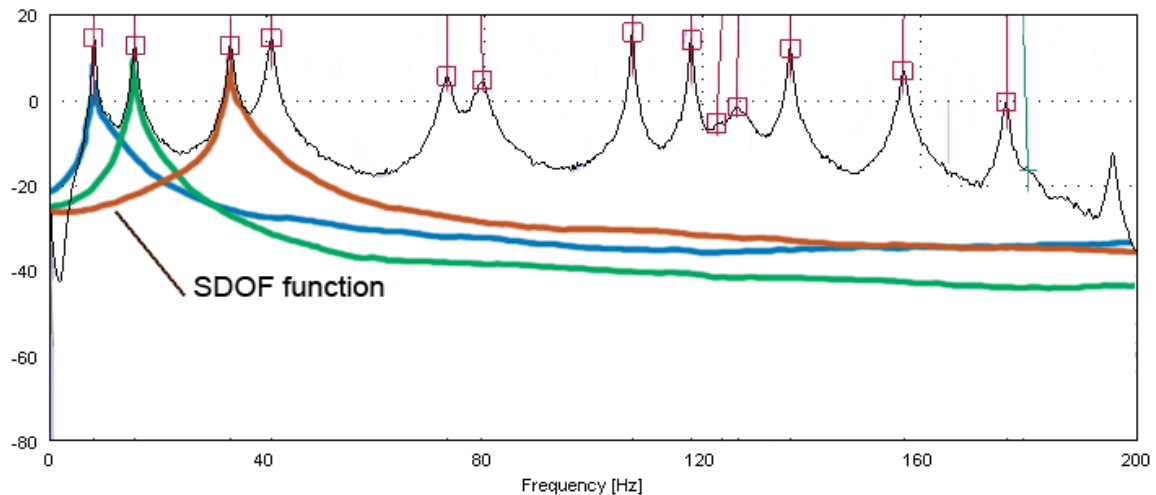


Figure 5.4: Estimated SDOF functions.

FDD is a very popular and user-friendly method and it gives precise values even though modes are closely spaced and the measurement contains noise [28].

### 5.2.2 Enhanced Frequency Domain Decomposition

The Enhanced Frequency Domain Decomposition (EFDD) method is an extension of the FDD technique explained in section 5.2.1. Besides an improved estimate of eigenfrequencies and mode shapes, the EFDD method can also estimate damping ratios for different modes. In EFDD the estimated SDOF functions (see Figure 5.4) by FDD peak-picking are used as reference vectors to compute MAC (explained further in section 5.3) values between the singular vectors for the different frequency lines.

If a computed MAC value is larger than a user specified MAC rejection level the corresponding singular value is included in the description of the SDOF function. By lowering this MAC rejection level more singular values are included in the description of the SDOF function and this could make the representation of this function less accurate [29]. According to [30] a good MAC rejection limit is around 0,9 and this will ensure a good representation of the SDOF function with small amount of noise around the chosen peak.

### 5.2.3 Stochastic Subspace Identification

The Stochastic Subspace Identification (SSI) technique is a very strong and effective modal identification method and it works mainly in the time domain. The algorithms of this method have been around for a decade and were announced by van Overschee and De Moor. As FDD and EFDD the SSI also uses SVD to extract the modal parameters [31].

The results from an SSI processed time data are viewed in a stabilization diagram (see Figure 5.5). In Figure 5.5 the singular values are presented in both SVD-lines and SVD subspace (see the diagram in the bottom right corner). The SSI will estimate both physical modes and non-physical modes. The difference is that the estimated physical modes are repeated for multiple model orders and fulfilling the damping a priori knowledge. The remaining modes shown in the diagram are considered to be unstable or noise modes [32]. More information about the SSI technique is given in [33].

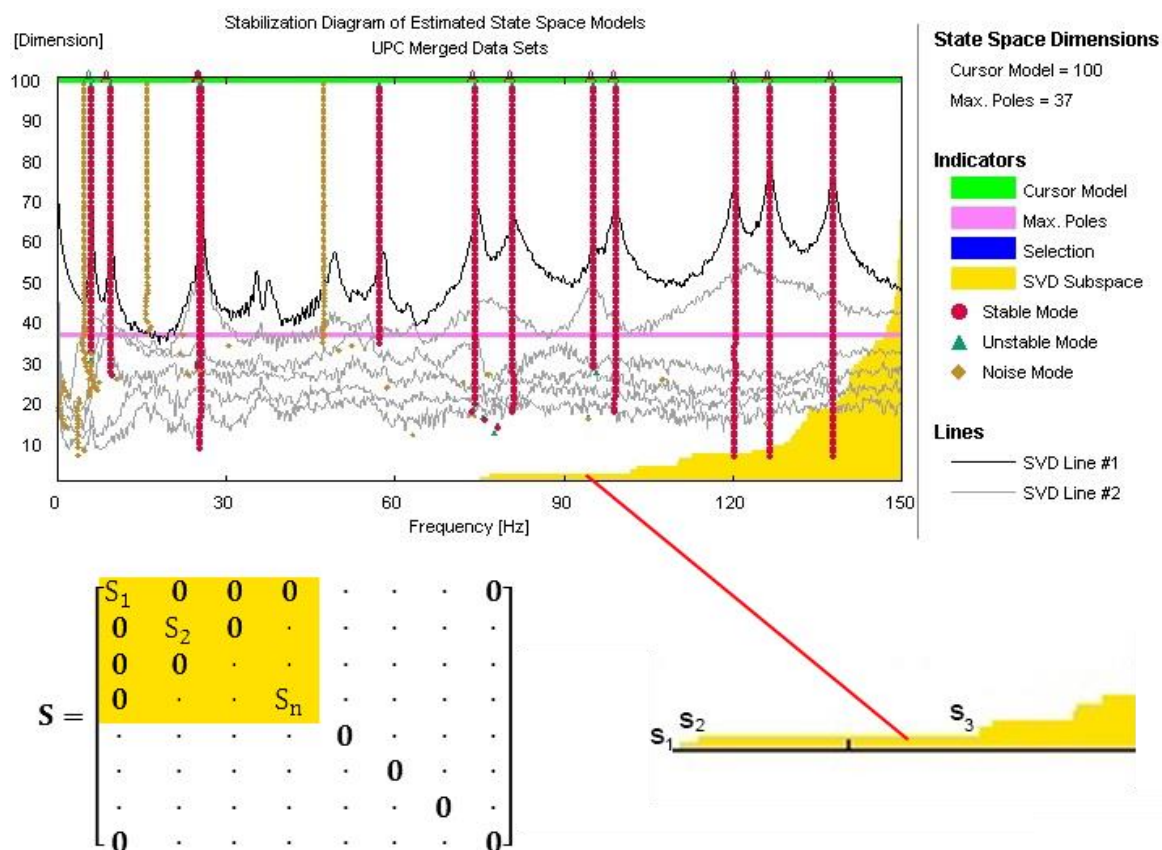


Figure 5.5: SSI plot.

### 5.3 Modal Assurance Criterion

The modal assurance criterion (MAC) technique is used to compare mode shapes analytically in both EMA and OMA. This could be mode shapes that are obtained from different extraction methods or from numerical calculations. The MAC value is real and bounded between 0 and 1, if this value is close to 1 the compared mode shapes are consistent (see Table 7.2). The MAC between the mode shapes  $\Phi_i$  and  $\Phi_j$  is defined by the following equation [32]:

$$\text{MAC} = \frac{(\Phi_i^T \Phi_j)^2}{(\Phi_i^T \Phi_i)(\Phi_j^T \Phi_j)} \quad (5.2)$$



# 6

## Finite Element Model

This chapter introduces the steel structure and how the structure was analyzed in the Finite Element (FE) program ABAQUS. The test setup is viewed in Figure 6.1 where the steel structure is resting on two steel pallets. These pallets are loaded with masses to make the structure as stable and well-defined as possible.

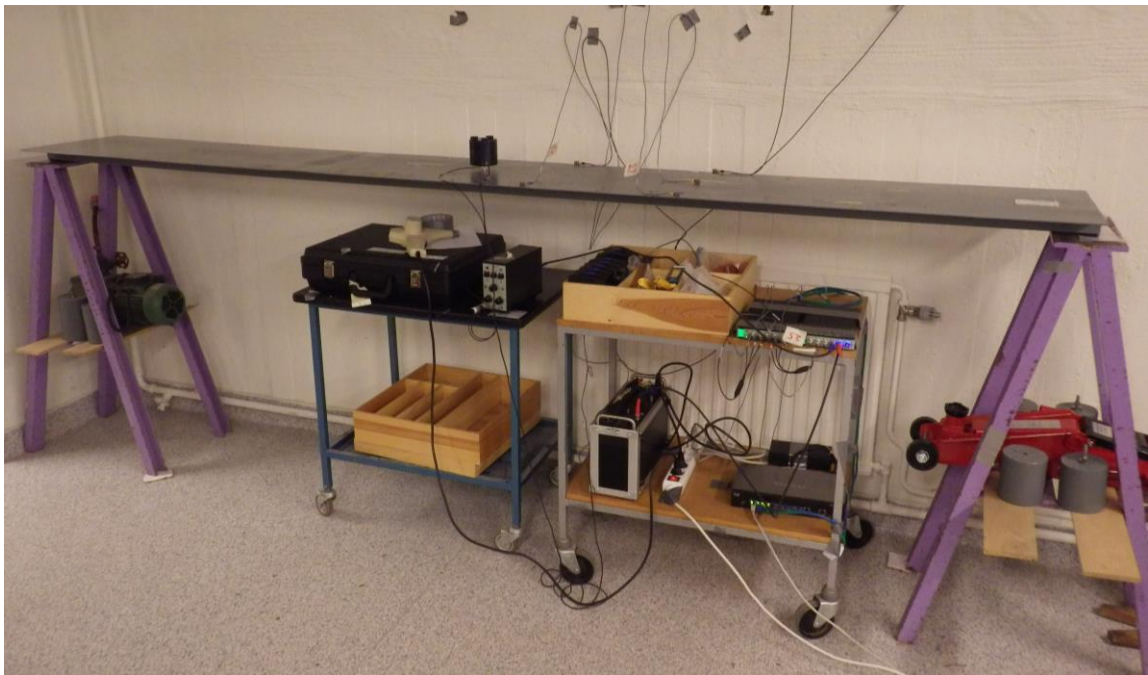


Figure 6.1: The steel structure and the weighted steel pallets.

## 6.1 Structure

The analyzed structure is a 3 m long and 0,4 m wide steel plate with two L-profiles welded underneath. On the ends of the plate the L-profiles are attached to two steel plates in order to obtain a stiffer cross section and better boundary conditions as these thin plates are the only parts that are in contact with the steel pallets. There are some drilled holes on the steel plate for attaching a shaker or masses. This simple structure is ideal for modal testing because of its well-defined geometry and slender cross section. The structure's geometry and material parameters are presented in Figure 6.2, Figure 6.3 and Table 6.1.

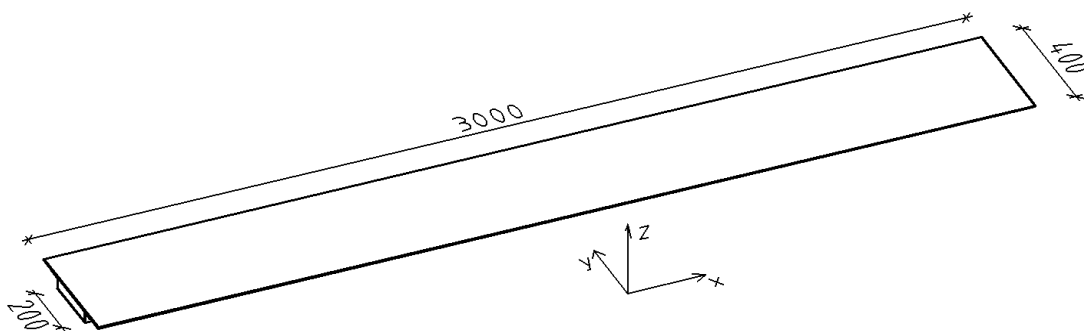


Figure 6.2: Shape, dimensions and coordinates for the structure [mm].

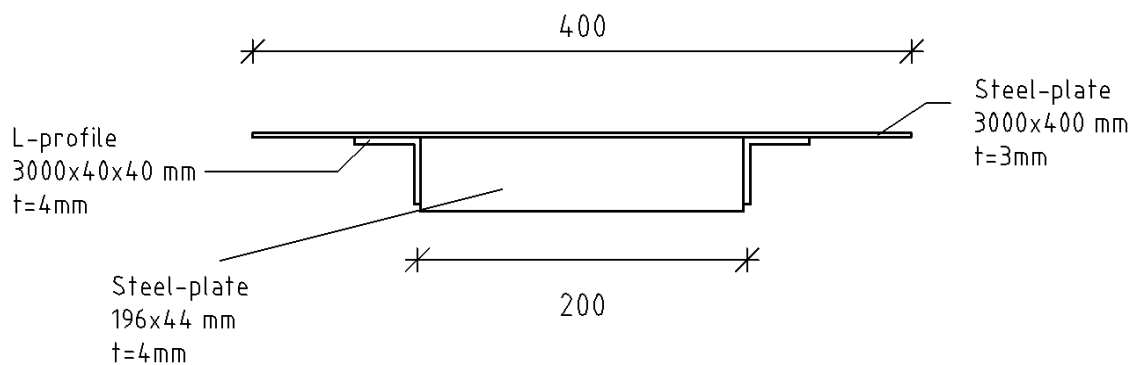


Figure 6.3: The different components of the structure [mm].

Table 6.1: Material properties.

Material	Young's modulus	Poisson's ratio	Density
Steel	210 GPa	0,3	7800 kg/m <sup>3</sup>

## 6.2 FE-Model in ABAQUS

To predict the different modes and eigenfrequencies of the structure a FE-model was made in ABAQUS (Figure 6.4). Because the structure consists of thin components the ideal elements for this structure are shell elements. The theory behind the finite element method and shell elements is not addressed in this thesis, for further reading, this theory can be observed in [34].

It's important to notice that it is an approximation to use shell elements because the L-profiles that are welded underneath the structure will act in the same plane as the 3 m steel plate. The inaccuracy of this approximation is relatively small and the benefit of using shell elements for this structure is that it doesn't require so many elements to get reasonable results, compared to solid elements.

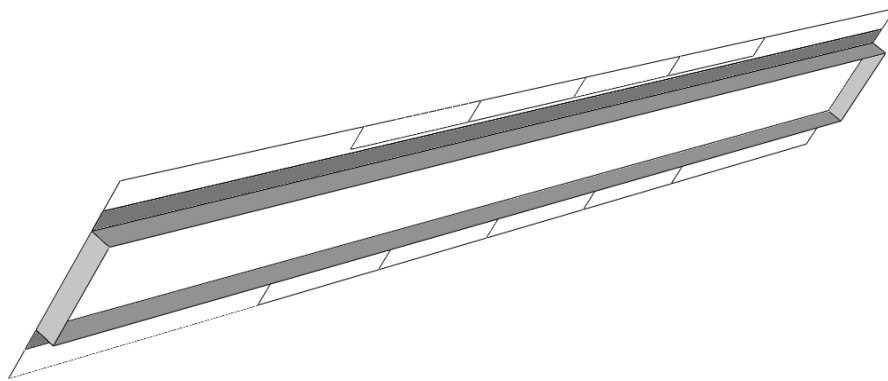


Figure 6.4: FE-model created in ABAQUS.

The amount of mesh that was required for this structure was determined by testing different mesh densities. As the FE-method is an approximate method where smaller elements gives accurate results there is a point where the change in the results is very small. As suspected, the mesh for the reinforcing parts needs smaller elements than the 3 m steel plate. Figure 6.5 shows the mesh sizes and the results from the eigenvalue analysis.

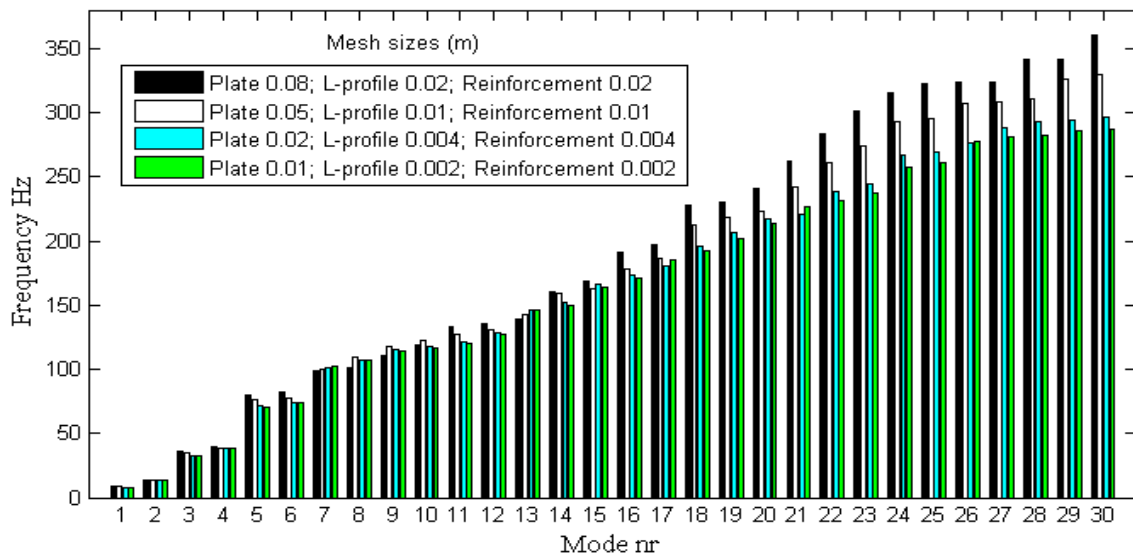


Figure 6.5: Mesh sizes.

The mesh that was chosen for the different parts is given in Table 6.2 and shown in Figure 6.6. This mesh was chosen because it was very small differences between the mesh sizes: 0,02; 0,004; 0,004 and the mesh sizes 0,01; 0,002; 0,002 and it will provide enough accuracy to compare FE results with laboratory measurements.

Table 6.2: Mesh on the structure's parts.

Part	Mesh (m)
3m Steel plate	0,02
L-profile	0,004
Reinforcing side plate	0,004

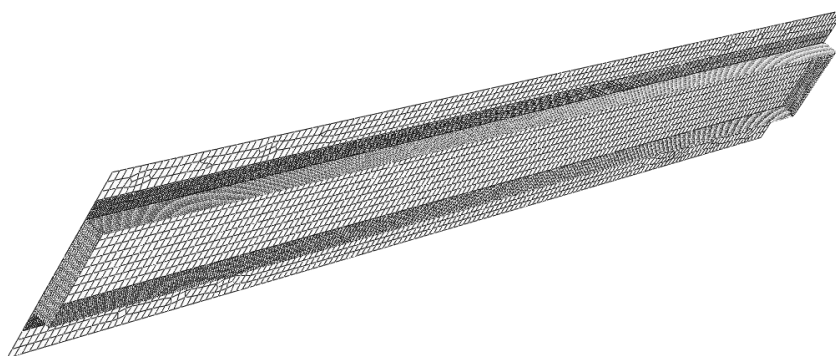


Figure 6.6: Meshed parts in the FE-model.

The structure is freely supported, which means that it has one fixed support and one roller support. To make these boundary conditions (see Figure 6.7) as accurate as possible rubber was placed beneath the first support to simulate the fixed end. On the roller support thin plastic was placed to make it possible for the structure to move in the x-direction (the coordinate system for the structure is given in Figure 6.2).



Figure 6.7: Rubber (pinned support) and plastic (roller support) boundary.

The eigenfrequencies and mode shapes obtained from the FE-analysis in ABAQUS are presented in Table 6.3 and Figure 6.8-Figure 6.15.

Table 6.3: Results from the eigenvalue analysis in ABAQUS.

Mode nr	Eigenfrequency (Hz)	Type
1	8,23	Bending
2	13,88	Torsion
3	32,53	Bending
4	38,25	Torsion
5	71,18	Bending
6	74,48	Torsion
7	101,66	Bending in plane
8	107,16	Bending
9	114,98	Bending
10	117,63	Bending
11	120,82	Torsion
12	127,78	Bending
13	146,64	Bending
14	151,65	Bending
15	166,26	Torsion
16	173,75	Bending
17	181,53	Bending
18	197,54	Bending
19	206,62	Torsion
20	217,53	Bending
21	221,84	Bending
22	239,37	Torsion
23	245,62	Bending

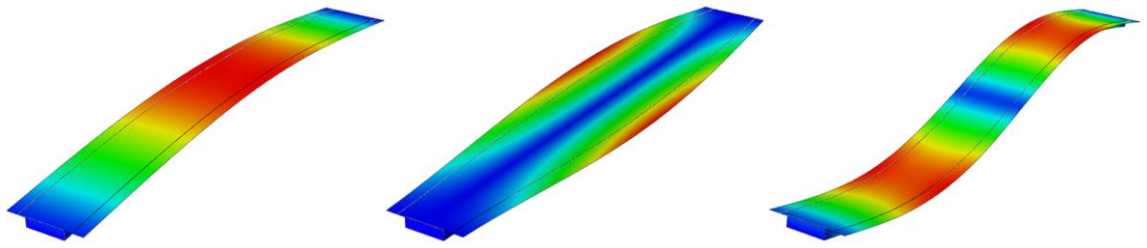


Figure 6.8: Mode 1: 8.23 Hz

Mode 2: 13.88 Hz

Mode 3: 32.53 Hz

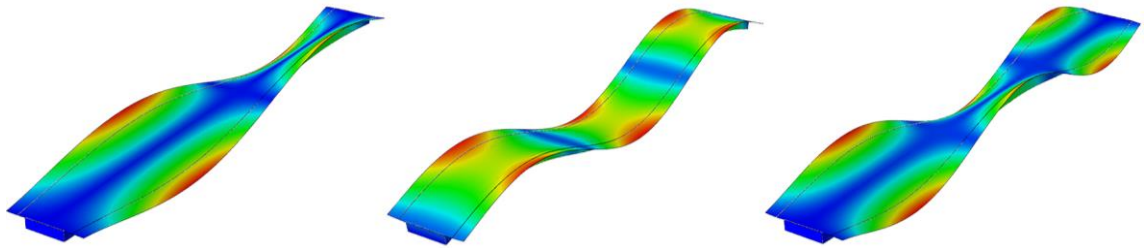


Figure 6.9: Mode 4: 38.25 Hz

Mode 5: 71.18 Hz

Mode 6: 74.48 Hz

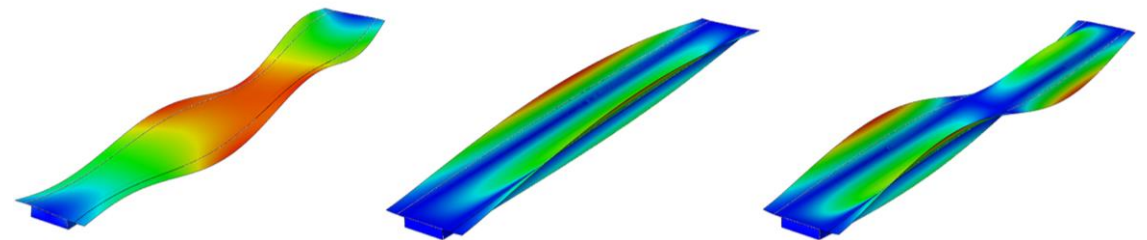


Figure 6.10: Mode 7: 101.66 Hz

Mode 8: 107.16 Hz

Mode 9: 114.98 Hz

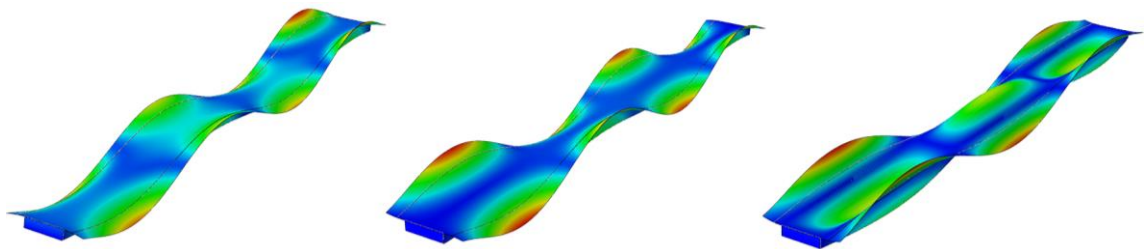


Figure 6.11: Mode 10: 117.63 Hz

Mode 11: 120.82 Hz

Mode 12: 127.78 Hz

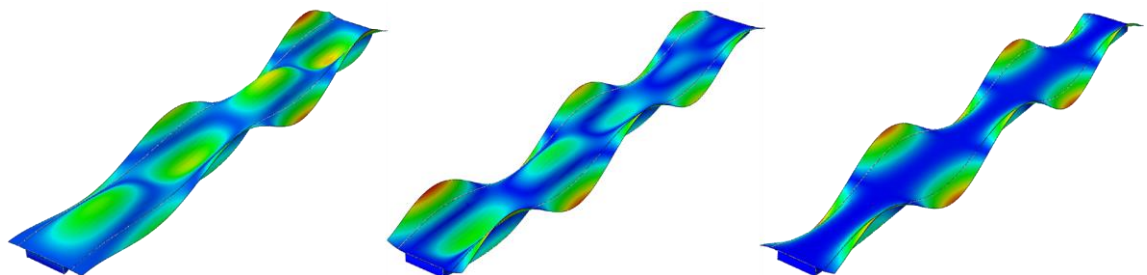


Figure 6.12: Mode 13: 146.64 Hz

Mode 14: 151.65 Hz

Mode 15: 166.26 Hz

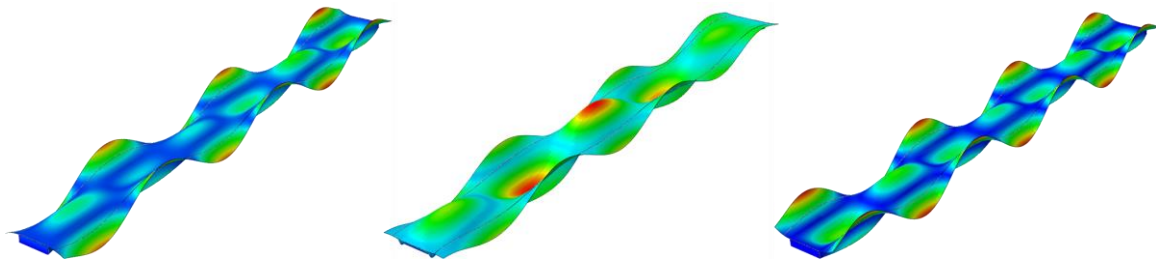


Figure 6.13: Mode 16: 173.75 Hz

Mode 17: 181.53 Hz

Mode 18: 197.54 Hz

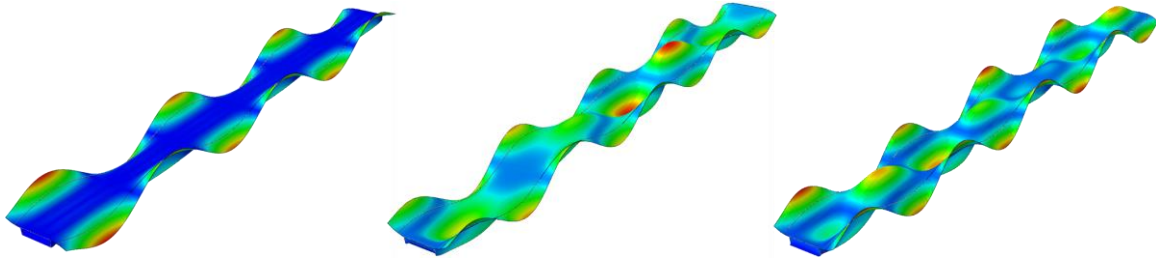


Figure 6.14: Mode 19: 206.62 Hz

Mode 20: 217.53 Hz

Mode 21: 221.84 Hz

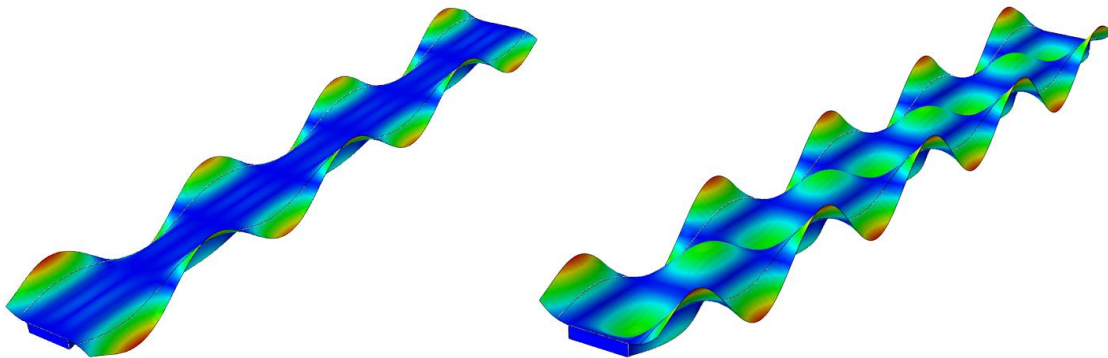


Figure 6.15: Mode 22: 239.37 Hz

Mode 23: 245.62 Hz

All these solved mode shapes (Figure 6.8-Figure 6.15) are either bending or torsional modes in the z-direction (see Figure 6.2) except for mode 7 in Figure 6.10. Mode 7 is an in-plane mode where the structure will bend in the y-direction.

### 6.3 Structure with Added Mass

The structure had drilled holes at different positions that made it possible to attach cylindrical masses on the structure (Figure 6.16). This will change the dynamic behavior of the structure and give other interesting results than the previous setup.



Figure 6.16: The structure with added masses.

The masses are cylindrical shaped and have the following dimensions:  $d=9,5$  cm and  $h=11,0$  cm (see Figure 6.17). The average weight of the masses is approximately 5,4 kg.



Figure 6.17: Cylindrical mass.

To make the modeling as simple as possible the masses were attached as point masses in ABAQUS (Figure 6.18).

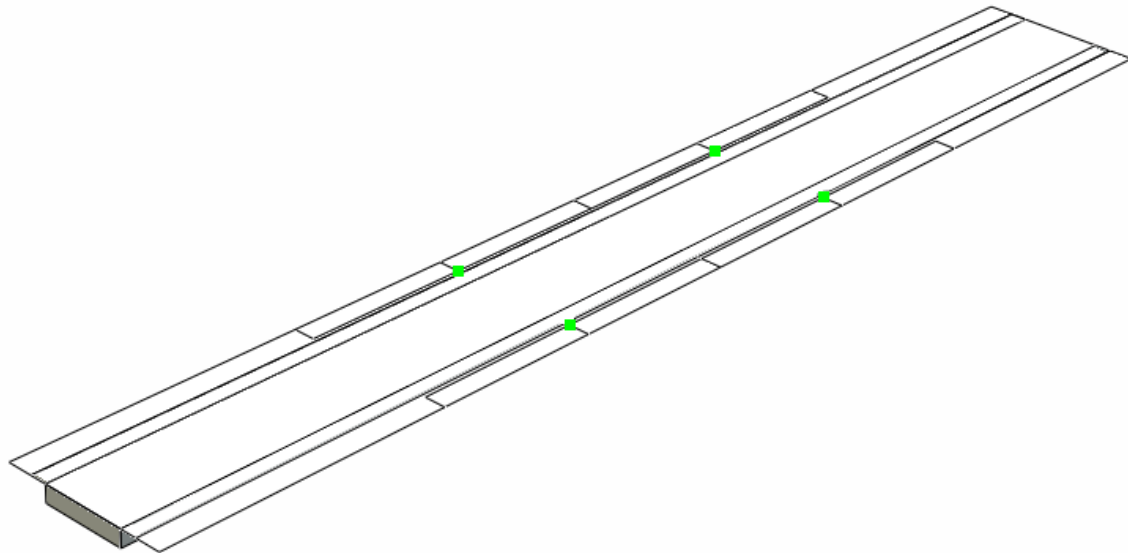


Figure 6.18: Point masses in the ABAQUS model.

The results from the numerical calculations, the impact measurement and the OMA performed on this mass loaded structure are given in Appendix D.

# 7

## Measurements

This chapter contains various measurements performed on the steel structure explained in chapter 6.

### 7.1 EMA Impact Hammer

The hardware and software that were used during the measurements were from B&K and the devices used in the hammer test are shown in Figure 7.1.

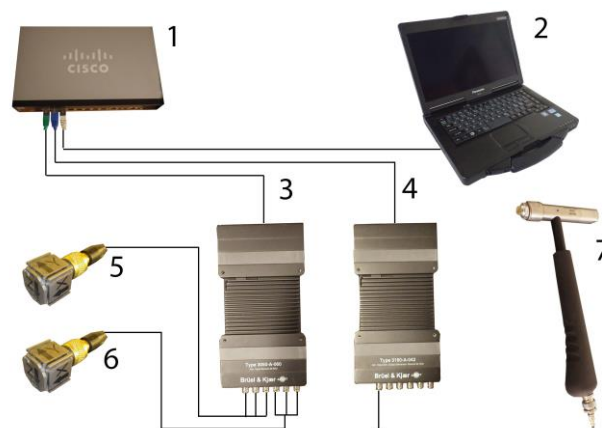


Figure 7.1: Impact hammer setup.

1. Switch for connecting front-ends to computer.
2. Computer with PULSE LabShop (version 18.1.1.13-2014-03-27) and PULSE Reflex (version 18.1.1.13-2014-03-27) software for signal analysis.
3. Front-end with six input channels (Type 3050-A-060) that captures the response signals.
4. Front-end with four input channels and two output channels (Type 3160-A-042) that captures the force signal from impact hammer.
- 5-6. Triaxial accelerometer mounted on the structure with a thin layer of wax.
7. Impact hammer connected to front-end. The force transducer is placed behind the tip of the hammer to register the applied force on the structure.

The measurement was performed using the program Pulse LabShop from B&K. By loading a specific template in the program the necessary steps of performing a hammer test were given. These steps involved hardware update, drawing simplified structure geometry (creating both lines and surfaces between the measurement points), create measurement sequences, adjusting the hammer trigger, hammer weighting and response weighting.

To increase the accuracy of the impacts all nodes that were excited were hit five times and the FRF was then averaged, the selected nodes that were excited are viewed in Figure 7.2. The nodes with hammer strikes (1-18) are connected by lines and surfaces to make it possible to visualize the different modes of vibration. The measured FRFs were exported into Pulse Reflex for further analysis and to extract the modal parameters with the RFP method (explained in section 4.2).

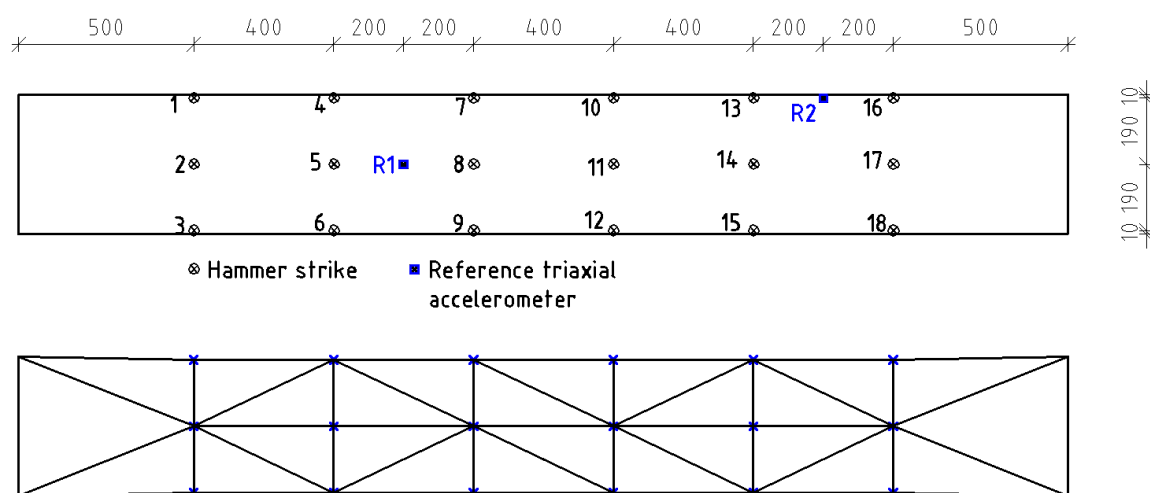


Figure 7.2: Positions of hammer strikes and reference accelerometers above, the obtained mesh below [mm] (a 3D-representation is given in Figure B - 1 in Appendix B).

The results from the impact measurement are given in Table 7.1 and Figure 7.5-Figure 7.9. All mode shapes and damping ratios were obtained using the RFP method in Pulse Reflex. Figure 7.3 shows the FRFs and the coherence functions that were obtained after averaging the first five strikes at point 1 (see Figure 7.2). The corresponding FRFs and coherence functions for all channels can be observed in Figure B - 2 in Appendix B. MAC between numerical and measured results are presented in Table 7.2.

Table 7.1: Eigenfrequencies and damping ratios obtained from impact measurement.

Mode nr	Eigenfrequency (Hz)	Modal damping (%)
1	8,39	2,44
2	16,11	1,92
3	33,68	1,40
4	40,96	0,88
5	73,15	0,47
6	80,13	0,93
7	-	-
8	107,30	0,19
9	118,11	0,24
10	124,64	0,39
11	127,72	0,57
12	136,65	0,27
13	157,32	0,23
14	176,37	0,29
15	182,15	0,76

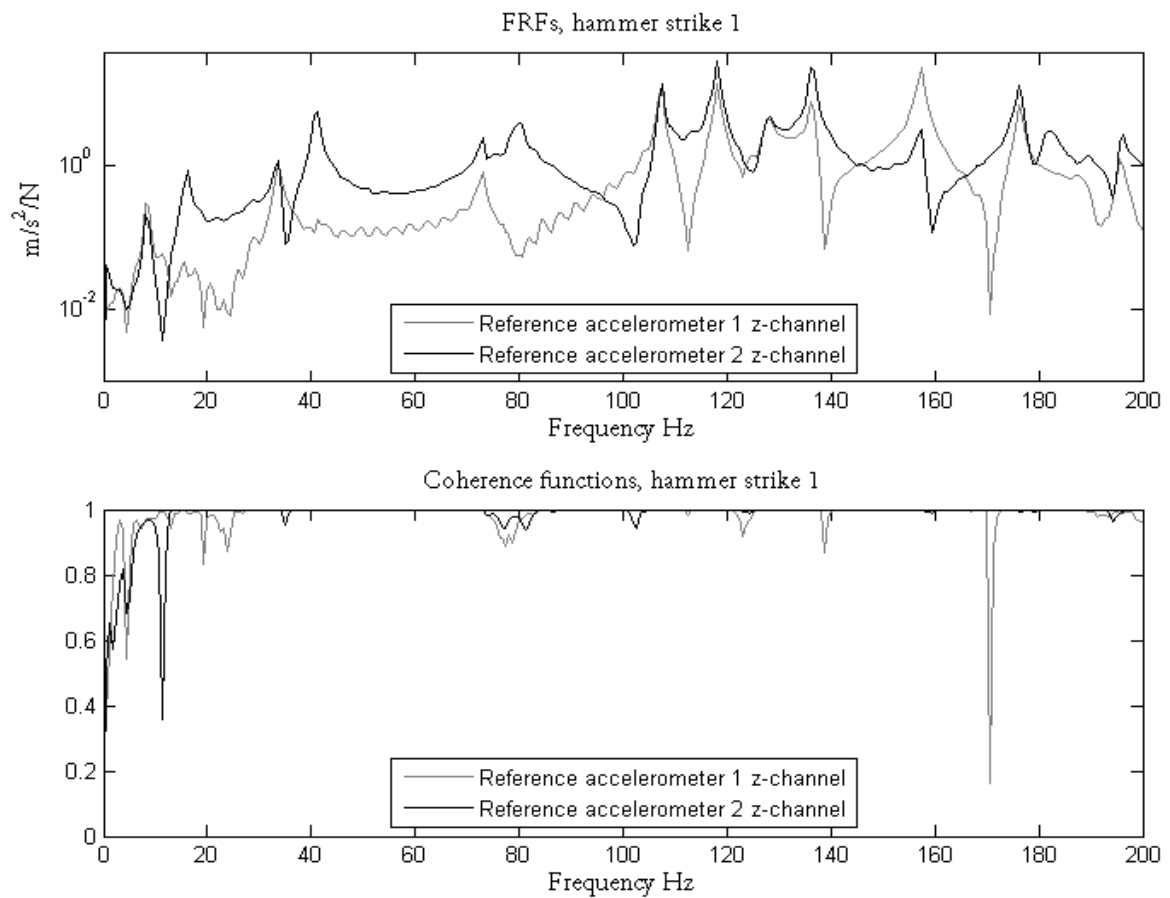


Figure 7.3: FRFs (above) and coherence functions (below) for hammer strike 1.

Figure 7.4 shows the FRFs and the coherence functions obtained from the first three striking positions (see Figure 7.2).

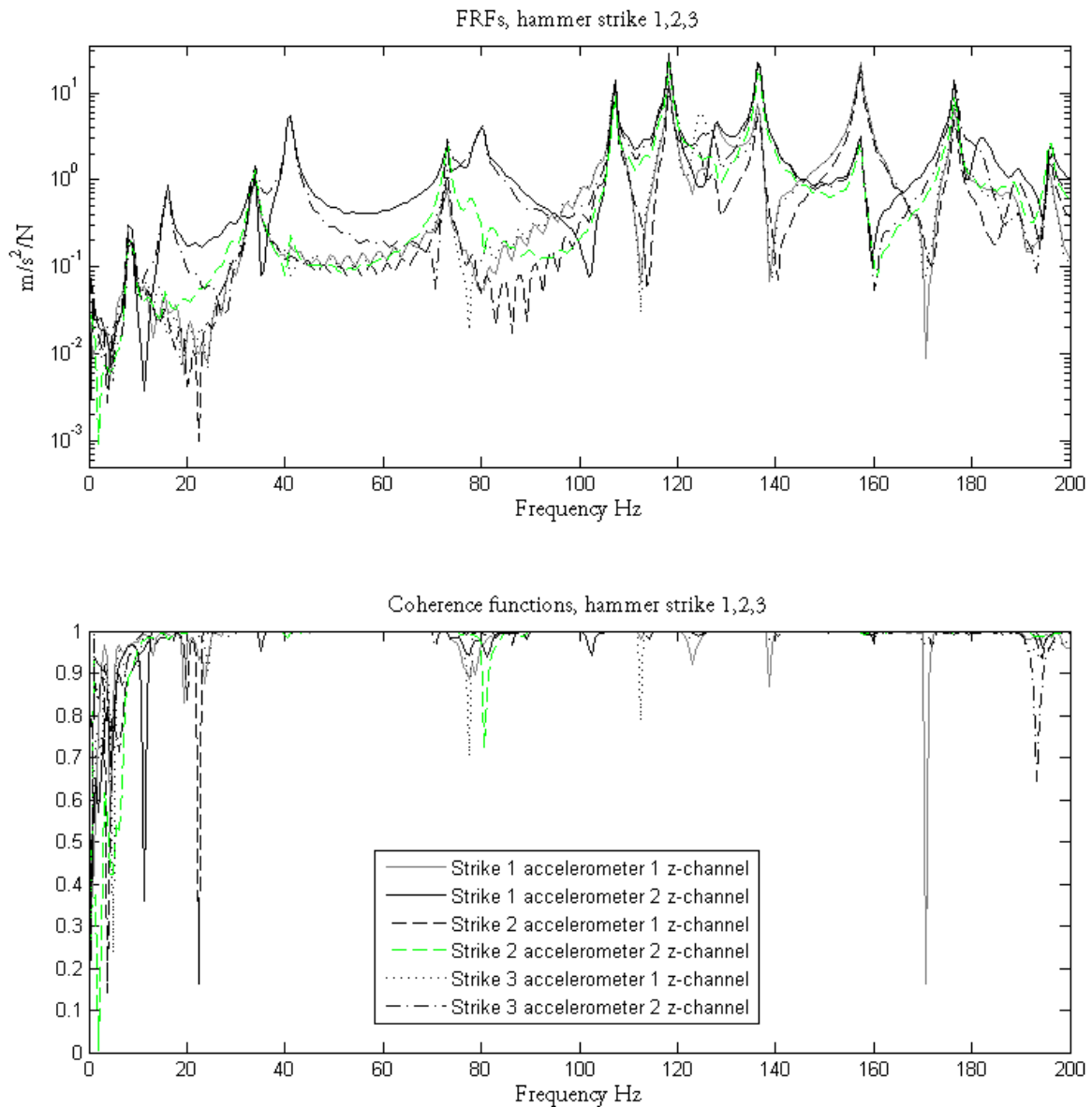


Figure 7.4: FRFs (above) and coherence functions (below) for hammer strike 1,2 and 3.

All FRFs and coherence functions (in z-direction) obtained with accelerometer 2 and impact hammer are presented in Figure B - 5 and Figure B - 6 in Appendix B.

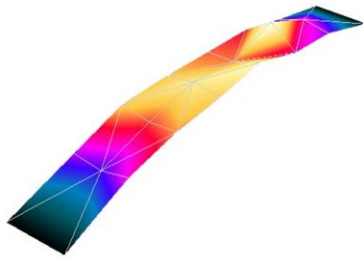
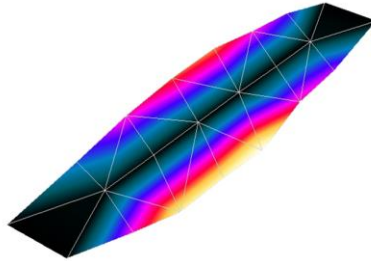
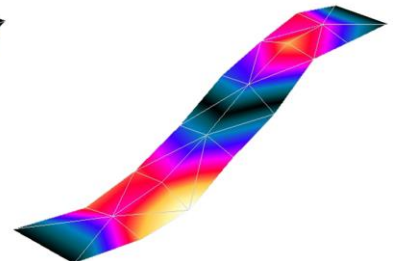


Figure 7.5: Mode 1: 8.39 Hz



Mode 2: 16.11 Hz



Mode 3: 33.68 Hz

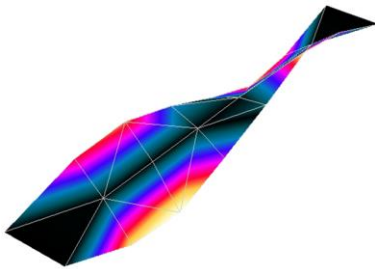
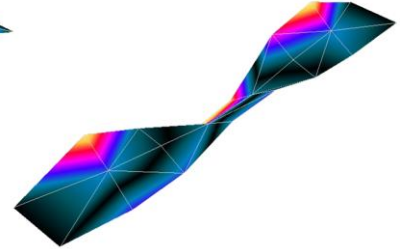


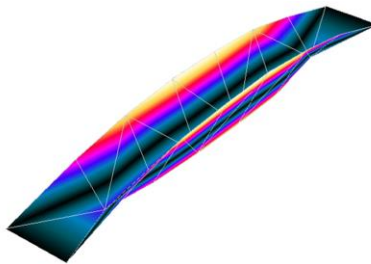
Figure 7.6: Mode 4: 40.96 Hz



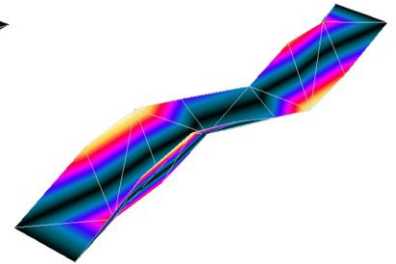
Mode 5: 73.15 Hz



Mode 6: 80.13 Hz



Mode 8: 107.30 Hz

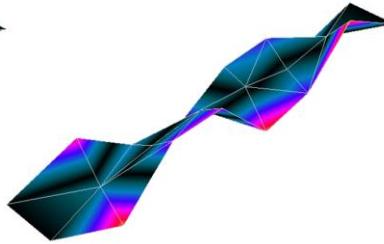


Mode 9: 118.11 Hz

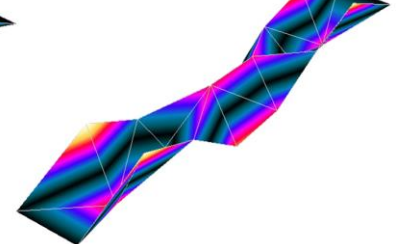
Figure 7.7: Mode 7: -



Figure 7.8: Mode 10: 124.64 Hz



Mode 11: 127.72 Hz



Mode 12: 136.65 Hz

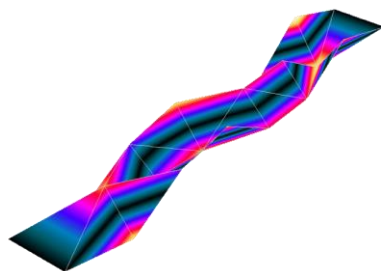
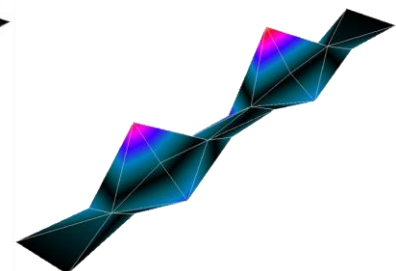


Figure 7.9: Mode 13: 157.32 Hz



Mode 14: 176.37 Hz



Mode 15: 182.15 Hz

Table 7.2: MAC table, comparing extracted modes from impact measurement with numerical calculations.

Nr	Nr	1	2	3	4	5	6	8	9	10	11	12	13	14	15
	EMA Hammer	8,39	16,11	33,68	40,96	73,15	80,13	107,30	118,11	124,64	127,72	136,65	157,32	176,37	182,15
	ABAQUS														
1	8,23	<b>0,966</b>	0,016	0,022	0,009	0,031	<b>0,064</b>	<b>0,199</b>	0,002	0,041	<b>0,133</b>	0,005	0,000	0,016	<b>0,188</b>
2	13,88	0,001	<b>0,954</b>	0,026	0,031	0,046	0,026	0,000	0,001	0,015	<b>0,065</b>	0,004	0,000	0,011	<b>0,134</b>
3	32,53	0,001	0,003	<b>0,903</b>	0,005	0,026	0,022	0,001	<b>0,227</b>	0,009	0,008	0,000	0,001	0,006	<b>0,054</b>
4	38,25	0,001	0,005	0,000	<b>0,934</b>	0,007	0,029	0,000	0,000	0,002	0,005	0,001	0,000	0,003	0,021
5	71,18	0,000	0,000	0,003	0,000	<b>0,707</b>	0,007	0,000	0,001	0,014	0,000	<b>0,316</b>	0,002	0,006	0,000
6	74,48	0,000	0,000	0,000	0,010	0,049	<b>0,715</b>	0,000	0,000	0,001	0,003	0,000	0,000	0,000	0,009
7	101,66	0,000	0,041	0,000	<b>0,060</b>	0,017	<b>0,135</b>	0,000	0,000	<b>0,138</b>	<b>0,308</b>	0,002	0,001	0,000	0,009
8	107,16	<b>0,165</b>	0,020	0,045	0,010	<b>0,097</b>	<b>0,086</b>	<b>0,996</b>	0,002	0,011	<b>0,067</b>	0,003	0,003	0,036	<b>0,276</b>
9	114,98	0,009	0,005	<b>0,186</b>	0,005	0,012	0,036	0,000	<b>0,992</b>	<b>0,075</b>	<b>0,099</b>	0,001	0,015	0,006	<b>0,094</b>
10	117,63	0,000	0,000	0,001	0,000	0,013	0,000	0,000	0,001	<b>0,407</b>	<b>0,135</b>	0,033	<b>0,546</b>	0,007	0,001
11	120,82	0,000	0,003	0,002	0,000	0,001	0,019	0,000	0,000	<b>0,210</b>	<b>0,414</b>	0,002	0,001	0,000	0,009
12	127,78	0,000	0,000	0,000	0,000	<b>0,101</b>	0,002	0,000	0,001	0,039	0,010	<b>0,958</b>	0,014	0,020	0,001
13	146,64	0,001	0,000	0,001	0,000	0,002	0,000	0,000	0,007	0,042	0,012	0,001	<b>0,910</b>	<b>0,057</b>	0,005
14	151,65	0,002	0,000	0,000	0,000	0,008	0,000	0,004	0,001	0,008	0,003	0,024	0,030	<b>0,846</b>	0,023
15	166,26	0,002	0,000	0,002	0,000	0,008	0,004	0,000	0,000	0,002	0,004	0,001	0,000	0,003	<b>0,252</b>

## 7.2 EMA Shaker

The shaker setup requires more hardware than the impact hammer test. The equipment used in the shaker measurement is viewed in Figure 7.10.

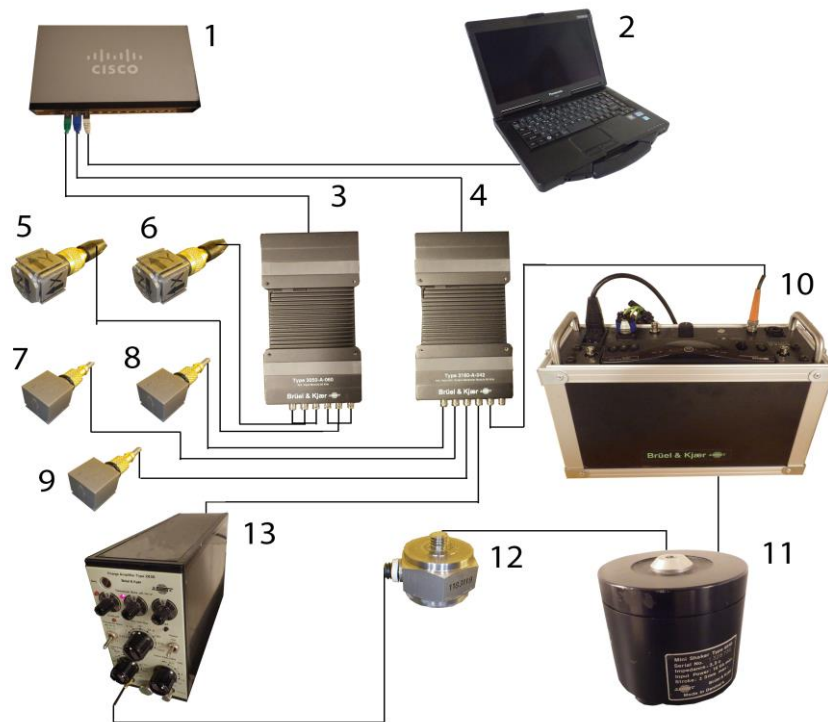


Figure 7.10: Shaker setup.

1. Switch for connecting front-ends to computer.
2. Computer with PULSE LabShop (version 18.1.1.13-2014-03-27) and PULSE Reflex (version 18.1.1.13-2014-03-27) software for signal analysis.
3. Front-end with six input channels (Type 3050-A-060) that captures the response signals.
4. Front-end with four input channels and two output channels (Type 3160-A-042) that both captures and sends out signals.
- 5-6. Triaxial accelerometer mounted on the structure with a thin layer of wax.
- 7-9. Uniaxial accelerometer mounted on the structure with a thin layer of wax.
10. Amplifier that strengthens the signal that is generated by the front-end, then sends this signal to the shaker.
11. Shaker that creates the force that is applied on the structure.
12. The force transducer was mounted on the structure with a small screw to measure the input force generated by the shaker.
13. Amplifier to strengthen the signal from the force transducer. The amplified signal is then registered in the front-end.

The shaker measurement was done using a specific template in Pulse Labshop, which included all steps to perform a successful measurement with a shaker as excitation source. First the geometry was drawn in a similar way as in the hammer test. Then the accelerometers were placed at the different nodes in the simplified geometry. It was possible to send out different types of signals to the shaker, the two types that were used were a frequency sweep from 5-200 Hz and a random signal (white noise) with a frequency range at 1,6 k Hz.

To understand how the shaker positions on the structure affect the different measurements, the shaker was attached at three different positions on the structure. The different shaker- and accelerometer positions are presented in Figure 7.11. Four measurement sequences had to be made to obtain the grid in Figure 7.11 (lower part).

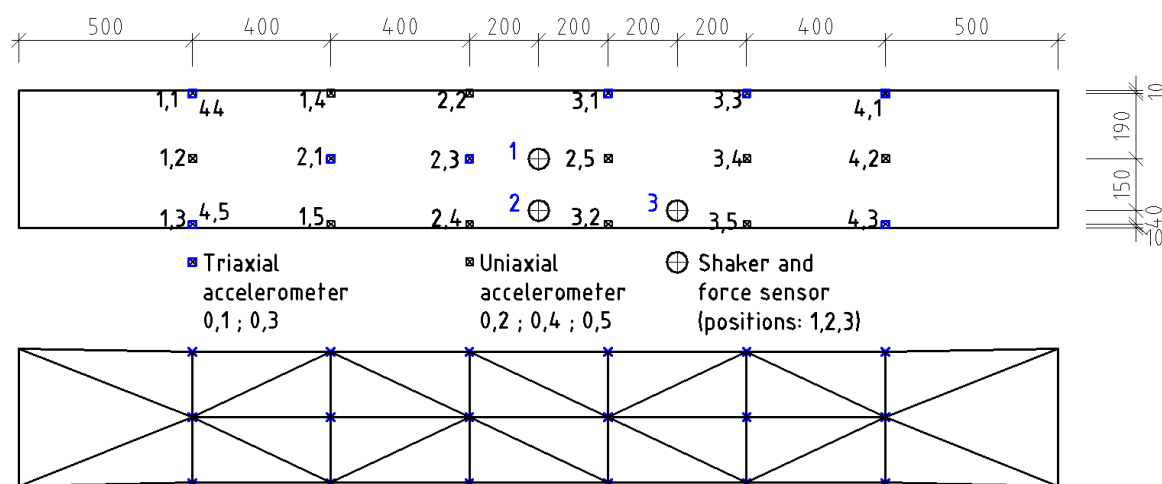


Figure 7.11: Shaker, force sensor and accelerometer positions [mm] (a 3D-representation is given in Figure B - 7 in Appendix B).

The obtained FRFs were exported to Pulse Reflex for measurement validation and modal parameter extraction.

The results obtained from the different shaker measurements are presented in Table 7.3. The mode shapes in Figure 7.14-Figure 7.18 and the damping ratios in Table 7.3 were extracted by the RFP method in Pulse Reflex. The results obtained from the shaker measurement in position 3 could also be observed in the different FRF plots (Figure 7.12 and Figure 7.13). The FRFs from position 1 and 2 are attached in Appendix B (Figure B - 9 - Figure B - 12). Triaxial accelerometer 1 and 2 and uniaxial accelerometer 1, 2 and 3 in these figures

correspond to triaxial accelerometer 0,1 and 0,3 and uniaxial 0,2, 0,4 and 0,5 in Figure 7.11. The extracted mode shapes are compared with the numerical results in Table 7.4.

Table 7.3: Shaker results.

Mode nr	Random			Position 3 Modal damping (%)	Sine sweep
	Position 1 Frequency (Hz)	Position 2 Frequency (Hz)	Position 3 Frequency (Hz)		Position 3 Frequency (Hz)
1	8,63	8,25	8,32	0,71	8,25
2	-	15,75	15,81	0,62	15,75
3	-	-	33,70	0,94	33,75
4	-	-	40,13	0,49	40,25
5	74,13	74,25	73,32	0,22	73,63
6	-	79,88	79,58	0,39	79,88
7	-	-	-	-	-
8	106,88	107,50	107,77	0,12	107,88
9	-	-	118,20	0,13	118,13
10	-	-	122,31	0,54	-
11	-	-	128,18	0,40	128,00
12	136,25	135,75	136,45	0,12	136,75
13	156,88	157,13	156,09	0,51	156,63
14	176,13	172,50	175,70	0,25	175,50
15	-	181,75	180,51	0,81	180,63

All FRFs and coherence functions (in z-direction) obtained with shaker (random excitation in position 3) and accelerometers are presented in Figure B - 18 and Figure B - 19 in Appendix B.

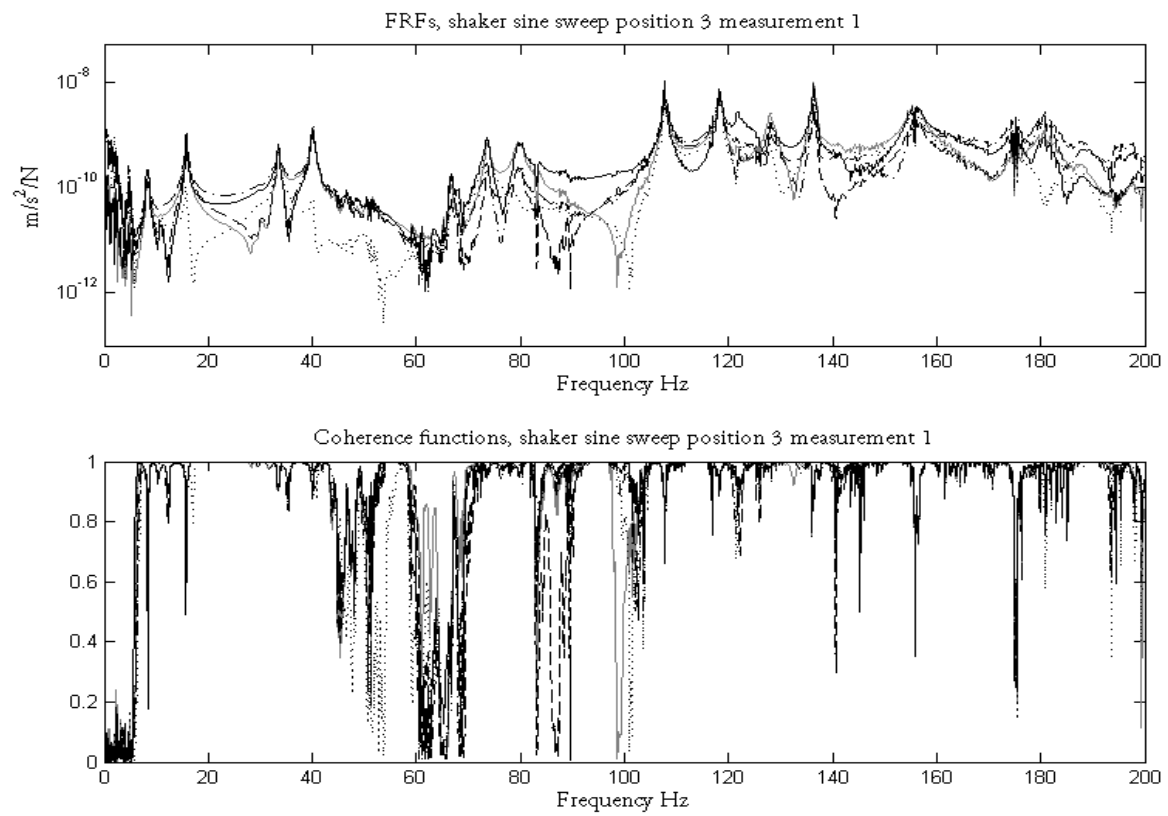


Figure 7.12: FRFs (above) and coherence functions (below) obtained from measurement 1 with sine sweep as input (see legend in Figure 7.13).

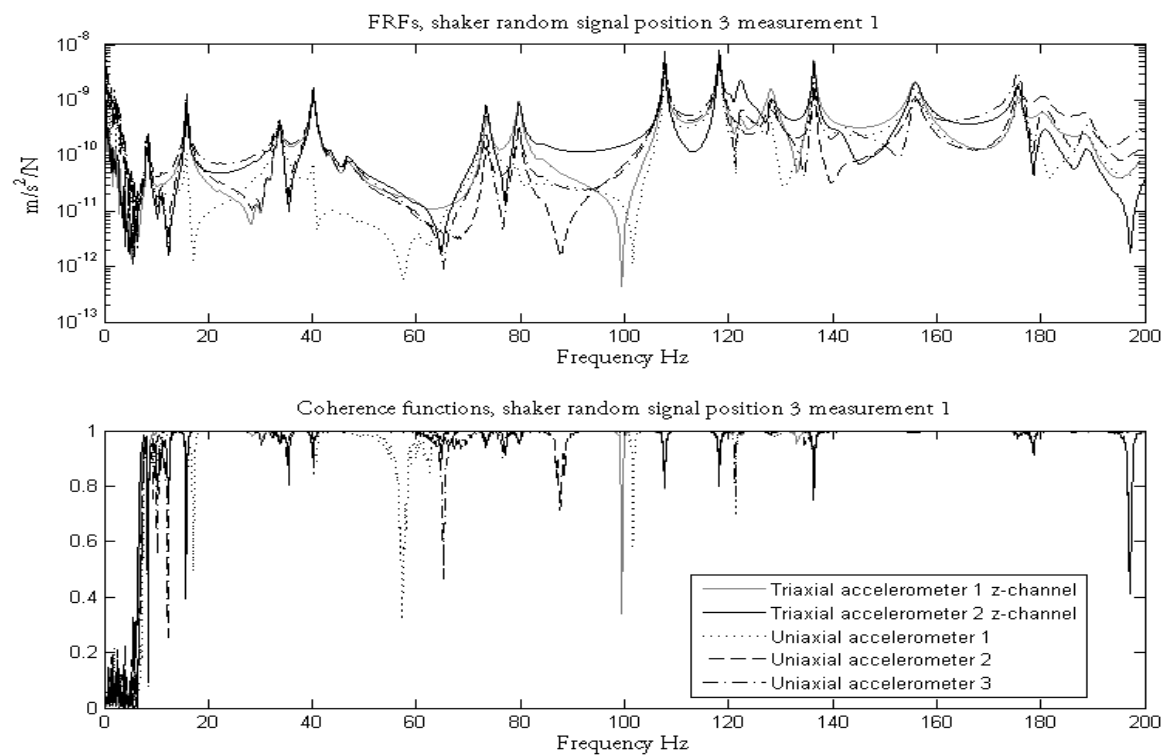


Figure 7.13: FRFs (above) and coherence functions (below) obtained from measurement 1 with random input signal.

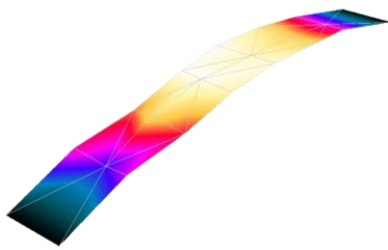
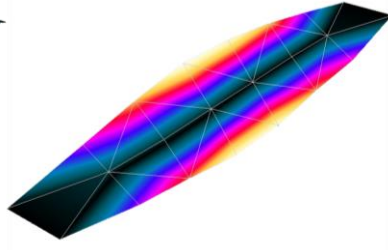
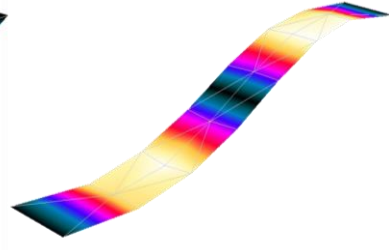


Figure 7.14: Mode 1: 8.32 Hz



Mode 2: 15.81 Hz



Mode 3: 33.70 Hz

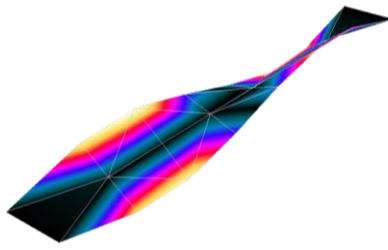
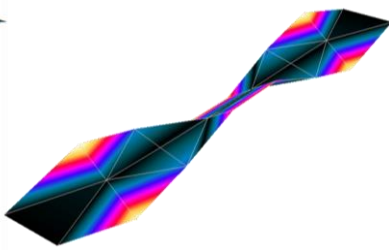


Figure 7.15: Mode 4: 40.13 Hz



Mode 5: 73.32 Hz



Mode 6: 79.58 Hz

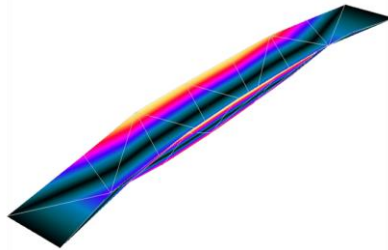
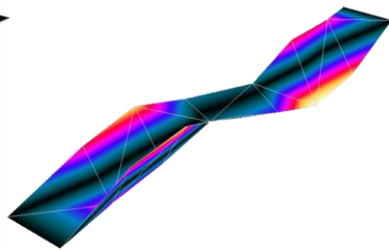


Figure 7.16: Mode 7-



Mode 8: 107.77 Hz

Mode 9: 118.20 Hz

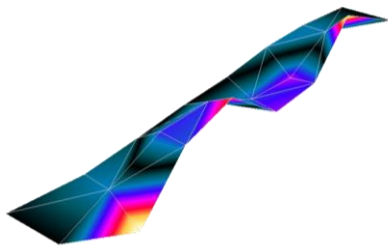
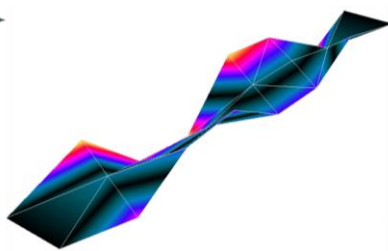
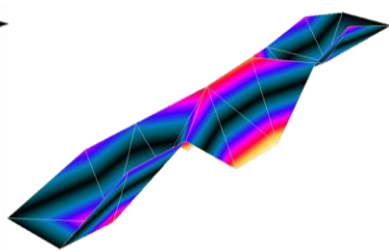


Figure 7.17: Mode 10: 122.31 Hz



Mode 11: 128.18 Hz



Mode 12: 136.45 Hz

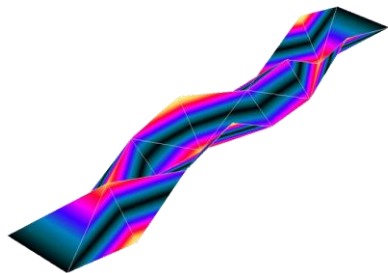
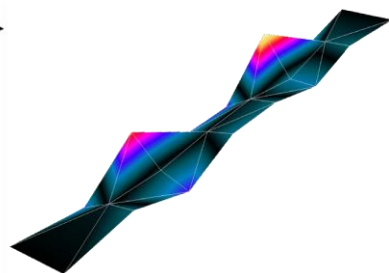


Figure 7.18: Mode 13: 156.09 Hz



Mode 14: 175.70 Hz



Mode 15: 180.51 Hz

Table 7.4: MAC table, comparing extracted modes from shaker measurement with numerical calculations.

Nr	EMA Shaker	1	2	3	4	5	6	8	9	10	11	12	13	14	15
	Nr	8,32	15,81	33,70	40,13	73,32	79,58	107,77	118,20	122,31	128,18	136,45	156,09	175,70	180,51
1	8,23	<b>0,973</b>	0,001	0,005	0,001	0,009	0,013	<b>0,199</b>	0,002	0,008	0,010	0,019	0,012	0,014	<b>0,151</b>
2	13,88	0,000	<b>0,982</b>	0,001	0,002	0,001	0,005	0,000	0,000	0,002	0,000	0,000	0,002	0,004	0,040
3	32,53	0,000	0,001	<b>0,959</b>	0,000	0,006	0,008	0,003	<b>0,245</b>	0,004	0,008	0,001	0,002	0,007	<b>0,094</b>
4	38,25	0,000	0,009	0,005	<b>0,984</b>	0,000	0,009	0,000	0,000	0,004	0,008	0,000	0,000	0,000	0,001
5	71,18	0,000	0,000	0,002	0,000	<b>0,915</b>	0,006	0,008	0,003	0,005	0,005	<b>0,262</b>	0,004	0,008	0,003
6	74,48	0,000	0,000	0,002	0,009	0,024	<b>0,937</b>	0,000	0,000	0,003	0,003	0,000	0,001	0,003	0,019
7	101,66	0,014	0,024	0,000	0,021	0,000	<b>0,066</b>	0,000	0,000	<b>0,050</b>	<b>0,130</b>	0,001	0,001	0,001	0,009
8	107,16	<b>0,194</b>	0,000	0,003	0,000	0,005	0,010	<b>0,965</b>	0,006	0,003	0,008	0,036	0,010	0,007	<b>0,070</b>
9	114,98	0,000	0,000	<b>0,189</b>	0,000	0,003	0,002	0,003	<b>0,948</b>	0,020	0,003	0,004	0,006	0,007	0,033
10	117,63	0,000	0,000	0,001	0,000	0,011	0,001	0,001	0,006	<b>0,464</b>	<b>0,148</b>	0,023	<b>0,518</b>	0,030	0,001
11	120,82	0,000	0,001	0,000	0,001	0,000	0,011	0,000	0,000	<b>0,300</b>	<b>0,762</b>	0,001	0,006	0,002	0,016
12	127,78	0,000	0,000	0,000	0,000	<b>0,159</b>	0,001	0,018	0,002	0,014	0,005	<b>0,868</b>	0,026	0,026	0,008
13	146,64	0,000	0,000	0,000	0,000	0,004	0,000	0,000	0,023	0,025	0,023	0,007	<b>0,874</b>	0,013	0,029
14	151,65	0,001	0,000	0,000	0,000	0,009	0,000	0,004	0,000	0,001	0,001	<b>0,077</b>	0,024	<b>0,869</b>	<b>0,075</b>
15	166,26	0,000	0,000	0,000	0,001	0,000	0,007	0,000	0,000	0,000	0,009	0,000	0,002	<b>0,051</b>	<b>0,524</b>

### 7.3 OMA

The equipment used for the OMA is shown in Figure 7.19.

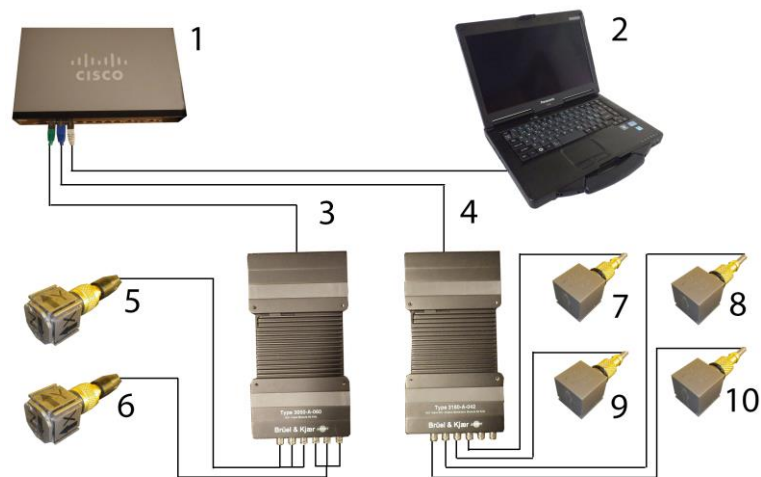


Figure 7.19: OMA setup.

1. Switch for connecting front-ends to computer.
2. Computer with PULSE LabShop (version 18.1.1.13-2014-03-27) and Operational Modal Analysis Pro (Full license 7760\_A\_5.4\_2012.10.23) software for signal analysis.
3. Front-end with six input channels (Type 3050-A-060) that captures the response signals.
4. Front-end with four input channels and two output channels (Type 3160-A-042) that captures the response signals.
- 5-6. Triaxial accelerometer mounted on the structure with a thin layer of wax.
- 7-10. Uniaxial accelerometer mounted on the structure with a thin layer of wax.

Pulse Labshop was also used in the OMA where a specific template for this type of measurement was loaded. The template involved steps like hardware update, drawing a simplified geometry, attach transducers at specific nodes and generate a measurement sequence. The OMA was performed using both the triaxial accelerometers as reference. The uniaxial accelerometers were used as “roving accelerometers”, which means that they were moved to different nodes during the measurement sequences (see Figure 7.20). To measure all nodes of interest four measurements had to be made. The random input force (white noise) that is required for OMA was created by hitting the structure at random positions with eight human fists/fingertips. The measurement time was set to 136 s and the span to 200 Hz in the analysis setup.

After the four measurements were made the measured time signals were exported to the OMA software (Artemis) for further analysis.

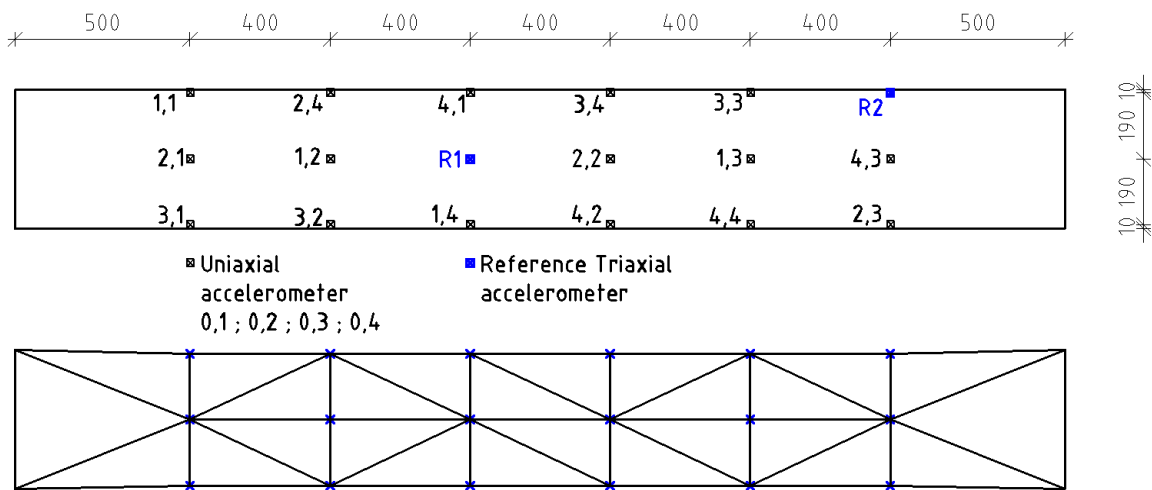


Figure 7.20: Transducer locations for the OMA [mm] (a 3D-representation is given in Figure B - 20 in Appendix B).

Two extraction methods were used to estimate the modal parameters: SSI and EFDD. The SSI results are presented in Figure 7.21, Table 7.5 and Figure 7.22-Figure 7.26. The results from the EFDD method are presented in Table 7.5 and the “peak picking” diagram is given in Figure B - 21 in Appendix B. The SSI and EFDD estimated mode shapes are compared (MAC) in Table 7.6. MAC between the numerical calculations and the SSI results are given in Table 7.7.

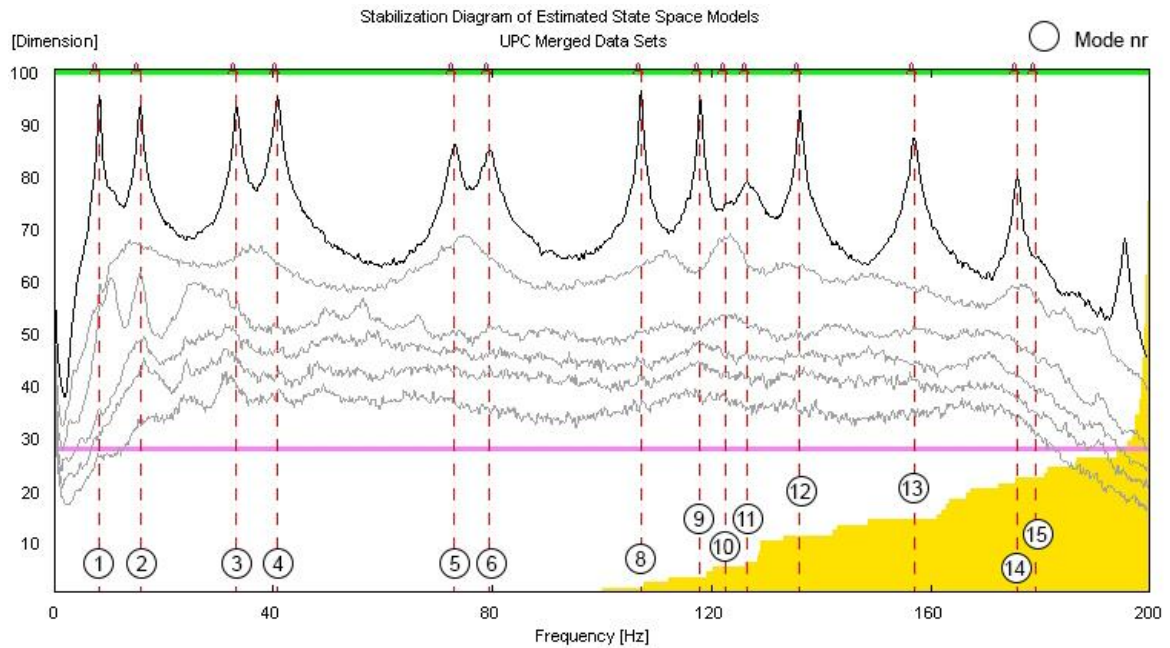


Figure 7.21: Stabilization diagram for SSI.

Table 7.5: OMA results (SSI and EFDD).

Mode nr	SSI Eigenfrequency (Hz)	SSI Modal damping (%)	EFDD Eigenfrequency (Hz)	EFDD Modal damping (%)
1	8,27	4,45	8,28	2,22
2	15,72	1,71	15,73	2,03
3	33,30	1,08	33,31	1,12
4	40,80	0,99	40,83	1,01
5	72,97	1,02	73,12	1,13
6	79,32	1,55	79,43	1,49
7	-	-	-	-
8	107,09	0,17	107,10	0,19
9	117,92	0,21	117,90	0,21
10	122,65	1,49	123,60	0,27
11	126,53	1,63	126,50	0,88
12	136,08	0,23	136,10	0,23
13	157,01	0,36	157,00	0,33
14	175,67	0,21	175,80	0,27
15	179,00	2,36	178,90	0,25

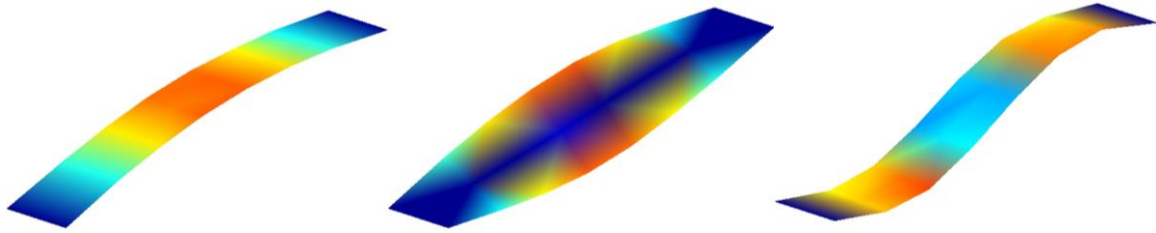


Figure 7.22: Mode 1: 8.27 Hz

Mode 2: 15.72 Hz

Mode 3: 33.30 Hz

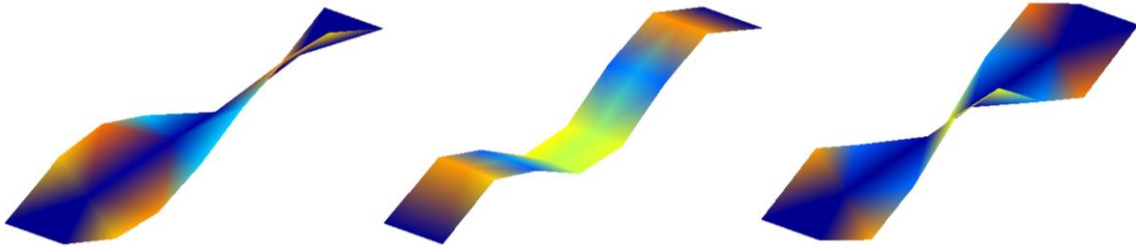


Figure 7.23: Mode 4: 40.80 Hz

Mode 5: 72.97 Hz

Mode 6: 79.32 Hz

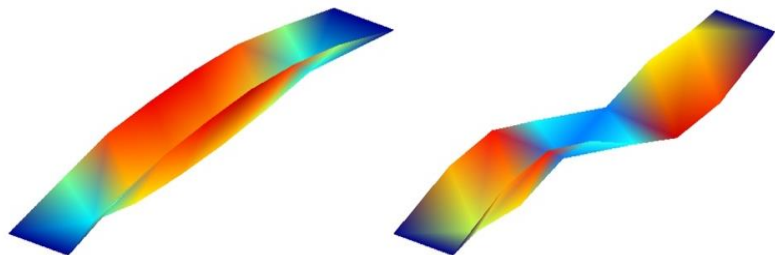


Figure 7.24: Mode 7: -

Mode 8: 107.09 Hz

Mode 9: 117.92 Hz

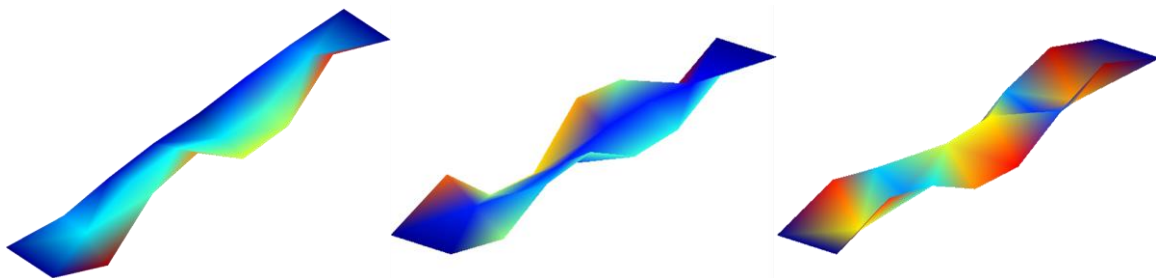


Figure 7.25: Mode 10: 122.65 Hz

Mode 11: 126.53 Hz

Mode 12: 136.08 Hz

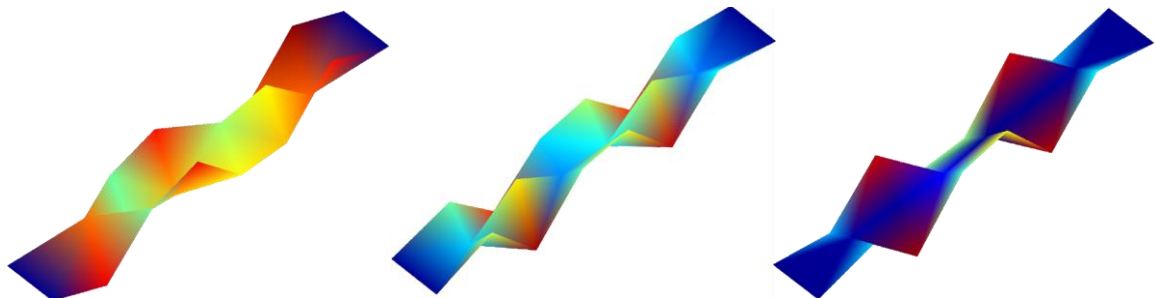


Figure 7.26: Mode 13: 157.01 Hz

Mode 14: 175.67 Hz

Mode 15: 179.00 Hz

Table 7.6: MAC between SSI and EFDD.

Nr	Nr	1	2	3	4	5	6	8	9	10	11	12	13	14	15
	EFDD SSI	8,28	15,73	33,31	40,83	73,12	79,43	107,10	117,90	123,60	126,50	136,10	157,00	175,80	178,90
1	8,28	0,999	0,000	0,000	0,000	0,002	0,000	0,196	0,000	0,000	0,000	0,000	0,000	0,001	0,007
2	15,72	0,000	1,000	0,000	0,000	0,000	0,000	0,000	0,000	0,012	0,000	0,000	0,000	0,000	0,000
3	33,30	0,000	0,000	0,998	0,001	0,000	0,000	0,000	0,201	0,055	0,000	0,000	0,000	0,000	0,011
4	40,80	0,000	0,000	0,002	1,000	0,001	0,001	0,000	0,000	0,000	0,004	0,000	0,000	0,000	0,004
5	72,97	0,001	0,000	0,000	0,000	0,993	0,002	0,000	0,000	0,000	0,003	0,195	0,001	0,005	0,002
6	79,32	0,000	0,001	0,000	0,001	0,006	0,990	0,000	0,000	0,000	0,000	0,001	0,000	0,000	0,047
8	107,10	0,195	0,000	0,000	0,000	0,000	0,000	0,999	0,000	0,000	0,000	0,001	0,000	0,002	0,003
9	117,90	0,000	0,000	0,198	0,000	0,000	0,000	0,000	1,000	0,165	0,007	0,001	0,005	0,000	0,011
10	122,70	0,000	0,000	0,001	0,005	0,005	0,001	0,000	0,017	0,670	0,070	0,003	0,120	0,003	0,009
11	126,50	0,001	0,000	0,000	0,004	0,003	0,001	0,000	0,001	0,095	0,969	0,006	0,028	0,000	0,012
12	136,10	0,001	0,000	0,000	0,000	0,201	0,000	0,001	0,000	0,001	0,009	0,999	0,000	0,027	0,002
13	157,00	0,000	0,000	0,001	0,000	0,001	0,001	0,000	0,005	0,141	0,053	0,000	0,998	0,001	0,000
14	175,70	0,000	0,000	0,000	0,000	0,005	0,000	0,001	0,000	0,007	0,000	0,034	0,001	0,990	0,124
15	179,10	0,001	0,006	0,003	0,001	0,000	0,068	0,000	0,004	0,002	0,008	0,000	0,001	0,015	0,718

Table 7.7: MAC between OMA (SSI) and ABAQUS.

Nr	Nr	1	2	3	4	5	6	8	9	10	11	12	13	14	15
	OMA ABAQUS	8,27	15,72	33,30	40,80	72,97	79,32	107,09	117,92	122,65	126,53	136,08	157,01	175,67	179,00
1	8,23	0,995	0,000	0,000	0,000	0,001	0,000	0,200	0,000	0,000	0,001	0,001	0,000	0,000	0,001
2	13,88	0,000	0,986	0,000	0,011	0,000	0,003	0,000	0,000	0,000	0,000	0,000	0,000	0,000	0,006
3	32,53	0,000	0,000	0,990	0,001	0,000	0,000	0,000	0,231	0,001	0,000	0,000	0,000	0,000	0,003
4	38,25	0,000	0,011	0,002	0,977	0,000	0,013	0,000	0,000	0,009	0,008	0,000	0,000	0,000	0,001
5	71,18	0,001	0,000	0,002	0,000	0,959	0,002	0,000	0,001	0,009	0,003	0,318	0,003	0,007	0,000
6	74,48	0,000	0,000	0,000	0,011	0,011	0,975	0,000	0,000	0,000	0,009	0,000	0,001	0,001	0,081
7	101,66	0,002	0,036	0,000	0,034	0,003	0,114	0,000	0,000	0,101	0,354	0,000	0,001	0,001	0,052
8	107,16	0,202	0,000	0,000	0,000	0,002	0,000	0,997	0,000	0,000	0,000	0,003	0,000	0,000	0,000
9	114,98	0,000	0,000	0,189	0,000	0,000	0,000	0,000	0,994	0,013	0,001	0,001	0,010	0,000	0,004
10	117,63	0,000	0,000	0,001	0,000	0,013	0,000	0,000	0,002	0,537	0,102	0,033	0,549	0,014	0,001
11	120,82	0,000	0,002	0,000	0,000	0,000	0,014	0,000	0,000	0,302	0,837	0,001	0,000	0,000	0,013
12	127,78	0,000	0,000	0,000	0,000	0,163	0,001	0,000	0,002	0,011	0,002	0,971	0,020	0,023	0,000
13	146,64	0,000	0,000	0,000	0,000	0,003	0,000	0,000	0,006	0,066	0,009	0,002	0,917	0,048	0,001
14	151,65	0,001	0,000	0,000	0,000	0,008	0,000	0,004	0,000	0,000	0,000	0,026	0,026	0,917	0,008
15	166,26	0,000	0,000	0,000	0,002	0,000	0,006	0,000	0,000	0,001	0,011	0,000	0,000	0,004	0,914

### 7.4 OMA with Finer Grid

To see how far up the measurement results could be compared to the numerical calculations one OMA with many measurement points was made. The selected transducer positions (0,1-0,4) and measurement sequences (1-9) are presented in Figure 7.27. Instead of using hands to create the “white noise” four homemade clubs with rubber balls and golf balls (see Figure 7.28) were used and this could reduce the nonlinear effects caused by large deformations. The time of each measurement sequence was set to 5 minutes (301,3 s) to increase the accuracy of the measurements. The results from this measurement can be observed in Appendix C.

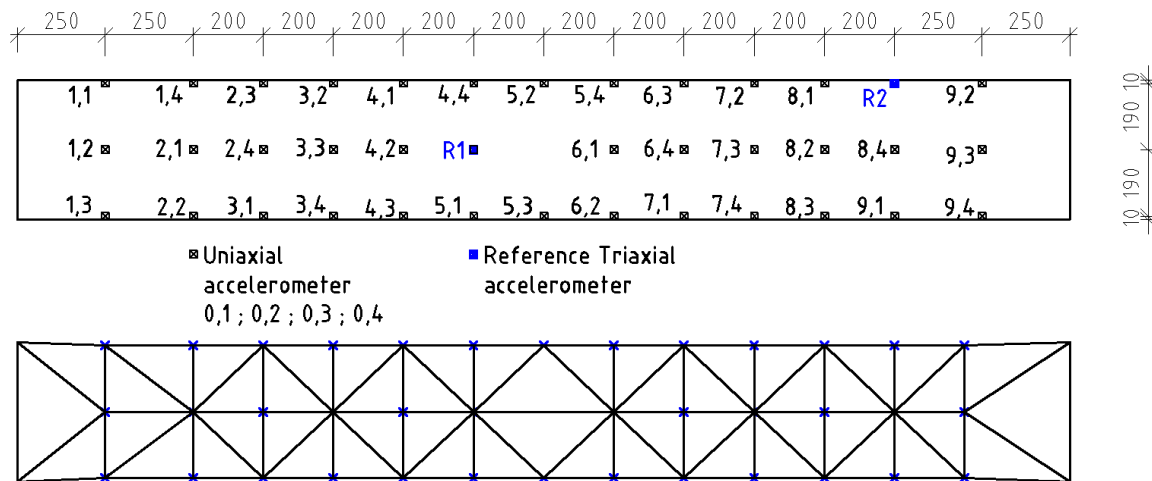


Figure 7.27: OMA with finer grid [mm] (3D-representation is given in Figure C - 1 in Appendix C).



Figure 7.28: Homemade clubs, two made of rubber (left) and two made of plastic (right).

# 8

## Discussion

An overview and more detailed discussions regarding the calculated and measured results in chapter 6 and 7 are presented in this chapter.

### 8.1 Overview

By observing all results in chapter 6 and 7 and comparing both mode shapes and eigenfrequencies the results look really promising. To make the comparison between the measured and the predicted eigenfrequencies easier the frequencies for the 15 lowest modes are viewed in Figure 8.1. The grid that was used in the various measurements can resolve 15 mode shapes, higher mode shapes require more measured points (higher resolution) to be compared visually with the numerical calculations.

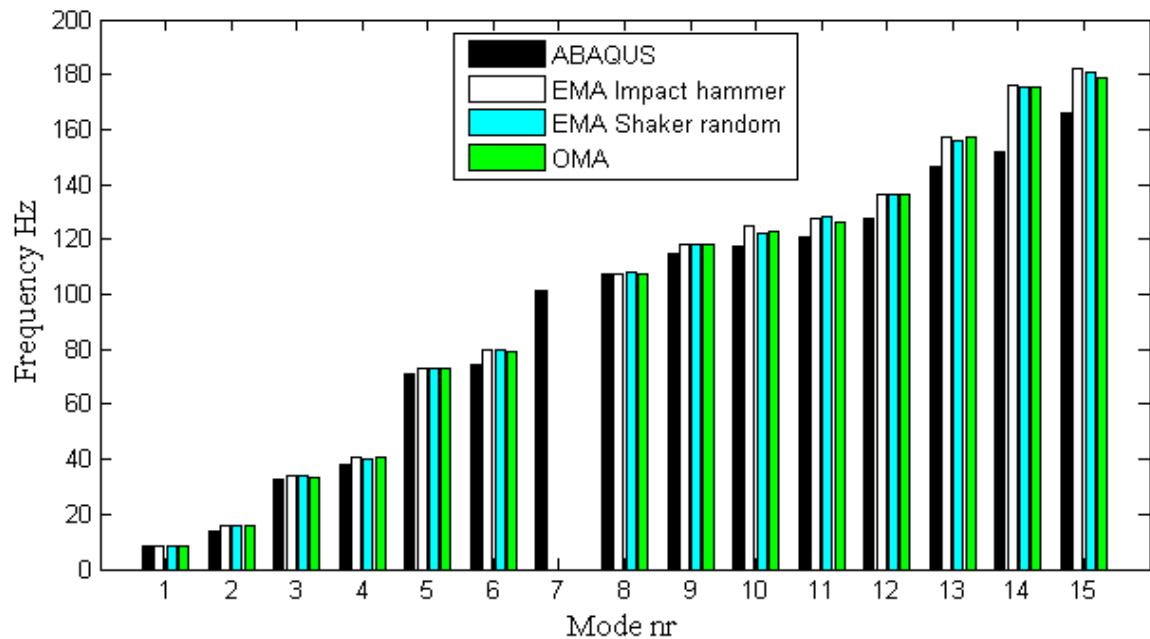


Figure 8.1: Eigenfrequencies for the different measurements.

All bars for the laboratory measurements follow the same pattern in Figure 8.1, the bar that deviates are the numerical calculations which is not so surprising. The numerical calculations comply with the measurements very good until mode number 9, then the eigenfrequencies start to differ from the measurements. The main reason of this deviation is probably due to the boundary conditions. The boundary with the thin plastic is more restraint to vault and move in the x-direction (Figure 6.2) than the roller support in the FE-model and this will increase the stiffness of the structure and therefore give higher measured eigenfrequencies. Mode 7 is an “in plane” mode and it bends in the stiff direction of the structure. This mode shape couldn't be excited because it would require a lot of force on the side (y-direction in Figure 6.2) and then the structure would move from its steel-pallets.

The obtained mode shapes are summarized in 3D MAC tables in Figure 8.2 where the EMA with impact hammer and shaker and the OMA are compared with the FE results in ABAQUS. The shaker and the OMA results are very similar, the only noticeable difference is that mode 15 in the OMA was slightly better estimated than the corresponding mode in the shaker measurement. There is no doubt that the impact measurement was the least accurate modal testing method by observing Figure 8.2. For this method mode 10 and 11 were very noisy and difficult to estimate. The estimations of mode 5 and 6 were also quite noisy in the impact measurement compared to the corresponding modes estimated in the shaker measurement and the OMA. Mode 15 was extremely noisy in the impact measurement and really hard to visually determine if it was a possible vibration mode at all.

Mode 10 has a low MAC value in all 3D MAC tables in Figure 8.2. In the hammer measurement the result for mode 10 is extremely noisy and very hard to visually compare with the numerical result. The obtained results for mode 10 from the shaker test and the OMA are very similar but differ a lot from the ABAQUS result. The mode tends to only move at one side of the structure. One explanation for this is that the shaker was placed unsymmetrically on the structure, making it to only register large vibrations at one side. The same goes for the OMA, the same side that was excited with the shaker was easier to excite with the hands. The structure was placed close to a wall and therefore the excitations with the hands were only available at one side of the structure. An unsymmetrical excitation could have been the reason why mode 10 moves a lot at one side in these measurements (see mode 10 in Figure 7.17 and Figure 7.25).

In all 3D MAC-tables in Figure 8.2 there is one bar that stands out and has a MAC value around 0.6, this bar indicates that mode 10 from the eigenvalue analysis and mode 13 from the measurements are very similar.

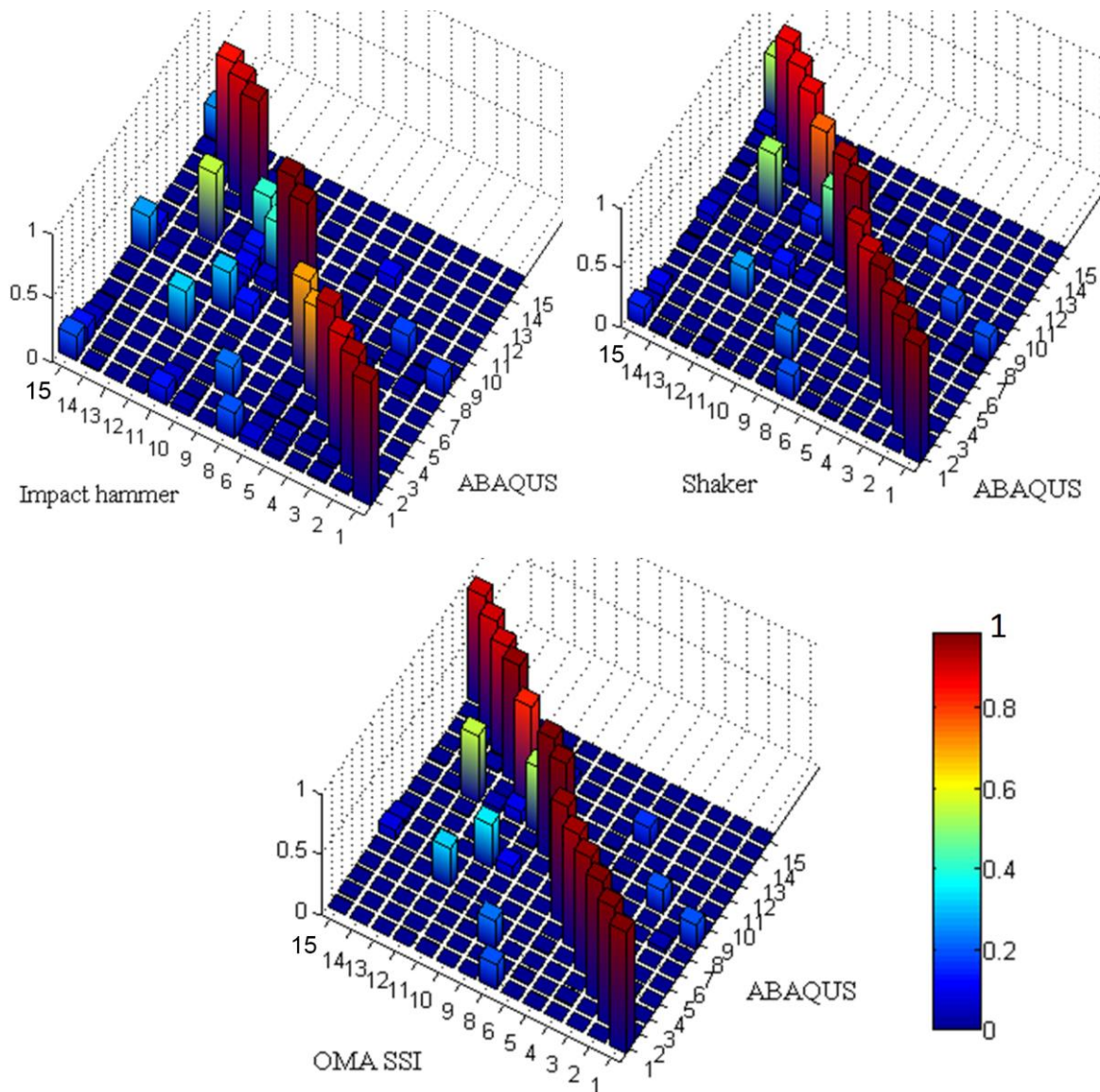


Figure 8.2: MAC between measured and numerical results.

The estimated damping ratios for all measurements in chapter 7 are presented in Figure 8.3. Studying this bar diagram gives a hint of how hard it is to estimate the modal damping. There is no way to tell which modal test that gave the best estimation, because all measurements are varying a lot. Even the two different extraction methods in OMA (EFDD and SSI) don't give consistent results. Perhaps mode 3, 8, 9, 12, 13 and 14 have some reasonable damping estimate because they are pretty close to the same value.

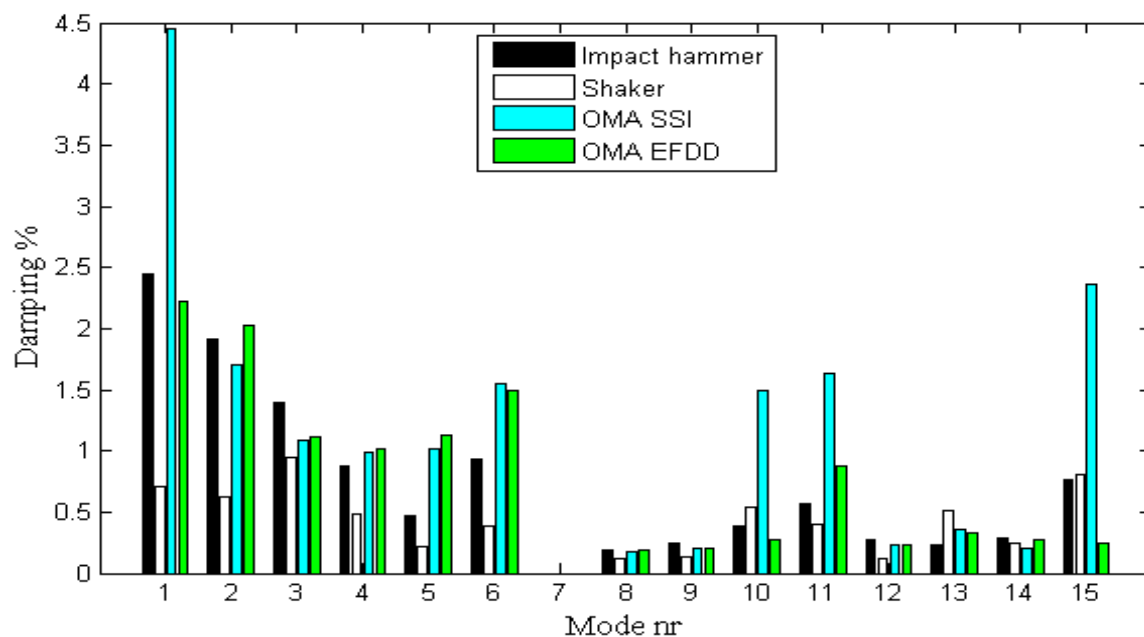


Figure 8.3: Damping ratios for the various measurements.

It was assumed that the accelerometers and force sensors worked perfectly fine and didn't require any calibration. This is not correct because you should always calibrate the piezoelectric transducers before any measurement so they work as they should and don't contain errors. The accelerometers and force sensors used in this thesis were calibrated approximately a year ago and have been sparingly used since then. Mentioned in section 3.4.2, the change in the measuring characteristics of piezoelectric transducers is below 2 %, after several years of usage. This is a very small change and since this thesis is a matter of comparison and all measurements were performed using the same equipment, the same potential (very small) error from the transducers is present in all measurements. These are the main reasons why the calibration part was neglected during the measurements.

## 8.2 EMA Impact Hammer

The impact measurement was very quick and simple because of the small set of hardware that was required and by only moving around the hammer to the different impact points, it was also very flexible. Two reference triaxial accelerometers were used to measure the structure's response and by looking at the peaks in Figure 7.3 it's easy to determine that reference accelerometer 2 gained the FRF with all interesting modes. Reference accelerometer 1 is placed in the middle of the plate (see Figure 7.2) allowing it to only measure the bending modes. So in this case one accelerometer would have been sufficient to measure all modes of

interest. All modes of this structure are either bending or torsional modes in the z-direction, so the amount of data could have been reduced even further with a uniaxial accelerometer (noisy FRF with x- and y-channel in Figure B - 2 in Appendix B). All 18 FRFs and coherence functions (z-direction) are given in Figure B - 5 and Figure B - 6 in Appendix B.

Two types of hammer tips were tested on the structure and the force- and transient spectrums of these two tips are viewed in Figure 3.12. With the rubber tip a much harder impact could be made on the structure without overloading the transducers. The transient spectrum in Figure 3.12 also reveals the frequency content of the different impacts and that both tips could be used to trigger all interesting modes in the range of 0-200 Hz. But mentioned in section 3.4.4 the impact force should be small to avoid large deformations and errors caused by nonlinearity. This is one reason why the plastic tip was chosen during the impact measurements, the other reason was that the impacts with the rubber tip often were detected as “dubbel hits” which could ruin the entire measurement. The problem with using too hard hammer tips is the nonlinearities caused by excited modes outside the studied frequency range. By looking at the lower FFT in Figure 8.4 it’s possible to see that there are some well excited modes above 200 Hz and they might bring some errors to the estimated FRFs.

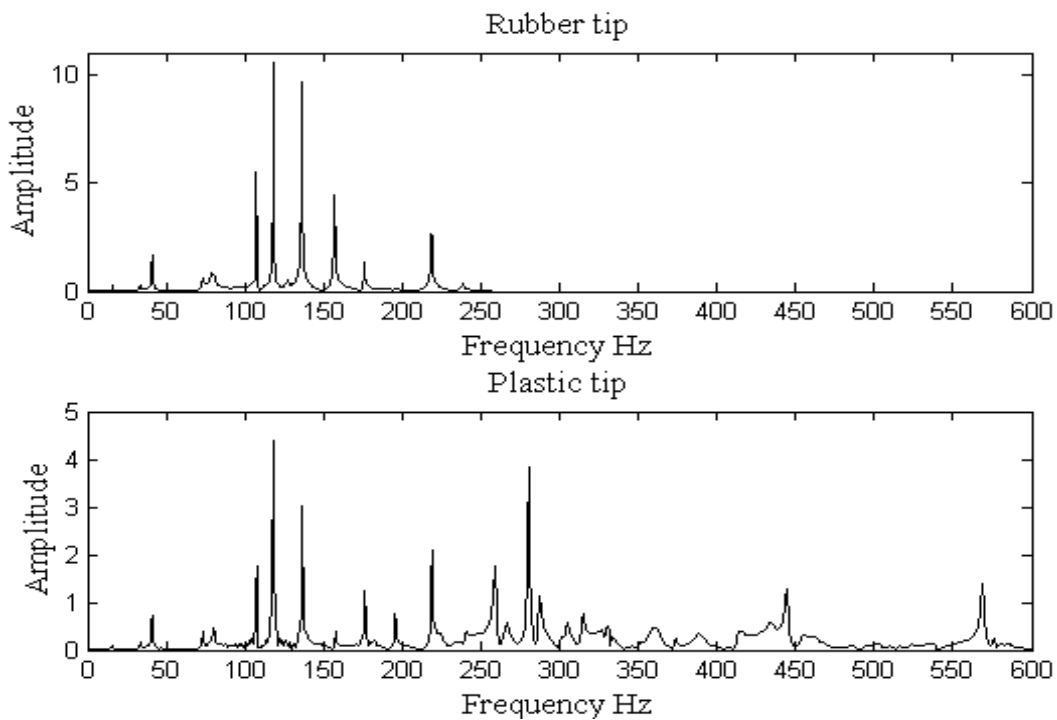


Figure 8.4: Excited eigenfrequencies with rubber (above) and plastic (below) hammer tip.

The results from the impact test can be viewed in Table 7.1 and Figure 7.5-Figure 7.9 and these results match the predicted mode shapes and eigenfrequencies very well by comparing them to the numerical calculations in Table 6.3 and Figure 6.8-Figure 6.12. All mode shapes were extracted by the RFP method. Mode 10 and 11 were very difficult to estimate and the RFP method required many iterations to find these unstable mode shapes. The MAC between the impact test and the numerical calculations can be observed in Table 7.2 and here it's much easier to certify the accuracy of the extracted mode shapes. In Table 7.2 the mode shapes 1-4, 8,9 and 12-14 have a MAC value very close to 1, which means that the overlap between the numerical results is very good. Mode 5 and 6 contain a little bit of noise were some nodes don't follow the "correct" movement of the mode, this is why the MAC values for these shapes are a little bit lower. These modes are still considered to be quite well estimated compared to mode 15 that has a MAC value below 0.5. Mode 15 in Figure 7.9 may look well estimated but the image is paused in the maximum deflected position, when it's animated the movement is very uneven.

The force sensor on the impact hammer was not properly calibrated, the nominal sensitivity for the hammer type used in the impact test is 22,7mV/N and this value was also used as the calibrated sensitivity. The correct calibrated sensitivity for this particular hammer is 20,90 mV/N so there is a small error in all hammer measurements. So a lesson for future measurements is to always check the calibrated values in the analysis program so it matches the values in the product sheets included with the measuring equipment.

### 8.3 EMA Shaker

The shaker measurement required more hardware and preparation than the hammer test. The force transducer that is connected to the structure and shaker was used as a reference point as the accelerometers were moved around to the selected nodes on the structure. The position of this reference and excitation point is essential for making a successful shaker measurement, by studying Table 7.3 it's easy to see that position 3 (Figure 7.11) was the optimal placement for the excitation source as it excited all modes of interest. The FRFs and coherence functions for position 1 and 2 with two different input signals can be observed in Appendix B in Figure B - 9 - Figure B - 12.

In the shaker measurements two types of signals were tested, sine sweep- and random input signal. The FRFs and coherence functions that were obtained in position 3 for the first measurement sequence of these two input signals can be viewed in Figure 7.12 and Figure 7.13. By looking at these two figures there is no doubt that the random input signal gave the best and less noisy FRFs. These results are quite logical, as the sine signal sweeps over a

resonance frequency there will be large deformations in the structure that give rise to noise in both force sensor and accelerometers. The coherence function explained in section 4.1 is an indicator of how much noise that is present during the measurement and there is much more noise (drops below 1) in the sine signal compared to the random signal. Perhaps a slower sine sweep could have given a better and less noisy estimation of the FRFs. All 18 FRFs and coherence functions (z-direction) generated by the random input signal are presented in Figure B - 18 and Figure B - 19 in Appendix B.

The quality of the random signals could be checked in a histogram and by plotting the probability density of the samples (see Figure B - 15 - Figure B - 17 in Appendix B). As the system is considered to be linear, a random input signal should generate a random output signal. By looking at Figure B - 16 and Figure B - 17 the random signal generated by the shaker was quite close to a perfect Gaussian probability distribution.

The eigenfrequencies, mode shapes and damping ratios for shaker position 3 with a random input signal were estimated by the RFP method and these results are viewed in Table 7.3 and Figure 7.14 - Figure 7.18. Compared to the impact test it was much easier for the program to find stable mode shapes with the RFP method. MAC was then performed to compare the extracted mode shapes and the numerical calculations (see Table 7.4). The first spontaneous reflection of the results in Table 7.4 is that the mode shapes were very well estimated. The MAC values of the mode shapes 1-6, 8 and 9 are very close to 1 and therefore well correlated with the numerical calculations. Mode 11-14 are also quite consistent with the numerical results compared to mode 10 and 15, which have a MAC value around 0,5.

To perform an EMA with a shaker seems to get more reliable mode shapes than the impact hammer by comparing the MAC tables. There were only two mode shapes that were slightly better estimated with the impact hammer and these were mode 12 and 13. Why these modes were better estimated could be due to the position of the shaker, perhaps an excitation point closer to the edge could trigger these two modes better.

There was no stinger connected between the transducer and the shaker during the measurements, and this will increase the risk of transverse forces that could contaminate the force signal.

## 8.4 OMA

The OMA in section 7.3 was performed using eight hands to simulate the white noise (stochastic input that is random in both time and space). The 3 m steel plate was deflecting a lot during the measurements because of the high force that was created when four people

were hitting the structure at the same time. The recorded signals for the four measurement sequences are presented in Figure B - 22 - Figure B - 33 along with both FFT-plots and histograms. The signals in measurement sequence 1 and 2 contained many recorded “spikes” where the structure was giving too much energy in the impacts (Figure B - 22 and Figure B - 25). The histograms (Figure B - 24 and Figure B - 27) created from these signals also reveal that several of the recorded samples are gathered around 0 which is not an ideal Gaussian distribution. Measurement sequence 3 and 4 are much better because the recorded time signals presented in Figure B - 28 and Figure B - 31 don't contain these high accelerations and the histograms in Figure B - 30 and Figure B - 33 confirm that the samples are more normally distributed. In Figure B - 34 and Figure B - 35 the probability distribution of the recorded samples are compared with the ideal Gaussian probability distribution. This reveals that even the samples in measurement sequence 3 and 4 are far from normally probability distributed and that all recorded random signals are quite bad.

There were also times when the structure moved a little bit from its original position on the steel pallets. Both large deflections and moving boundary are nonlinear behaviors which is bad for both EMA and OMA. Despite these sources of errors the results were surprisingly good and can be observed in Table 7.5 and Figure 7.22 - Figure 7.26.

To validate the estimated modal parameters two OMA extraction methods were used: SSI and EFDD. To verify how accurate the mode shapes are from the extraction methods they were compared using MAC (Table 7.6). All modes in Table 7.6 except for mode 10 and 15 were really close to 1 so they are considered to be reliable mode shapes. The SSI method found all modes of interest automatically. To get all modes with the EFDD method mode 10, 11, 13 and 15 had to be “peaked out” manually. This is the main reason why mode 10 and 15 differ from the other modes in the MAC table, because the peaks were unclear and therefore hard to select (see Figure B - 21 in Appendix B).

It seems that the SSI method is a more powerful tool to estimate mode shapes and therefore the results obtained by the SSI method are compared with the numerical calculations in a MAC table (see Table 7.7). These results are even better than the shaker measurement and all MAC values are close to 1 except for mode 10. Mode 10 has diverged from the numerical calculations in all measurements, so perhaps the numerical model is too flawless and doesn't consider imperfections on the structure like welds or that the plate is uneven at some places. By comparing mode 10 in Figure 7.17 with the corresponding mode in Figure 7.25 it's not impossible to imagine that this is the actual mode shape for this structure.

The main source of errors is the nonlinear effects of the large deflections that occurred while exciting the structure during the OMA.

## 8.5 OMA with Finer Grid

The results from this measurement are attached in Appendix C and by comparing Figure 7.21 obtained in the previous OMA and Figure C - 2 it's very clear that the excitation made by the rubber- and golf balls and the longer measurement sequences gave more accurate results. The peaks are much clearer in Figure C - 2 and Figure C - 3 and there is also less "noise" between the peaks.

The estimated eigenfrequencies from SSI and EFDD are presented in Figure 8.5. All frequencies extracted from these methods match really well for each mode nr. Mode shape 15 and 22 couldn't be extracted from the EFDD because they were closely spaced modes with no clear peaks in the stability diagram. This makes the manual peak picking impossible. The mode shapes extracted by SSI and EFDD are compared in two MAC tables (Table C - 2 and Table C - 3) and the results look outstanding. All comparable mode shapes have a MAC value that doesn't drop below 0,9 which is a sign of reliable results, this also applies for mode 10 that differed from the previous OMA.

The mode shapes that couldn't be found were mode 7, 17, 19 and 20. Two possible explanations why mode 17, 19 and 20 couldn't be located are that they weren't properly excited or that they don't exist in the real steel plate. The FE-model is still an approximation of the real structure and it doesn't take imperfections into account.

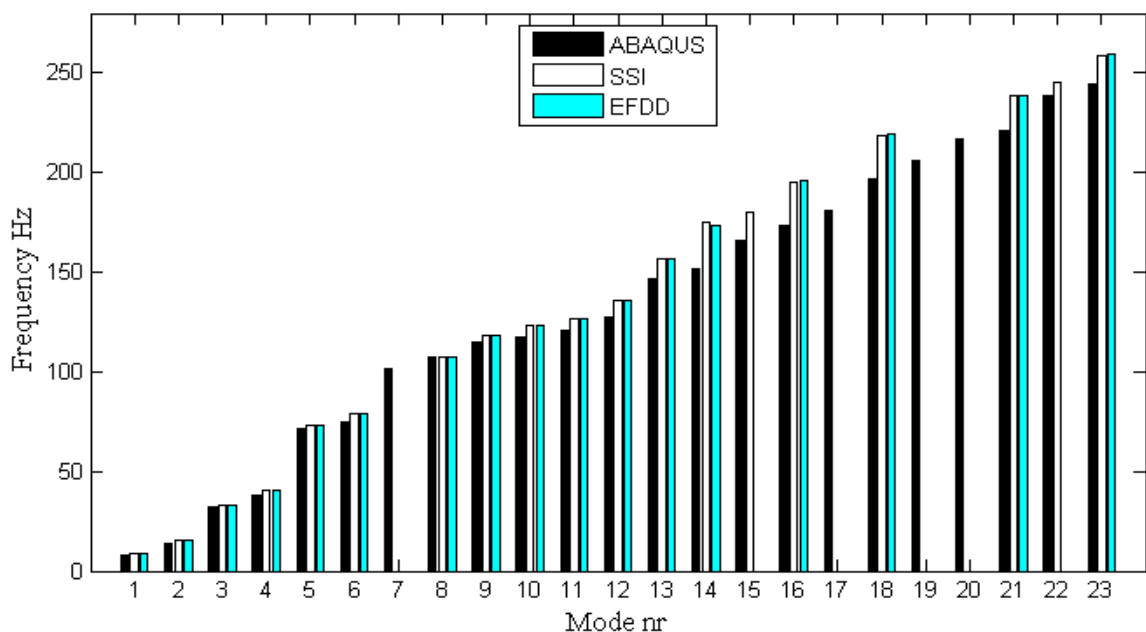


Figure 8.5: Comparing eigenfrequencies for both numerical calculations and OMA results.

MAC values between the predicted (numerical) and the extracted SSI mode shapes are presented in Table C - 4 and Table C - 5. The MAC values for mode 10 and 11 have reduced a bit from the previous OMA (Table 7.7). This is quite logical because the more nodes available for comparison, the greater is the chance of getting reduced MAC values. The results in Table C - 4 also reveal that the SSI extracted mode 10 is more similar to the numerical estimated mode 11 and that the measured mode shape has a more torsional behavior. Mode 22 viewed in Figure C - 11 may look similar to the numerical mode shape (Figure 6.15) but by observing the low MAC value in Table C - 5, it's an indication that the nodes don't coincide. Beside the outliers mentioned above the comparable remaining modes have MAC values above 0,8 which are really good results. The two MAC tables in Appendix C (Table C - 4 and Table C - 5) are summarized and presented in 3D in Figure 8.6.

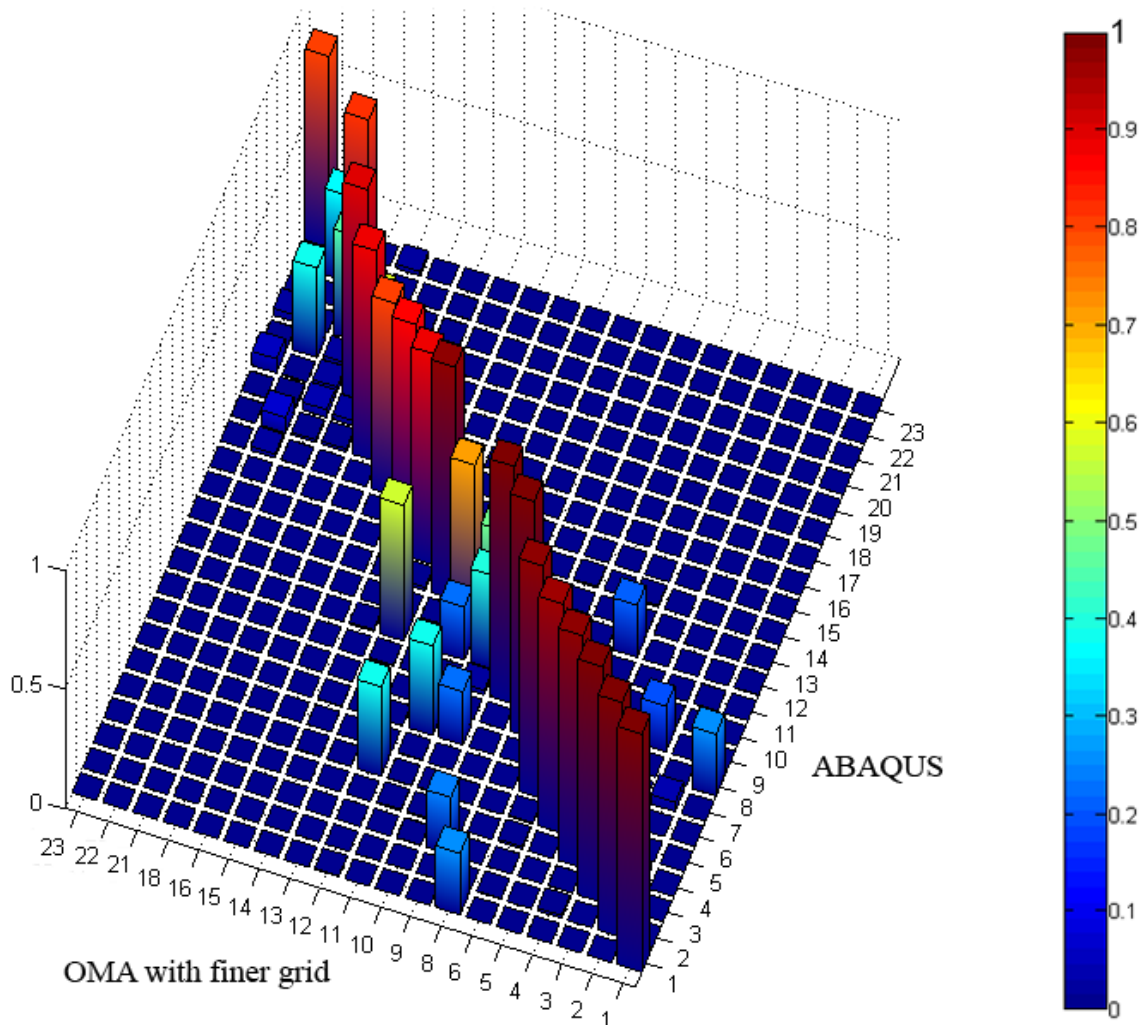


Figure 8.6: 3D MAC table, OMA with finer grid.

Discussed in section 8.1 the estimated damping ratios differed a lot between the SSI and EFDD technique. By observing Figure 8.7 the estimated damping ratios by SSI and EFDD are more similar. Perhaps a more controlled excitation with smaller amplitudes increases the reliability of the estimated damping ratios.

Another interesting observation is that the excitation with the clubs gives lower damping ratios than the excitation with the hands (see Figure 8.3 and Figure 8.7). Perhaps the large amount of hands that are exciting the structure tend to cancel out the vibrations, making the structure more damped than it really is. The excitations with the clubs were more controlled and the vibrations had time to die out during the measurement.

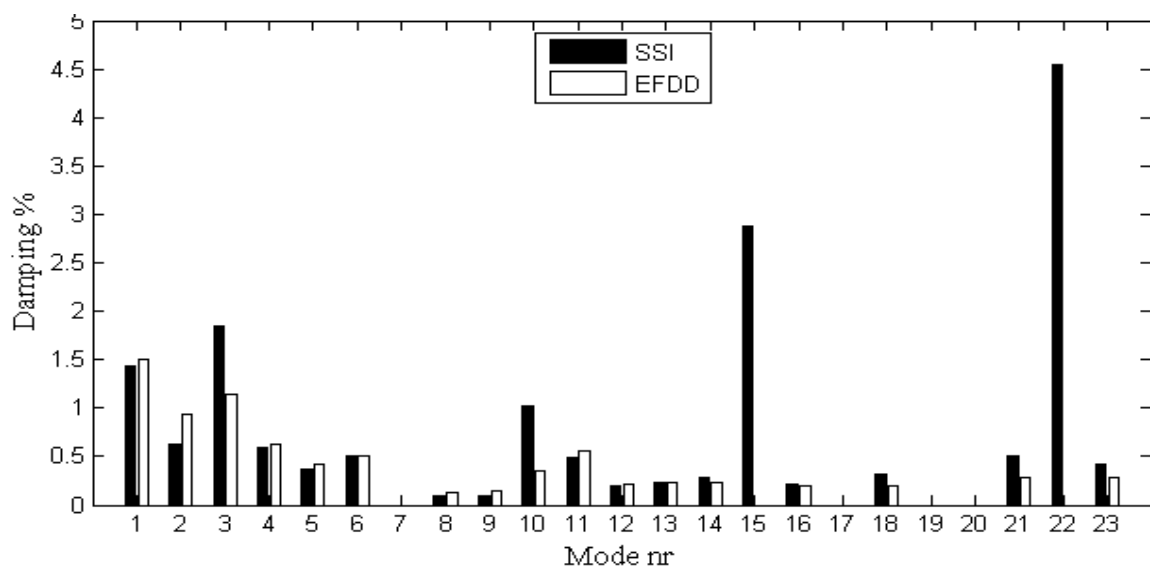


Figure 8.7: Damping ratios for SSI and EFDD.

## 8.6 Structure with Added Mass

An impact measurement and OMA was performed on the structure with four added mass cylinders (section 6.3). The results from both the numerical calculations and the measurements are given in Appendix D. The main reasons why these measurements were performed were to study the accuracy of the measurements on a more complex structure and also to verify the extraction methods' ability to estimate mode shapes that are extremely closely spaced (mode 3 and 4 in Figure D - 2 and Figure D - 3). The estimated eigenfrequencies are presented in Figure 8.8 and the first observation is that the numerical calculations tend to differ from the measurements already at mode 5. This is probably an effect caused by the boundary conditions, the structure is heavier and this will increase the reaction forces at the supports and also the friction at the support with the thin plastic,

causing a stiffer behavior of the plate. Another observation is that the added masses to the structure are lowering the eigenfrequencies.

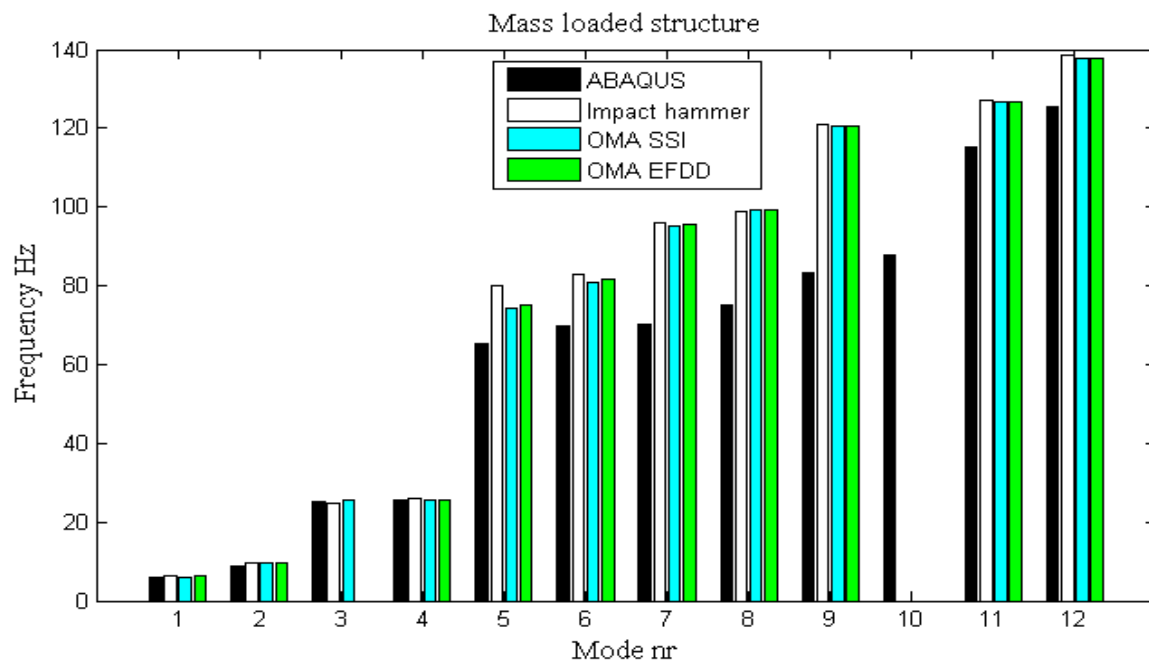


Figure 8.8: Eigenfrequencies for the mass loaded structure.

There is no doubt that the four added masses to the structure made the results harder to interpret by watching the MAC values that are presented in Table D - 4 and Table D - 6. It seems like the hammer results were slightly better than the OMA results by studying these two tables. The estimation of the mode shapes in the impact measurement was carried out using the RFP method. This method was able to estimate both mode 3 and 4 with good precision. Both EFDD and SSI were used to estimate the mode shapes in the OMA. The EFDD method wasn't able to estimate mode 3 and the SSI method gave a quite noisy estimation of this closely spaced mode shape. A 3D representation of Table D - 4 and Table D - 6 is given in Figure 8.9.

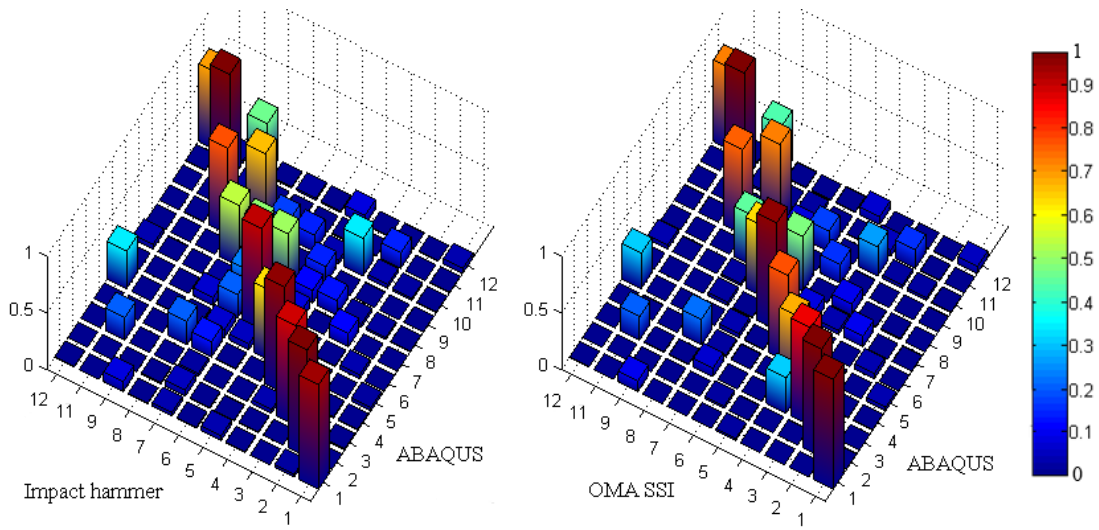


Figure 8.9: 3D MAC tables for hammer test and OMA on mass loaded structure.

As mentioned earlier the modal damping is very difficult to estimate and the results that are given in Figure 8.10 show no different. There are extreme variations of the estimated damping ratios in Figure 8.10. The impact measurement gives a very high damping estimate, perhaps the high force that was applied on the structure with the rubber tip is the main reason of this extreme deviation.

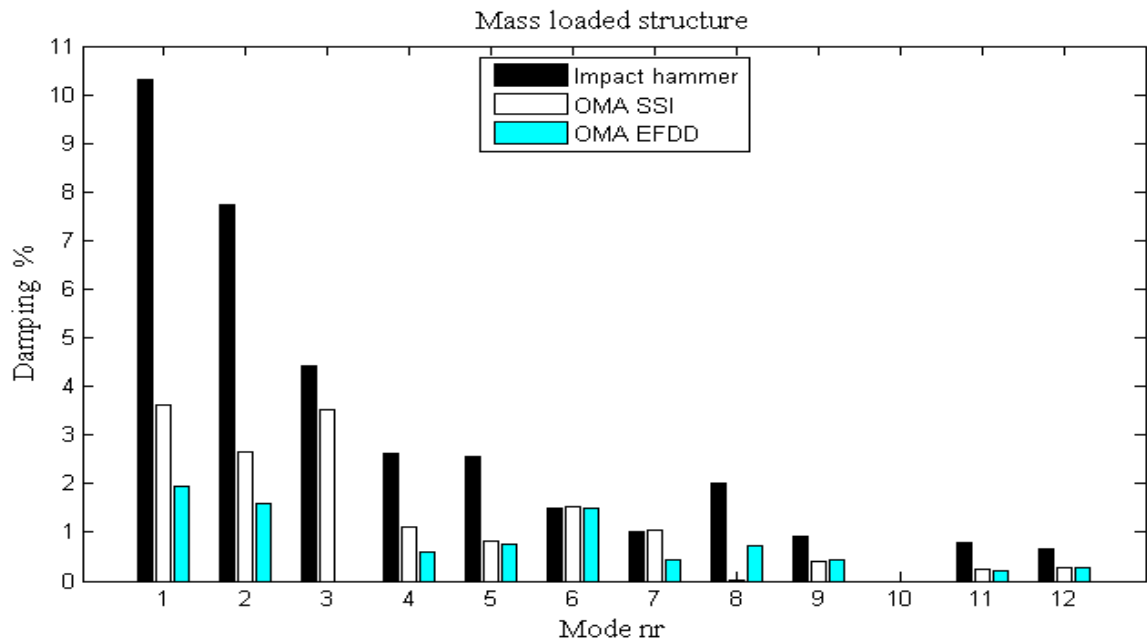


Figure 8.10: Damping ratios for the mass loaded structure.



# 9

## Final Remarks

This chapter contains a conclusion of the highlights discussed in chapter 8 and also suggestions for further studies.

### 9.1 Conclusions

All different modal testing methods have proven to be very useful at estimating eigenfrequencies and mode shapes. The impact hammer provided a fast and flexible measurement, while the shaker required more preparations but the results were more accurate and reliable. The clearest FRFs was obtained using a random input signal in the shaker. The RFP method was able to extract all modes of interest in the shaker measurement with good precision. The RFP method has also proven to be very useful at extracting modes that are closely spaced. The OMA technique worked surprisingly well and the identification methods SSI and EFDD were able to estimate many modes and eigenfrequencies with high accuracy, even though the recorded signals were far from Gaussian white noise. Both SSI and EFDD were powerful extraction methods but the SSI was slightly better though it was able to find all modes of interest automatically and also even closely spaced mode shapes.

The estimated damping ratios were extremely difficult to interpret as they differed a lot between the various measurements. Perhaps there is some connection between the applied force (energy) on the structure and the estimated modal damping as the modal damping tends to decrease with less applied force. Another possible explanation why the extracted modal damping differed could be the amount of nonlinearities in the measurements.

All these measurements were performed on a simple steel structure in an ideal environment with no disturbing background noise. Measuring on real operating bridges is an entirely different matter, background noise caused by wind, waves or nearby traffic could make the execution of the EMA very difficult. The EMA would require large devices to artificially excite the bridge and there might be some problems performing this excitation in a

controlled manner without causing any damage to the structure. OMA seems to be the optimal choice when measuring vibrations on large civil engineering structures like bridges, because by only measuring the output data, the bridge could be fully operational without disturbing the traffic during the measurements. OMA does require longer time records than EMA, but with today's low storage costs and fast CPUs to process the large amount of data, this is no longer an issue.

## 9.2 Further Studies

This thesis has only touched the surface of an entire ocean of applications in modal testing and signal analysis, there is much more to learn and investigate.

In the EMA only SIMO tests have been made. Impact measurements are limited to only one input signal, but in a shaker measurement it's possible to use more than one input source, so called MIMO test (Multiple-Input-Multiple-Output). How does one extra shaker effect the measurement? Which extraction methods are available for MIMO tests? How does the shaker weight effect the measurements?

Only one extraction method has been used in the EMA. Which extraction methods are the most commonly used in commercial software and what is the difference between the frequency domain and time domain extraction methods?

There are more shaker signals available to validate, for example burst and pseudo random signals. How do these signals differ from the random signal used in this thesis?

Are there methods that can reveal the effects of nonlinearities in measurements?

The SHM technique explained in section 5.1 seems to be a great application in OMA. How does this damage detection theory and technology work? Is it possible to apply this technology on all structures or are there some limitations or drawbacks?

In all measurements in chapter 7 there were one mode shape (mode 10 in Figure 7.8, Figure 7.17 and Figure 7.25) that differed a lot from the numerical calculations (Figure 6.11). This mode shape is probably the real mode shape of the structure and the FE model needs to be updated to better comply with the structure's modal behavior. How could we use obtained results from measurements to update an existing FE model?

As discussed in chapter 8 the modal damping is very difficult to estimate. Are there methods available to perhaps verify the extracted modal damping? How could we use the modal damping to better describe the vibration decay of an excited structure? Could we use FE calculations to predict the modal damping?



# 10

## Bibliography

1. **History of bridges.** History of bridges. [Online] [Cited: 30. 06, 2014.]  
<http://www.historyofbridges.com/>.
2. **Bengtsson, Marcus.** Öresund Bridge. *Wikipedia*. [Online] [Cited: 01. 07, 2014.]  
[http://sv.wikipedia.org/wiki/Snedkabelbro#mediaviewer/Fil:%C3%96resund\\_bridge.JPG](http://sv.wikipedia.org/wiki/Snedkabelbro#mediaviewer/Fil:%C3%96resund_bridge.JPG).
3. **Austrell, Per-Erik.** *Övervakning, last- och kapacitetsbestämning för broar-pilotstudie*. Lund : s.n., 2013.
4. **Reynders, Edwin, et al.** *Combined experimental-operational modal testing of footbridges*. 2010.
5. **Maia, et al.** *Theoretical and experimental modal analysis*. Baldock : Research studies press LTD, 1997.
6. **Stellaris, Botaurus.** *Wikipedia. Tacoma Narrows bridge*. [Online] [Cited: 01. 07, 2014.]  
[http://sv.wikipedia.org/wiki/Tacoma\\_Narrows\\_Bridge#mediaviewer/Fil:Tacoma-narrows-bridge-collapse.jpg](http://sv.wikipedia.org/wiki/Tacoma_Narrows_Bridge#mediaviewer/Fil:Tacoma-narrows-bridge-collapse.jpg).
7. **Chopra, Anil K.** *Dynamics of structures*. s.l. : Pearson Education Inc, 2007.
8. **Brandt, Anders.** *Noise and vibration analysis : signal analysis and experimental procedures*. Chichester : John Wiley & Sons, Ltd, 2011.
9. **Brandt, Anders.** *Abravibe-toolbox. Abravibe*. [Online] [Cited: 08. 04, 2014.]  
<http://www.abravibe.com/toolbox.html>.
10. **Brüel & Kjær.** Brüel & Kjær. [Online] [Cited: 22. 09, 2014.]  
<http://www.bksv.se/Products/frontends/lanxi>.
11. **Ewins, D.J.** *Modal testing: theory and practice*. Letchworth : Research studies and press LTD, 1986.
12. **Brüel & Kjær.** *Measuring vibration*. Naerum : Bruel & Kjaer, 1982.

13. **Agilent Technologies.** *The fundamentals of modal testing.* U.S.A : s.n., 1997.
14. **Avenir Technologies.** Avenir Technologies. [Online] [Cited: 01. 07, 2014.] <http://www.avenirtechnologies.co/impact-hammers/>.
15. **Conha, Á and Caetano, E.** *Experimental modal analysis of civil engineering structures.* Copenhagen : Sound and vibration, 2006.
16. **DØssing, Ole.** *Structural testing, part 1 mechanical mobility measurements.* Denmark : Bruel & Kjaer, 1988.
17. **Avitabile, Peter.** *Modal space in our own little world.* Massachusetts : Modal Analysis and Controls Laboratory, 2013.
18. **Alvin, K.F., et al.** *Structural system identification: from reality to models.* K.C. Park : Computers and structures, 2003.
19. **Richardson, Mark H and Formenti, David L.** *Parameter estimation from frequency response measurements using rational fraction polynomials.* Orlando : Structural Measurement Systems, Inc., 1982.
20. **Gomaa, F, et al.** *Validation study illustrates the accuracy of operational modal analysis identification.* Menofia : s.n., 2012. p. 10.
21. **Reynders, Edwin.** *System identification methods for (operational) modal analysis: review and comparison.* Barcelona : K.U.Leuven, Dept. of civil engineering, 2012.
22. **Structural Vibration Solutions.** Svibs. [Online] [Cited: 25. 01, 2014.] [http://www.svibs.com/solutions/what\\_is\\_oma.aspx](http://www.svibs.com/solutions/what_is_oma.aspx).
23. **Maurizio, Bocca, et al.** *A synchronized wireless sensor network for experimental modal analysis in structural health monitoring.* Helsinki : Computer-Aided Civil and Infrastructure Engineering, 2011.
24. **Chang, Peter C and Flatau, Alison.** *Review paper: Health monitoring of civil infrastructure.* 2003.
25. **Partnerships BC.** Partnerships British Columbia. [Online] [Cited: 01. 07, 2014.] <http://www.partnershipsbc.ca/files-4/project-pitt-river.php>.
26. **BCSIMS.** British columbia smart infrastructure monitoring system. [Online] [Cited: 01. 07, 2014.] <http://www.bcsims.ca/>.
27. **Gade, Svend, et al.** *Frequency domain techniques for operational modal analysis.* Copenhagen, Denmark : Proceedings of IOMAC Conference, 2005.

28. **Brincker, Rune, et al.** *Automated frequency domain decomposition*. Denmark : Department of Civil Engineering, 2007.
29. **Jacobsen, Niels Jorgen, et al.** *Using EFDD as a robust technique to deterministic excitation in operational modal analysis*. Denmark : Svibs.com, 2007.
30. **Batel, Mehdi.** *Operational modal analysis-another way of doing modal testing*. Georgia : Sound and vibration, 2002.
31. **Bricker, Rune and Andersen, Palle.** *Understanding stochastic subspace identification*. Denmark : svibs.com.
32. **Andersen, Palle.** *Webinar ARTeMIS*. Denmark : s.n., 2014.
33. **Andersen, Palle and Bricker, Rune.** *The stochastic subspace identification techniques*. Aalborg : svibs.com.
34. **Ottosen, Niels Saabye and Petersson, Hans.** *Introduction to the finite element method*. Harlow : Pearson Education Limited, Prentice Hall, 1992.



# Appendix A

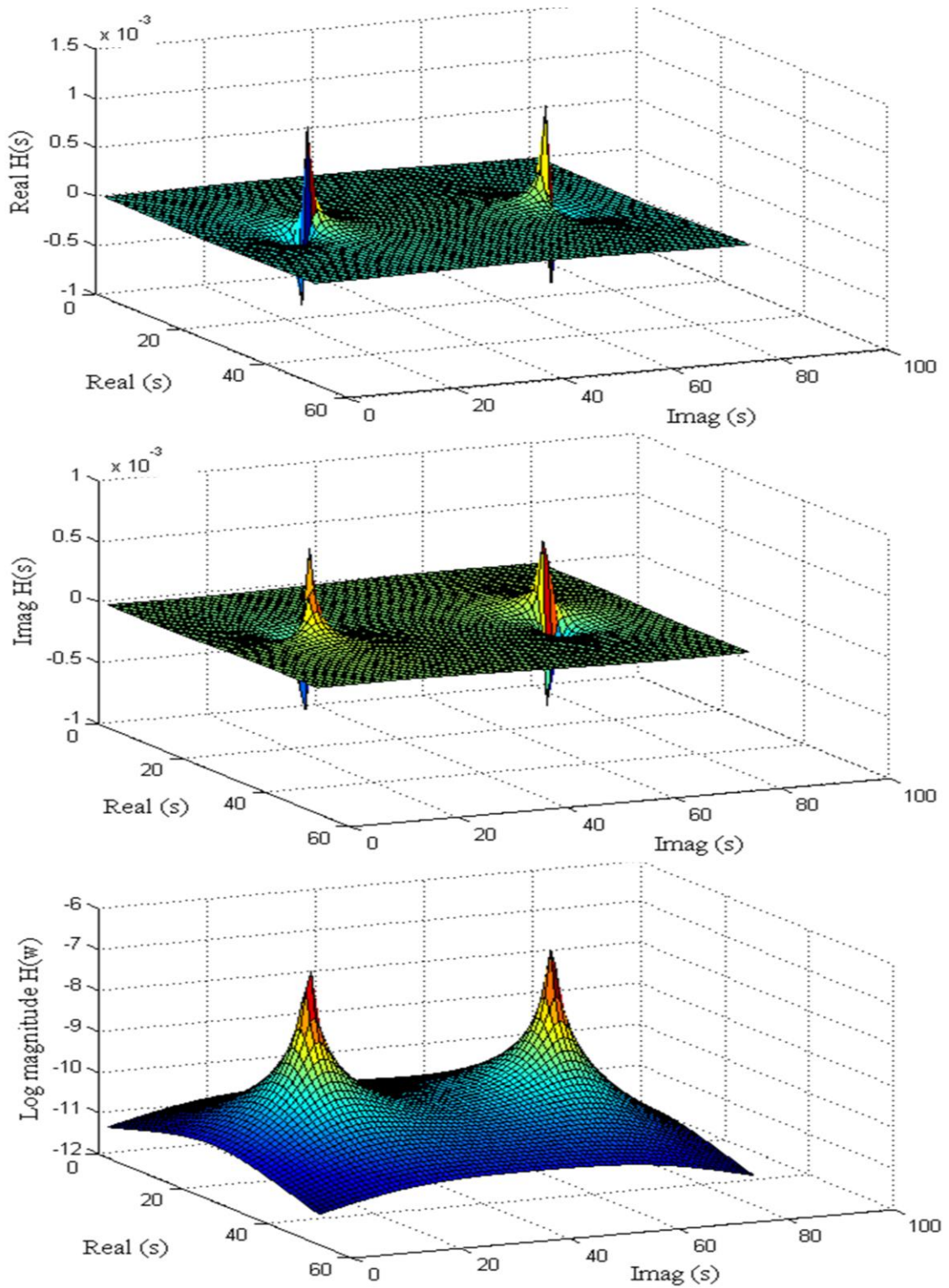


Figure A - 1: Transfer function: Real, imaginary and log magnitude for the SDOF example (see Appendix E).

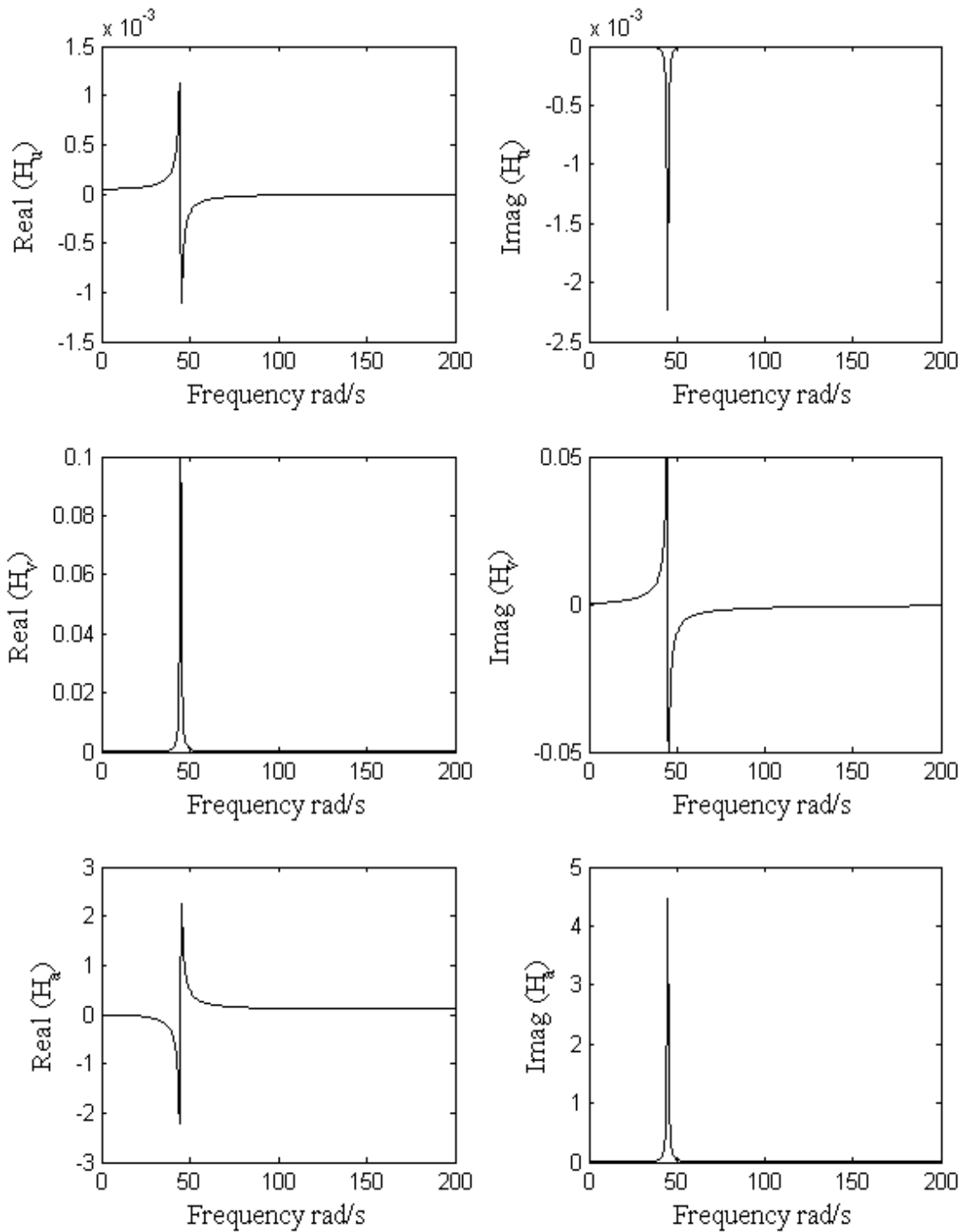


Figure A - 2: Real and imaginary plots of FRF (receptance, mobility and acceleration), SDOF example (see Appendix E).

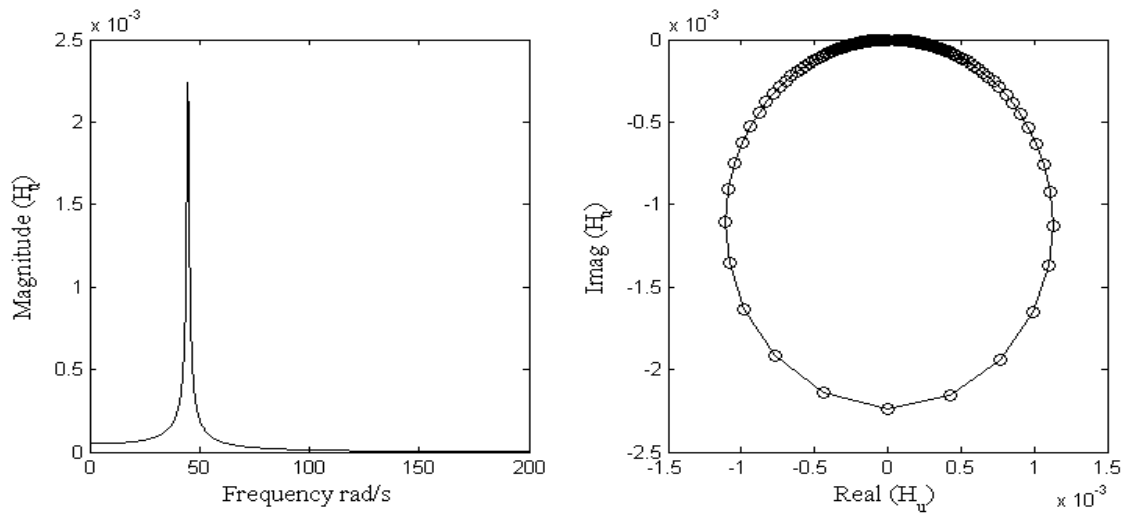


Figure A - 3: Magnitude and Nyquist plot of FRF, SDOF example (see Appendix E).

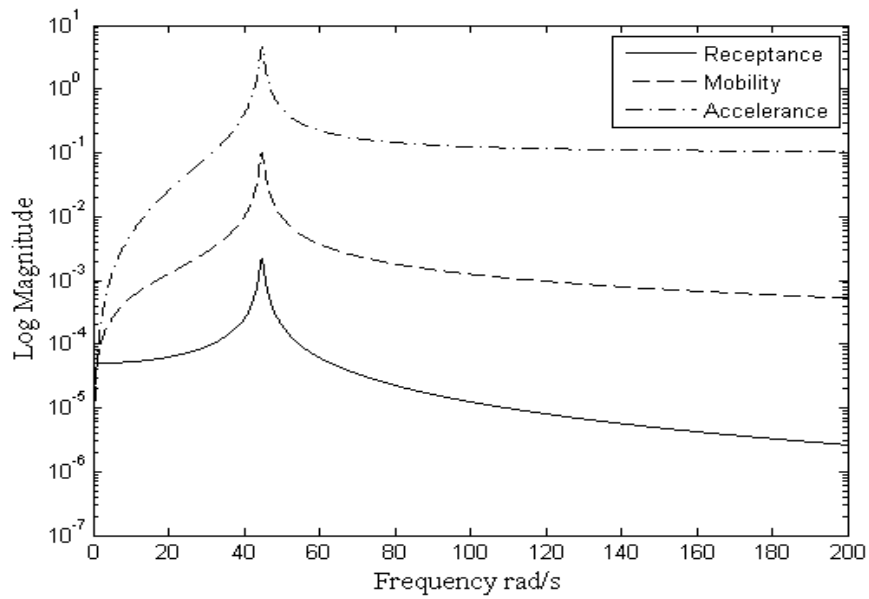


Figure A - 4: FRF log magnitude (receptance, mobility and acceleration), SDOF example (see Appendix E).

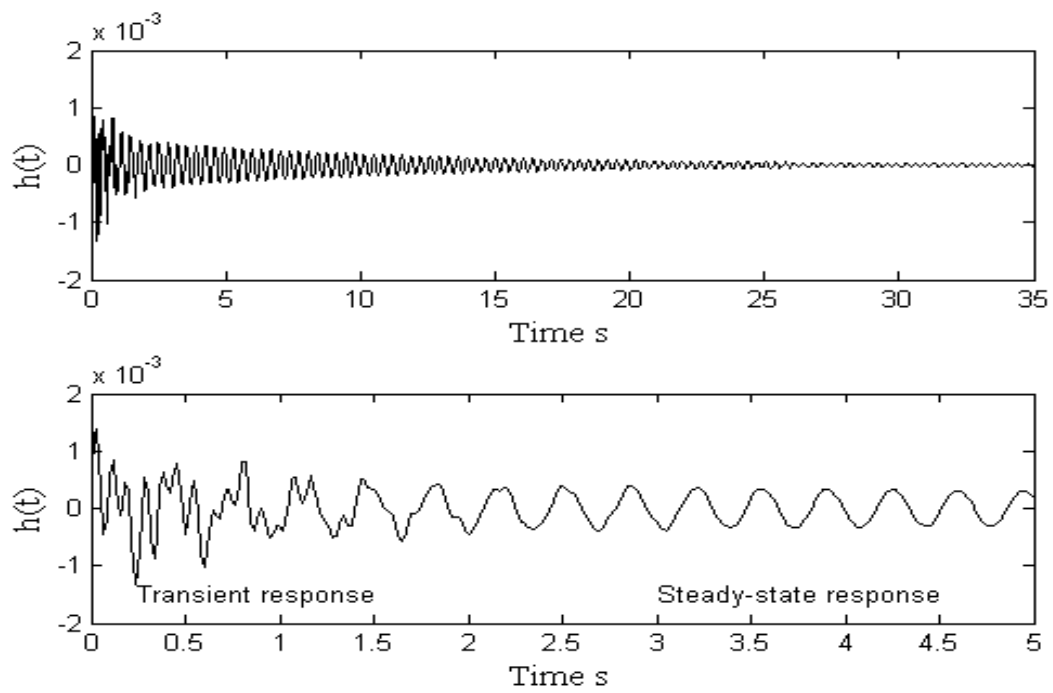


Figure A - 5: Impulse response function, 3DOF example (see Appendix E).

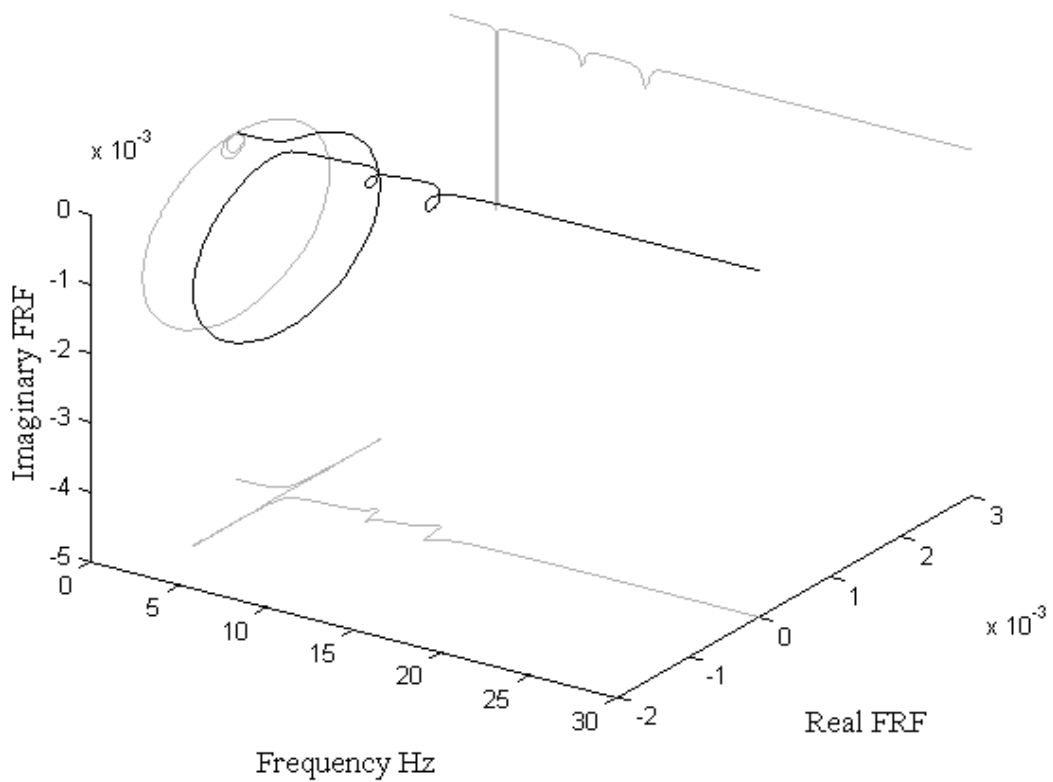


Figure A - 6: 3D plot of FRF, 3DOF example (see Appendix E).

# Appendix B

Additional information to the measurements in section 7.1-7.3 is attached in this appendix.

## B.1 EMA Impact Hammer

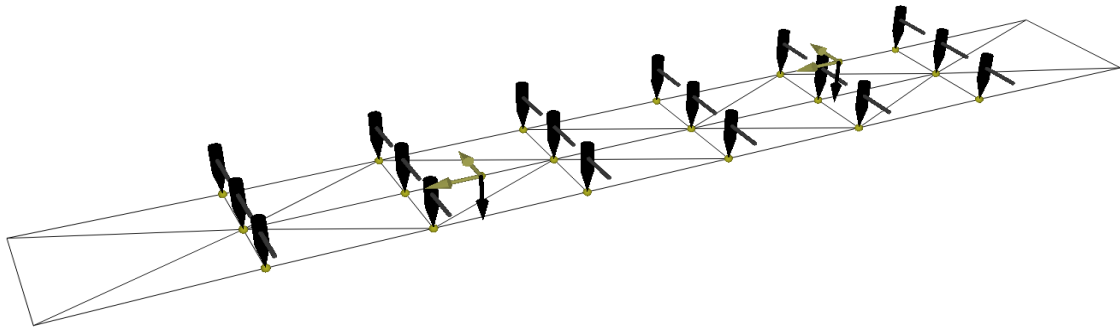


Figure B - 1: 3D representation of the impact measurement (see Figure 7.2).

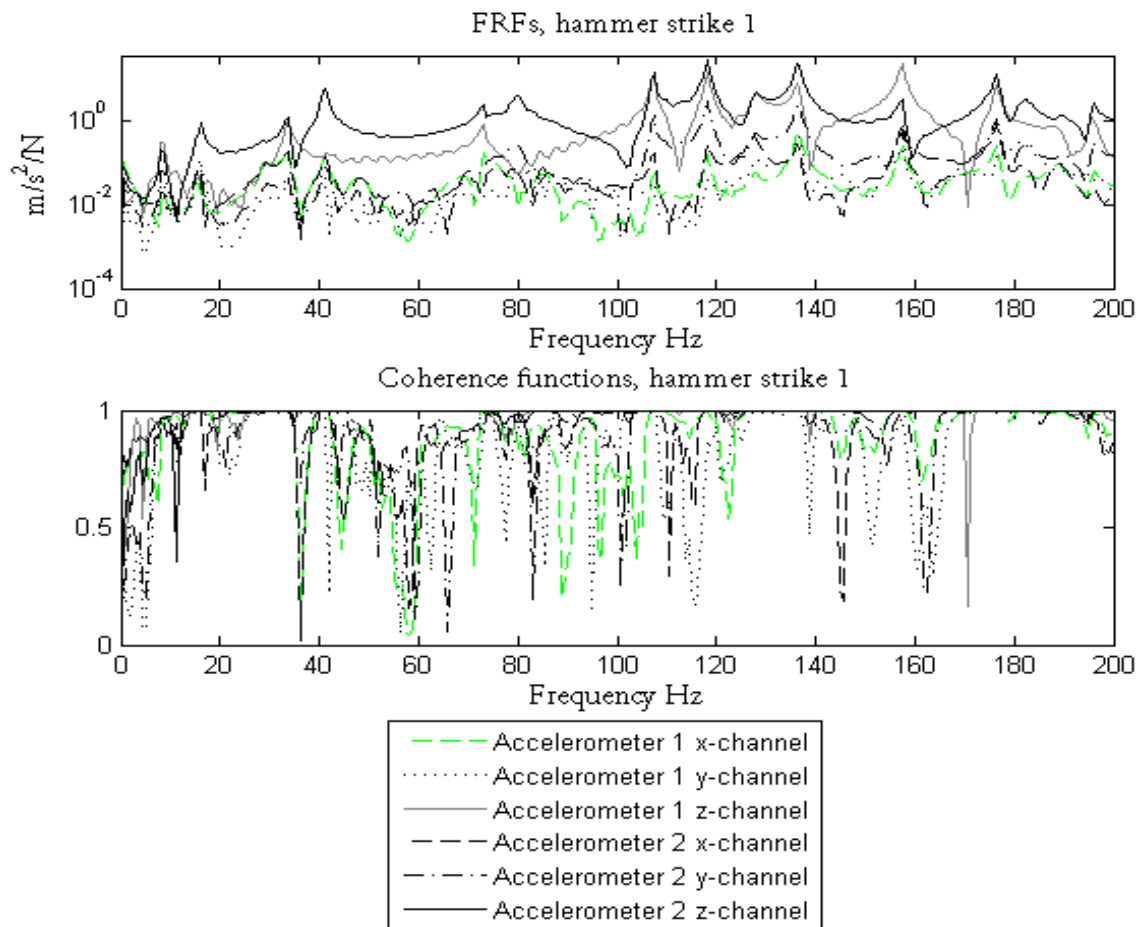


Figure B - 2: FRF (above) and coherence function (below) for hammer strike 1, all measured channels.

## Hammer strike at position 1

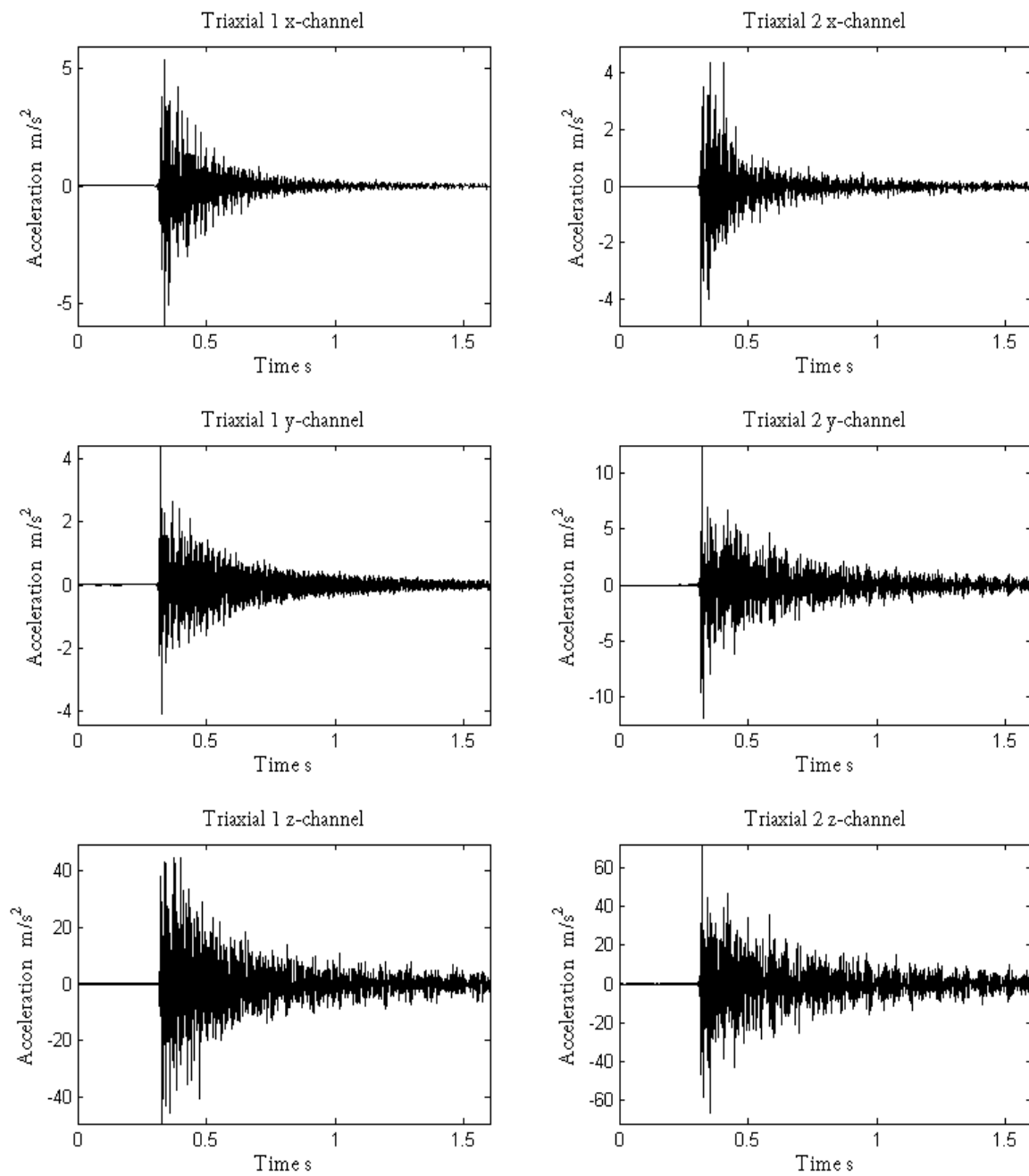


Figure B - 3: Response plot of hammer strike 1.

## Hammer strike at position 1

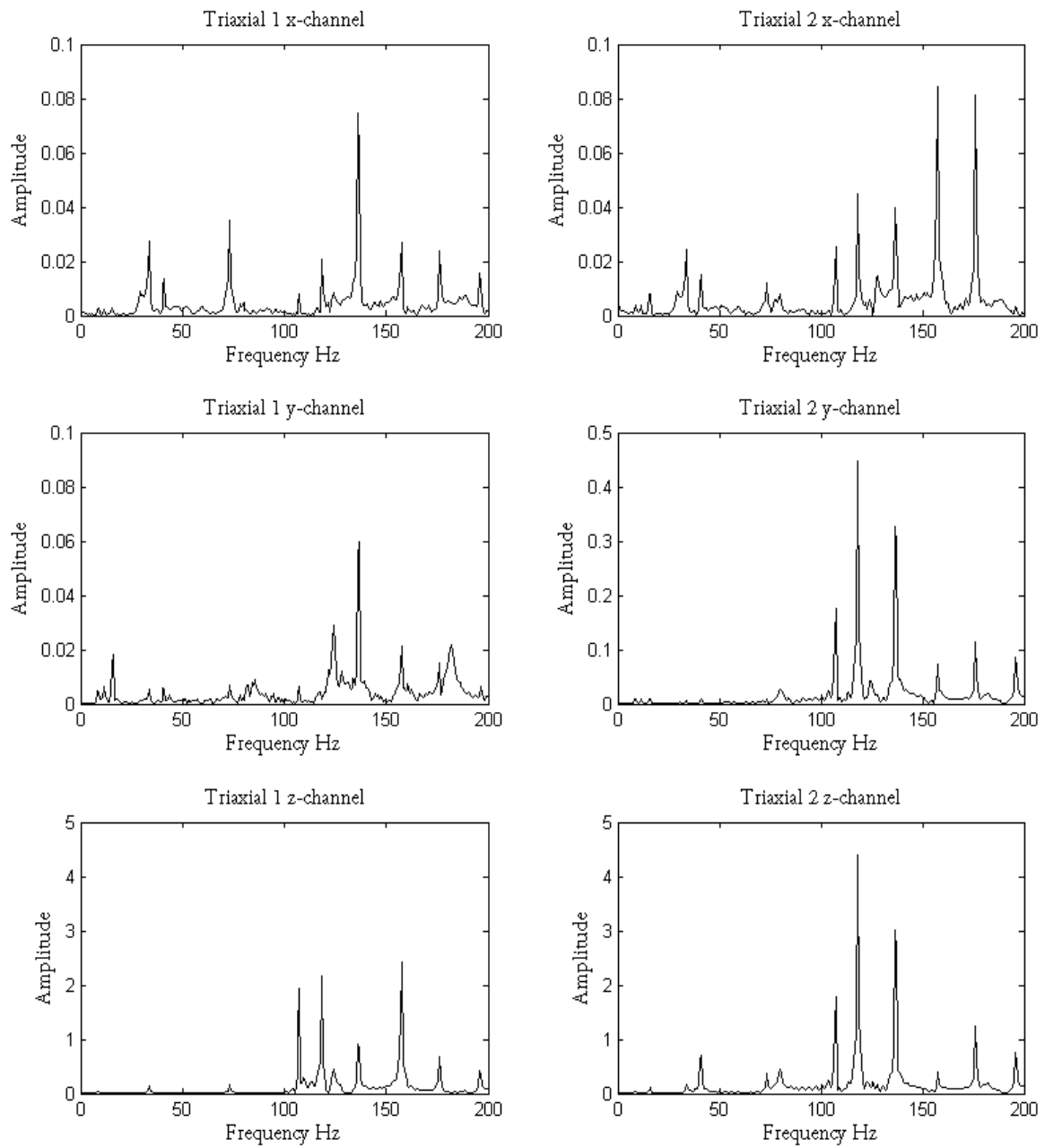


Figure B - 4: FFT analysis on the measured responses in Figure B - 3.

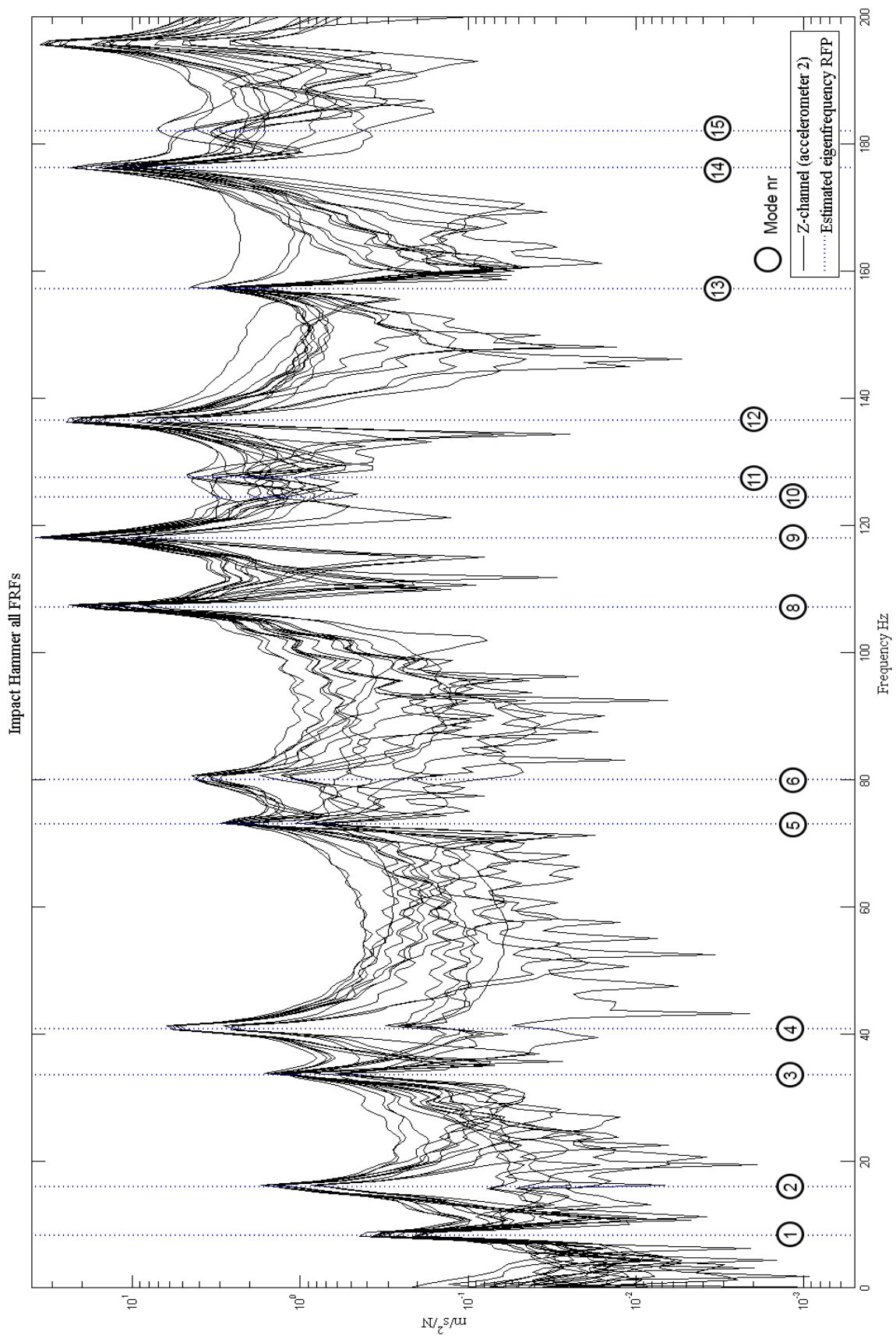


Figure B - 5: All FRFs generated by reference accelerometer 2 (z-channel) and impact hammer.

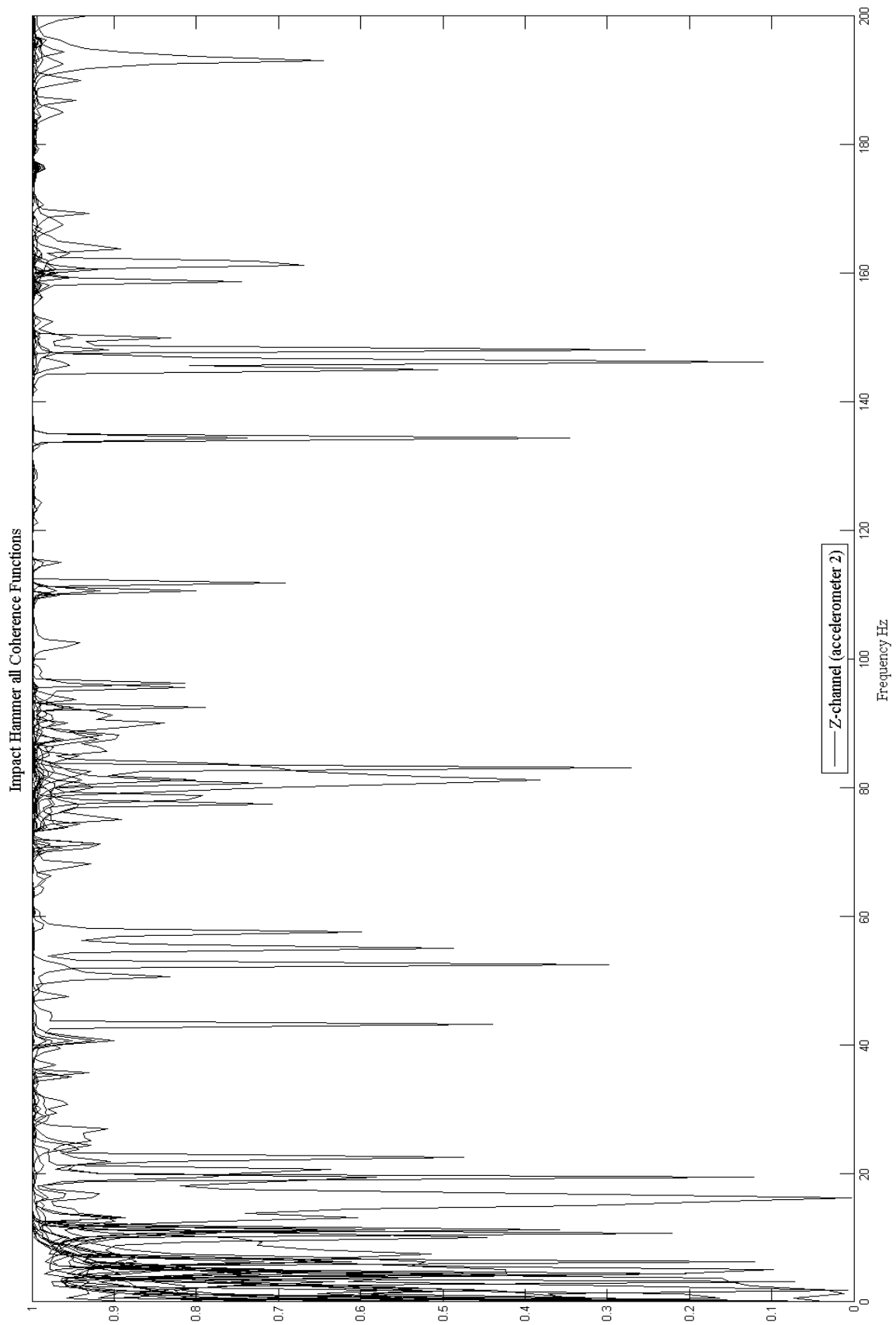


Figure B - 6: All coherence functions generated by reference accelerometer 2 (z-channel) and impact hammer.

## B.2 EMA Shaker

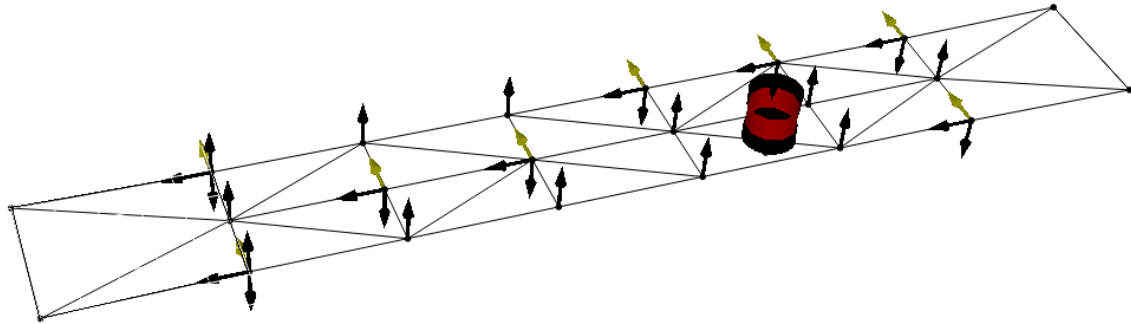


Figure B - 7: 3D representation of shaker measurement (position 3) and transducer directions (see Figure 7.11).

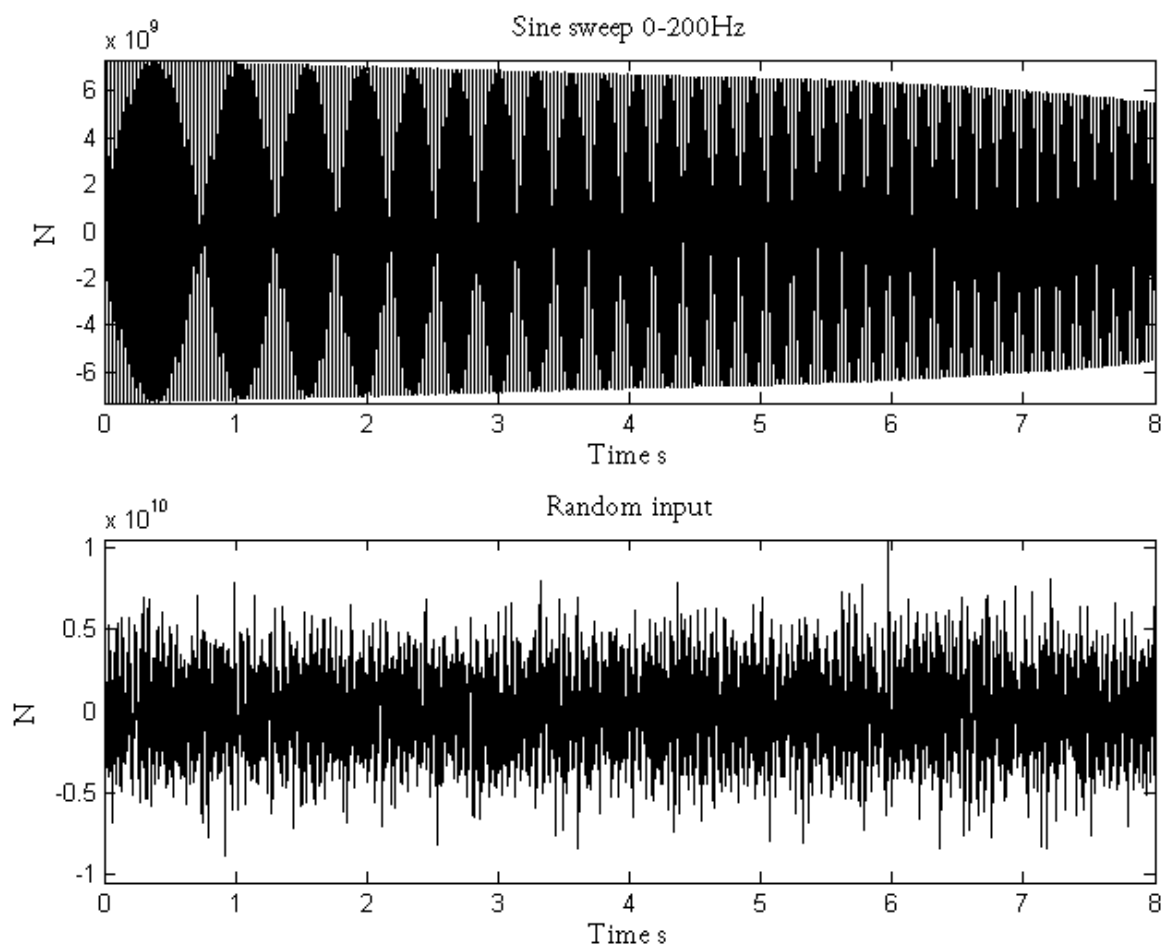


Figure B - 8: Force spectra in time domain (sine signal above and random signal below).

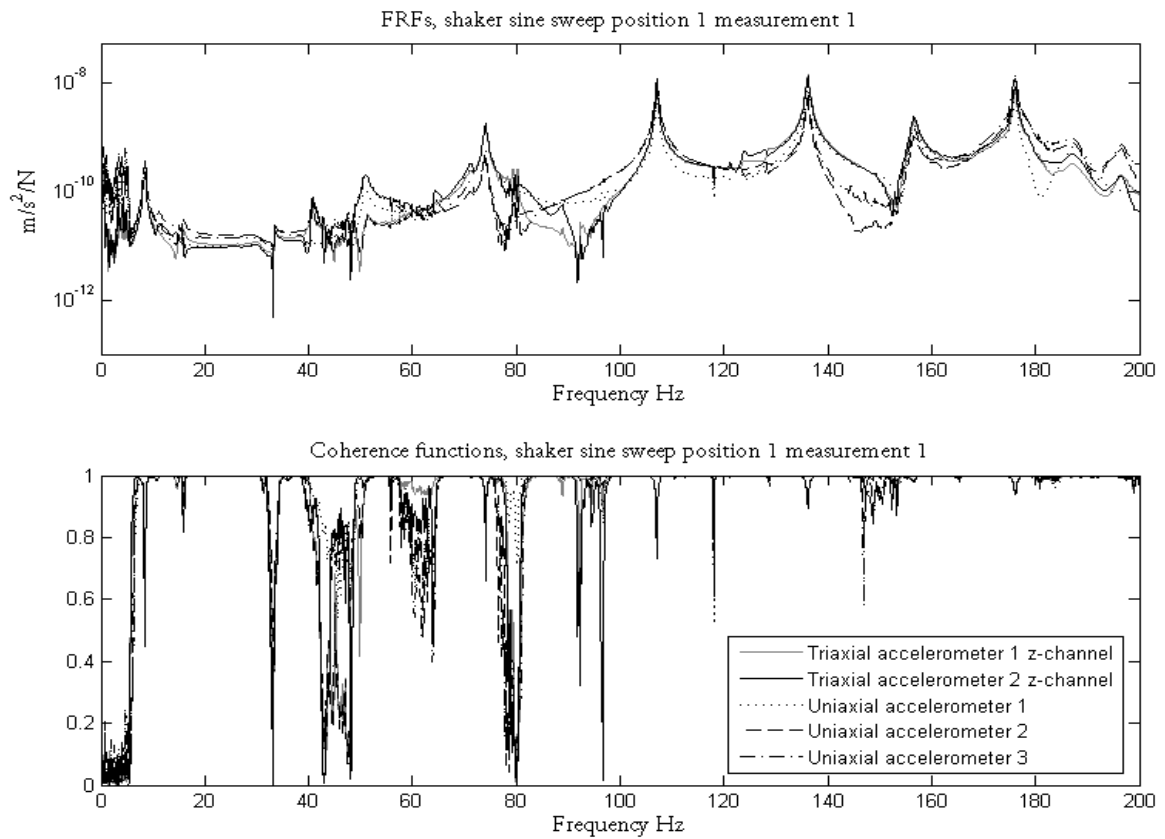


Figure B - 9: FRFs (above) and coherence functions (below) shaker position 1, sine sweep.

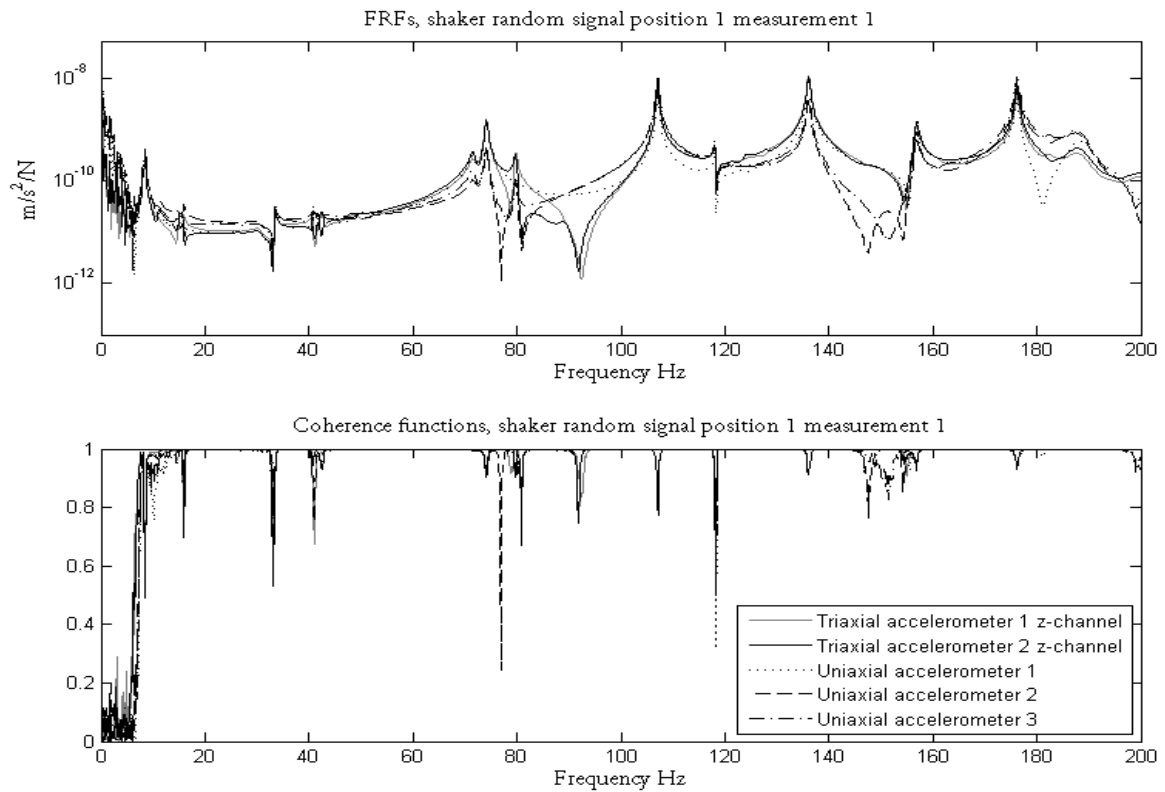


Figure B - 10: FRFs (above) and coherence functions (below) shaker position 1, random signal.

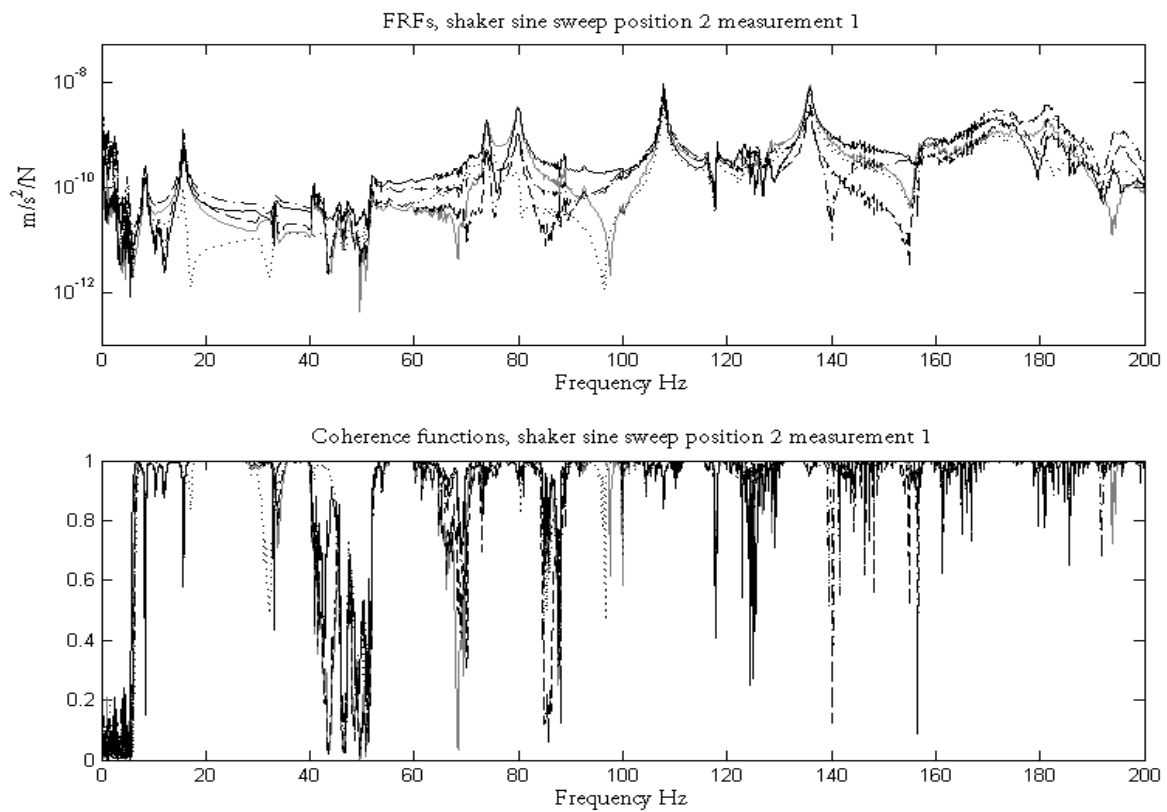


Figure B - 11: FRFs (above) and coherence functions (below) shaker position 2, sine sweep (the legend can be viewed in Figure B - 12).

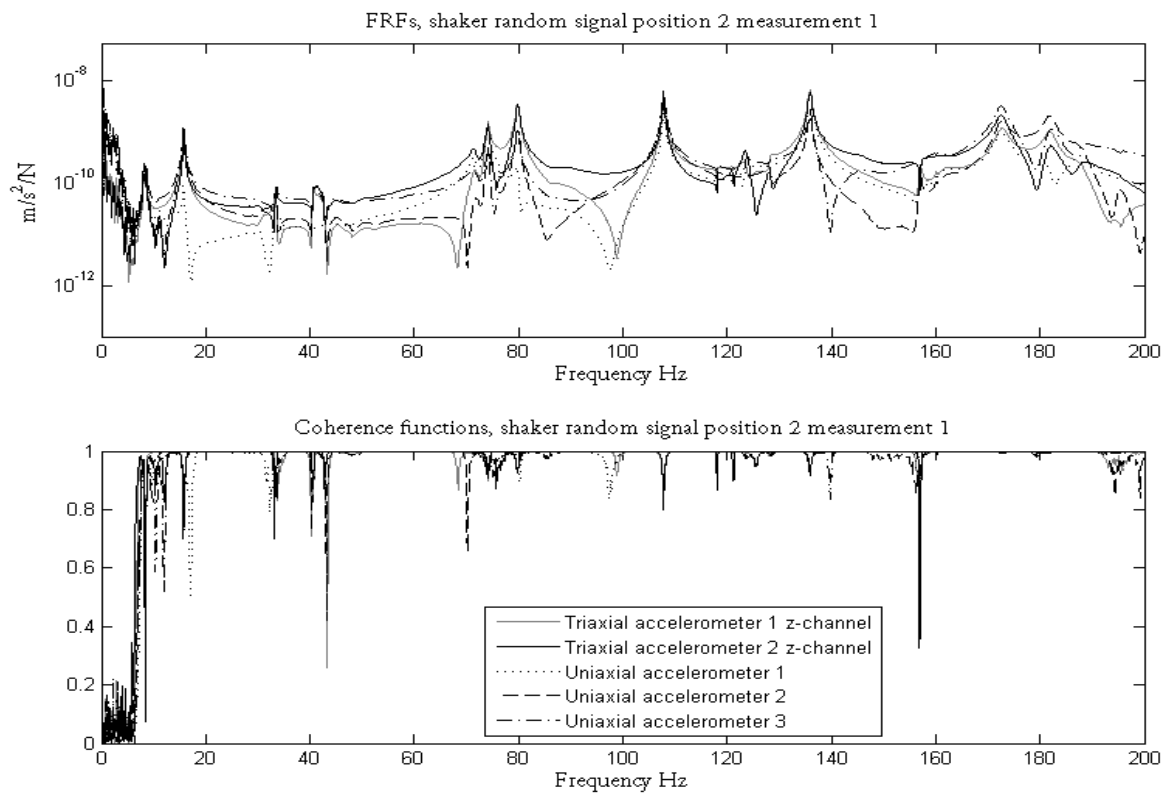


Figure B - 12: FRFs (above) and coherence functions (below) shaker position 2, random signal.

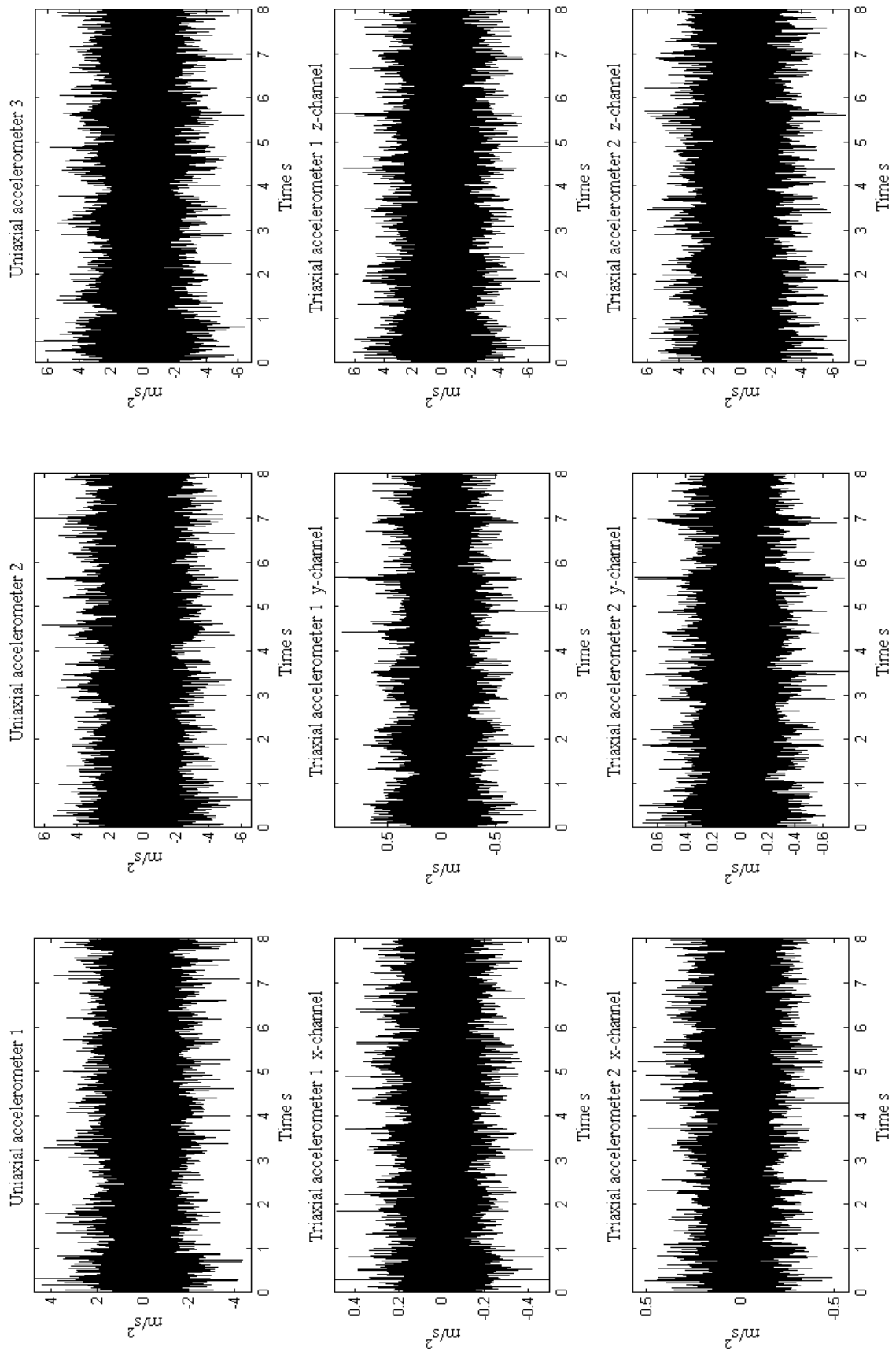


Figure B - 13: Random output signals, measurement sequence 1.

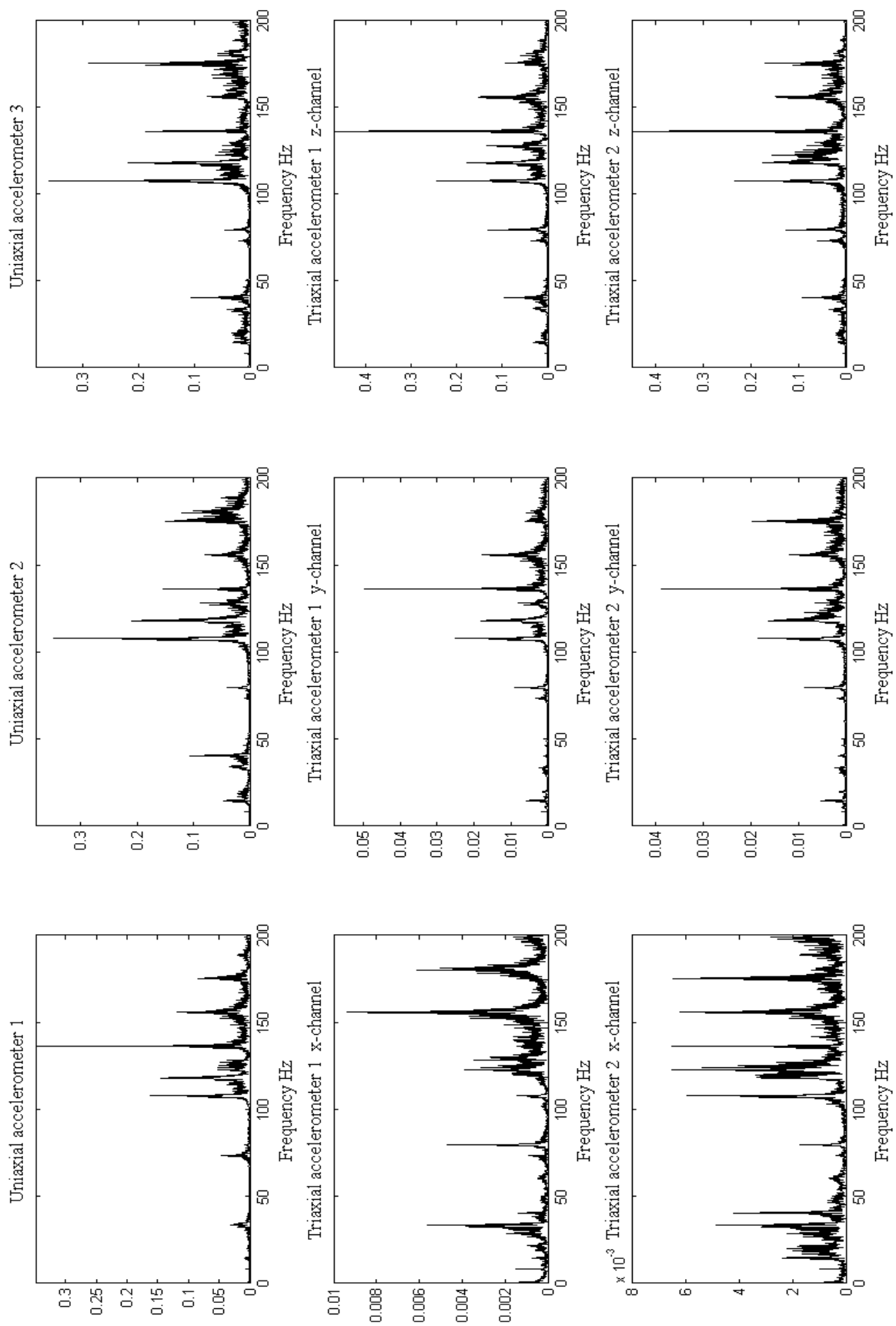


Figure B - 14: FFT performed on random time signals (Figure B - 13).

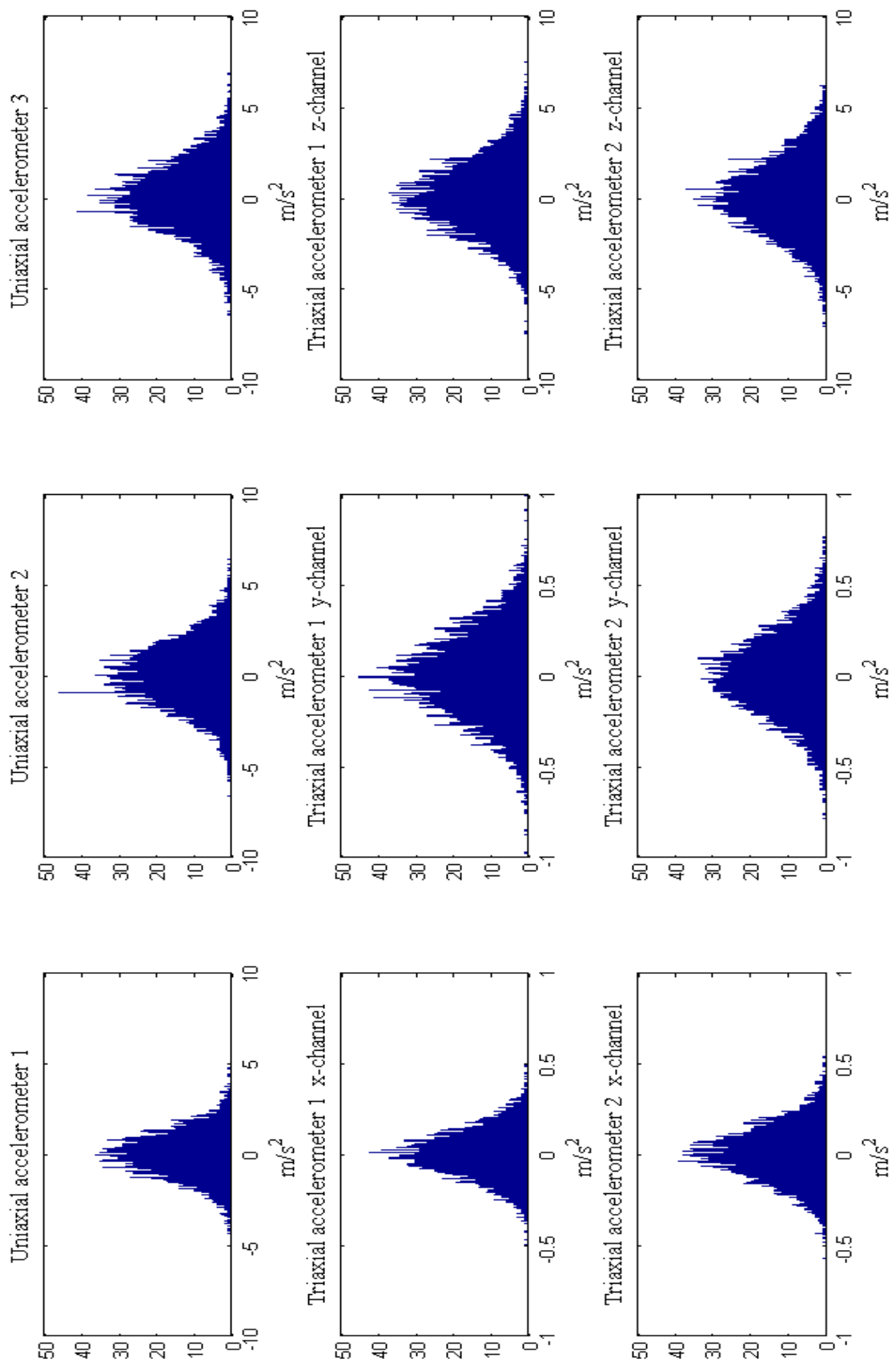


Figure B - 15: Histograms generated from random time signals (Figure B - 13).

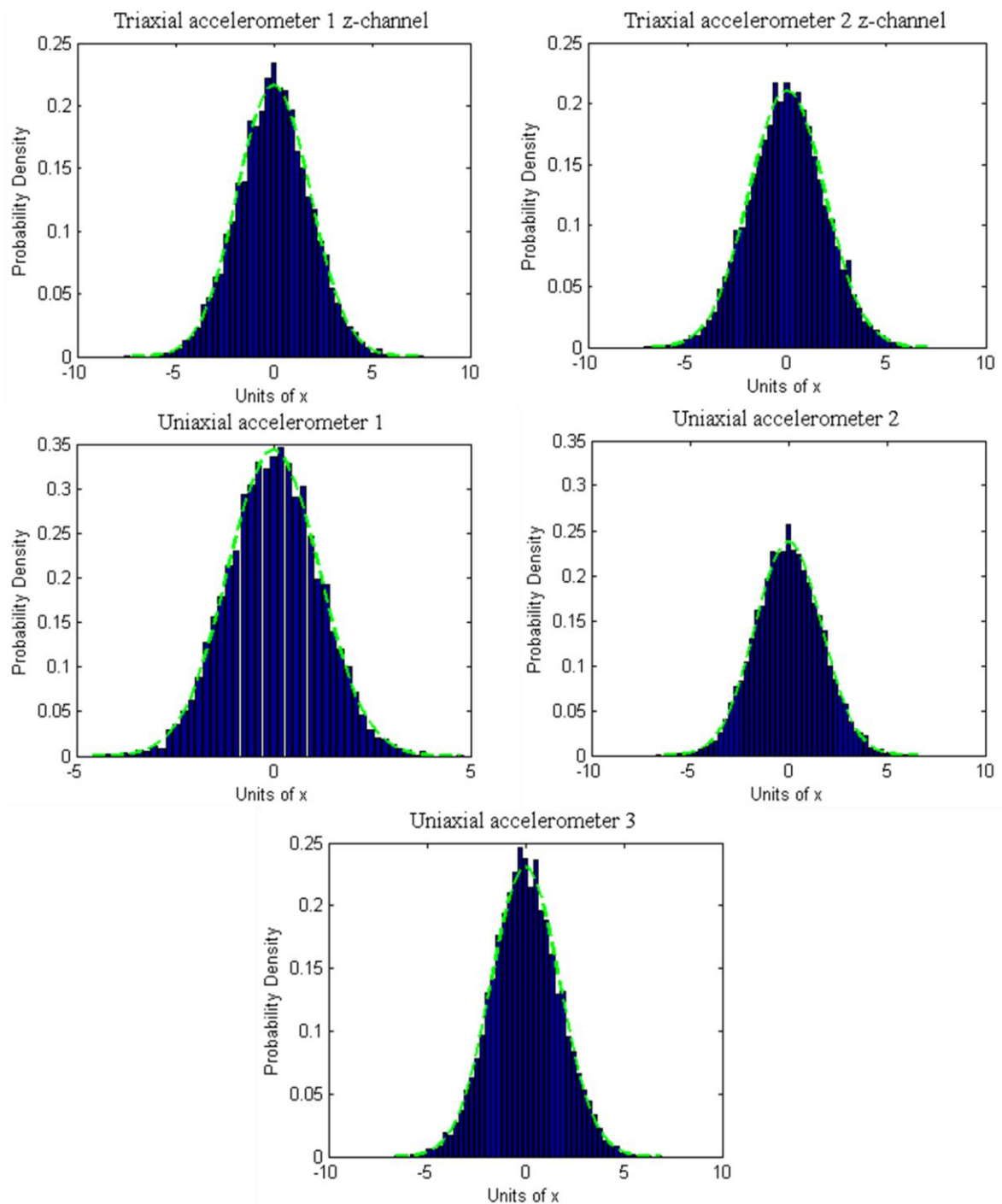


Figure B - 16: Probability plots created by Abravibe toolbox [9].

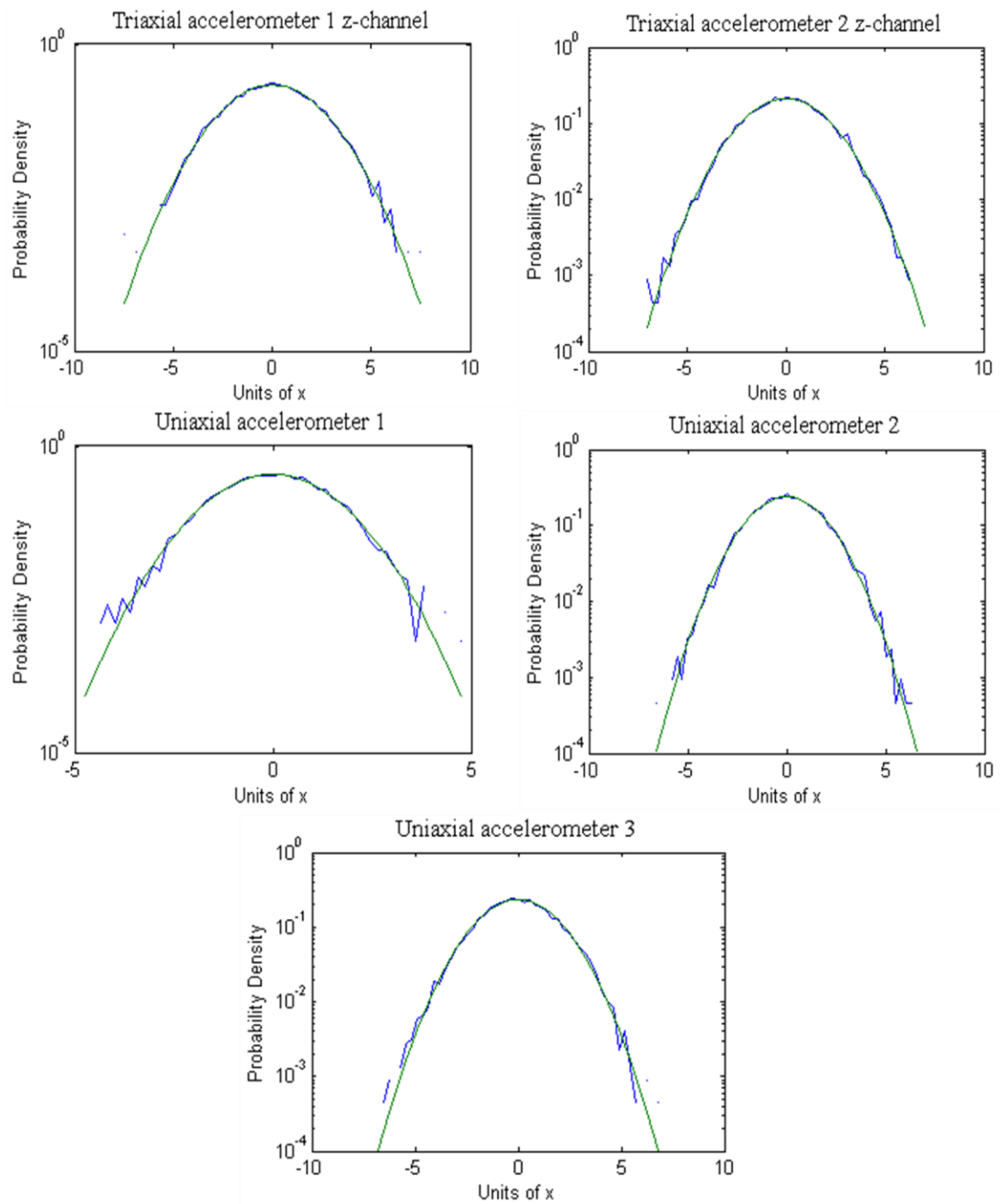


Figure B - 17: Probability density, logarithmic plots created by Abravibe toolbox [9].

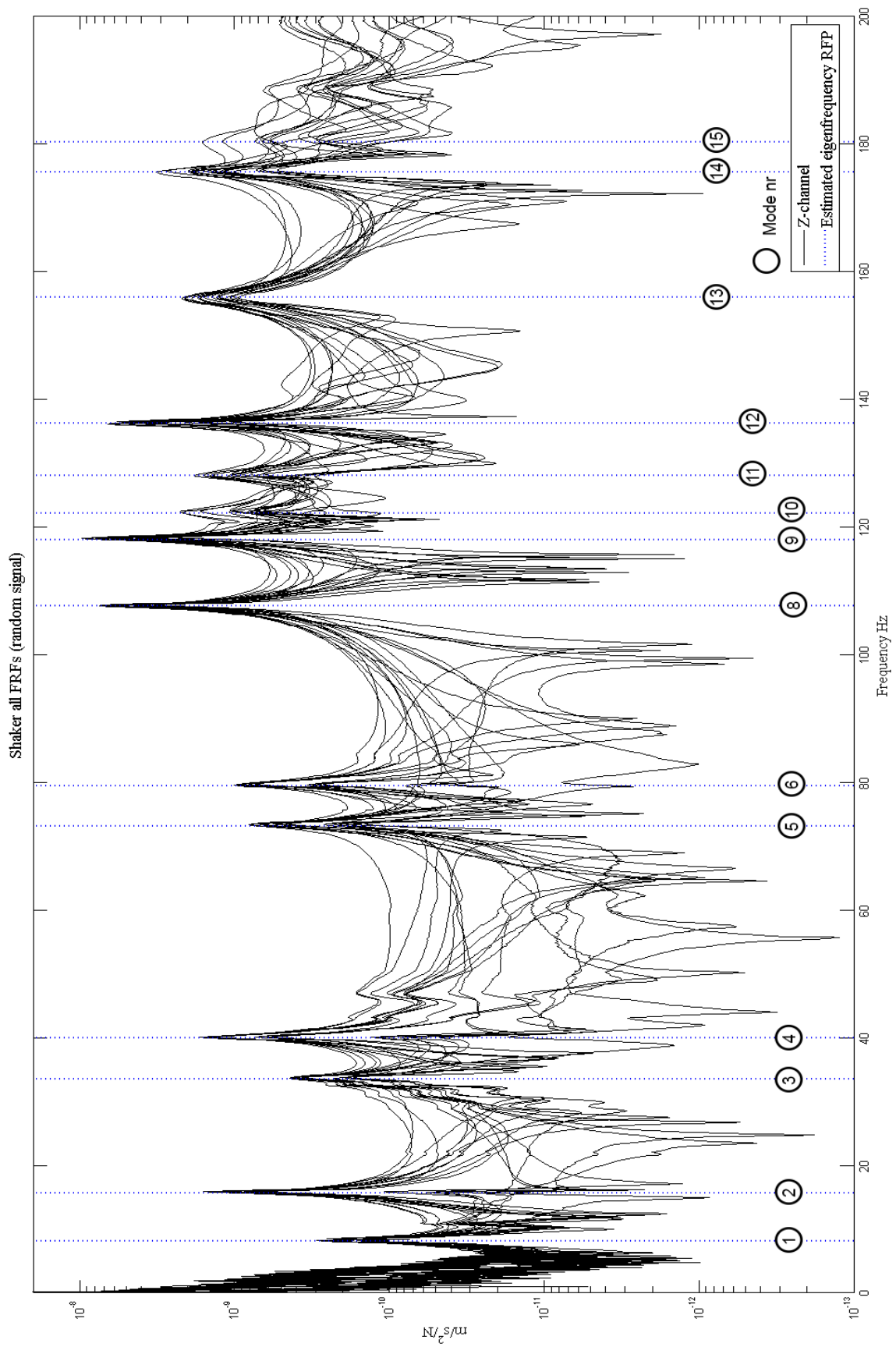


Figure B - 18: All FRFs (z-channel) generated by the shaker in position 3 (random excitation).

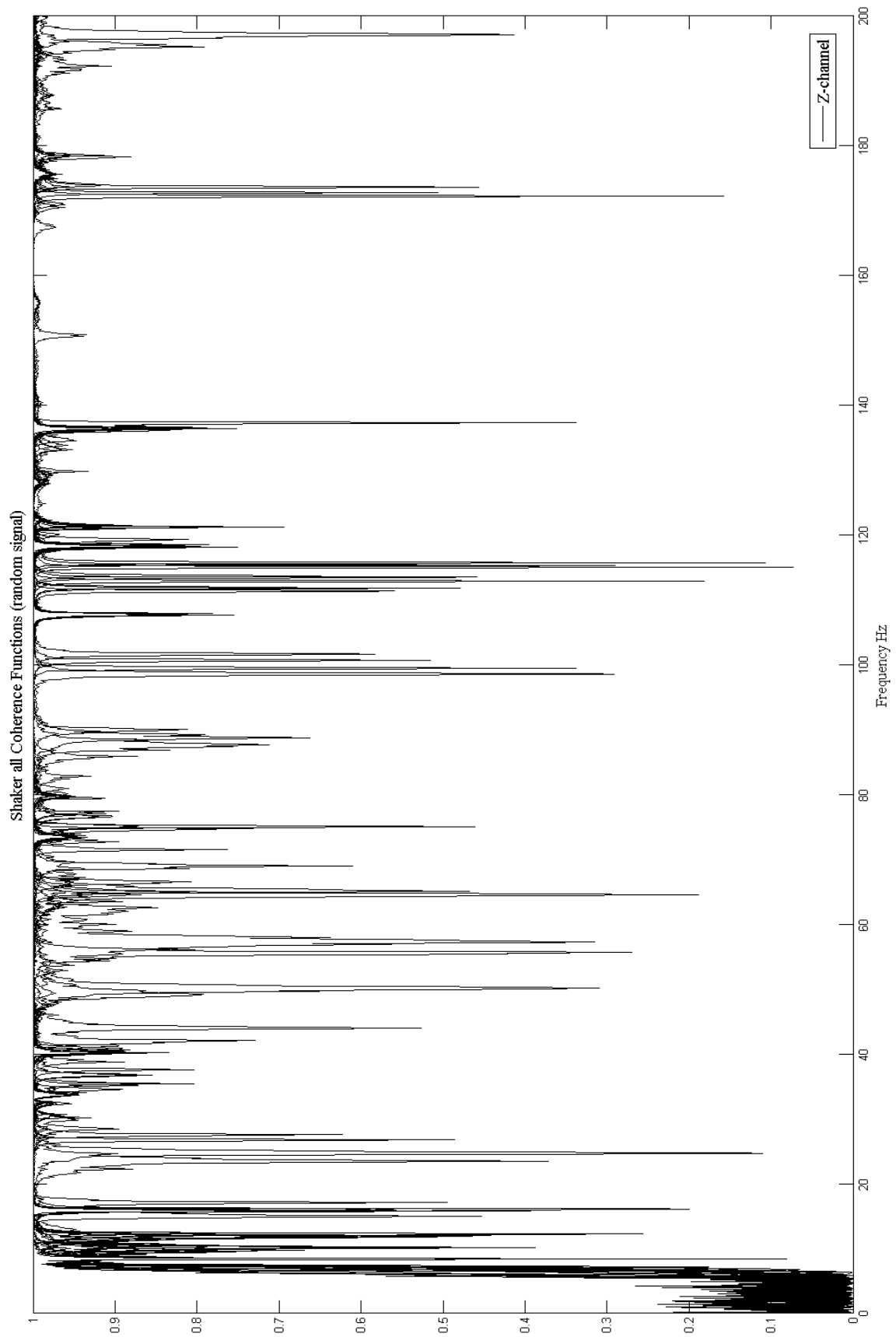


Figure B - 19: All coherence functions (z-channel) generated by the shaker in position 3 (random excitation).

### B.3 OMA

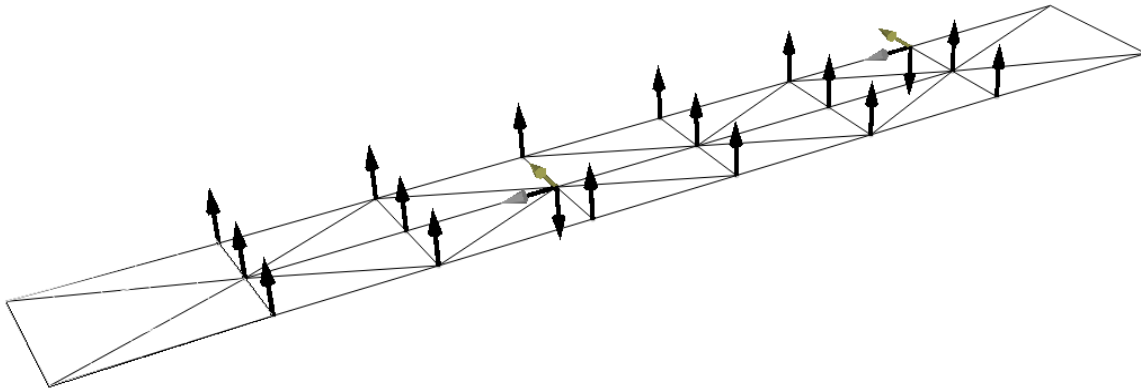


Figure B - 20: 3D representation of the OMA (see Figure 7.20).

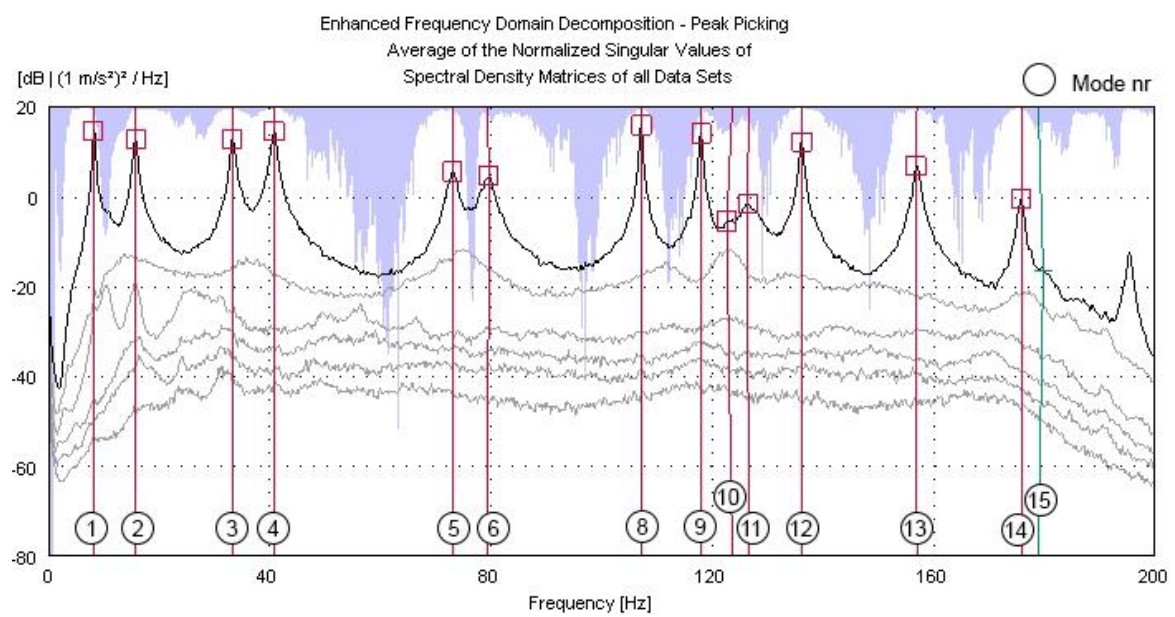


Figure B - 21: EFDD, peak picking.

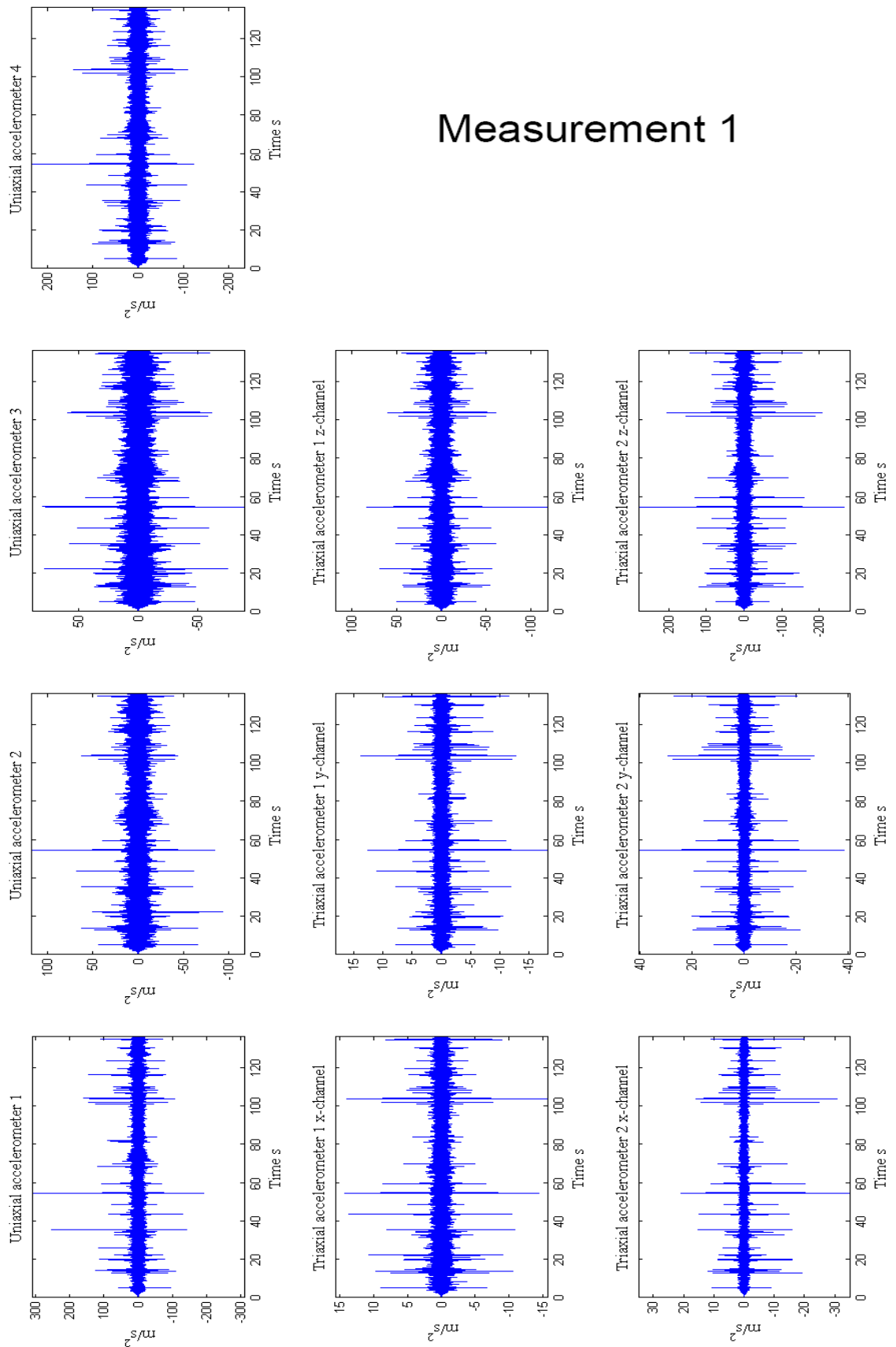


Figure B - 22: OMA sequence 1, time signal.

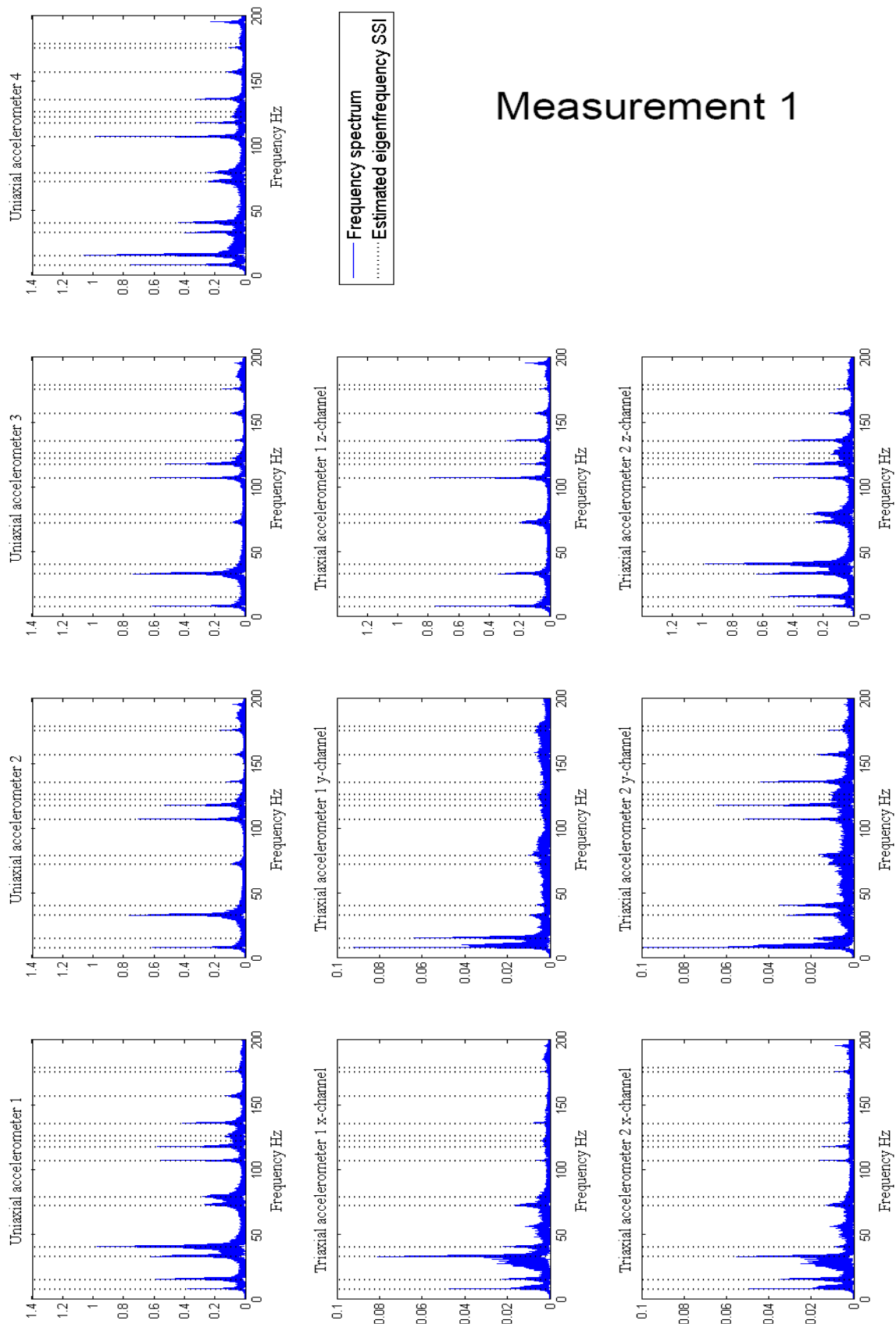


Figure B - 23: OMA sequence 1, frequency domain.

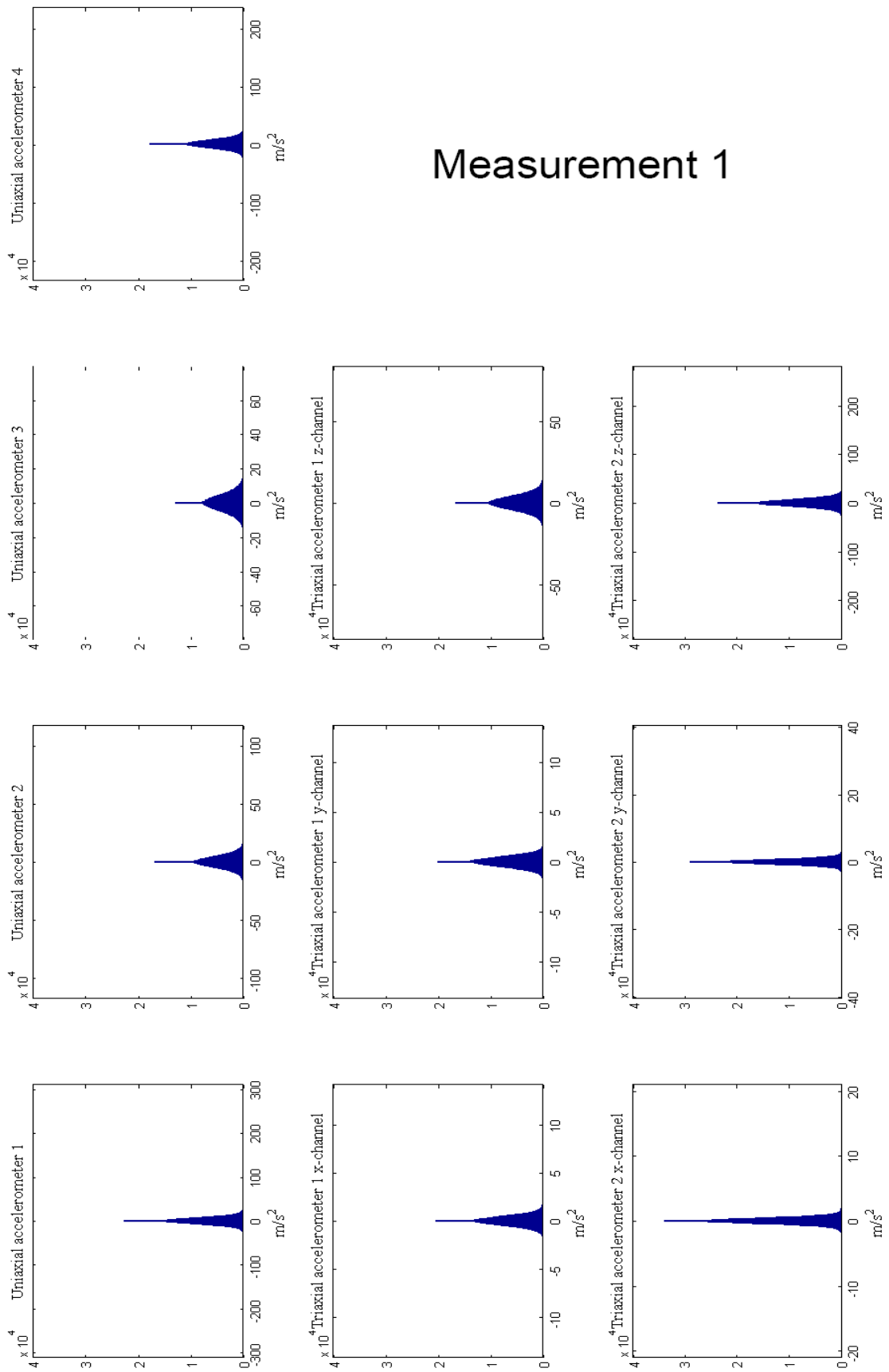


Figure B - 24: OMA sequence 1, histogram.

## Measurement 2

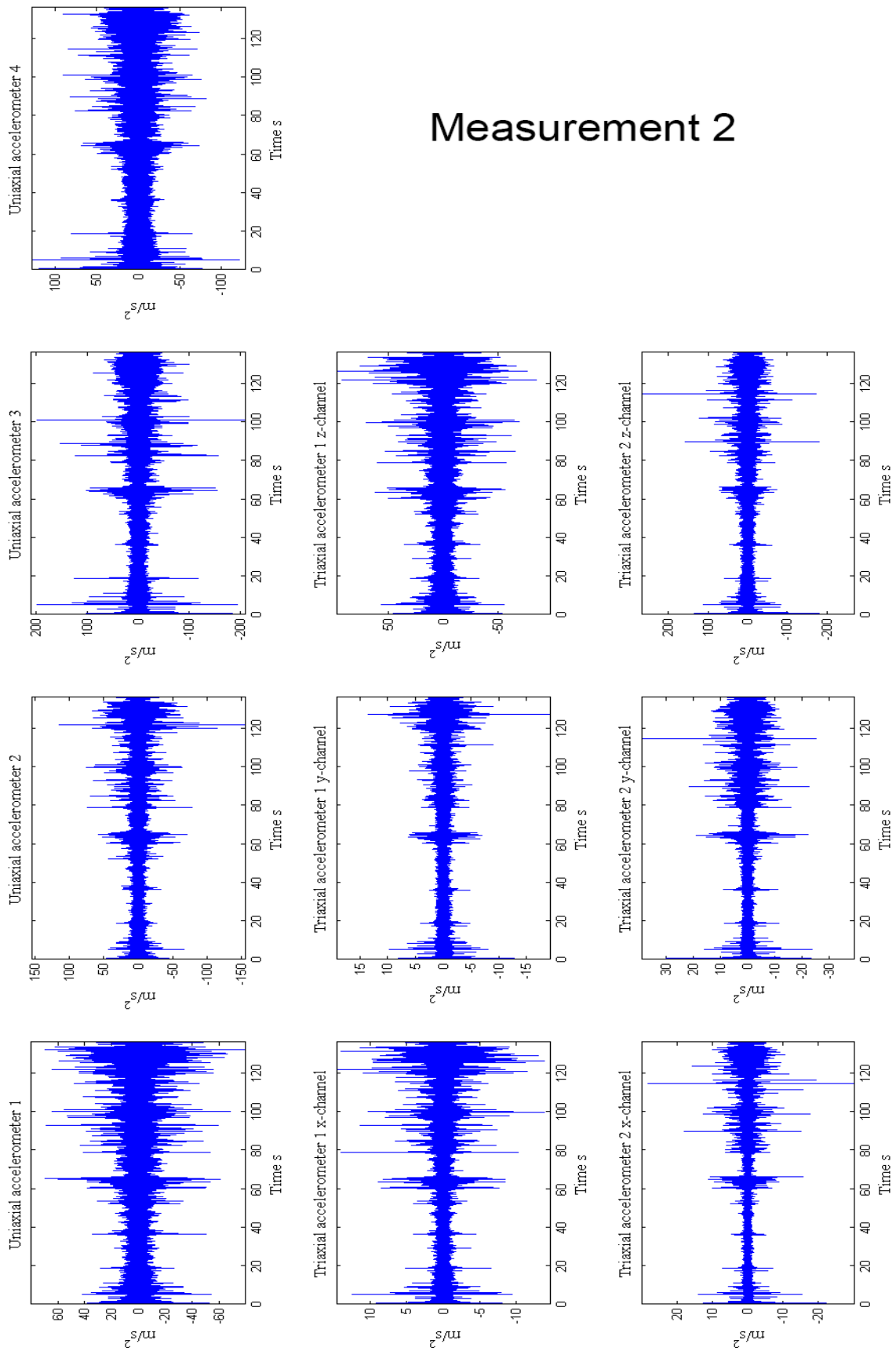


Figure B - 25: OMA sequence 2, time signal.

## Measurement 2

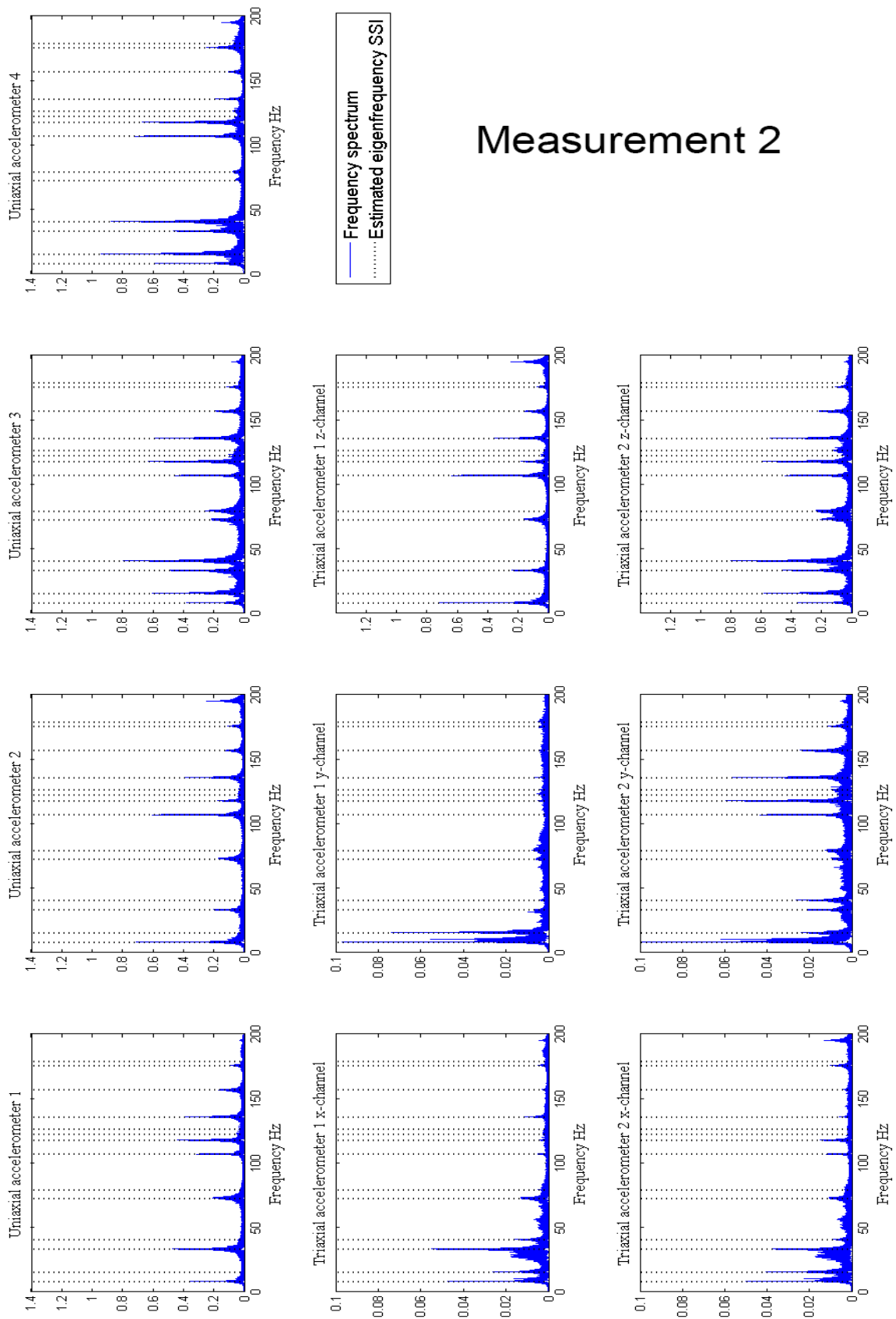


Figure B - 26: OMA sequence 2, frequency domain.

## Measurement 2

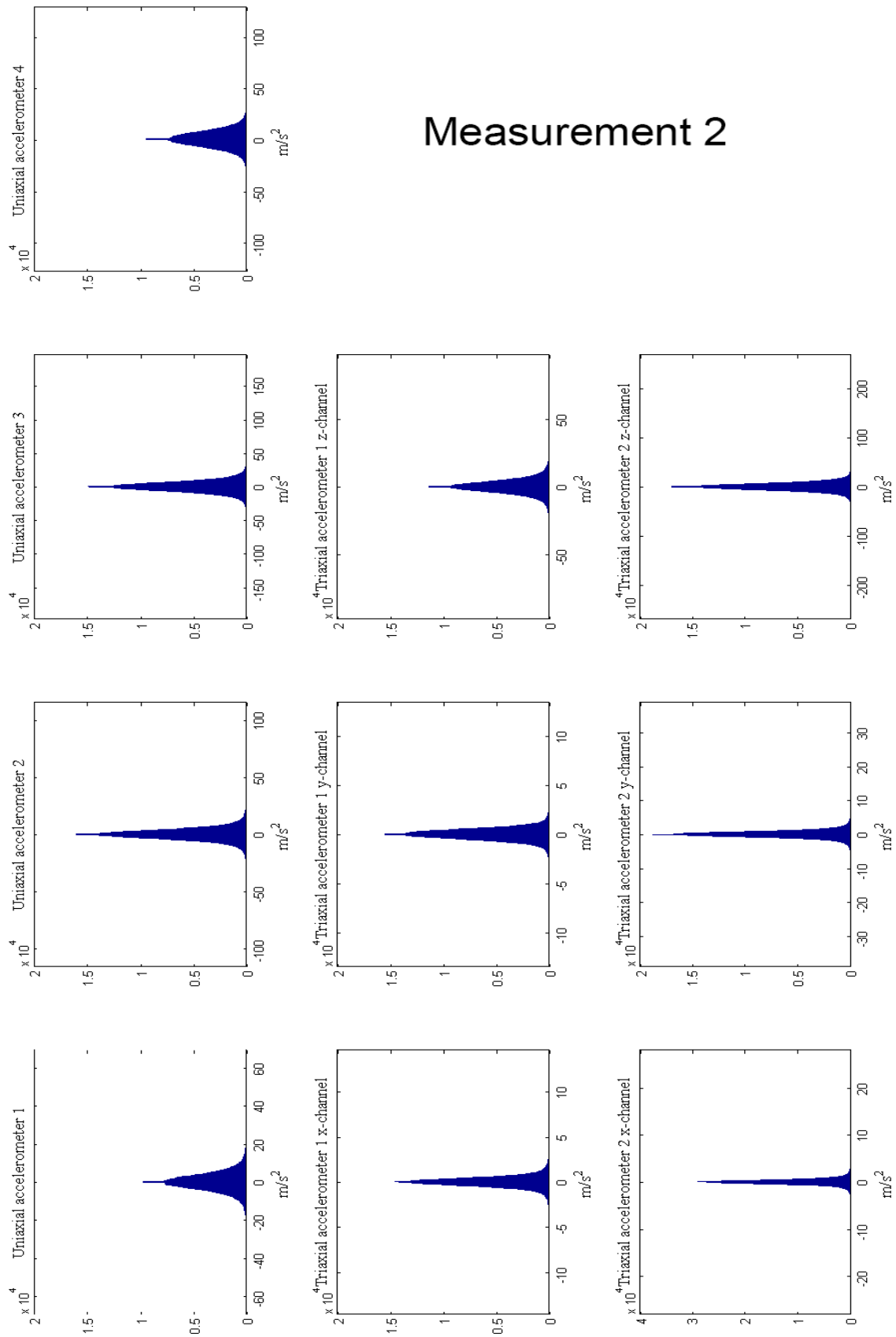


Figure B - 27: OMA sequence 2, histogram.

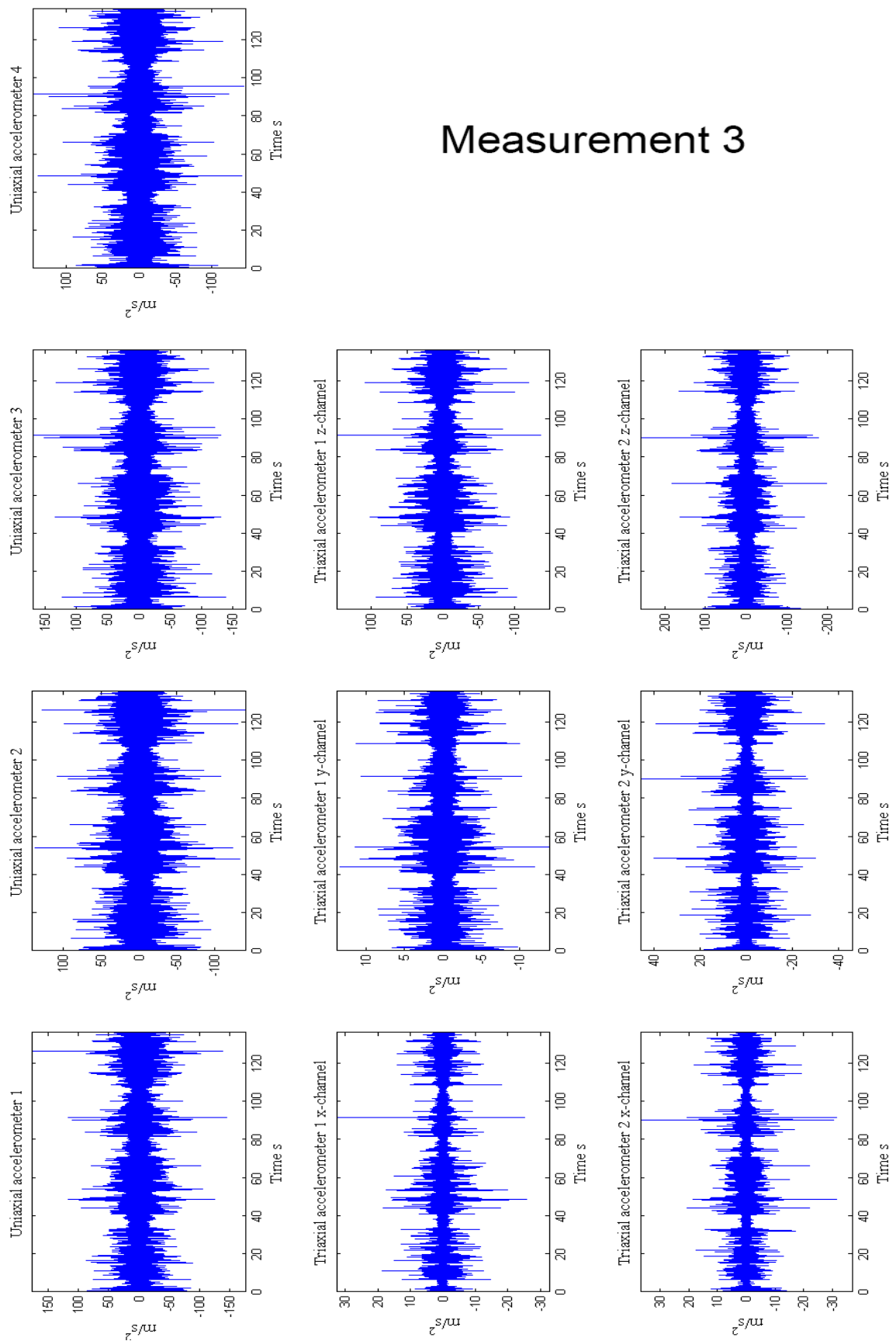


Figure B - 28: OMA sequence 3, time signal.

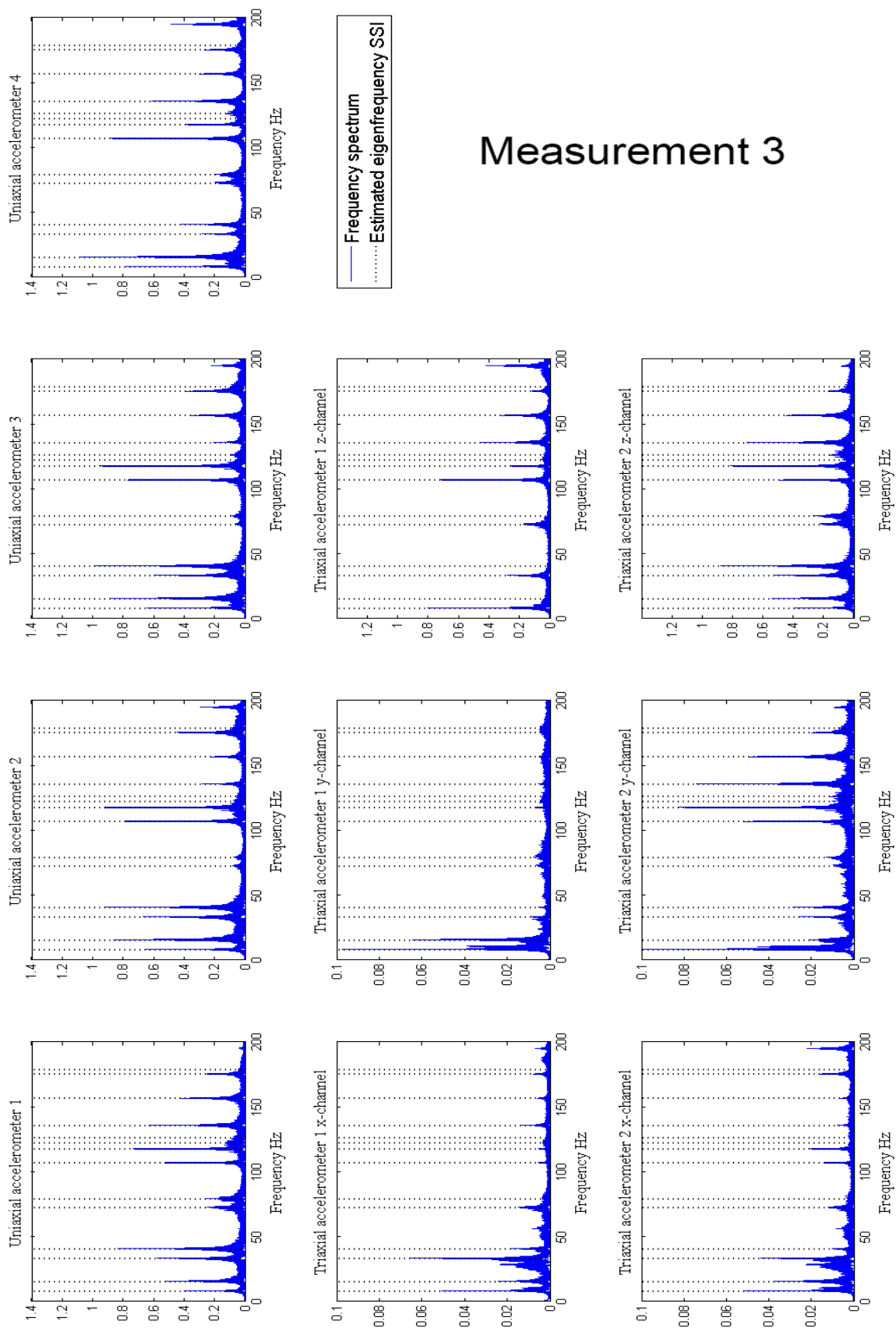


Figure B - 29: OMA sequence 3, frequency domain.

### Measurement 3

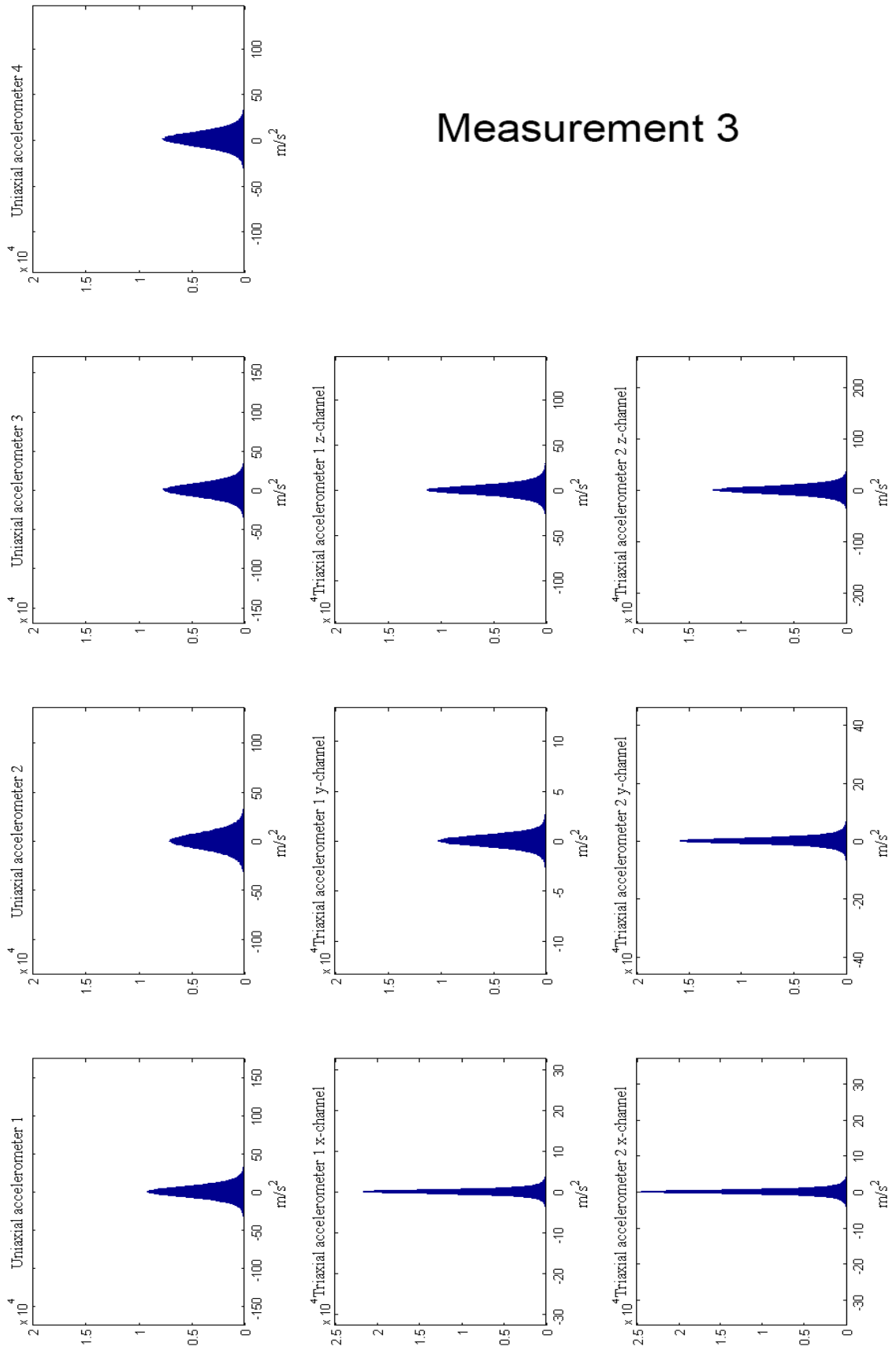


Figure B - 30: OMA sequence 3, histogram.

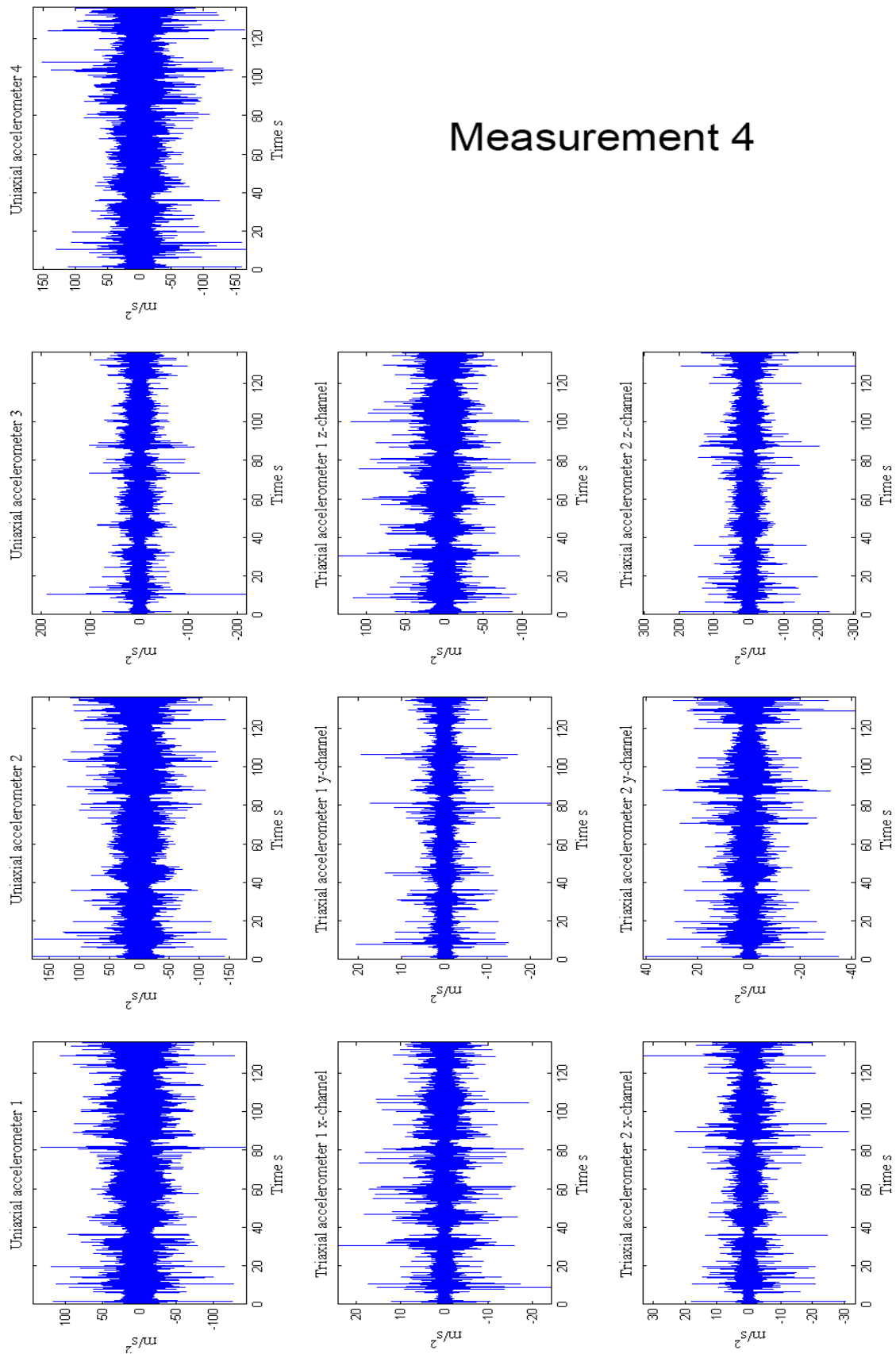


Figure B - 31: OMA sequence 4, time signal.

# Measurement 4

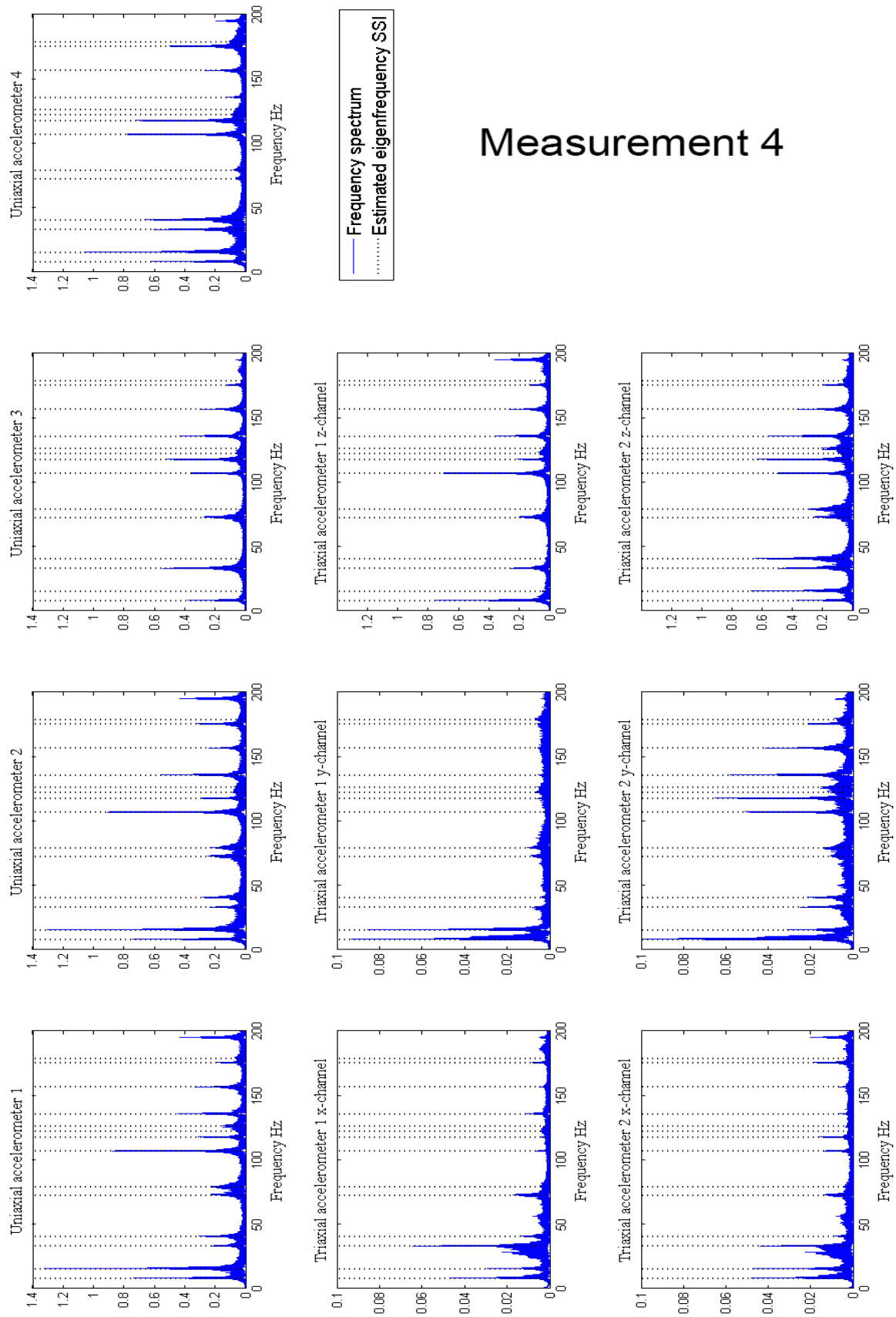


Figure B - 32: OMA sequence 4, frequency domain.

# Measurement 4

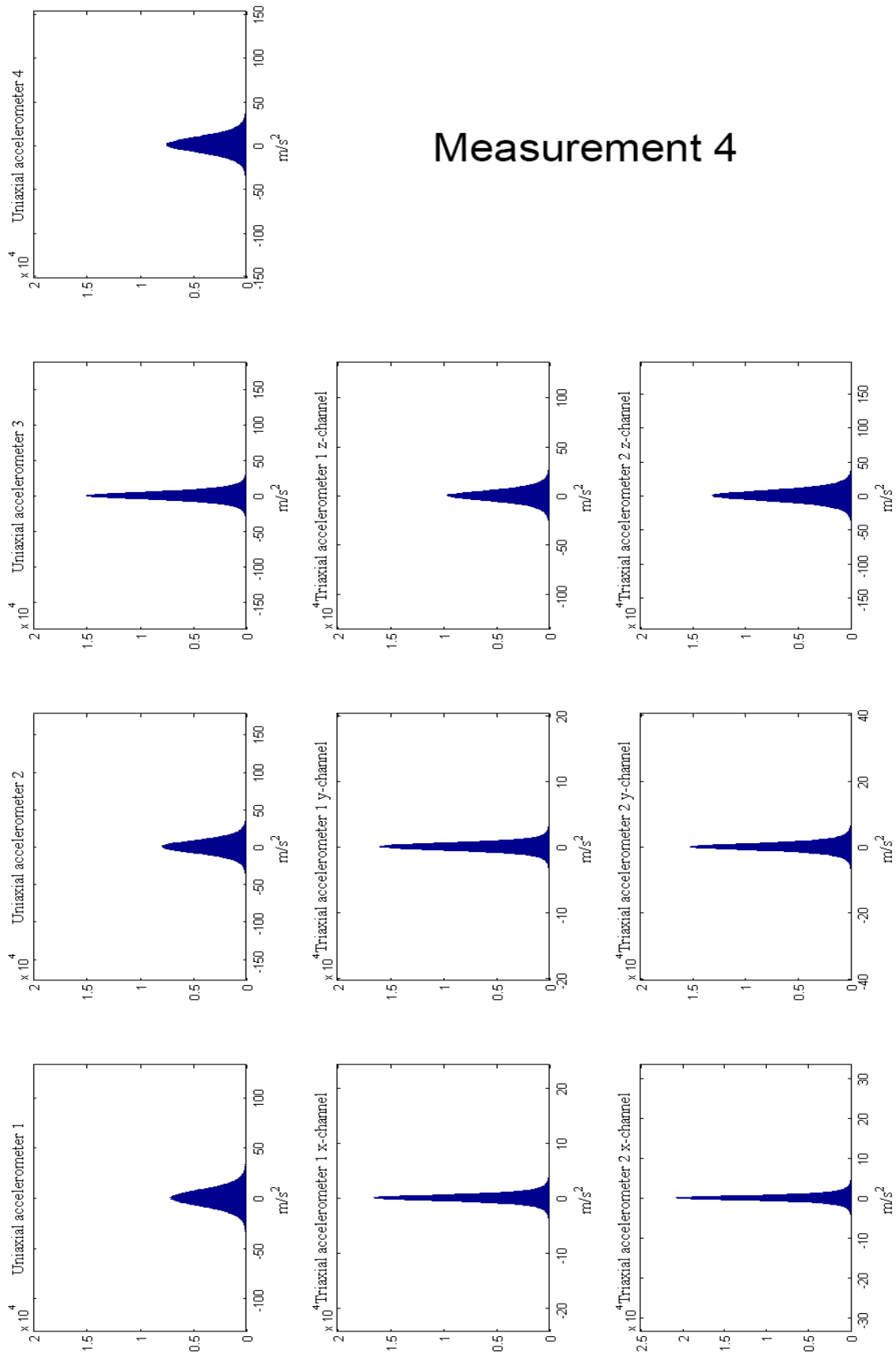
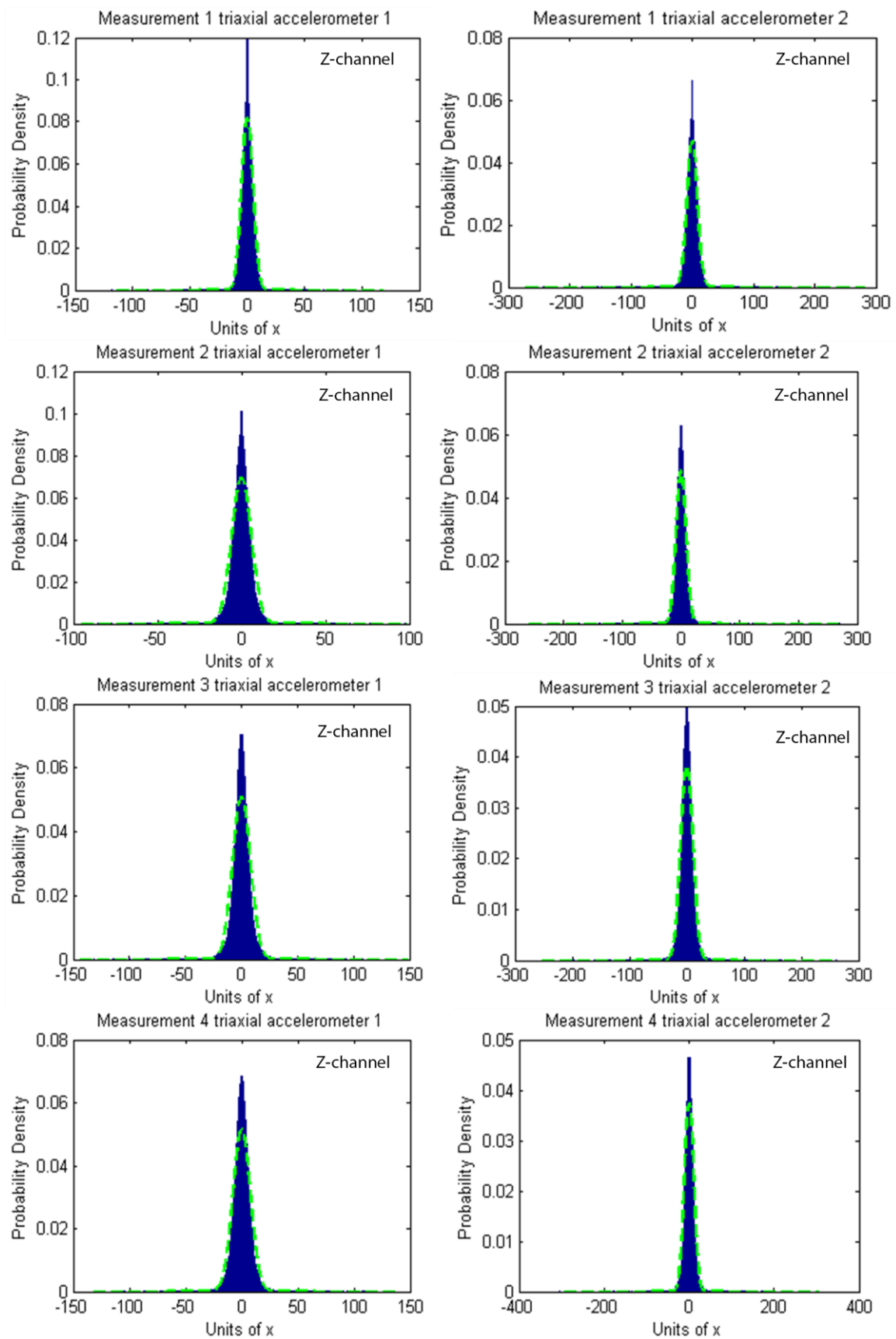


Figure B - 33: OMA sequence 4, histogram.



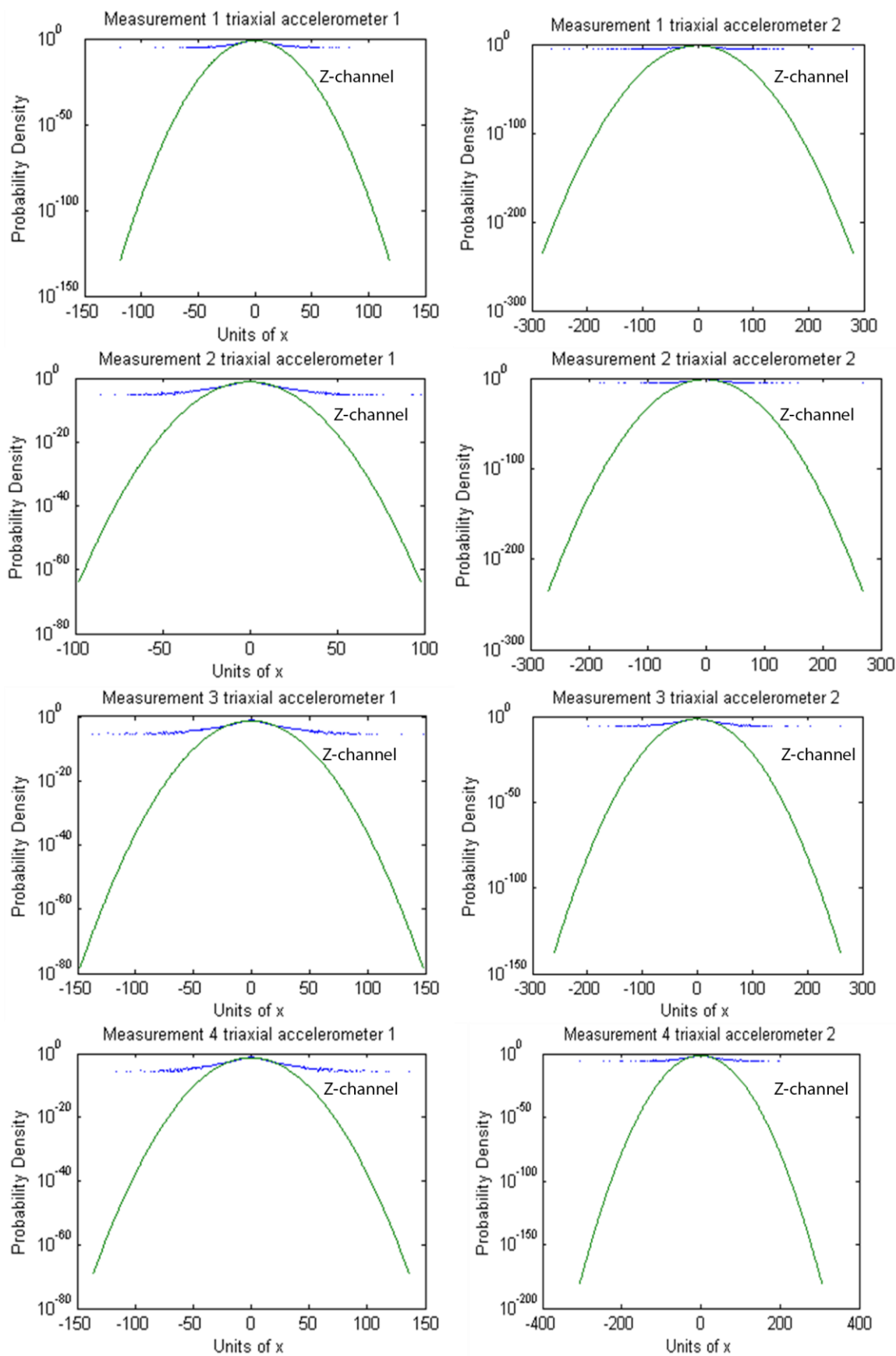


Figure B - 35: Probability density, logarithmic plot (triaxial accelerometer 1 and 2 z-channel).

# Appendix C

The results obtained from the OMA with finer grid are given in Figure C - 2, Figure C - 3, Table C - 1, Figure C - 4-Figure C - 11 and Table C - 2-Table C - 5. Exported modes to Pulse Reflex are presented in Figure C - 12-Figure C - 19. Time signals, frequency plots and histograms for the nine measurement sequences are presented in Figure C - 20-Figure C - 22.

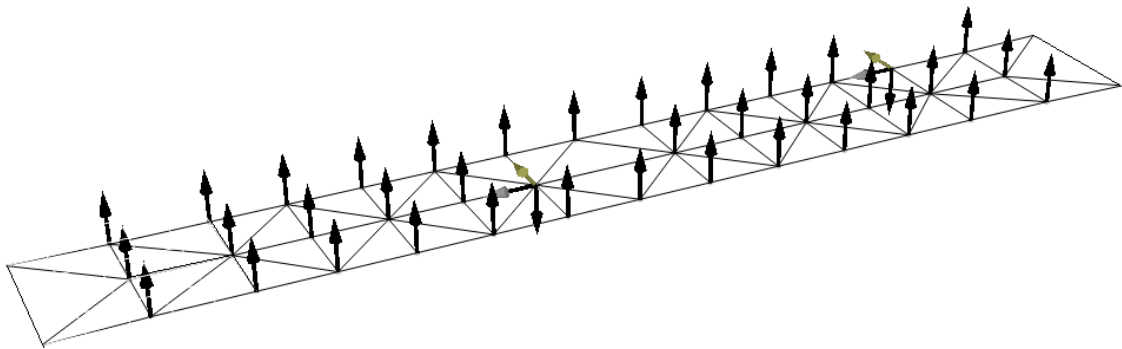


Figure C - 1: 3D representation of OMA with finer grid (see Figure 7.27).

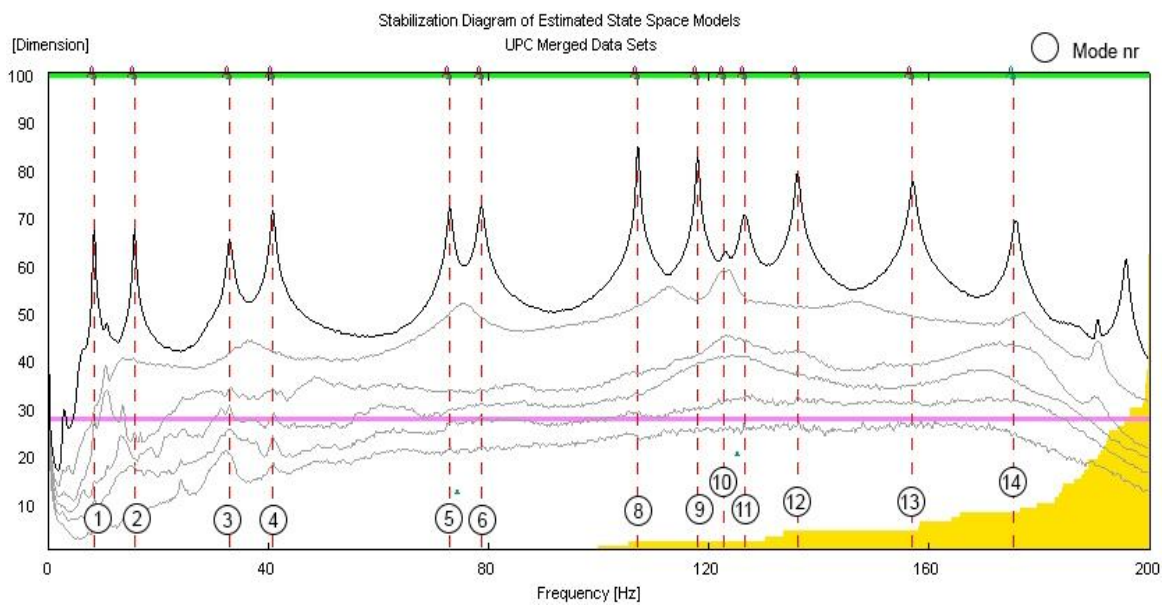


Figure C - 2: Stabilization diagram (SSI), 0-200 Hz.

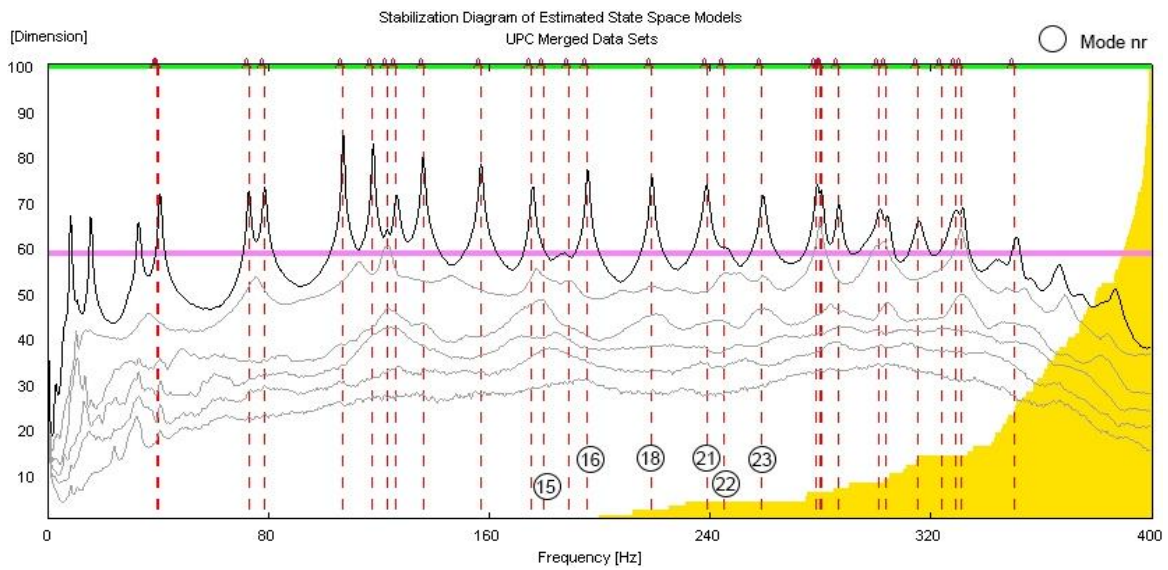


Figure C - 3: Stabilization diagram (SSI), 0-400 Hz.

Table C - 1: OMA results.

Mode	Eigenfrequency SSI (Hz)	Damping SSI (%)	Eigenfrequency EFDD (Hz)	Damping EFDD (%)
1	8,47	1,44	8,43	1,51
2	15,76	0,63	15,77	0,94
3	33,05	1,85	33,05	1,14
4	40,86	0,60	40,87	0,62
5	73,01	0,37	72,99	0,42
6	78,66	0,51	78,73	0,50
7	-	-	-	-
8	107,10	0,09	107,20	0,13
9	117,90	0,10	118,00	0,15
10	122,90	1,03	123,00	0,35
11	126,50	0,49	126,60	0,55
12	136,10	0,20	136,10	0,22
13	157,00	0,23	157,10	0,23
14	175,40	0,29	173,70	0,23
15	179,80	2,87	-	-
16	195,40	0,21	195,80	0,19
17	-	-	-	-
18	218,80	0,31	219,00	0,19
19	-	-	-	-
20	-	-	-	-
21	238,70	0,50	238,70	0,29
22	245,00	4,54	-	-
23	258,80	0,42	259,3	0,29

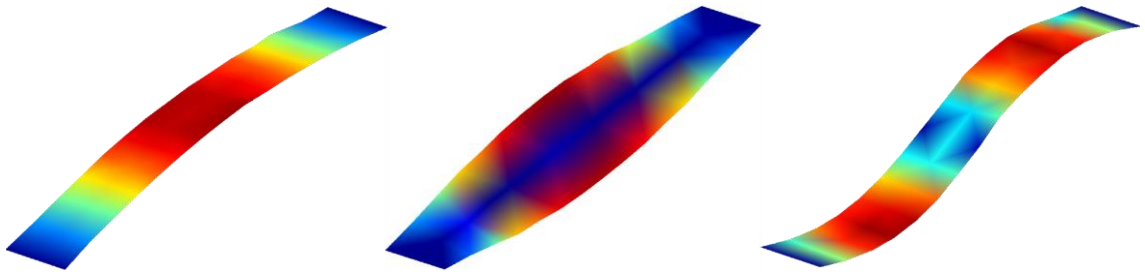


Figure C - 4: Mode 1: 8.47 Hz

Mode 2: 15.76 Hz

Mode 3: 33.05 Hz

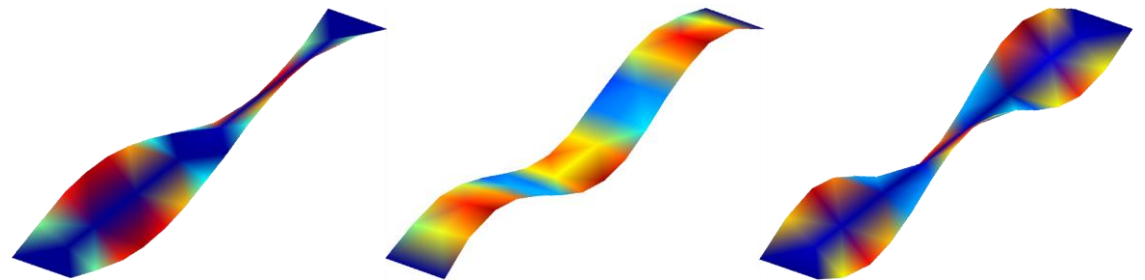


Figure C - 5: Mode 4: 40.86 Hz

Mode 5: 73.01 Hz

Mode 6: 78.66 Hz

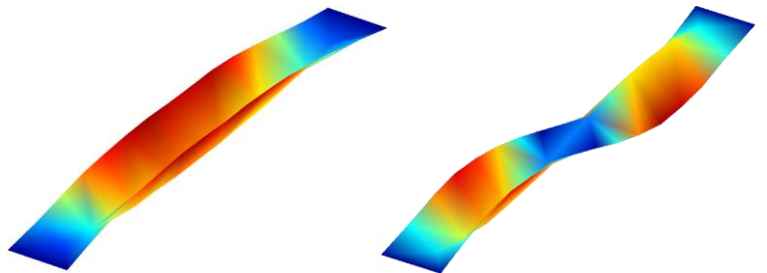


Figure C - 6: Mode 7: -

Mode 8: 107.10 Hz

Mode 9: 117.90 Hz

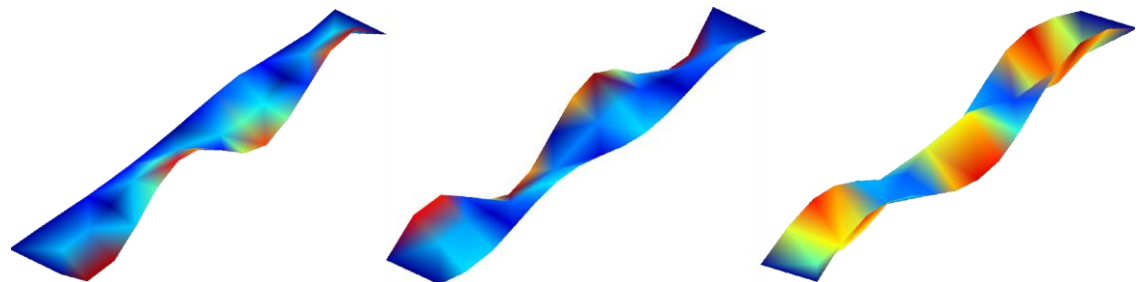


Figure C - 7: Mode 10: 122.90 Hz

Mode 11: 126.50 Hz

Mode 12: 136.10 Hz

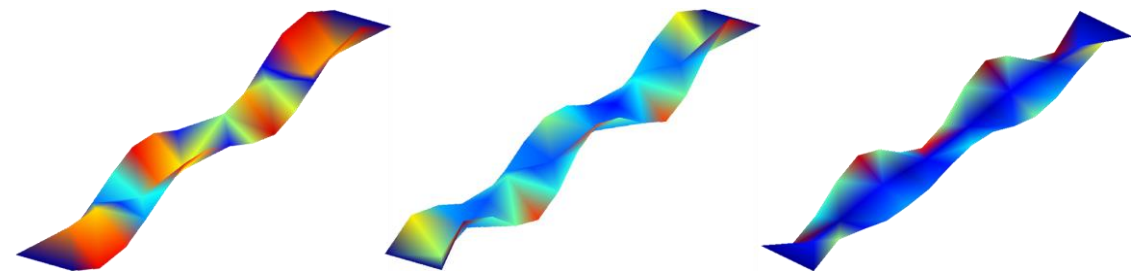


Figure C - 8: Mode 13: 157.00 Hz

Mode 14: 175.40 Hz

Mode 15: 179.80 Hz

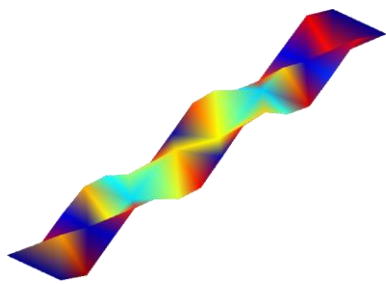
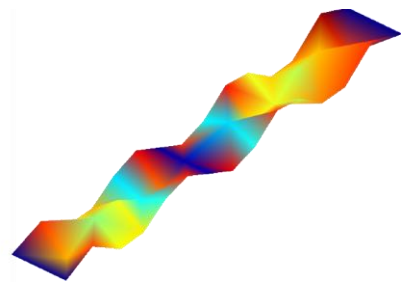
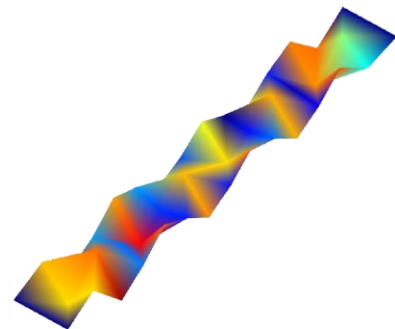


Figure C - 9: Mode 16: 195.40 Hz



Mode 18: 218.80 Hz

Mode 17: -



Mode 21: 238.70 Hz

Figure C - 10: Mode 19: -

Mode 20: -

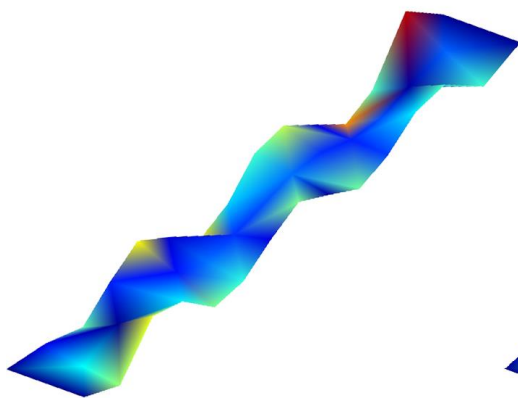
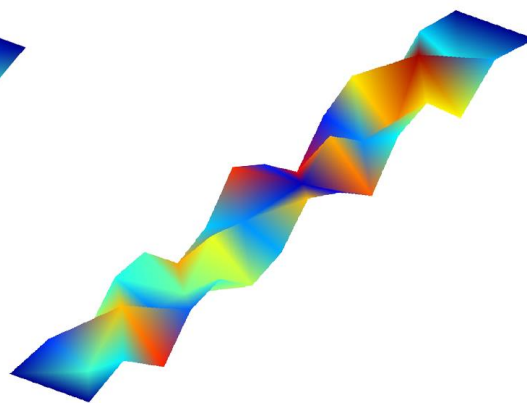


Figure C - 11: Mode 22: 245.00 Hz



Mode 23: 258.80 Hz

Exporting the modes in Figure C - 4-Figure C - 11 to Pulse Reflex gives another view of the extracted modes (see Figure C - 12-Figure C - 19).

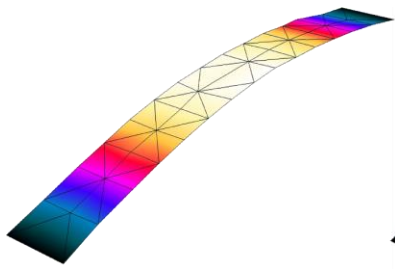
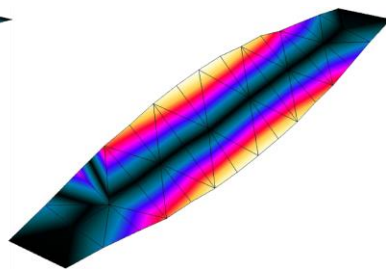
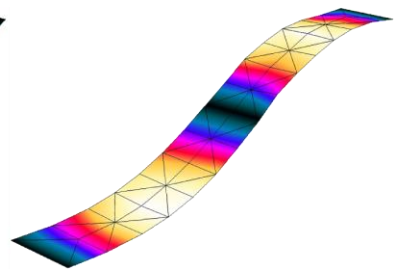


Figure C - 12: Mode 1: 8.47 Hz



Mode 2: 15.76 Hz



Mode 3: 33.05 Hz

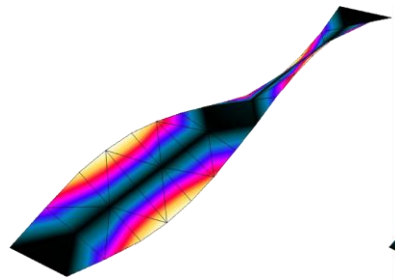
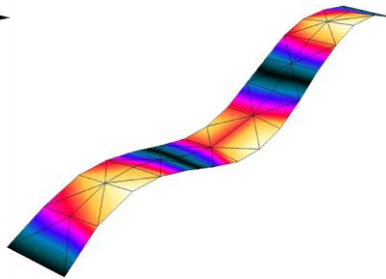
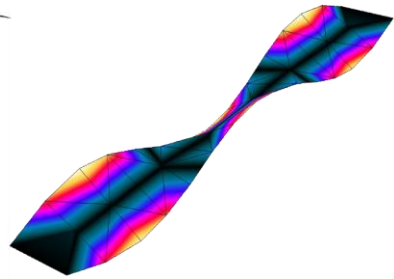


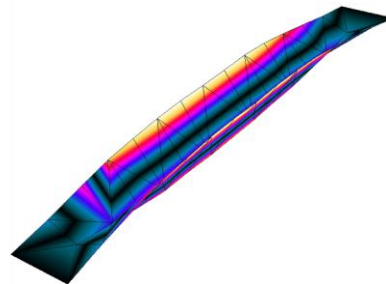
Figure C - 13: Mode 4: 40.86 Hz



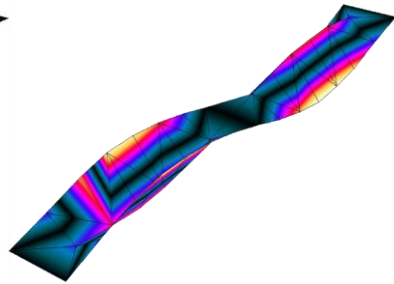
Mode 5: 73.01 Hz



Mode 6: 78.66 Hz



Mode 8: 107.10 Hz



Mode 9: 117.90 Hz

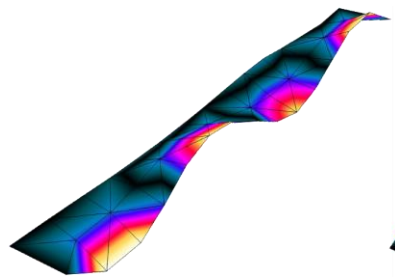
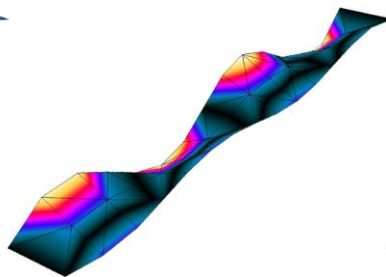
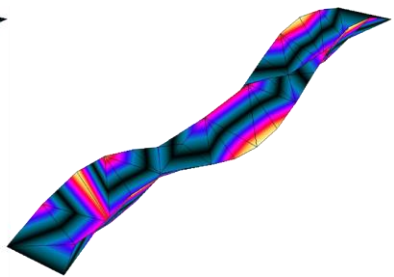


Figure C - 15: Mode 10: 122.90 Hz



Mode 11: 126.50 Hz



Mode 12: 136.10 Hz

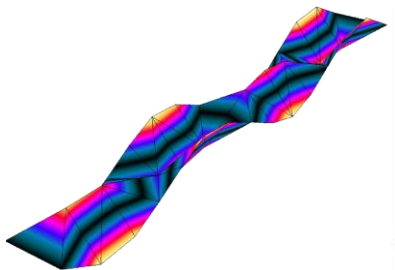
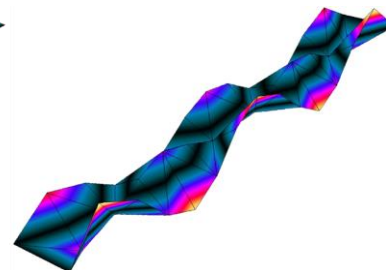
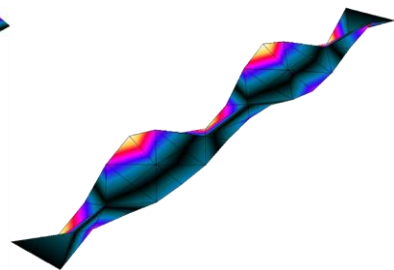


Figure C - 16: Mode 13: 157.00 Hz



Mode 14: 175.40 Hz



Mode 15: 179.80 Hz



Figure C - 17: Mode 16: 195.40 Hz

Mode 17: -



Mode 18: 218.80 Hz

Figure C - 18: Mode 19: -

Mode 20: -



Mode 21: 238.70 Hz

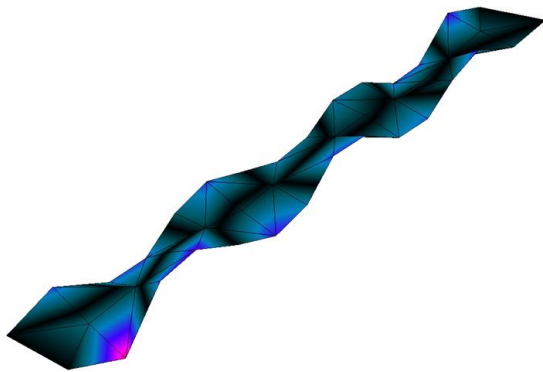
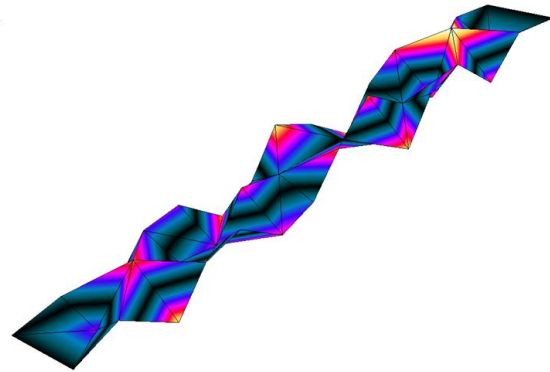


Figure C - 19: Mode 22: 245.00 Hz



Mode 23: 258.80 Hz

Appendix C

Table C - 2: MAC between SSI and EFDD.

Nr	Nr \ EFDD	1	2	3	4	5	6	8	9	10	11	12	13	14
	SSI	8,43	15,77	33,05	40,87	72,99	78,73	107,20	118,00	123,00	126,60	136,10	157,10	173,70
1	8,47	<b>1,000</b>	0,000	0,000	0,000	0,000	0,000	<b>0,256</b>	0,000	0,003	0,000	0,004	0,000	0,000
2	15,76	0,000	<b>1,000</b>	0,000	0,000	0,000	0,001	0,000	0,000	0,004	0,000	0,000	0,000	0,001
3	33,05	0,000	0,000	<b>0,994</b>	0,002	0,001	0,000	0,000	<b>0,201</b>	0,013	0,000	0,000	0,002	0,002
4	40,86	0,000	0,000	0,002	<b>0,999</b>	0,000	0,000	0,000	0,000	0,003	0,006	0,000	0,000	0,000
5	73,01	0,000	0,000	0,000	0,000	<b>0,999</b>	0,001	0,003	0,000	0,000	0,001	<b>0,257</b>	0,001	0,013
6	78,66	0,000	0,001	0,000	0,000	0,001	<b>0,997</b>	0,000	0,000	0,004	0,002	0,001	0,000	0,001
8	107,10	<b>0,254</b>	0,000	0,000	0,000	0,003	0,000	<b>0,999</b>	0,000	0,002	0,000	0,000	0,000	0,008
9	117,90	0,000	0,000	<b>0,205</b>	0,000	0,000	0,000	0,000	<b>0,999</b>	<b>0,076</b>	0,006	0,000	0,006	0,004
10	122,90	0,000	0,000	0,002	0,003	0,002	0,002	0,001	0,017	<b>0,908</b>	<b>0,051</b>	0,005	<b>0,090</b>	0,012
11	126,50	0,000	0,000	0,000	0,003	0,001	0,000	0,000	0,001	0,025	<b>0,981</b>	0,003	<b>0,058</b>	0,000
12	136,10	0,005	0,000	0,000	0,000	<b>0,249</b>	0,002	0,000	0,000	0,003	0,003	<b>0,999</b>	0,000	0,017
13	157,00	0,000	0,000	0,000	0,000	0,001	0,000	0,000	0,003	<b>0,105</b>	<b>0,067</b>	0,001	<b>0,996</b>	0,006
14	175,40	0,001	0,001	0,000	0,000	0,005	0,000	0,002	0,000	0,000	0,000	0,002	0,001	<b>0,915</b>

Table C - 3: MAC between SSI and EFDD.

Nr	Nr \ EFDD	16	18	21	23
	SSI	195,80	219,00	238,70	259,30
15	179,80	0,000	0,005	0,002	0,001
16	195,40	<b>0,997</b>	0,001	0,006	0,000
18	218,80	0,000	<b>0,996</b>	0,001	0,008
21	238,70	0,004	0,001	<b>0,991</b>	0,001
22	245,00	0,023	0,004	0,006	0,009
23	258,80	0,000	0,007	0,001	<b>0,989</b>

Table C - 4: MAC between OMA (SSI) and ABAQUS.

Nr	Nr \ OMA	1	2	3	4	5	6	8	9	10	11	12	13	14
	ABAQUS	8,47	15,76	33,05	40,86	73,01	78,66	107,06	117,94	122,85	126,47	136,06	156,98	175,44
1	8,22	<b>0,997</b>	0,000	0,000	0,000	0,000	0,000	<b>0,258</b>	0,000	0,000	0,000	0,004	0,000	0,001
2	13,97	0,000	<b>0,984</b>	0,000	0,012	0,000	0,003	0,000	0,000	0,000	0,000	0,000	0,000	0,000
3	32,47	0,000	0,000	<b>0,989</b>	0,001	0,000	0,001	0,000	<b>0,241</b>	0,002	0,000	0,000	0,000	0,000
4	38,24	0,000	0,014	0,003	<b>0,973</b>	0,000	0,009	0,000	0,000	0,006	0,006	0,000	0,000	0,000
5	71,05	0,000	0,000	0,001	0,000	<b>0,961</b>	0,005	0,000	0,001	0,004	0,002	<b>0,374</b>	0,002	0,004
6	74,47	0,000	0,000	0,000	0,011	0,014	<b>0,975</b>	0,000	0,000	0,000	0,003	0,000	0,000	0,001
7	101,65	0,000	0,040	0,000	0,039	0,003	<b>0,131</b>	0,000	0,000	<b>0,223</b>	<b>0,375</b>	0,001	0,000	0,003
8	106,88	<b>0,259</b>	0,000	0,000	0,000	0,007	0,000	<b>0,995</b>	0,000	0,002	0,001	0,001	0,000	0,000
9	114,97	0,000	0,000	<b>0,192</b>	0,000	0,000	0,000	0,000	<b>0,996</b>	0,019	0,001	0,001	0,004	0,000
10	117,54	0,000	0,000	0,004	0,000	0,010	0,000	0,000	0,000	<b>0,391</b>	<b>0,222</b>	0,023	<b>0,568</b>	0,007
11	120,87	0,000	0,001	0,000	0,000	0,000	0,011	0,000	0,000	<b>0,473</b>	<b>0,711</b>	0,002	0,000	0,000
12	128,22	0,003	0,000	0,000	0,000	<b>0,218</b>	0,001	0,002	0,000	0,010	0,001	<b>0,976</b>	0,014	0,002
13	147,41	0,000	0,000	0,001	0,000	0,003	0,000	0,000	0,006	0,042	0,025	0,002	<b>0,884</b>	<b>0,088</b>
14	152,56	0,000	0,000	0,000	0,000	0,007	0,000	0,006	0,000	0,001	0,000	0,007	0,036	<b>0,865</b>

Table C - 5: MAC between OMA (SSI) and ABAQUS.

	Nr	15	16	18	21	22	23
Nr	OMA	179,76	195,45	218,81	238,73	244,71	258,80
	ABAQUS						
15	166,58	<b>0,807</b>	0,000	0,000	0,002	0,017	0,001
16	173,75	0,001	<b>0,882</b>	0,013	0,011	<b>0,065</b>	0,001
17	181,53	0,002	<b>0,588</b>	0,021	0,032	0,015	0,001
18	197,54	0,007	0,001	<b>0,889</b>	0,022	0,004	<b>0,060</b>
19	206,62	0,000	0,002	0,000	0,016	<b>0,375</b>	0,002
20	217,53	0,018	0,017	<b>0,092</b>	<b>0,442</b>	0,001	0,029
21	221,84	0,002	0,005	0,002	<b>0,825</b>	0,001	0,008
22	239,37	0,001	0,000	0,000	0,002	<b>0,361</b>	0,007
23	245,62	0,000	0,000	0,019	0,001	0,001	<b>0,800</b>

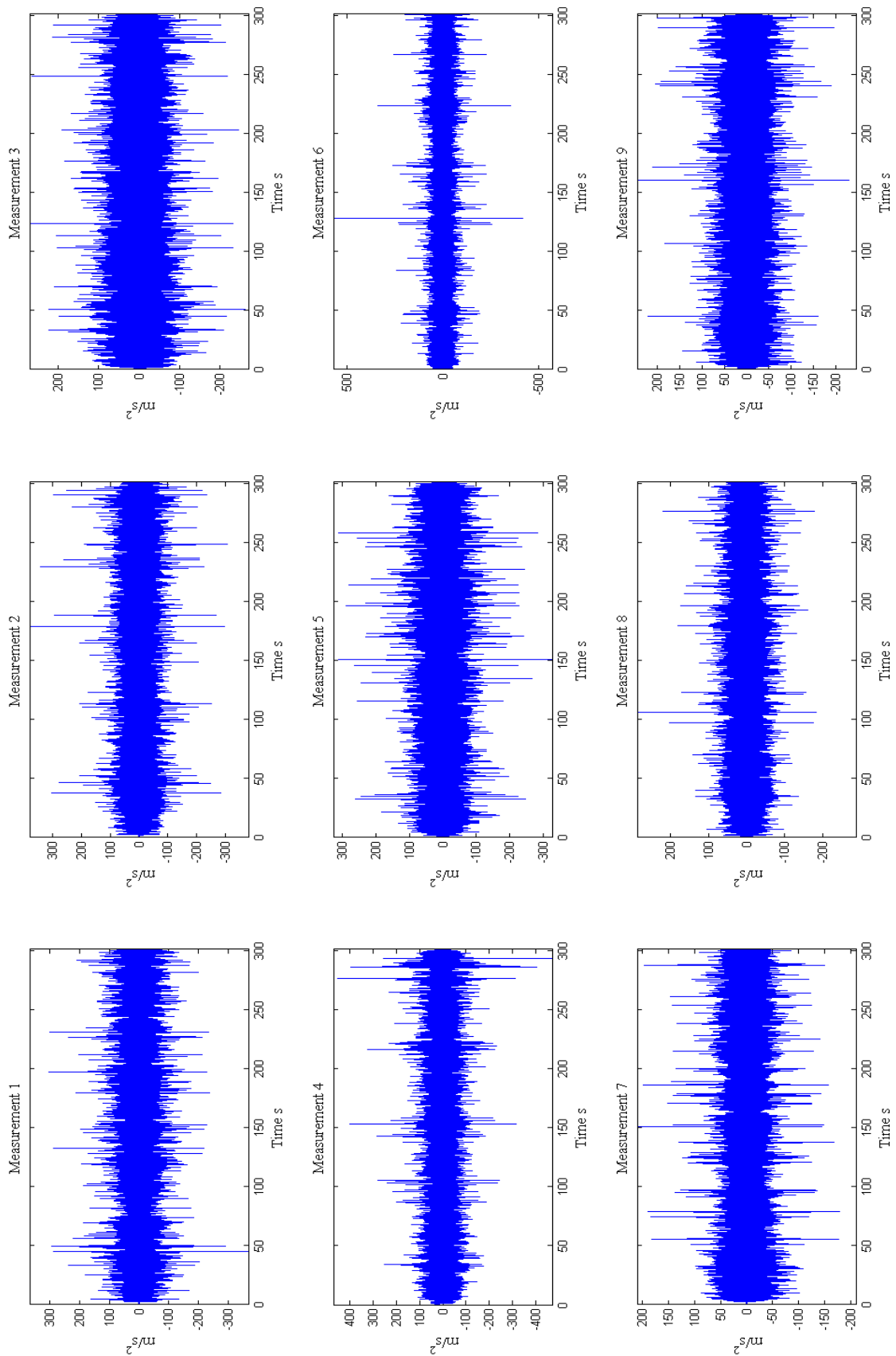


Figure C - 20: Time plots for reference accelerometer 2 z-channel, all 9 measurements.

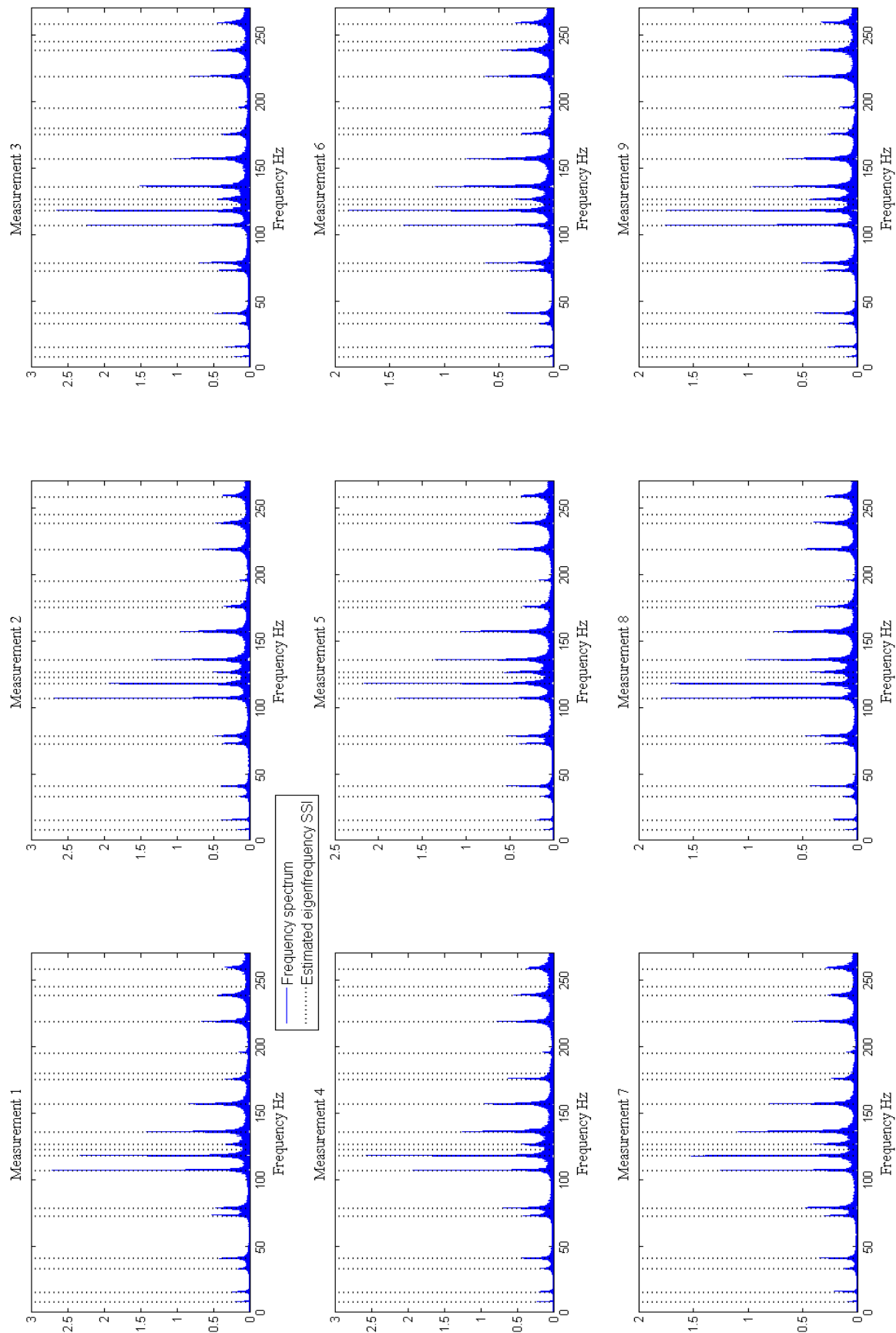


Figure C - 21: Frequency plots for reference accelerometer 2 z-channel, all 9 measurements.

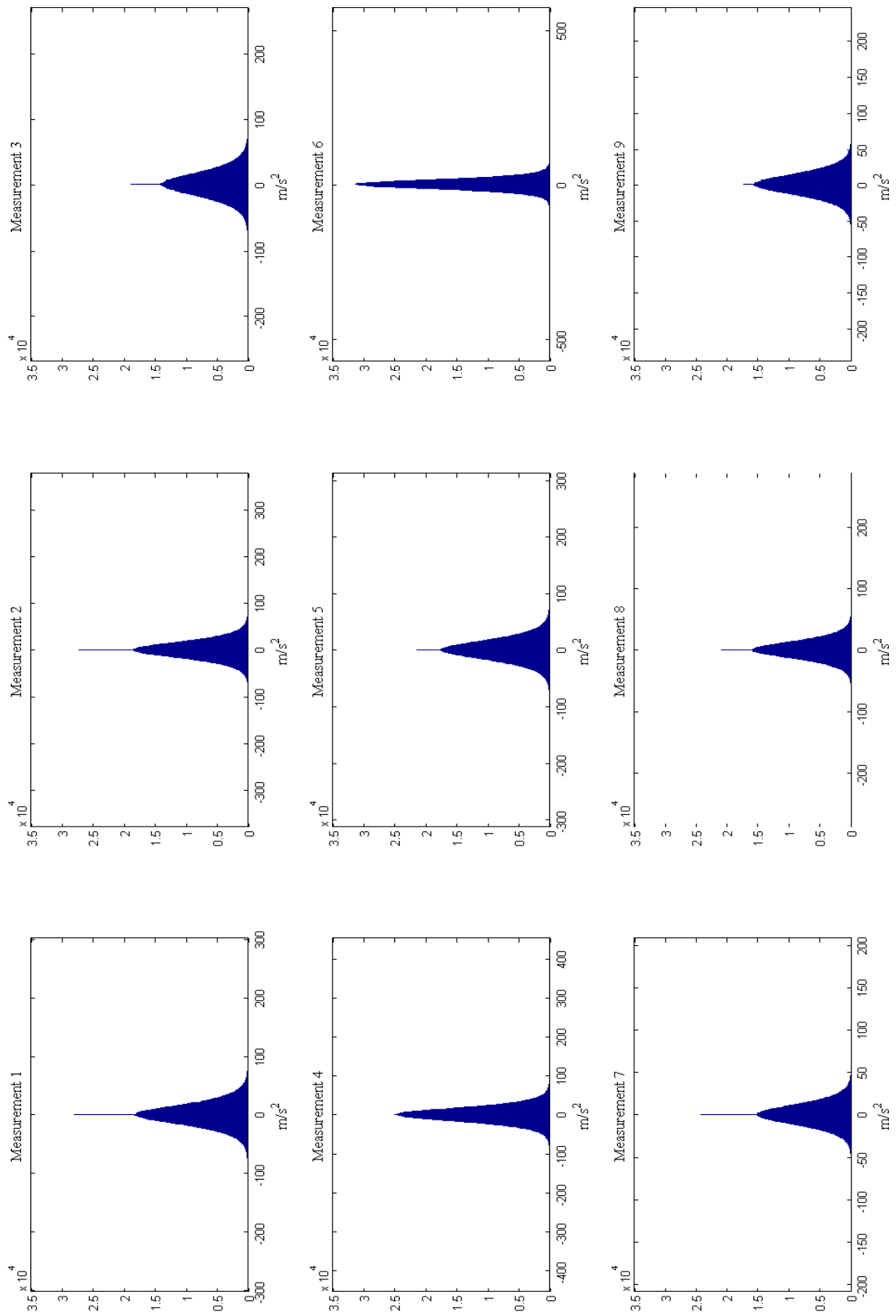


Figure C - 22: Histograms for reference accelerometer 2 z-channel, all 9 measurements.



# Appendix D

The results obtained from the mass loaded structure are presented in this chapter. The masses are placed in a symmetrical pattern which can be viewed in Figure D - 1. The weights of the mass cylinders are given in Table D - 1.

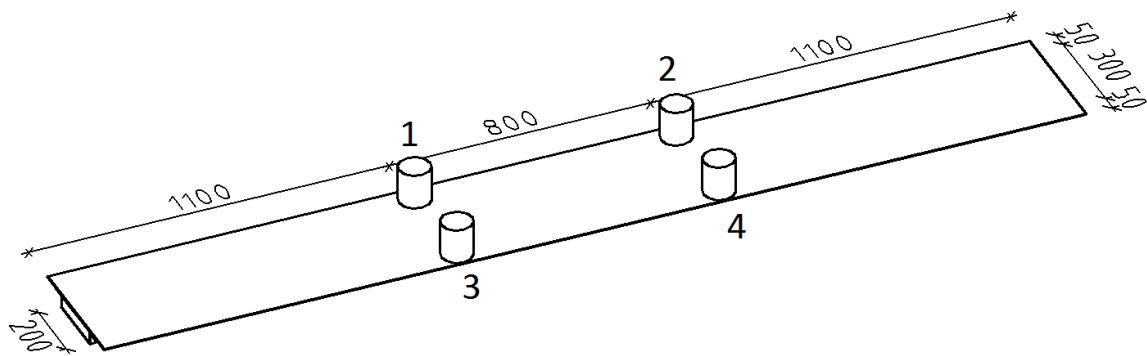


Figure D - 1: Steel structure with added mass cylinders [mm].

Table D - 1: Weight of the cylindrical masses.

Mass nr	Weight (kg)
1	5,428
2	5,450
3	5,444
4	5,436

## D.1 ABAQUS Results

The results obtained from the eigenvalue analysis in ABAQUS are presented in Table D - 2 and Figure D - 2-Figure D - 5.

Table D - 2: Results from the eigenvalue analysis in ABAQUS.

Mode	Eigenfrequency (Hz)
1	6,05
2	8,79
3	25,03
4	25,73
5	65,40
6	69,82
7	70,13
8	74,99
9	83,50
10	87,91
11	115,39
12	125,34

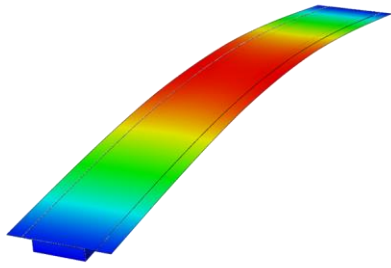
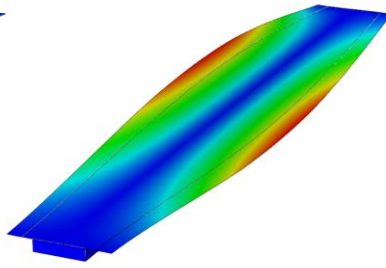
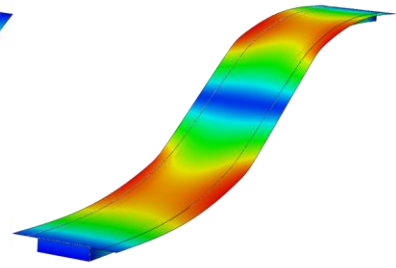


Figure D - 2: Mode 1: 6.05 Hz



Mode 2: 8.79 Hz



Mode 3: 25.03 Hz

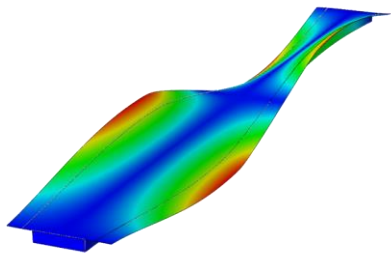
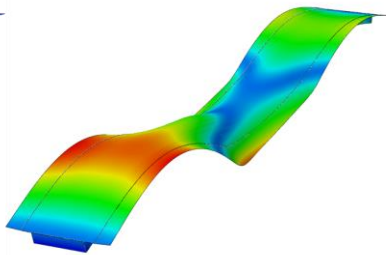
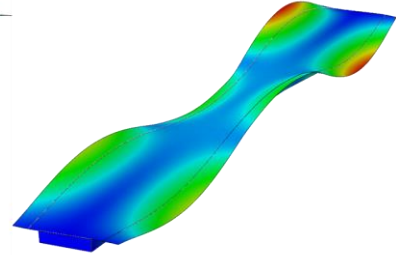


Figure D - 3: Mode 4: 25.73 Hz



Mode 5: 65.40 Hz



Mode 6: 69.82 Hz

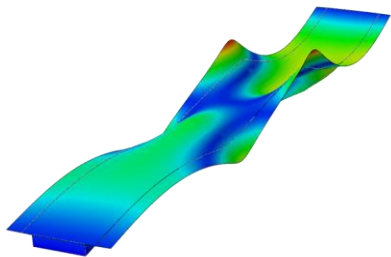
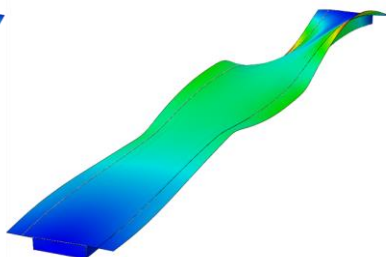
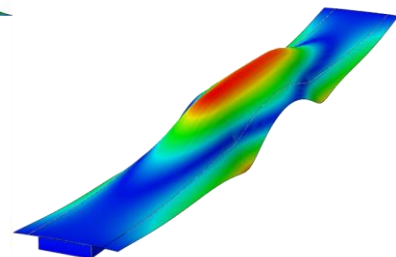


Figure D - 4: Mode 7: 70.13 Hz



Mode 8: 74.99 Hz



Mode 9: 83.50 Hz

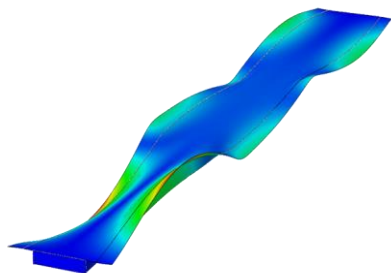
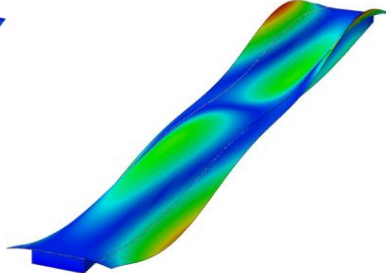
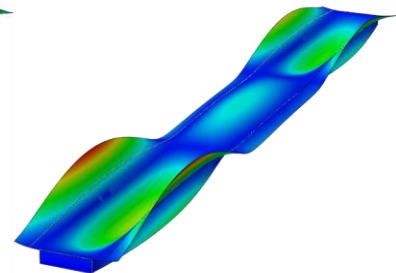


Figure D - 5: Mode 10: 87.91 Hz



Mode 11: 115.39 Hz



Mode 12: 125.34 Hz

## D.2 EMA Impact Hammer

The impact measurement on the structure with added masses was performed in the same way as the previous impact measurement described in section 7.1. But in this impact test the rubber tip was used instead of the plastic tip to prevent errors caused by excited modes outside the frequency range. By adding masses to the structure the eigenfrequencies will be lower and an impact with the rubber tip would contain all frequencies needed for this measurement. A double hit detector was used during the impacts to make sure that no faulty signals were used to compute the FRFs. The results are presented in Table D - 3, Figure D - 6, Figure D - 7-Figure D - 10 and Table D - 4.

Table D - 3: Results from impact measurement with mass loaded structure.

Mode	Eigenfrequency (Hz)	Damping (%)
1	6,22	10,32
2	9,52	7,73
3	24,76	4,43
4	25,87	2,62
5	79,86	2,57
6	83,02	1,49
7	95,83	1,02
8	98,69	2,00
9	121,13	0,92
10	-	-
11	127,17	0,78
12	138,64	0,65

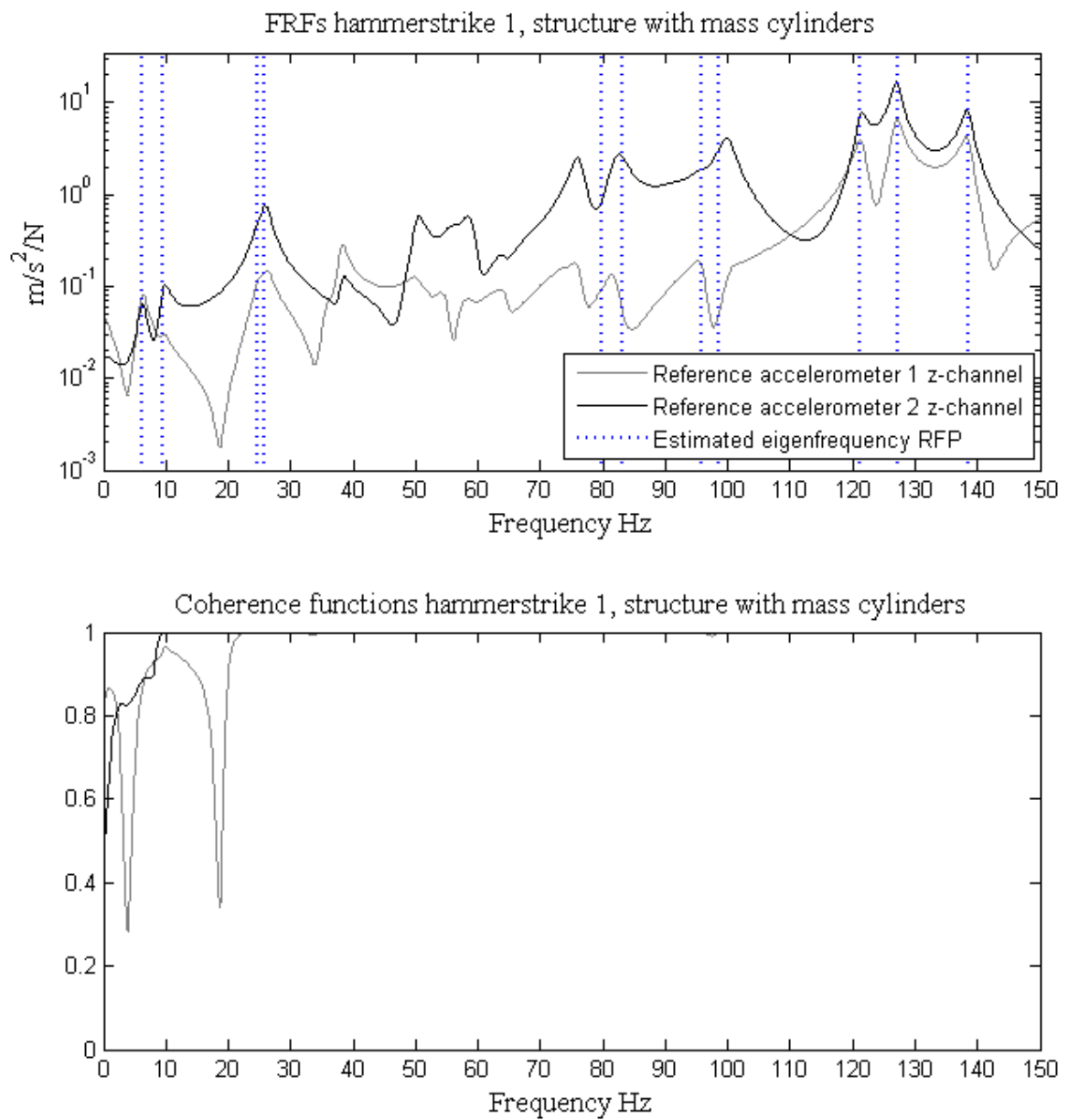


Figure D - 6: FRFs and coherence function obtained from hammer strike position 1.

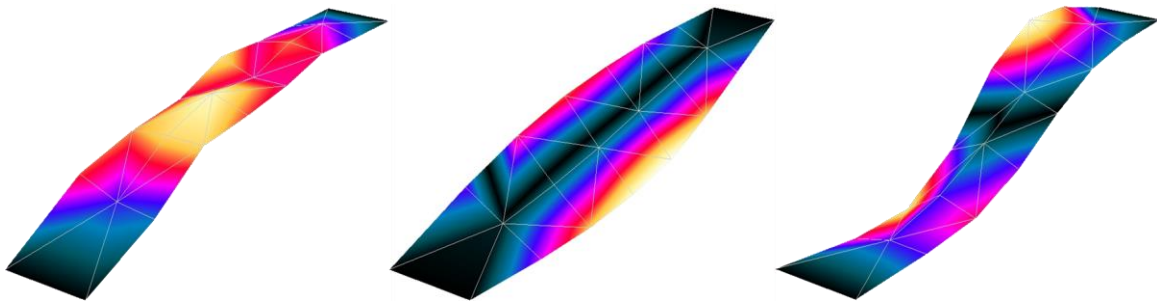


Figure D - 7: Mode 1: 6.22 Hz

Mode 2: 9.52 Hz

Mode 3: 24.76 Hz

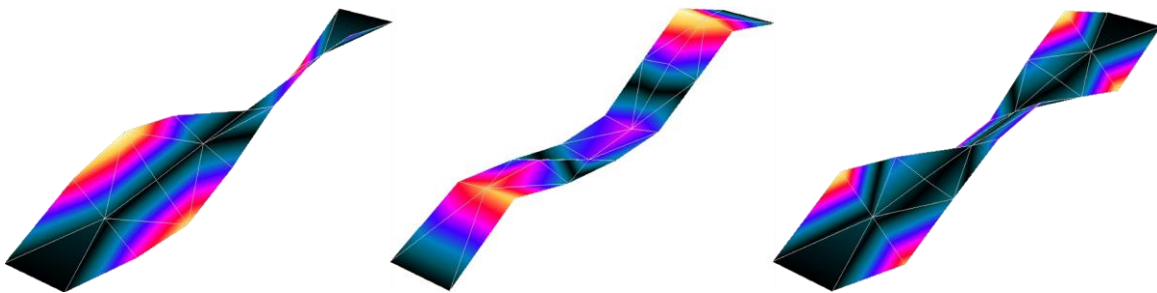


Figure D - 8: Mode 4: 25.87 Hz

Mode 5: 79.86 Hz

Mode 6: 83.02 Hz

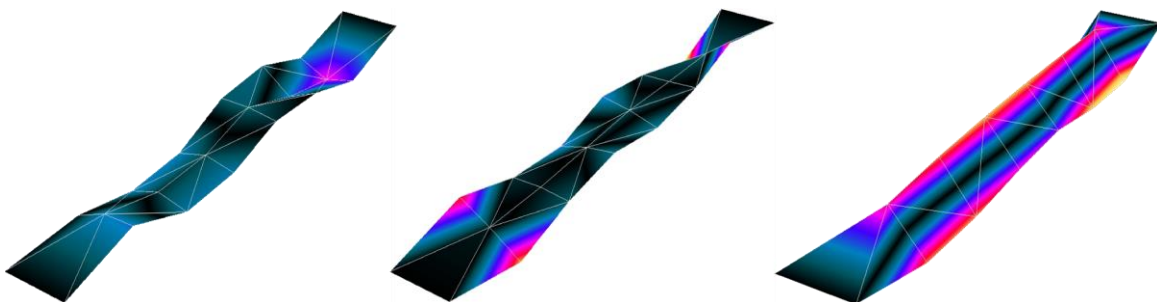


Figure D - 9: Mode 7: 95.83 Hz

Mode 8: 98.69 Hz

Mode 9: 121.27 Hz

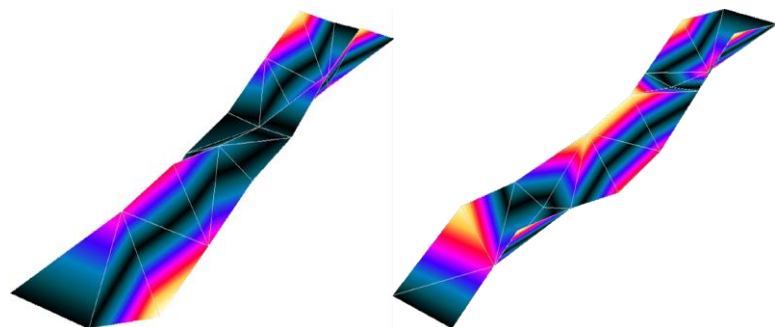


Figure D - 10: Mode 10: -

Mode 11: 127.17 Hz

Mode 12: 138.64 Hz

Table D - 4: MAC between impact measurement and numerical results.

Nr	Nr	1	2	3	4	5	6	7	8	9	11	12
	EMA Hammer	6,22	9,52	24,76	25,87	79,87	83,03	95,83	98,69	121,27	127,17	138,64
	ABAQUS											
1	6,05	<b>0,924</b>	0,025	0,003	0,007	0,041	0,008	0,032	0,005	<b>0,088</b>	0,000	0,007
2	8,79	0,001	<b>0,947</b>	0,004	0,008	0,003	0,009	<b>0,058</b>	0,012	0,000	0,000	0,001
3	25,03	0,009	0,000	<b>0,882</b>	0,032	0,001	0,000	0,027	0,000	0,002	<b>0,198</b>	0,001
4	25,73	0,010	0,013	<b>0,106</b>	<b>0,943</b>	0,004	0,008	<b>0,133</b>	<b>0,208</b>	0,000	0,000	0,000
5	65,40	0,028	0,000	0,005	0,002	<b>0,618</b>	<b>0,052</b>	<b>0,067</b>	0,013	0,002	0,001	<b>0,332</b>
6	69,82	0,001	0,033	0,006	0,005	<b>0,181</b>	<b>0,895</b>	<b>0,202</b>	<b>0,070</b>	0,001	0,000	0,001
7	70,13	0,001	0,000	<b>0,118</b>	0,003	<b>0,080</b>	0,008	<b>0,239</b>	0,015	0,000	0,002	0,043
8	74,99	0,007	0,017	0,029	<b>0,128</b>	<b>0,110</b>	<b>0,500</b>	<b>0,486</b>	<b>0,537</b>	0,002	0,000	0,000
9	83,50	0,004	0,000	0,001	0,000	<b>0,145</b>	0,014	0,015	0,015	<b>0,758</b>	0,009	0,000
10	87,91	0,006	0,018	0,033	<b>0,332</b>	0,030	<b>0,146</b>	<b>0,172</b>	<b>0,647</b>	0,002	0,000	0,001
11	115,39	0,006	0,001	<b>0,138</b>	0,004	0,012	0,001	0,002	0,001	0,017	<b>0,959</b>	0,007
12	125,34	0,042	0,001	0,003	0,001	<b>0,080</b>	0,008	0,016	0,007	<b>0,458</b>	0,023	<b>0,684</b>

### D.3 OMA

This measurement was performed in the same way as described in section 7.3 but this time with six hands exciting the structure for 5 minutes (301,3 s). The results are given in Table D - 5, Figure D - 11, Figure D - 12-Figure D - 15 and Table D - 6. Time signals, frequency plots and histograms for the four measurement sequences are presented in Figure D - 16-Figure D - 18.

Table D - 5: Extracted eigenfrequencies and damping ratios.

Mode	Eigenfrequency SSI (Hz)	Damping ratio SSI (%)	Eigenfrequency EFDD (Hz)	Damping ratio EFDD (%)
1	6,09	3,63	6,19	1,94
2	9,72	2,64	9,67	1,60
3	25,46	3,52	-	-
4	25,65	1,10	25,75	0,60
5	74,30	0,81	75,03	0,77
6	81,00	1,54	81,49	1,51
7	95,22	1,06	95,39	0,43
8	99,18	0,025	99,27	0,73
9	120,41	0,40	120,50	0,42
10	-	-	-	-
11	126,55	0,24	126,60	0,21
12	137,87	0,28	137,80	0,28

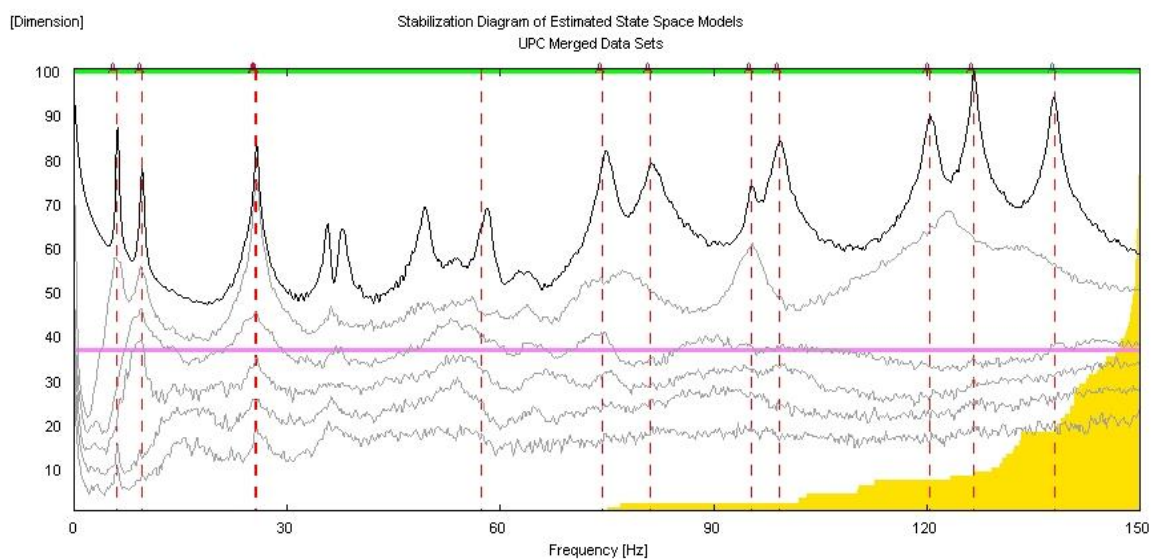


Figure D - 11: Stabilization diagram and estimated mode shapes (dashed lines) from SSI.

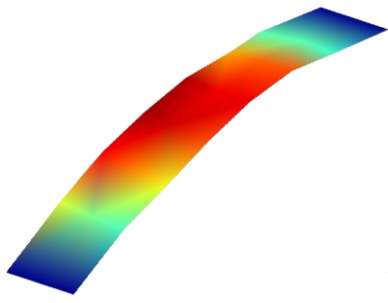
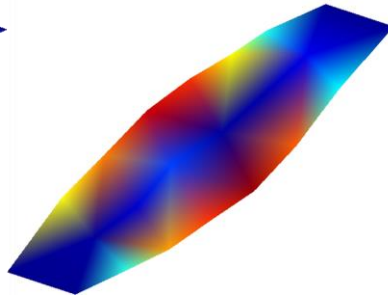
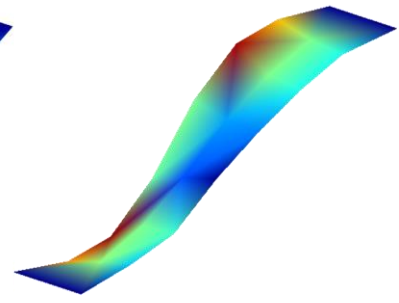


Figure D - 12: Mode 1: 6.09 Hz



Mode 2: 9.72 Hz



Mode 3: 25.46 Hz

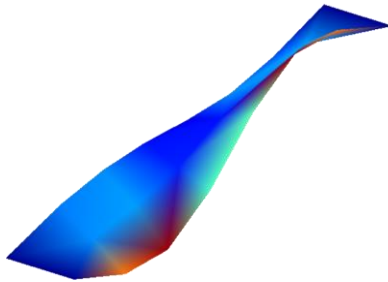
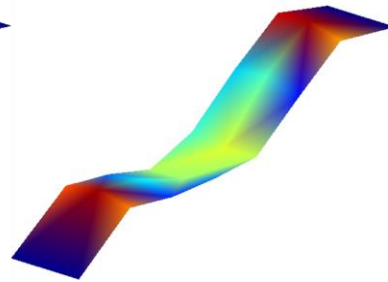
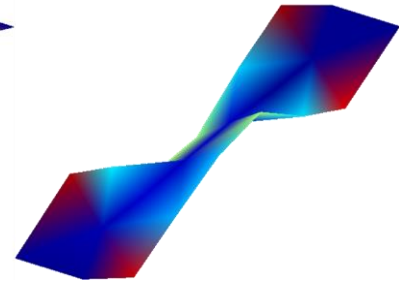


Figure D - 13: Mode 4: 25.65 Hz



Mode 5: 74.30 Hz



Mode 6: 81.00 Hz

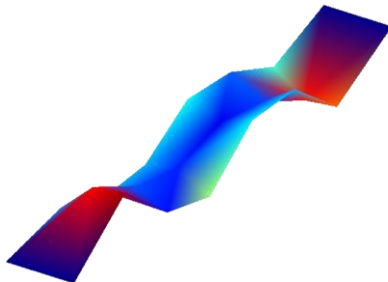
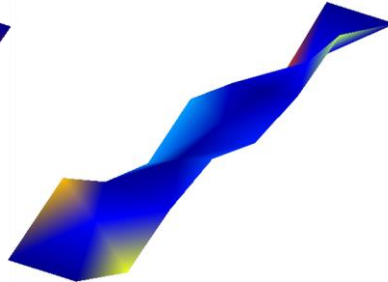
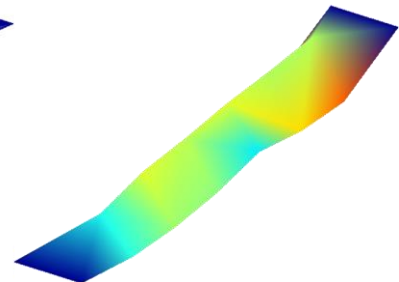


Figure D - 14: Mode 7: 95.22 Hz



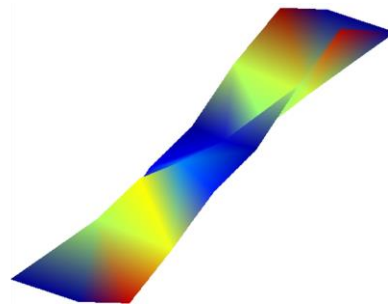
Mode 8: 99.18 Hz



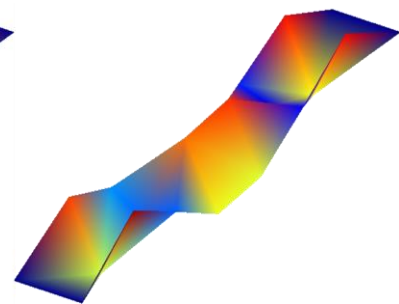
Mode 9: 120.41 Hz



Figure D - 15: Mode 10: -



Mode 11: 126.55 Hz



Mode 12: 137.87 Hz

Table D - 6: MAC table comparing numerical and SSI extracted mode shapes.

	Nr	1	2	3	4	5	6	7	8	9	11	12
Nr	OMA	6,09	9,72	25,46	25,65	74,30	81,00	95,22	99,18	120,41	126,55	137,87
	SSI											
ABAQUS												
1	6,05	<b>0,971</b>	0,001	0,002	0,000	0,017	0,001	0,000	0,000	<b>0,095</b>	0,000	0,004
2	8,79	0,003	<b>0,956</b>	0,003	0,005	0,002	0,022	0,000	0,005	0,000	0,000	0,001
3	25,03	0,000	0,002	<b>0,862</b>	<b>0,313</b>	0,001	0,000	<b>0,073</b>	0,003	0,005	<b>0,208</b>	0,000
4	25,73	0,006	0,009	<b>0,109</b>	<b>0,676</b>	0,005	0,003	0,019	<b>0,225</b>	0,000	0,001	0,000
5	65,40	0,031	0,001	0,006	0,001	<b>0,762</b>	0,002	0,033	0,000	0,001	0,001	<b>0,311</b>
6	69,82	0,000	0,045	0,000	0,004	0,006	<b>0,946</b>	0,006	0,028	0,001	0,000	0,000
7	70,13	0,003	0,001	<b>0,096</b>	0,036	<b>0,090</b>	0,000	<b>0,627</b>	0,022	0,000	0,003	0,040
8	74,99	0,001	0,012	0,009	<b>0,098</b>	0,004	<b>0,476</b>	0,010	<b>0,442</b>	0,001	0,000	0,000
9	83,50	0,002	0,000	0,000	0,001	<b>0,166</b>	0,000	0,000	0,004	<b>0,748</b>	0,004	0,001
10	87,91	0,004	0,023	0,027	<b>0,258</b>	0,000	<b>0,180</b>	<b>0,085</b>	<b>0,728</b>	0,003	0,000	0,000
11	115,39	0,000	0,004	<b>0,163</b>	<b>0,054</b>	0,005	0,000	0,029	0,002	0,021	<b>0,968</b>	0,002
12	125,34	<b>0,060</b>	0,001	0,004	0,001	<b>0,070</b>	0,002	0,001	0,003	<b>0,436</b>	0,011	<b>0,719</b>

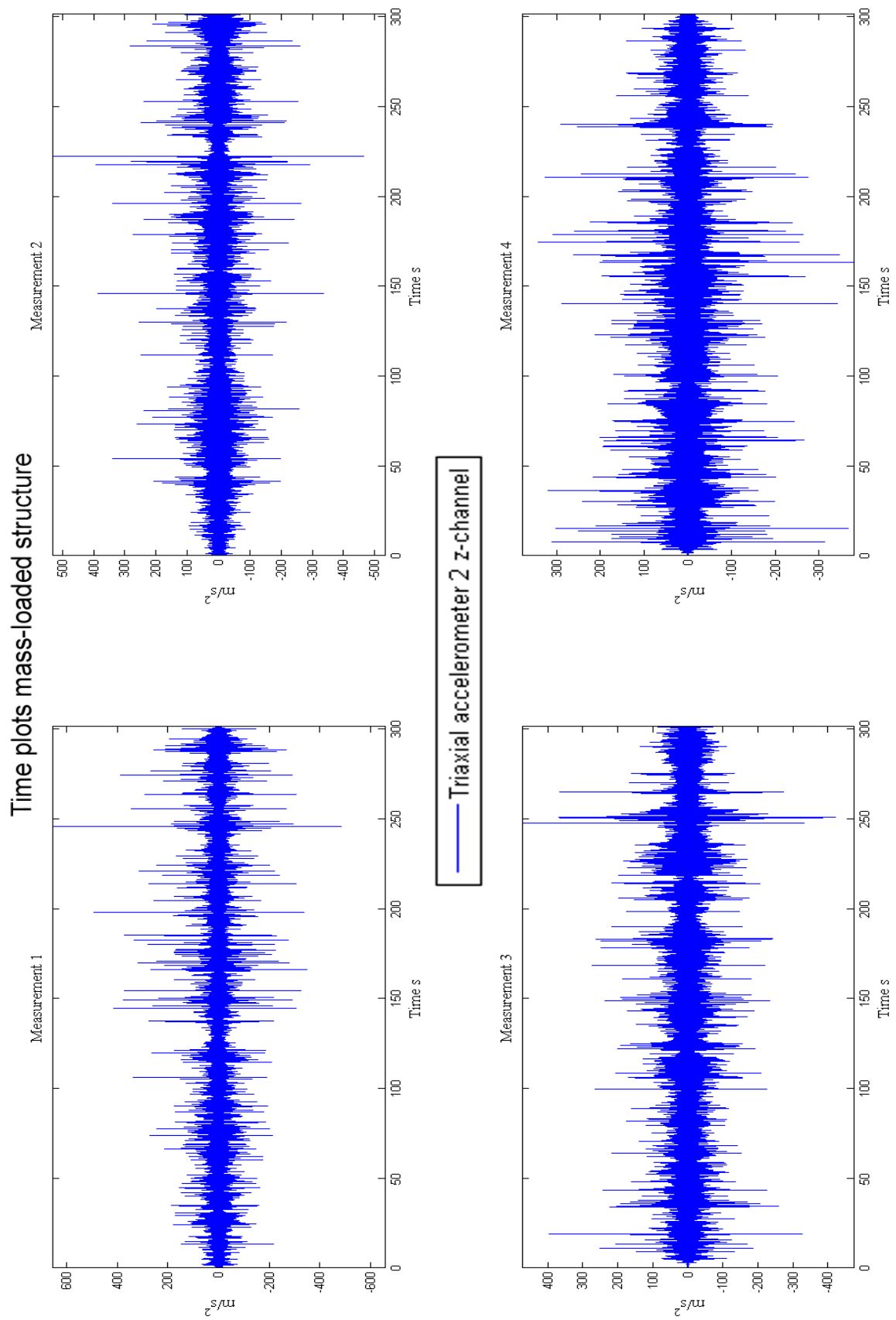


Figure D - 16: Time plots for reference accelerometer 2 z-channel.

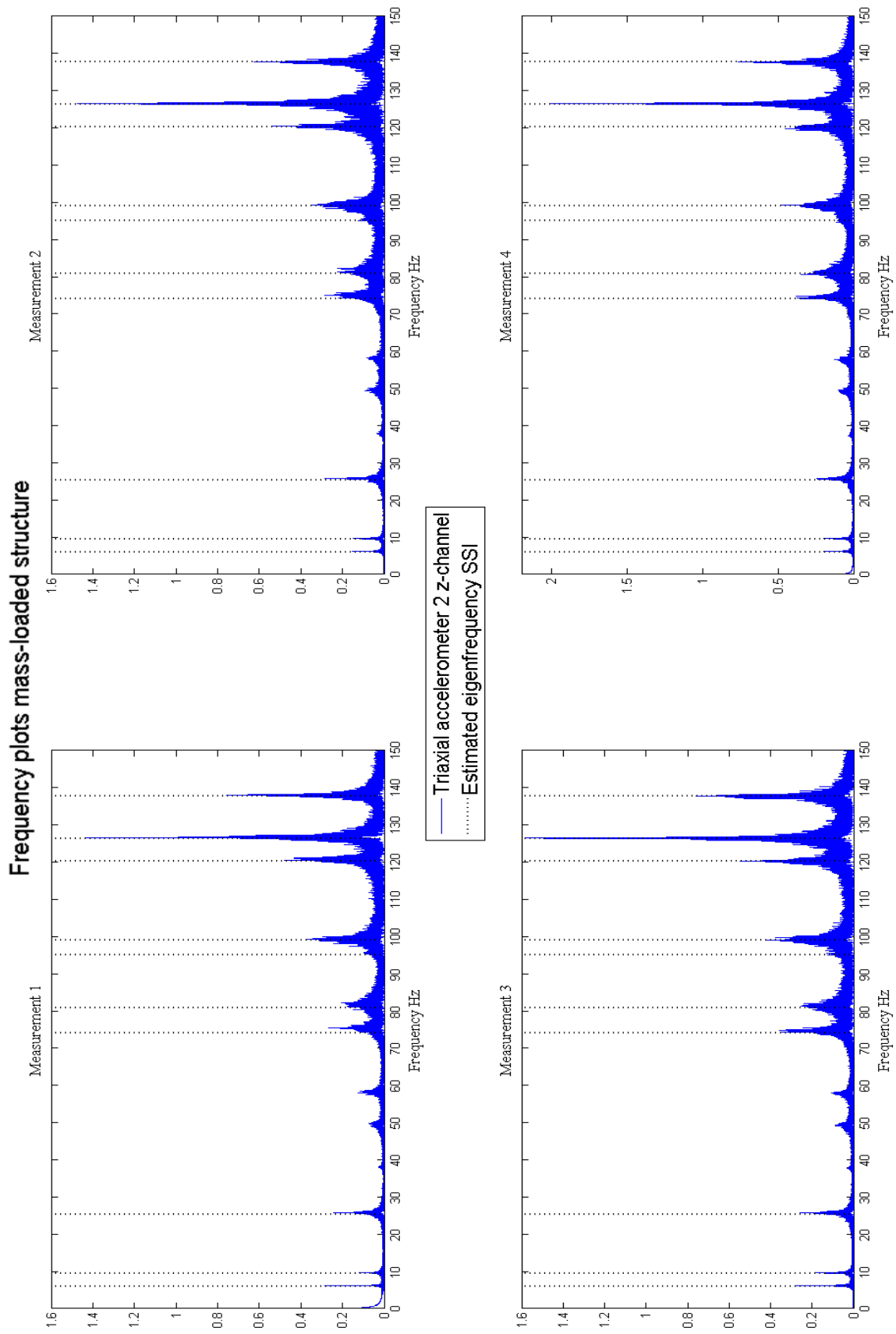


Figure D - 17: Frequency plots for reference accelerometer 2 z-channel.

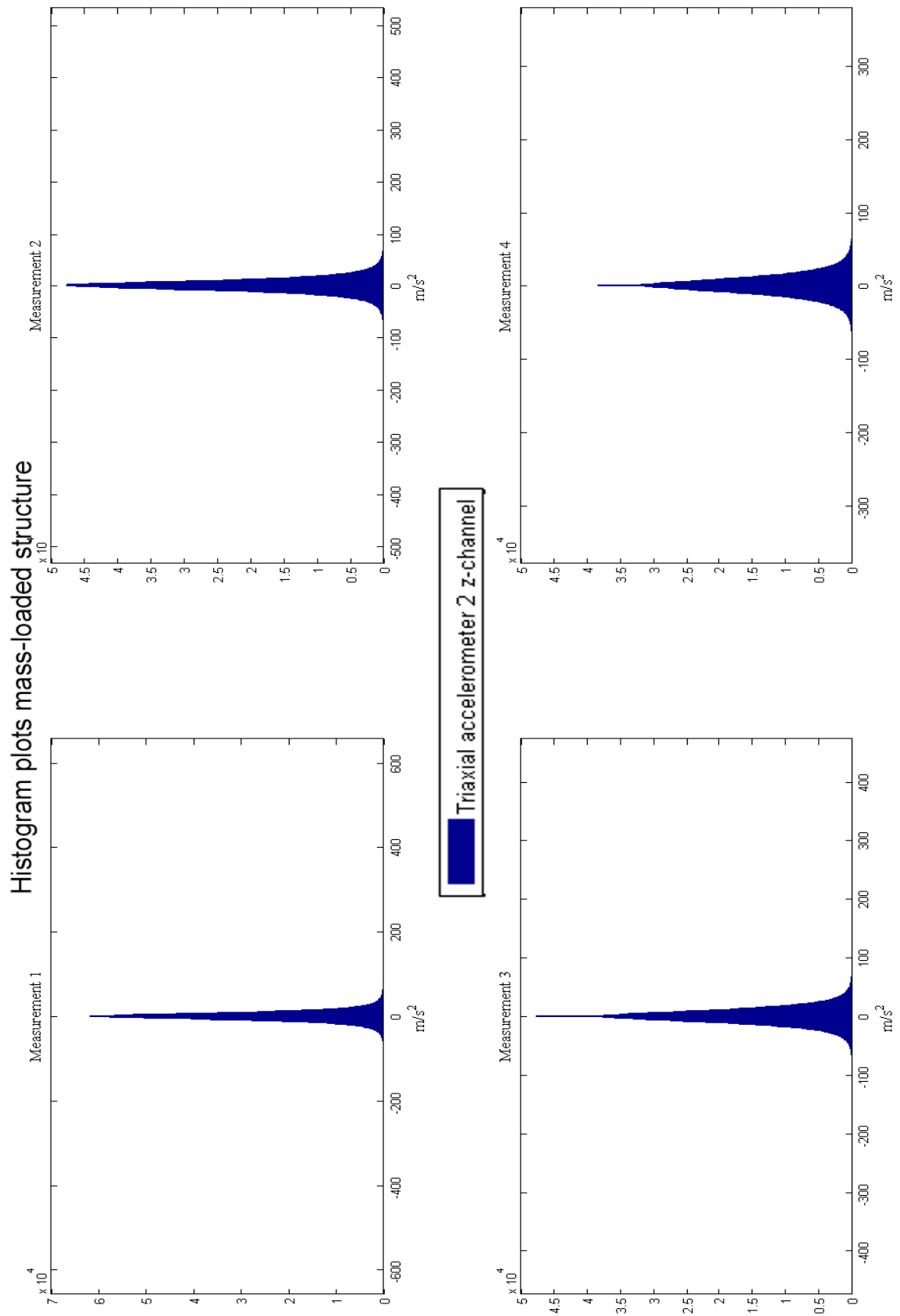


Figure D - 18: Histograms for reference accelerometer 2 z-channel.



# Appendix E

The Matlab codes that were used to generate some of the figures in chapter 2 are given in this appendix.

## E.1 SDOF Example

Figure E - 1 describes the SDOF system that has been used to generate Figure 2.2 - Figure 2.6 and Figure A - 1 - Figure A - 4.

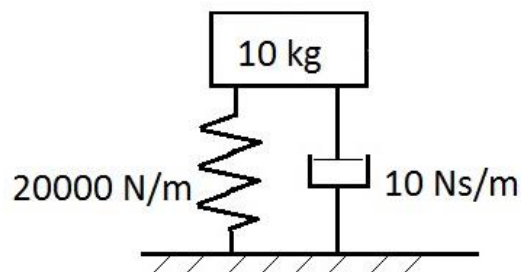


Figure E - 1: SDOF example.

```
%-----  
---  
  
%SDOF Example  
  
%Tobias Kristensson  
  
%Master thesis  
  
%Last modified 2014-09-22  
  
%-----  
---  
  
%% Settings  
format long  
clear all  
close all  
  
FontSize=12;  
Titlesize=12;  
FontName='Times New Roman';  
  
n=2000;           %Number of points in plots  
  
m=10;            %Mass kg  
c=10;            %Dampingcoefficient Ns/m  
k=20000;         %Stiffness N/m
```

```

w=linspace(0,200,n);
omega_n=sqrt(k/m);

%% Receptance plots

Hr=1.0./((-m.*w.*w+k)+j.*c.*w); %Eq. (2.23)

%-----3D plot-----
---
figure(1)
plot3(w,real(Hr),imag(Hr),'k')
xlabel('Frequency rad/s','FontName',FontName,'FontSize',FontSize)
ylabel('Real (H_u)','FontName',FontName,'FontSize',FontSize)
zlabel('Imag (H_u)','FontName',FontName,'FontSize',FontSize)
pause

%-----Nyquist plot-----
---
figure(2)
subplot(1,2,2)
plot(real(Hr),imag(Hr),'k-o')
% title('FRF Nyquist diagram','FontName',FontName,'FontSize',Titlesize)
xlabel('Real (H_u)','FontName',FontName,'FontSize',FontSize)
ylabel('Imag (H_u)','FontName',FontName,'FontSize',FontSize)
pause

%-----Real plot of FRF-----
---
figure(3)
subplot(3,2,1);
plot(w,real(Hr),'k')
% title('Receptance FRF','FontName',FontName,'FontSize',Titlesize)
xlabel('Frequency rad/s','FontName',FontName,'FontSize',FontSize)
ylabel('Real (H_u)','FontName',FontName,'FontSize',FontSize)

%-----Imaginary plot of FRF-----
---
figure(3)
subplot(3,2,2);
plot(w,imag(Hr),'k')
% title('Receptance FRF','FontName',FontName,'FontSize',Titlesize)
xlabel('Frequency rad/s','FontName',FontName,'FontSize',FontSize)
ylabel('Imag (H_u)','FontName',FontName,'FontSize',FontSize)

%-----Magnitude plot of FRF-----
---
figure(2)
subplot(1,2,1)
M=(real(Hr).^2+imag(Hr).^2).^(1/2); %Magnitude
plot(w,M,'k')
% title('Receptance FRF','FontName',FontName,'FontSize',Titlesize)
xlabel('Frequency rad/s','FontName',FontName,'FontSize',FontSize)
ylabel('Magnitude (H_u)','FontName',FontName,'FontSize',FontSize)
pause

%% Mobility plots

```

```

Hm=(j*w)./((-m.*w.*w+k)+j.*c.*w); % Eq.(2.23)*jw

%-----Real plot of FRF-----
---
figure(3)
subplot(3,2,3);
plot(w,real(Hm),'k')
% title('Mobility FRF','FontName',FontName,'FontSize',Titlesize)
xlabel('Frequency rad/s','FontName',FontName,'FontSize',FontSize)
ylabel('Real (H_v)','FontName',FontName,'FontSize',FontSize)

%-----Imaginary plot of FRF-----
---
figure(3)
subplot(3,2,4);
plot(w,imag(Hm),'k')
% title('Mobility FRF','FontName',FontName,'FontSize',Titlesize)
xlabel('Frequency rad/s','FontName',FontName,'FontSize',FontSize)
ylabel('Imag (H_v)','FontName',FontName,'FontSize',FontSize)

%% Accelerance plots

Ha=(-w.^2)./((-m.*w.*w+k)+j.*c.*w); % Eq.(2.23)*jw*jw

%-----Real plot of FRF-----
---
figure(3)
subplot(3,2,5);
plot(w,real(Ha),'k')
% title('Accelerance FRF','FontName',FontName,'FontSize',Titlesize)
xlabel('Frequency rad/s','FontName',FontName,'FontSize',FontSize)
ylabel('Real (H_a)','FontName',FontName,'FontSize',FontSize)

%-----Imaginary plot of FRF-----
---
figure(3)
subplot(3,2,6);
plot(w,imag(Ha),'k')
% title('Accelerance FRF','FontName',FontName,'FontSize',Titlesize)
xlabel('Frequency rad/s','FontName',FontName,'FontSize',FontSize)
ylabel('Imag (H_a)','FontName',FontName,'FontSize',FontSize)
pause

%----Logaritmic plot of receptance-----
---
figure(5)
semilogy(w,M,'k-')
xlabel('Frequency rad/s','FontName',FontName,'FontSize',FontSize)
ylabel('Log Magnitude','FontName',FontName,'FontSize',FontSize)
hold on

%----Logaritmic plot of Mobility-----
---
M=(real(Hm).^2+imag(Hm).^2).^(1/2); %Magnitude
semilogy(w,M,'k--')
hold on

```

```

%----Logaritmik plot of Accelerance-----
---
Ma=(real(Ha).^2+imag(Ha).^2).^(1/2); %Magnitude
semilogy(w, Ma, 'k-.')
legend('Receptance', 'Mobility', 'Accelerance', 'location', 'NorthEast')
pause

%% Deformation response factor Rd and phase angle

wvec=linspace(0,3,n);
zeta=c/(2*m*omega_n);
E=[zeta 0.1 0.2 0.7 1];

figure(6)
subplot(1,2,1)
Rdmat=[];
for i=1:n
    for r=1:5
        Rd=abs(1/(1-wvec(i)^2+j*2*E(r)*wvec(i))); %Eq. (2.26)
        Rdmat(r,i)=Rd;
    end
end
plot(wvec, Rdmat(1,:), 'k', wvec, Rdmat(2,:), 'k--', wvec, Rdmat(3,:), 'k-
.', wvec, Rdmat(4,:), 'k:', wvec, Rdmat(5,:), 'c')
axis([0 3 0 10])
xlabel('\omega/\omega_n', 'FontName', FontName, 'FontSize', FontSize)
ylabel('Deformation response factor R
_d', 'FontName', FontName, 'FontSize', FontSize)
legend('\zeta=0.011', '\zeta=0.1', '\zeta=0.2', '\zeta=0.7', '\zeta=1', 'loca
tion', 'NorthEast')

%Phase angle
figure(6)
subplot(1,2,2)
Omat=[]
for i=1:n
    for r=1:5
        O=angle(1-wvec(i)^2+j*2*E(r)*wvec(i))*180/pi;
        Omat(r,i)=O;
    end
end
plot(wvec, Omat(1,:), 'k', wvec, Omat(2,:), 'k--', wvec, Omat(3,:), 'k-
.', wvec, Omat(4,:), 'k:', wvec, Omat(5,:), 'c')
axis([0 3 0 180])
xlabel('\omega/\omega_n', 'FontName', FontName, 'FontSize', FontSize)
ylabel('Phase angle \phi', 'FontName', FontName, 'FontSize', FontSize)
legend('\zeta=0.011', '\zeta=0.1', '\zeta=0.2', '\zeta=0.7', '\zeta=1', 'loca
tion', 'SouthEast')
pause

%% Impulse response plot
a=[m, c, k];
b=[0, 0, 1];
[A, s, q]=residue(b, a);

figure(18)
t=linspace(0,4,n);

```

```

x_t=A(1).*exp(s(1).*t)+A(2).*exp(s(2).*t); %Eq. (2.22)
decay=2*imag(A(2))*exp(real(s)*t);
plot(t,x_t,'-k',t,decay,'--r')
xlabel('Time s','FontName',FontName,'FontSize',FontSize)
ylabel('Amplitude','FontName',FontName,'FontSize',FontSize)
legend('h(t)','Xe^{-\sigma t}')
pause

%% Laplace domain 3D plots
rotation=65;
el=25;

figure(19)
[sigma,omega]=meshgrid(-50:2:50,-80:2:80);

s1=sigma+j*omega; %Eq. (2.12)

H=A(1)./(s1-s(1))+A(2)./(s1-s(2)); %Eq. (2.20)

surf(real(H))
title('Real Part','FontName',FontName,'FontSize',Titlesize)
xlabel('Real (s)','FontName',FontName,'FontSize',FontSize)
ylabel('Imag (s)','FontName',FontName,'FontSize',FontSize)
zlabel('Real H(s)','FontName',FontName,'FontSize',FontSize)
view(rotation,el);

figure(20)
surf(imag(H))
title('Imaginary Part','FontName',FontName,'FontSize',Titlesize)
xlabel('Real (s)','FontName',FontName,'FontSize',FontSize)
ylabel('Imag (s)','FontName',FontName,'FontSize',FontSize)
zlabel('Imag H(s)','FontName',FontName,'FontSize',FontSize)
view([rotation,el]);

figure(23)
subplot(2,1,1);
surf(abs(H))
title('Magnitude','FontName',FontName,'FontSize',Titlesize)
xlabel('Real (s)','FontName',FontName,'FontSize',FontSize)
ylabel('Imag (s)','FontName',FontName,'FontSize',FontSize)
zlabel('Magnitude H(s)','FontName',FontName,'FontSize',FontSize)
view([rotation,el]);

figure(23)
subplot(2,1,2);
surf(angle(H))
title('Phase','FontName',FontName,'FontSize',Titlesize)
xlabel('Real (s)','FontName',FontName,'FontSize',FontSize)
ylabel('Imag (s)','FontName',FontName,'FontSize',FontSize)
zlabel('Phase H(s)','FontName',FontName,'FontSize',FontSize)
view([rotation,el]);

figure(22)
surf(log(abs(H)))
title('Log Magnitude','FontName',FontName,'FontSize',Titlesize)
xlabel('Real (s)','FontName',FontName,'FontSize',FontSize)
ylabel('Imag (s)','FontName',FontName,'FontSize',FontSize)

```

```
zlabel('Log magnitude H(w)', 'FontName', FontName, 'FontSize', FontSize)
view([rotation, el]);
pause
close all
```

## E.2 MDOF Example

Figure E - 2 describes the MDOF system that was used to create Figure 2.8, Figure A - 5 and Figure A - 6.

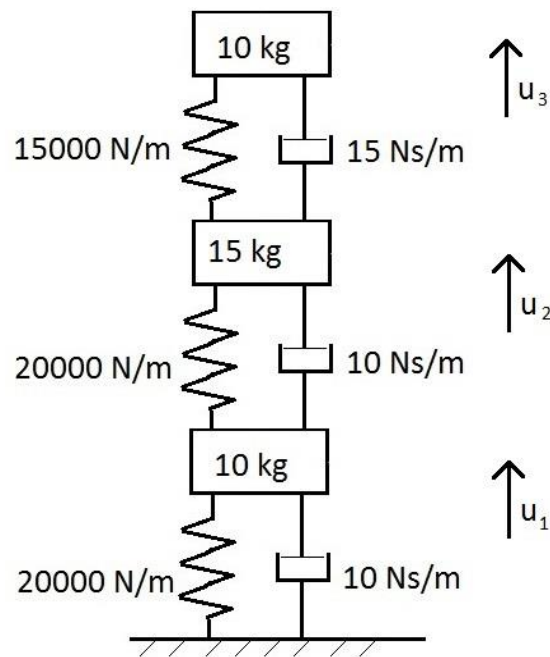


Figure E - 2: MDOF (3DOF) example.

```

%-----
---

%MDOF Example

%Tobias Kristensson

%Master thesis 2014

%Last modified 2014-09-24

%-----
---

%% Settings
clear all
close all
n=200;

FontSize=12;
Titlesize=12;
FontName='Times New Roman';

```

```

M=[10 0 0;0 15 0;0 0 10]; %Mass matrix
K=[20+20 -20 0;-20 20+15 -15;0 -15 15]*10^3; %Stiffness matrix
C=[10+10 -10 0;-10 10+15 -15;0 -15 15]; %Damping matrix

grey=[1 1 1]*0.7;

%% Calculate eigenfrequencies and eigenvectors
[frequencies, O]=eigen(M,K)
omegasquare=(frequencies.*2*pi).^2;
yvec=linspace(10^-9,10^-1,n)';
fvec=ones(n,1);

%% Calculating the FRF using AbraVibe Toolbox
FRFnr=input('FRFnr'); %(for 3DOF sytem FRFnr=1,2,3)
f=(0:0.001:30)';
Hd=mck2frf(f,M,C,K,1,FRFnr,'d'); %Using Eq.(2.38)

figure(1)
subplot(2,1,1)
H1=mck2frf(f,M,C,K,1,1,'d');
H2=mck2frf(f,M,C,K,1,2,'d');
H3=mck2frf(f,M,C,K,1,3,'d');
semilogy(f,abs(H1),'k',f,abs(H2),'k--',f,abs(H3),'k-')
xlabel('Frequency Hz','FontName',FontName,'FontSize',FontSize)
ylabel('FRF m/N','FontName',FontName,'FontSize',FontSize)
axis([0 30 10^-8 10^-2])
legend('H_1','H_2','H_3','location','northeast')
subplot(2,1,2)
yvec=linspace(-200,200,n)';
plot(f,angledeg(H1),'k',f,angledeg(H2),'k--',f,angledeg(H3),'k-')
xlabel('Frequency Hz','FontName',FontName,'FontSize',FontSize)
ylabel('Phase Degrees','FontName',FontName,'FontSize',FontSize)
legend('H_1','H_2','H_3','location','northeast')

%% Plot Impulse Response Function
figure(2)
subplot(2,1,1)
[h5,t]=frf2ir(Hd,f); %Using Eq.(2.39)
plot(t,h5,'k')
xlabel('Time s','FontName',FontName,'FontSize',FontSize)
ylabel('h(t)','FontName',FontName,'FontSize',FontSize)
axis([0 35 -2e-3 2e-3])

%% Plot Impulse Response Function zoomed
figure(2)
subplot(2,1,2)
[h5,t]=frf2ir(Hd,f);
plot(t,h5,'k')
xlabel('Time s','FontName',FontName,'FontSize',FontSize)
ylabel('h(t)','FontName',FontName,'FontSize',FontSize)
text(0.25, -1.5e-3,'Transient response')
text(3, -1.5e-3,'Steady-state response')
axis([0 5 -2e-3 2e-3])

%% 3D view of FRF
zfreal=-5*10^-3*ones(length(f),1);

```

```
yfimag=3*10^-3*ones(length(f),1);
xfreimag=zeros(length(f),1);
rotation=34;
el=35;

figure(3)
plot3(f,real(Hd),imag(Hd),'k')
hold on
plot3(f,real(Hd),zfreal,'color',grey)
hold on
plot3(f,yfimag,imag(Hd),'color',grey)
hold on
plot3(xfreimag,real(Hd),imag(Hd),'color',grey)
xlabel('Frequency Hz','FontName',FontName,'FontSize',FontSize)
ylabel('Real FRF','FontName',FontName,'FontSize',FontSize)
zlabel('Imaginary FRF','FontName',FontName,'FontSize',FontSize)
view(rotation,el);
pause
close all
```